Spatio-temporal variations in aerosol properties over western India

A THESIS

submitted to

SARDAR PATEL UNIVERSITY

for the Award of

DOCTOR OF PHILOSOPHY

in

PHYSICS

by

Rajesh T. A.

Under the Supervision of

Prof. S. Ramachandran
Guide
Space and Atmospheric Sciences Division
Physical Research Laboratory
Ahmedabad, India

Prof. P. C. Vinodkumar
Co-Guide
Department of Physics
Sardar Patel University
Vallabh Vidyanagar, India

September 2018

Date: 17/Sep/2018

CERTIFICATE

Certified that the work incorporated in this thesis entitled **"Spatio-temporal variations in aerosol properties over western India"**, submitted by **Mr. Rajesh T. A.** comprises the results of independent and original investigations carried out. The materials obtained from other sources and used in the thesis have been duly acknowledged appropriately.

Place: Vallabh Vidyanagar
Date: 17/Sep/2018
Registration No.: 640, Date: 29/10/2013

Rajesh T. A.
(Research Student)

Certified that the work mentioned above was carried out under my/our guidance.

Prof. S. Ramachandran
(Research Guide)

Prof. P. C. Vinodkumar
(Research Co-Guide)

Forwarded Through:

Prof. P. Janardhan
Dean
Physical Research Laboratory
Ahmedabad

प्रो. जनार्दन पद्मनाभन
Prof. Janardhan Padmanabhan
डीन, भौतिक अनुसंधान प्रयोगशाला
Dean, Physical Research Laboratory
(भारत सरकार, अंतरिक्ष विभाग की यूनिट)
(Unit of Department of Space, Govt. of India)
नवरंगपुरा, अहमदाबाद-380 009 भारत
Navrangpura, Ahmedabad-380 009 India

Prof. P. C. Vinodkumar
Head
Department of Physics
Sardar Patel University

HEAD
DEPARTMENT OF PHYSICS
SARDAR PATEL UNIVERSITY
VALLABH VIDYANAGAR

DECLARATION

*I, Rajesh T. A., S/o Mr. T. K. Ayyappen, resident of D-5, PRL Residences, Vikramnagar, Bopal-Ambli Road, Ahmedabad - 380058, hereby declare that the research work incorporated in the present thesis entitled "***Spatio-temporal variations in aerosol properties over western India***" is my own work and is original. This work (in part or in full) has not been submitted to any University for the award of a Degree or a Diploma. I have properly acknowledged the material collected from secondary sources wherever required. I solely own the responsibility for the originality of the entire content.*

Date: Rajesh T. A.

Dedicated

To my

Mummy (Omana), Pappa (Ayyappen),

Wife (Seena), and Son (Rishabh)

Acknowledgments

It is a great pleasure to thank all those who helped, supported, and encouraged me in various ways in the accomplishment of this thesis.

At the outset, I would like to express my sincere gratitude to my thesis guide, Prof. S. Ramachandran (Chairperson, Space and Atmospheric Sciences Division, Physical Research Laboratory), for his invaluable guidance, fruitful discussions, motivation, constant encouragement, kind support and cooperation at each and every stage of the work. This work would not have been possible without his active support. His discussions were critical to understanding and building upon the results of my research. I owe my indebtedness for his sincerity, patience, deep concern and wholehearted support for the fulfillment of this thesis.

I am extremely thankful to my thesis co-guide Prof. P. C. Vinodkumar (Head, Department of Physics, Sardar Patel University) for his support and cooperation during the thesis tenure.

I am greatly indebted to Dr. Anil Bhardwaj, Director, Physical Research Laboratory (PRL), for providing all the necessary facilities to carry out the work.

I am grateful to Prof. U. H. Patel (former Head), Department of Physics, Sardar Patel University for her guidance, support and cooperation during this work. I am also very thankful to all the faculty members of the department for their encouragement. My thanks are also to all other staff members of the department and university office (Academic section and Accounts section) for their continuous support and help.

I thank Prof. J. N. Goswami (Former Director), Prof. U. Sarkar (Former Director), Prof. P. Janardhan (Dean), Prof. Shyam Lal, and (Late) Prof. R. Ramesh for encouragement at various stages of my research. I would like to thank Dr. Y. B. Acharya for the kind support and guidance. I also thank Dr. Bhushit (Head

Academic services) and Academic Committee for help rendered during the thesis work. I would like to thank Director office (Pauline madam), Registrar office (Pradeep bhai), and Dean office (Hiral ben) for the continuous support and help.

My special thanks to Venkataramani for his unconditional support, cooperation, guidance and discussions on various occasions during the study period. I thank my colleagues Malai, Vishnu, Sunilkumar, Mitesh, and Vinchhi bhai for their association and help in managing the various scientific instruments and laboratory. I acknowledge the kind help and support rendered by Atul regarding computer related issues, and I always found him ready for help without any hesitation. I would like to express my sincere thanks to all members of Space and Atmospheric Sciences Division, especially Prof. R. Sekar, Prof. D. Pallamraju, Dr. D. Chakrabarty, Dr. Som Kumar Sharma, Dr. Lokesh Sahu, Dr. Harish Gadhavi, Dr. A. Guharay, RP, Aditya, Pankaj, Shashank, Anil, Pradeep, Sneha, Mahipat, Hetal, Atar, Bighnaraj for their help in various stages.

I am grateful to the members of the PRL IR Gurushikhar Observatory, Mt. Abu; Rajesh bhai, Mathur ji, Kothari ji, Jain bhai, Padam bhai, Nafees, and all other members for providing facilities for smoothly carrying out the experiments at Gurushikhar.

I acknowledge the NOAA Air Resources Laboratory (ARL) for the provision of the HYSPLIT transport and dispersion model and/or READY website (http://www.ready.noaa.gov) used in this work. I acknowledge NCEP Reanalysis derived data provided by the NOAA/OAR/ESRL PSD, Boulder, Colorado, USA, from their Web site at https://www.esrl.noaa.gov/psd/. I also acknowledge MODIS, OMI, AIRS, and TRMM data used in the study which are downloaded from the GES-DISC Interactive Online Visualization and Analysis Infrastructure, NASA.

I would like to thank the members of the Computer center; Jigar bhai, Tejas, Alok, Hitendra, Girish, Rahul, Prashant, and all other members for the help in computer related problems. I acknowledge the help from Nishtha madam, and all the members of PRL library. I wish to thank the members of the Civil and Maintenance department; Mahirale ji, Sanjay bhai, Viral bhai, Ketan bhai, Ram Lakhan, Nambiar ji, Rakesh bhai, Nilesh bhai, Jitu bhai, Sandip bhai, Vijay bhai, Vasu bhai, Rajesh bhai, and Shailesh bhai for their help in main-

taining the laboratory. The support extended by the members of the Workshop department; Ubale ji, Hitesh bhai, Vishnu bhai, Rajesh bhai, Vipul bhai, Bipin, Pramod regarding various development and maintenance works in the laboratory are gratefully acknowledged.

I wish to express my sincere thanks to the members of the Purchase department; Hemal bhai, Siva bhai, Nandini madam, Priti madam (now in Accounts), Manisha, Amee (now in Accounts), and Raza for their help in procuring the materials on time. I would like to thank all the members of the Stores department; Rashmi bhai, Sunil bhai, Neethu, and all other members for rendering their services promptly. I am grateful to the cooperation and support received from the Accounts department; Dixit sir (presently Registrar, PRL), Yugal bhai, Suresh bhai, Hitesh bhai, Keyur bhai, Ishita (now in Purchase), and Parul madam (now in Purchase). I would like to thank the members of the Administration; Ratin, Anand bhai, Sasi, Senthil Babu, Richa, Jayashree madam, and Kartik bhai, and all other members for their help in various stages. Also my sincere thanks to the members of Dispensary; Dr. Shital, Dr. Samir, and all other members for providing me the medical assistance as and when required.

I thank my friends Panda ji, Sudheer, Ravi da, Anil bhai, Neeraj bhai, Gautum, Sachi for their nice company and help. I would like to thank Hitesh, Manan, Hardik, Tanvi, Bhumi, Ankit for providing a friendly atmosphere in the Department of Physics, Sardar Patel University. I am thankful to Dr. Rohit Srivastava, ICCSIR for his support and cooperation.

I sincerely express my gratitude towards my parents for their encouragement, care, concern and blessings throughout my life. Perhaps words are inadequate to express any kind of acknowledgement for my wife, Seena and son, Rishabh, without whom I never would have made it through this process. I have found them always standing with me when required. Without their moral support, understanding and cooperation, it would have been impossible for me to finish this work.

Rajesh T. A.

Abstract

Aerosols exhibit large spatio-temporal variabilities in their optical, physical and chemical properties, and can influence our planet by interacting with incoming solar and outgoing terrestrial radiation. The objectives of the thesis are to characterize the spatial and temporal variabilities in optical and physical properties of aerosols, source apportion black carbon aerosols, and to estimate the aerosol radiative forcing and their seasonal variability over distinct environments (urban, and high altitude remote). Aerosol characteristics were measured and examined over an urban (characterized by high aerosol concentrations dominated by anthropogenic aerosols) (Ahmedabad (23.03^{o}N, 72.55^{o}E, 55 m above mean sea level (AMSL)), and a high altitude remote region (with low aerosol concentration dominated by transport mechanisms) (Gurushikhar (24.65^{o}N, 72.78^{o}E, 1680 m AMSL). These study locations in western India are influenced by similar meteorology. The influence of atmospheric aerosols on the Earth-atmosphere radiation budget is examined using radiative transfer model. The shortwave aerosol radiative forcing is estimated using two single scattering albedo (*SSA*) values, one derived from the surface measurements of aerosol scattering and absorption coefficients (Method 1), and the other derived from remote sensing satellite measurement (Method 2). Further, to delineate the impact of black carbon (BC) aerosols on the Earth-atmosphere radiation budget the shortwave radiative forcing is computed for BC aerosols only over both the study locations.

Over the urban site, Ahmedabad, high values of scattering (β_{sca}) and absorption (β_{abs}) coefficients are found during morning and late evening due to a substantial increase in the anthropogenic activities and the atmospheric boundary layer dynamics. The scattering and absorption coefficients decrease as day advances (due to the evolution of the atmospheric boundary layer) and

attains a minimum value around afternoon. On the contrary, β_{sca} and β_{abs} over Gurushikhar are higher in the afternoon hrs when compared to forenoon and night because of atmospheric boundary layer dynamics which when accompanied with strong thermal convection aid an upward movement of pollutants to the observational site from the surrounding foothills.

The surface single scattering albedo shows a rare diurnal variability over Gurushikhar when compared to Ahmedabad. The near surface *SSA* is lower over Ahmedabad than Gurushikhar due to the dominance of absorbing aerosols over Ahmedabad from the anthropogenic emissions. The diurnal variation in *Ångström exponent* (α), *backscatter fraction* (*b*), and *asymmetry parameter* (*g*) over Gurushikhar do not show any morning or evening peaks as observed over Ahmedabad consistent with β_{sca} and β_{abs} variations. The maximum α observed during winter suggests the dominance of smaller size aerosols. The minimum α and *b*, and maximum *g* found during monsoon suggest the dominance of larger particles reaching the observational site from the marine region (Arabian Sea). The aerosol optical depth (*AOD*) over Gurushikhar is lower than Ahmedabad, as Ahmedabad is consistently influenced by the high magnitude of anthropogenic emissions, whereas the remote high altitude Gurushikhar is influenced by local and longrange transported aerosols.

The black carbon (BC) mass concentrations, and its equivalent BC from fossil fuel (BC_{FF}) and wood burning (BC_{WB}) exhibit strong diurnal variations over Ahmedabad compared to Gurushikhar due to the combined effects of the diurnal evolution of atmospheric boundary layer and consistent anthropogenic emissions. A distinct BC variation is observed over Gurushikhar with an increase in BC concentration during noontime as seen in β_{abs}. The diurnal contribution of BC_{FF} in total BC dominates throughout the day at both the observational sites. The annual mean contribution of BC_{FF} to total BC mass concentration is 80 and 72% over Ahmedabad and Gurushikhar respectively. This comparison indicates that even a high altitude remote site can have com-

parable fossil fuel contribution due to emissions produced over urban regions.

The study highlights the roles of single scattering albedo and aerosol optical depth (*AOD*) in the aerosol radiative forcing estimate. The differences in the forcing (*ARF*) for composite aerosol following Methods 1 and 2 is attributed to the differences in *SSA* values viz; surface and column. *ARF* estimated using surface *SSA* (lower) (Method 1) is always higher than column *SSA* (higher) (Method 2). The spectral aerosol properties for the black carbon (BC) aerosols exhibit significant variation in the *AOD* for BC aerosols only, but *SSA* and *g* remain the same. The forcing for BC aerosols only over Ahmedabad is higher by a factor of 2-3 than Gurushikhar when *AOD* also varies by the same factor, which confirms the linear dependence of *AOD* on the *ARF*. Over an urban location(Ahmedabad), *TOA* forcing is comparable for Method 1 and BC aerosols only, whereas significant variations are found in *SFC* and *ATM* forcing due to *AOD*. On the contrary, the *TOA* forcing flips sign from +ve to -ve following Method 2 as compared to BC aerosols only. Over a high altitude remote location (Gurushikhar), the forcing values are comparable from both the methods as the *SSA* values are comparable. The *TOA* forcing is always negative as *SSA* is higher over Gurushikhar. The study reveals that over an urban and a high altitude remote locations the BC aerosols alone can contribute in the range of 20 to 60% to the shortwave atmospheric forcing.

It is to be noted that when a high altitude remote site is in the same region as that of an urban aerosol source location, and both theses locations are governed by the same meteorology and atmospheric dynamics, then aerosol measurements over the high altitude region can serve as regional background which is the case here. Results indicate that although Gurushikhar is a high altitude remote site, it is significantly influenced by the local and longrange transported aerosols through convection and advection. The study reveals that Gurushikhar lacks anthropogenic emissions and the aerosol properties over Gurushikhar do not exhibit any significant inter-annual variability, confirming that Gurushikhar is a regional background site for aerosols in western

India. These results can be used as inputs in regional and global climate models for the estimation of climate forcing, to further improve our understanding on the spatio-temporal variability and radiative effects of aerosols over different environments.

Key words: *Atmospheric Aerosols, Scattering Coefficient, Absorption Coefficient, Single Scattering Albedo, Ångström Exponent, Backscatter Fraction, Asymmetry Parameter, Aerosol Optical Depth, Black Carbon, Source Apportionment, Radiative Forcing, Heating Rate, Nephelometer, Aethalometer, Remote Sensing, Optical Properties Model, Radiative Transfer Model, Observations, Urban Region, High Altitude Remote Site.*

Contents

List of Acronyms

ABL	Atmospheric Boundary Layer
AIRS	Atmospheric InfraRed Sounder
AMSL	Above Mean Sea Level
AOD	Aerosol Optical Depth
ATM	Atmosphere
ARF	Aerosol Radiative Forcing
BC	Black carbon
CO_2	Carbon dioxide
DISORT	Discrete Ordinates Radiative Transfer
DU	Dobson Unit
ECMWF	European Centre for Medium-Range Weather Forecast
EOS	Earth Observing System
HEPA	High Efficiency Particulate Air
HYSPLIT	Hybrid Single-Particle Lagrangian Integrated Trajectory
IPCC	Intergovernmental Panel on Climate Change
MODIS	MODerate resolution Imaging Spectroradiometer
NCAR	National Center for Atmospheric Research
NCEP	National Center for Environmental Prediction
OMI	Ozone Monitoring Instrument
OPAC	Optical Properties of Aerosols and Clouds
PPM	Part Per Million
PPT	Part Per Trillion
RH	Relative Humidity
RMS	Root Mean Square
SBDART	Santa Barbara DISORT Atmospheric Radiative Transfer
SF	Scaling Factor
SFC	Surface
SSA	Single Scattering Albedo
TOA	Top Of the Atmosphere
TRMM	Tropical Rainfall Measuring Mission

Notations and Symbols

α	Ångström exponent
β_{ext}	Aerosol extinction coefficient
β_{sca}	Aerosol scattering coefficient
β_{abs}	Aerosol absorption coefficient
β_{bsca}	Aerosol backscattering coefficient
σ	Mass specific attenuation cross section
λ	Wavelength
τ	Total optical depth
$\tau_{Rayleigh}$	Rayleigh scattering optical depth
$\tau_{aerosol}$	Aerosol optical depth
τ_{mol}	Optical depth due to molecular absorption
$\triangle P$	Pressure difference
A	Filter spot area
ARF_{ATM}	Atmospheric forcing
ARF_{SFC}	Surface forcing
ARF_{TOA}	Top of the atmospher forcing
b	Aerosol backscatter fraction
BC_{FF}	Fossil fuel component of *BC*
BC_{WB}	Wood burning component of *BC*
BC(Day)	Day time BC mass concentration
BC(Night)	Night time BC mass concentration
$BC(Day)_{FF}$	Fossil fuel component of *BC(Day)*
$BC(Night)_{FF}$	Fossil fuel component of *BC(Night)*
$BC(Day)_{WB}$	Wood burning component of *BC(Day)*
$BC(Night)_{WB}$	Wood burning component of *BC(Night)*
BC(M)	Morning (05:00-10:55 hrs) BC mass concentration
BC(A)	Afternoon (11:00-15:55 hrs) BC mass concentration
BC(E)	Evening (16:00-20:55 hrs) BC mass concentration
BC(N)	Night (21:00-04:55 hrs) BC mass concentration

$BC(M)_{FF}$	Fossil fuel component of *BC(M)*
$BC(M)_{WB}$	Wood burning component of *BC(M)*
$BC(A)_{FF}$	Fossil fuel component of *BC(A)*
$BC(A)_{WB}$	Wood burning component of *BC(A)*
$BC(E)_{FF}$	Fossil fuel component of *BC(E)*
$BC(E)_{WB}$	Wood burning component of *BC(E)*
$BC(N)_{FF}$	Fossil fuel component of *BC(N)*
$BC(N)_{WB}$	Wood burning component of *BC(N)*
C	Enhancement parameter
C_p	Specific heat capacity
f	Filter loading effect compensation parameter
g	Aerosol asymmetry parameter
I	Direct solar irradiance
I_0	Extraterrestrial solar irradiance
m	Air mass
Q_{ext}	Aerosol extinction efficiency
Q_{sca}	Aerosol scattering efficiency
Q_{abs}	Aerosol absorption efficiency
r^2	Coefficient of determination
$R(ATN)$	Correction for filter loading effect
V	Volume of air through filter spot

List of Figures

List of Tables

List of Publications

1. *Black carbon aerosol mass concentration, absorption and single scattering albedo from single and dual spot aethalometers: Radiative implications*
   T.A. Rajesh, and S. Ramachandran
   Journal of Aerosol Science, 119, 77-90, 2018.

2. *Characteristics and source apportionment of black carbon aerosols over an urban site*
   T.A. Rajesh, and S. Ramachandran
   Environmental Science and Pollution Research, 24, 8411-8424, 2017.

3. *Contribution of aerosol components to aerosol optical depth over a semi-arid location in western India*
   T.A. Rajesh, S. Ramachandran and Toshihiko Takemura
   IASTA-Bulletin, ISSN:0971-4510, Vol. 22 Issue 1 & 2, 398-401, 2016.

4. *Aerosol optical depth and its component trends over Vallabh Vidyanagar, Anand*
   T.A. Rajesh, S. Ramachandran and P. C. Vinodkumar
   IASTA-Bulletin, ISSN:0971-4510, Vol. 22 Issue 1 & 2, 402-405, 2016.

5. *Black carbon aerosols over urban and high altitude remote regions: Characteristics and Radiative implications*
   T.A. Rajesh, and S. Ramachandran
   Atmospheric Environment, 194, 110-122, 2018.

6. *Aerosol optical properties over Gurushikhar, Mt. Abu: A high altitude mountain site in India*
   T.A. Rajesh, and S. Ramachandran
   Aerosol and Air Quality Research, 19, 1259-1271, 2019.

Chapter 1

Introduction

Earth is surrounded by a thin blanket of life-giving gaseous envelope named *atmosphere*. The envelope of air that surrounds the Earth is composed of $\sim$ 78% nitrogen and 21% oxygen by volume. The remaining 1% volume is made up of several minor and trace constituents which include argon (Ar), carbon dioxide (CO_2), neon (Ne), helium (He), methane (CH_4), hydrogen (H_2), water vapor (H_2O), ozone (O_3), oxides of nitrogen (NO, NO_2), carbon monoxide (CO), hydrogen sulfide (H_2S), ammonia (NH_3) etc. found in infinitesimal amounts (parts per million (ppm) to parts per trillion (ppt) by volume), and suspended particulate matter (aerosols), which are widely variable in space and time. Despite being in small amounts aerosols play very important and crucial roles in the physico-chemical properties of the atmosphere, and the Earth-atmosphere radiation balance.

The Earth's atmosphere shows significant and distinct variations in temperature as a function of altitude. The atmosphere is generally classified on the basis of atmospheric composition and temperature gradient. The Earth's atmosphere from the surface to 100 km is called as the *homosphere* where all the constituents are well mixed, and above the homosphere lies the *heterosphere* wherein constituents (gases) are fractionated according to their molecular weight. The atmosphere characterised by the temperature gradient is divided into various horizontal layers as *troposphere*, *stratosphere*, *mesosphere*, and *thermosphere* (Figure 1.1). The transition altitudes distinguishing these layers are called *tropopause*, *stratopause*, and *mesopause* respectively. Tro-

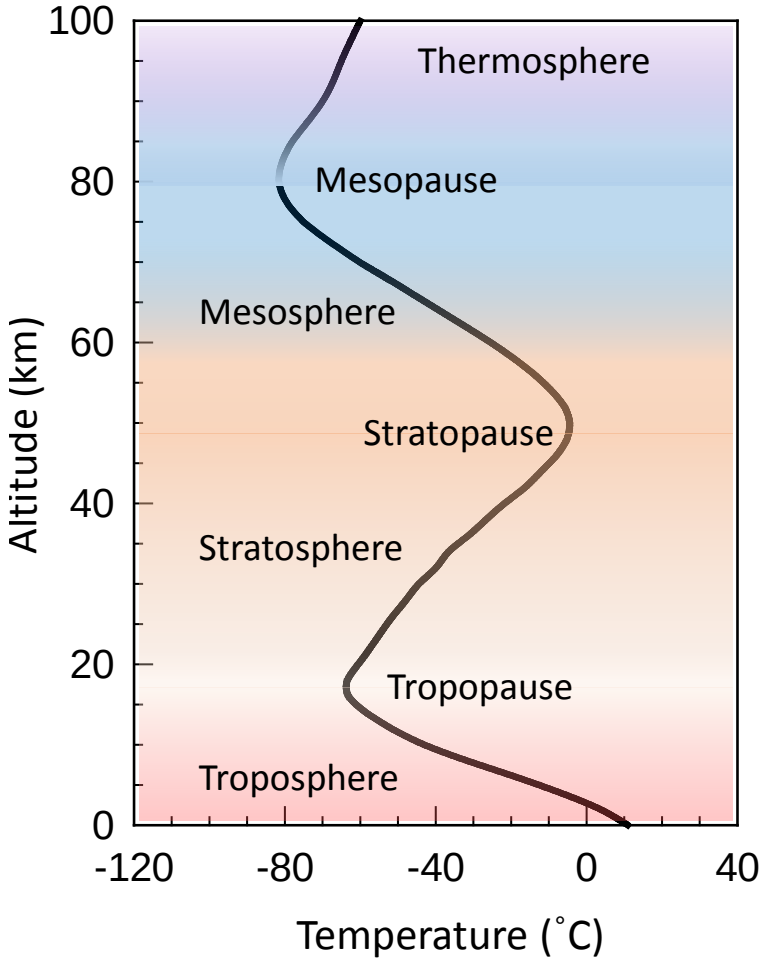

Figure 1.1: *Global annual mean temperature structure of the Earth's atmosphere (data taken from U.S. Standard Atmosphere, 1966).*

posphere is the lowest layer of the Earth's atmosphere and extends from the Earth's surface upto 15-18 km in the tropics (Figure 1.1), and 8-10 km in the poles. Temperature decreases with altitude at the rate of 6.5^{o}C per km in the troposphere (wet adiabatic lapse rate) and is characterized by strong convective mixing (Figure 1.1). Above the troposphere lies the stratosphere. The temperature increases with altitude (Figure 1.1) due to the significant absorption of ultra-violet (UV) component of the solar radiation by the ozone in the stratosphere. Troposphere and stratosphere account for more than 99.9%

of the mass of the atmosphere. Above the stratosphere lies the mesosphere, where the temperature decreases with altitude (Figure 1.1) and rapid vertical mixing takes place. The region above the mesopause is the thermosphere where temperature increases with altitude due to the absorption of solar radiation by atomic oxygen.

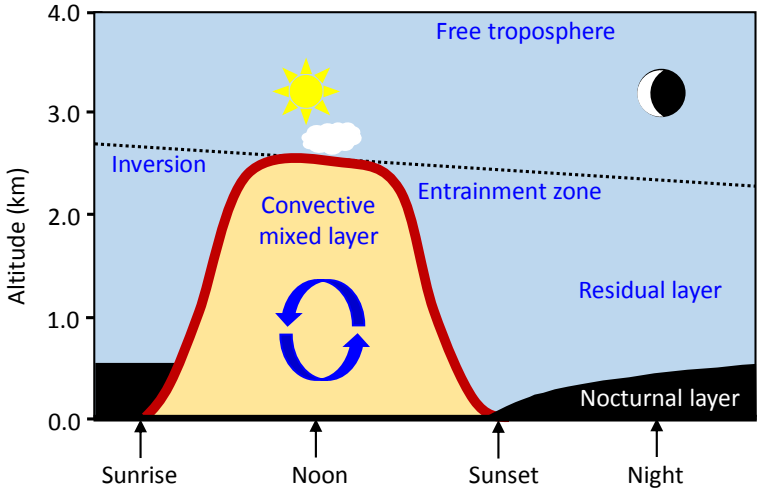

Figure 1.2: *Schematic of the diurnal variation of Atmospheric Boundary Layer (based on Stull, 1988).*

In the troposphere, the lowest part of the atmospheric layer which is strongly influenced by the Earth's surface is called the *atmospheric boundary layer* (ABL) or planetary boundary layer, which holds most of the atmospheric constituents produced (natural and anthropogenic) at the Earth's surface. The atmospheric layer extending from the top of the ABL to the tropopause is referred as *free troposphere*. ABL acts as a buffer which couples the Earth's surface with the lower troposphere, and is directly influenced by the incoming solar energy. ABL evolves with the diurnal solar cycle (Figure 1.2). The height of the ABL exhibits significant spatio-temporal variation (ranging from few meters (stable conditions) to several kilometers (convective conditions)). ABL during day time is characterised by strong convection (convective mixed layer) and becomes turbulent due to the diurnal variation of the temperature and

shearing force (due to Earth's surface friction on the surface wind). Turbulence in the convective mixed layer results in an effective dilution, and transport of the surface emitted pollutants. The convective mixed layer is capped by temperature inversion layer called as entrainment zone which confines pollutants and inhibits mixing below it. Entrainment zone isolates the ABL from the free troposphere. After sunset the air turbulence decreases due to radiative cooling which results in the formation of inversion layer (nocturnal layer) near the Earth's surface (Figure 1.2). A non-turbulent residual layer forms above the stable nocturnal layer. During night time the emitted pollutants can remain trapped within the stable nocturnal layer. The heating of the Earth's surface starts after sunrise which results in the mixing of the accumulated pollutants within the nocturnal layer with the convective mixed layer. The ABL dynamics plays an important and significant role in the diurnal distribution of the surface emitted pollutants (*Seinfeld and Pandis*, 1998).

1.1 Atmospheric aerosols

The particles (solid or liquid) suspended in air with radii range from 0.001 to 100 μm are called as atmospheric aerosols. They exhibit variability in shape, size, concentration and composition depending on the strength and nature of sources, production mechanisms, mixing characteristics, and scavenging processes. Aerosols of different sizes, magnitude and composition are produced by natural and anthropogenic sources, and can be transported to different regions depending on favorable meteorological (winds) conditions. Aerosols play a vital role in various atmospheric processes such as visibility, air pollution, cloud formation, radiation balance, atmospheric electricity, etc. Aerosol size is a crucial parameter that determines its interaction with the solar and terrestrial radiation, affects the physical and chemical properties, and their lifetime. Typically, the size (radius) of atmospheric aerosols span over five orders of magnitude, and based on their sizes and production mechanisms, the atmospheric aerosols can be classified as (i) *nucleation mode* (0.001 to 0.1 μm), (ii) *accumulation mode* (0.1 to 1.0 μm), and (iii) *coarse* (particles radii $>$ 1.0 μm)

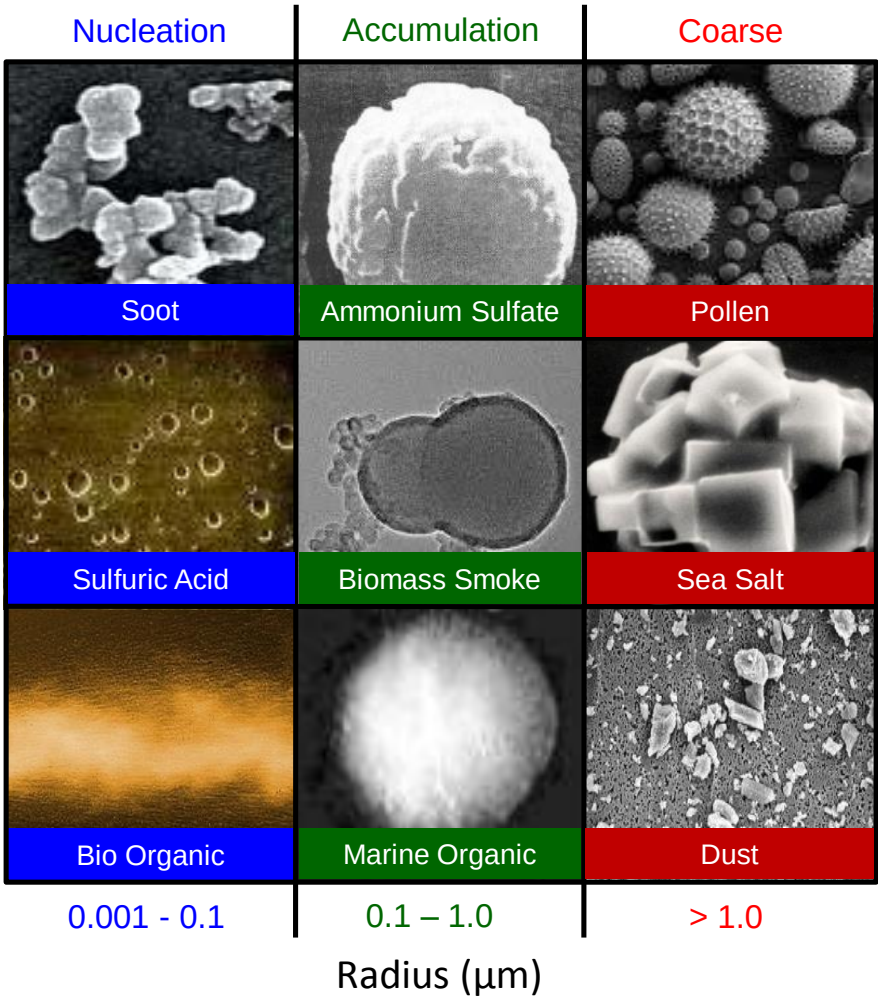

Figure 1.3: *Different aerosol types in the nucleation, accumulation and coarse modes (based on Brasseur et al., 2003).*

(*Whitby*, 1978) (Figure 1.3). The aerosols in the nucleation and accumulation modes are referred as fine mode particles.

1.2 Sources, sinks and residence times of aerosols

Depending on the production sources, aerosols are classified as natural (e.g. sea salt, dust) and anthropogenic (e.g. black carbon). Typically, natural aerosols contribute $\sim$ 80% of the total aerosol in mass in the atmosphere

(*Warneck*, 1988). Aerosols which are directly injected into the atmosphere are known as primary aerosols (e.g. wind blown dust, pollen grains, sea salt, black carbon from incomplete combustion of fossil fuel or biomass burning). There

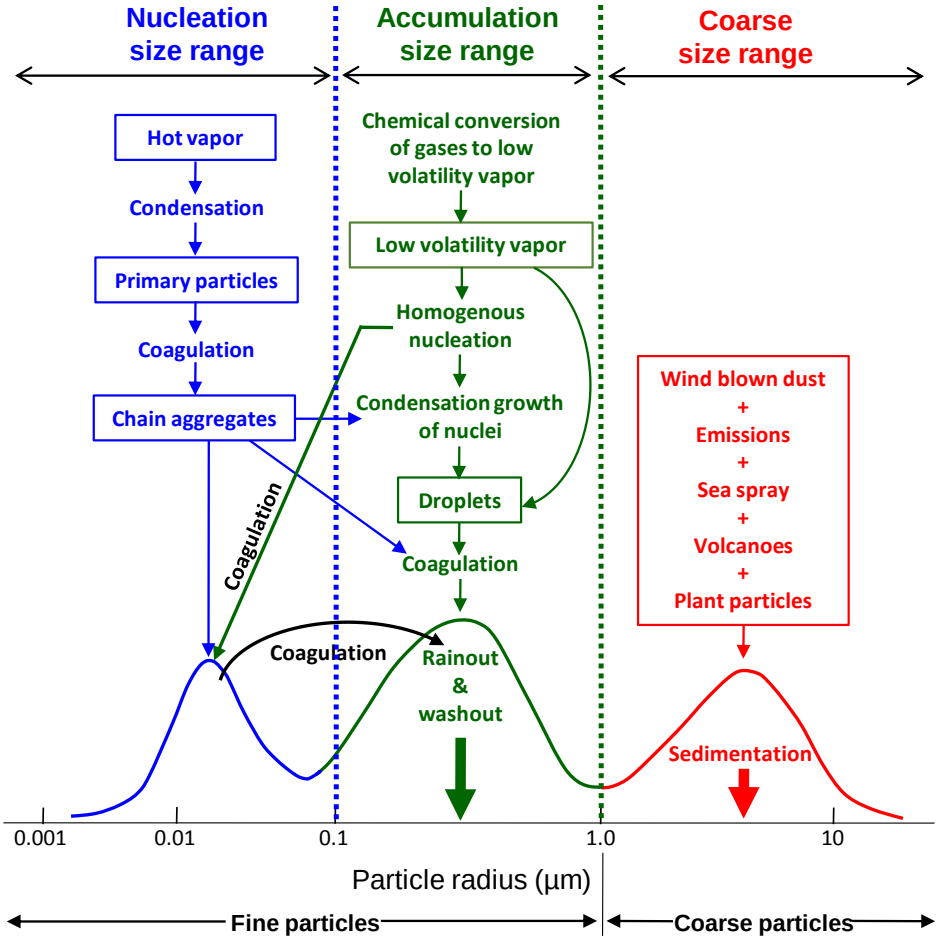

Figure 1.4: *Schematic of size distribution of aerosols (based on Whitby, 1978).*

are several inorganic species in the atmosphere (sulfates, nitrates etc.) which are produced from the gas-to-particle conversion mechanism and these are known as secondary aerosols. Aerosols in the size range < 1.0 μm are mostly produced through condensation (gas-to-particle conversion) and coagulation processes (Figure 1.4), whereas particles > 1.0 μm are emitted directly by mechanical processes such as wind blown dust, sea spray, etc. (Figure 1.4). The coagulation is the process by which aerosols undergo random collisions and

coalesce which results in a decrease in smaller size aerosols. The rate of coagulation is a function of mobility and the number density of aerosols (*Warneck*, 1988). Aerosols in the accumulation mode are produced either by coagulation of nucleation mode aerosols or by heterogeneous condensation of gaseous vapor onto smaller nucleation mode particles (Figure 1.4). Typically, the chemical nature of aerosols is mainly governed by their production source while their size distribution depends on their production mechanism. Mostly ($>$ 99%) these aerosols are found in the atmosphere from the surface up to 40 km. The frequency of occurrence of aerosols from extraterrestrial sources (planetary accretion, comet debris and meteor shower) in the upper atmosphere ($>$ 50 km) is rare and contribute $<$ 1% in the atmosphere (*d'Almeida et al.*, 1991).

The number concentration of the atmospheric aerosols exhibits large spatio-temporal variations. High number concentration of particles are found near to sources and their concentration decreases with distance from sources. Typically, the total aerosol number concentration over an urban and a rural region is found to be $\sim 10^6$ and 10^3 cm^{-3} respectively (*Heintzenberg*, 1997). In general, the total particle number concentration in the lower troposphere varies in the range of about 10^2 to 10^5 cm^{-3}, and the concentration in the free troposphere is typically 1-2 orders of magnitude lower than lower troposphere (*Heintzenberg*, 1997). Aerosols in the stratosphere are significantly less in number (few to tens of particles). Stratospheric aerosols are produced by the the diffusion of natural gases (like hydrogen sulfide, carbonyl sulfide, carbon disulfide, sulfur dioxide, etc.) from the troposphere. The number concentration of stratospheric aerosols increases significantly after a major volcanic eruption (*Ramachandran et al.*, 2000).

Aerosols in the nucleation mode are primarily lost by coagulation processes. Although coagulation decreases the aerosol number concentration but the total volume remains constant. In the condensation process the aerosol number concentration remains constant but the total particle volume increases. When both (condensation and coagulation) processes exists

then aerosol number concentration decreases and the total aerosol volume increases (*Seinfeld and Pandis*, 1998). Nucleation mode aerosols undergo higher rate of condensation growth and coagulation, resulting in their transformation into accumulation mode aerosols. Atmospheric aerosols are removed from the atmosphere by dry and wet deposition processes. The removal of atmospheric aerosols vary as function of aerosol sizes, types, their residence times and altitude. Dry deposition refers to the removal of aerosols from the atmosphere to the Earth's surface. It includes gravitational settling and impaction, and diffusion of particles to surface, which are active near the Earth's surface. Wet removal of aerosols involves two processes, namely, below-cloud scavenging and in-cloud scavenging (*Seinfeld and Pandis*, 1998). The capture and removal of aerosol by the falling hydrometeors (rain, snow, cloud and fog drops) are called below cloud scavenging processes. In-cloud processes consist of activation of aerosols into cloud condensation nuclei, attachment of aerosols to the pre-existing cloud drops, and removal of aerosol containing cloud droplets produced by the first two processes by large falling hydrometeors. Aerosols found in the size range of 0.1-10 μm are mainly removed by wet deposition, and for aerosols $>$ 10 μm sedimentation is the dominant removal process (*Jaenicke*, 1993).

The time spent by the aerosols in the atmosphere from their production to removal or conversion can be referred to as *residence time* of atmospheric aerosols. It depends on their size, chemical composition, phase (solid or liquid), morphology and altitude at which they are present. Nucleation mode aerosols are removed efficiently by coagulation processes, and hence, their residence time is very short. The residence time for coarse mode ($>$ 10 μm) aerosols is also short in the atmosphere due to sedimentation (gravitational settling) (Figure 1.5). The residence time of atmospheric aerosols in the accumulation mode is the longest ($\sim$ 7-10 days), because the coagulation and sedimentation processes are least significant in this size range. The aerosols in the accumulation mode is removed predominantly from the atmosphere by wet deposition processes (Figure 1.5). The residence time of aerosol types also

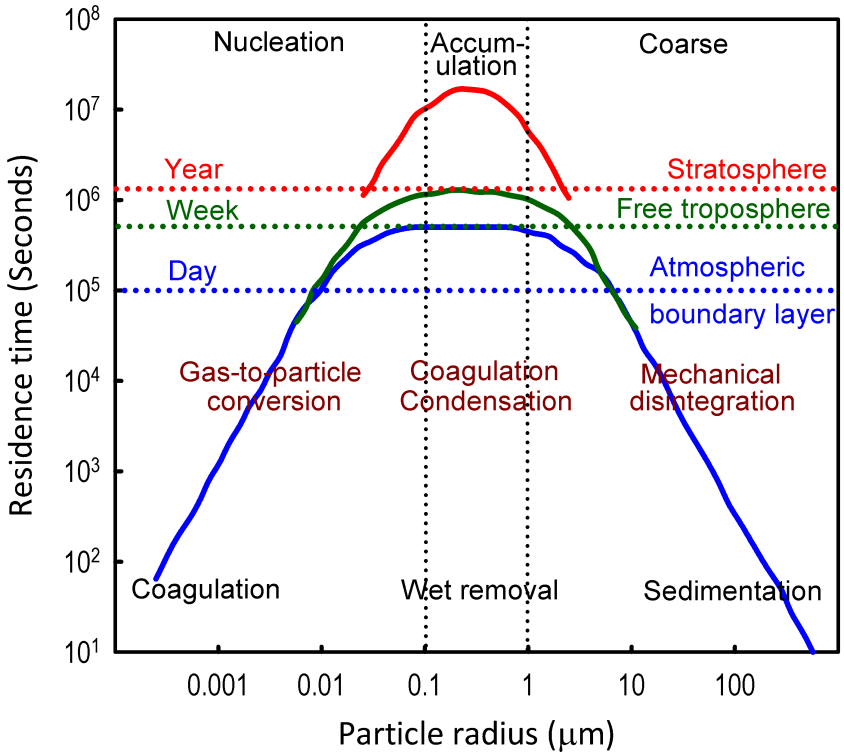

Figure 1.5: *Residence time of atmospheric aerosols depicted as function of size (based on Jaenicke, 1993).*

vary; sulfate, sea salt, dust and black carbon aerosols have a residence time on the order of 2-7 days (*Textor et al.*, 2006). The residence time is of the order of few days within the atmospheric boundary layer, few weeks in free troposphere and few years in the stratosphere (*Jaenicke*, 1993) (Figure 1.5).

1.3 Significance of atmospheric aerosols

Aerosols have the potential to significantly influence our planet by interacting with incoming solar (shortwave) and outgoing terrestrial (longwave) radiations through three distinct radiative effects, viz. (i) *direct effect*, (ii) *semi-direct effect*, and (iii) *indirect effect* (*IPCC*, 2007). The quantification of the effect of

a species in modifying the balance between the incoming and outgoing flux in the Earth-atmosphere system is defined as radiative forcing of the species (*IPCC*, 2013). Positive and negative radiative forcing indicate the warming and cooling the Earth-atmosphere system respectively. The direct radiative effect of aerosols involve scattering and absorption of solar and terrestrial radiation in the atmosphere (*IPCC*, 2007). Both these processes reduce the direct solar flux reaching the Earth's surface and thus induce a net cooling effect on the surface (negative forcing). In the shortwave region, a scattering aerosol (e.g., sulfate) will cool the atmosphere, while an absorbing aerosol (e.g., black carbon) will warm the atmosphere. Absorption of solar radiation by aerosols leads to heating of the air, which can result in an evaporation of cloud droplets which is referred to as *semi-direct effect*. Semi-direct effect is a consequence of the direct effect of absorbing aerosols and may have a significant warming impact on climate by 'burning off' of the low clouds that scatter solar radiation back to space but have little impact on outgoing longwave radiation. Indirect radiative forcing by aerosol is the overall process by which aerosols perturb the Earth-atmosphere radiation balance by modulating the cloud albedo and amount (*IPCC*, 2013). Aerosol plays an important and significant role in the formation of clouds, and serves as cloud condensation nuclei around which cloud droplets are formed. Higher aerosol concentration can increase the formation of smaller droplets with decreased droplet radius, which leads to an increase in cloud albedo and hence leads to a cooling effect known as Twomey effect (*Twomey*, 1977). The aerosol radiative forcing in the longwave regime contributes about 10% to the net aerosol radiative forcing. This contribution is much smaller than the contribution of shortwave aerosol radiative forcing to the net forcing (*Ramanathan et al.*, 2001a; *Ganguly et al.*, 2005; *Ramachandran et al.*, 2006).

Aerosol properties (optical, physical and chemical) exhibit large spatial and temporal variability, hence the radiative effects of aerosol can be different in contrast to greenhouse gases. Aerosol plays a significant role in the Earth's radiation budget and is a large source of uncertainty in the predic-

tion of climate change (*IPCC*, 2013). The major sources that contribute to the uncertainty on aerosols and their radiative forcing are, uncertainties in their properties (optical, physical, and chemical), uncertainties/assumptions involved in the estimates of radiative forcing, and inaccuracy in their atmospheric burden and the anthropogenic contribution (*IPCC*, 2013). The inaccuracies in aerosol properties arise from uncertainties in its size distribution, chemical composition, and meteorological effects. In order to increase the level of scientific understanding, it is necessary to have spatial and high temporal resolution measurement of various aerosol properties. There exists a large uncertainty in the forcing due to different aerosol species because of significant uncertainty in their sources (natural and anthropogenic), and their spatio-temporal variations (*Ramachandran et al.*, 2012). Further, of the various aerosol species the black carbon aerosol (anthropogenic source) is the second largest source to global warming, after carbon dioxide (CO_2) (*Ramanathan and Carmichael*, 2008) and hence, the estimation of radiative forcing due to black carbon aerosol is important to delineate/determine the anthropogenic contribution with respect to the total (composite) radiative forcing.

Black carbon (BC) aerosol is the optically absorbing component of carbonaceous aerosols and is produced by incomplete combustion of fossil fuel (coal, diesel, petrol, etc.), biofuel (biodiesel, biogas, ethanol, etc.) and biomass (woods, shrubs, dry leaves, etc.). It absorbs incoming shortwave solar radiation and outgoing longwave terrestrial radiation, and is therefore an important contributor to the direct radiative forcing through warming the atmosphere. It has a short lifetime ($\sim$ 7-10 days) in the atmosphere but exhibit significant spatial and temporal variability in its sources and emission. The physical (size distribution and morphology) and chemical (composition and mixing state) properties of the atmospheric BC aerosols are complex and variable in nature (*Xianda et al.*, 2016). BC aerosol significantly affects the human health (respiratory and lung diseases, *Mauderly and Chow* (2008)), vegetation (crop yields, *Chameides et al.* (1999)), ecosystem (terrestrial and aquatic,

Forbes et al. (2006)), monsoon *Wang et al.* (2009), and glaciers (*Lau et al.*, 2006; *Li et al.*, 2016). The emissions from fossil fuel burning consists of large amount of black carbon aerosols as compared to organic carbon, whereas biomass (wood) burning consists dominantly organic carbon aerosols. Typically, black carbon and organic carbon aerosols are found to absorb in the near infrared and ultraviolet wavelengths respectively (*Sandradewi et al.*, 2008). The black carbon aerosols produced from the combustion of fossil fuel and biomass are found to exhibit a largest uncertainty in aerosol emissions (*Bond et al.*, 2004). A significant uncertainty in forcing arises because of the lack of information about the amount of BC aerosol emitted into the atmosphere, its size distribution, contribution from different sources (fossil fuel and biomass burning), and its mixing state. The relative contributions of BC mass from the combustion of fossil fuel and biomass to the total BC mass concentration are used to quantify the dominant source (fossil fuel or biomass) of BC aerosols. Due to the above there is a significant interest in studying the characteristics of black carbon aerosols and their radiative and climatic impact over different environments (e.g. urban (*Ramachandran and Rajesh*, 2007; *Sreekanth et al.*, 2007; *Beegum et al.*, 2009; *Panicker et al.*, 2010; *Ramachandran and Kedia*, 2010; *Wang et al.*, 2011; *Dumka et al.*, 2013; *Safai et al.*, 2013; *Tiwari et al.*, 2013; *Gong et al.*, 2016; *Rajesh and Ramachandran*, 2017), rural/semi-urban (*Gadhavi and Jayaraman*, 2010; *Kumar et al.*, 2011; *Aruna et al.*, 2013; *Singh et al.*, 2015), ocean (*Kedia et al.*, 2012; *Kompalli et al.*, 2013), and mountain sites (*Dumka et al.*, 2010; *Raju et al.*, 2011; *Kant et al.*, 2012; *Srivastava et al.*, 2012; *Panwar et al.*, 2013; *Udayasoorian et al.*, 2014; *Sarkar et al.*, 2015)).

1.4 Motivation

The Indian subcontinent and its surrounding regions are the prime sources for different types of aerosols (natural and anthropogenic origin) such as mineral dust, black carbon, sea salt, sulfate, etc., and in addition, the subcontinent experiences tropical climatic conditions which results in significant variations in temperature, relative humidity and rainfall on seasonal time scales.

Hence, large spatio-temporal variabilities have been observed in aerosol characteristics over India. The study on the influence of aerosols from natural and anthropogenic sources on radiative effects has been undertaken over different environments in Indian subcontinent and adjoining oceanic regions (e.g., *Ramanathan et al.* (2001b); *Jayaraman et al.* (2006); *Ganguly et al.* (2006); *Ramachandran and Cherian* (2008); *Kedia et al.* (2010); *Pathak et al.* (2010); *Ramachandran and Kedia* (2012); *Jose et al.* (2016); *Sharma et al.* (2017); *Verma et al.* (2017); *Srivastava et al.* (2018)). But, aerosols are still a significant source of uncertainty in climate change prediction because of limited information of aerosol characteristics on temporal and regional scales. The measurements of aerosol characteristics and their radiative effects over India (*Pandithurai et al.*, 2004; *Niranjan et al.*, 2005; *Jayaraman et al.*, 2006; *Ramachandran et al.*, 2006; *Sreekanth et al.*, 2007) and over oceans surrounding peninsular India (*Jayaraman et al.*, 1998; *Ramanathan et al.*, 2001b; *Ramachandran*, 2005; *Kedia and Ramachandran*, 2009, 2011) have been extensively reported, but relatively a few measurements exist over western India (*Ganguly and Jayaraman*, 2006; *Ramachandran and Rajesh*, 2007; *Ramachandran and Kedia*, 2010). The western India is densely populated, and is surrounded by desert (Thar), ocean (Arabian Sea) and large land mass with different aerosol species produced and transported from different regions. Also, studies documenting the contribution of fossil fuel and biomass burning (wood burning) to total BC are scarce. In addition, investigation on the simultaneous measurements of BC characteristics over a source region, and a nearby background region are not available, which is required to simulate better the seasonal BC aerosol distribution in regional and global models, and estimate their radiative effects more accurately.

The present study focuses on the space-time characteristics of optical and physical properties of aerosols, source apportionment of black carbon aerosols, and their radiative effects over an urban, and a high altitude remote region. Typically, urban emissions are influenced by anthropogenic activities. The high altitude remote region is influenced by local and longrange transported aerosols through convective and advective processes. When the

high altitude remote location is in the same region as that of an urban aerosol source region, and is governed by the same meteorology and atmospheric dynamics, then aerosol measurements over the high altitude region can serve as regional representative background.

1.5 Objectives

With an objective to investigate the spatio-temporal variations in aerosol properties over western India, for the first time, simultaneous measurements of various aerosol properties were conducted over distinct environments (urban, and high altitude remote) for the scientific reasons mentioned above.

The specific objectives of the present thesis are:

1. *To characterize the spatial and temporal variabilities in optical and physical properties of aerosols over urban, and high altitude remote locations.*
2. *To characterize the spatial and temporal variabilities in black carbon aerosol, and its source apportionment over urban, and high altitude remote locations.*
3. *To estimate the total direct aerosol radiative forcing and the radiative forcing due to black carbon aerosols only, and their seasonal variability over urban, and high altitude remote regions using the aerosol optical and physical characteristics.*

Aerosol characteristics were measured and analysed over an urban environment (characterized by highest aerosol concentrations dominated by anthropogenic aerosols) (Ahmedabad (23.03^{o}N, 72.55^{o}E, 55 m above mean sea level), and a high altitude remote region (with low aerosol concentration dominated by transport mechanisms) (Gurushikhar (24.65^{o}N, 72.78^{o}E, 1680 m above mean sea level) over western India. Further, utilising the measured aerosol characteristics and models, radiative forcing for composite and BC

aerosols are estimated and discussed.

The thesis consists of six chapters. The present chapter (**Chapter 1**) gives a brief introduction to the Earth's atmosphere, atmospheric aerosols, their sources and sinks in the atmosphere, size distribution and their composition. It consists of a brief description on how the aerosols perturb the Earth-atmosphere radiation budget. In addition, this chapter consists a brief review of the previous research in India, thus, setting the stage for the motivation, objectives and importance of the thesis. **Chapter 2** provides a brief description of the various instruments used in the study along with their measurement techniques. Methodology, and data analysis are discussed in this chapter. It also consists a description about the satellite data obtained from different sensors which are used in the present study. The uncertainties involved in various measurements are also discussed in this chapter. A brief description of various computational tools used for radiative transfer estimation, namely, Optical Properties of Aerosols and Clouds (OPAC) (*Hess et al.*, 1998), and Santa Barbara DISORT Atmospheric Radiative Transfer (SBDART) (*Ricchiazzi et al.*, 1998) are also included. **Chapter 3** discusses the measured optical and physical properties of aerosols over the study locations in western India. **Chapter 4** deals with the spatial and temporal characteristics of black carbon aerosol and its source apportionment over an urban and a high altitude remote locations. **Chapter 5** discusses the seasonal variabilities in the radiative forcing over urban and high altitude remote locations in western India. In order to quantify the effect of BC aerosols on the radiation budget the aerosol radiative forcing is estimated for composite and BC aerosols, and discussed. **Chapter 6** summarises the major results from the study and discusses the scope for future work.

Chapter 2

Measurements, Methodology and Data Analysis

The present chapter discusses the measurement techniques and working principles of the various in situ instruments used in the study. Details about the various remote sensing data are presented. It also discusses the meteorological data and reanalysis datasets utilised in the study. In addition, it also presents a brief description about the models used in the present work, Optical Properties of Aerosols and Clouds (OPAC) model used to estimate the spectral characteristics of various aerosol properties, and Santa Barbara DISORT Atmospheric radiative transfer (SBDART) model used to compute aerosol radiative forcing. Details on data analysis and the methodology adapted are discussed. Finally, the importance and the environment of the study regions are discussed.

2.1 Surface aerosol measurements

The aerosol scattering (β_{sca}) and absorption (β_{abs}) coefficients were measured using multiwavelength nephelometer (*model 3563, TSI Inc., USA*) and multiwavelength aethalometer (*AE31 and AE33, Magee Scientific, USA*) respectively. The scattering and absorption coefficients data over Ahmedabad and Gurushikhar (the study locations) collected during 2015 and 2016 are utilised in the work.

2.1.1 Integrating nephelometer

Aerosol scattering coefficients (β_{sca}) and backscattering coefficients (β_{bsca}) were measured using Integrating nephelometer (Model No. 3563, TSI Inc., USA) at 0.45, 0.55 and 0.70 μm. The instrument aspires sample into the measurement chamber, which is lit by a white light source and the resultant scattered light is measured by photomultiplier tube detectors at three wavelengths (0.45, 0.55 and 0.70 μm) (Figure 2.1).

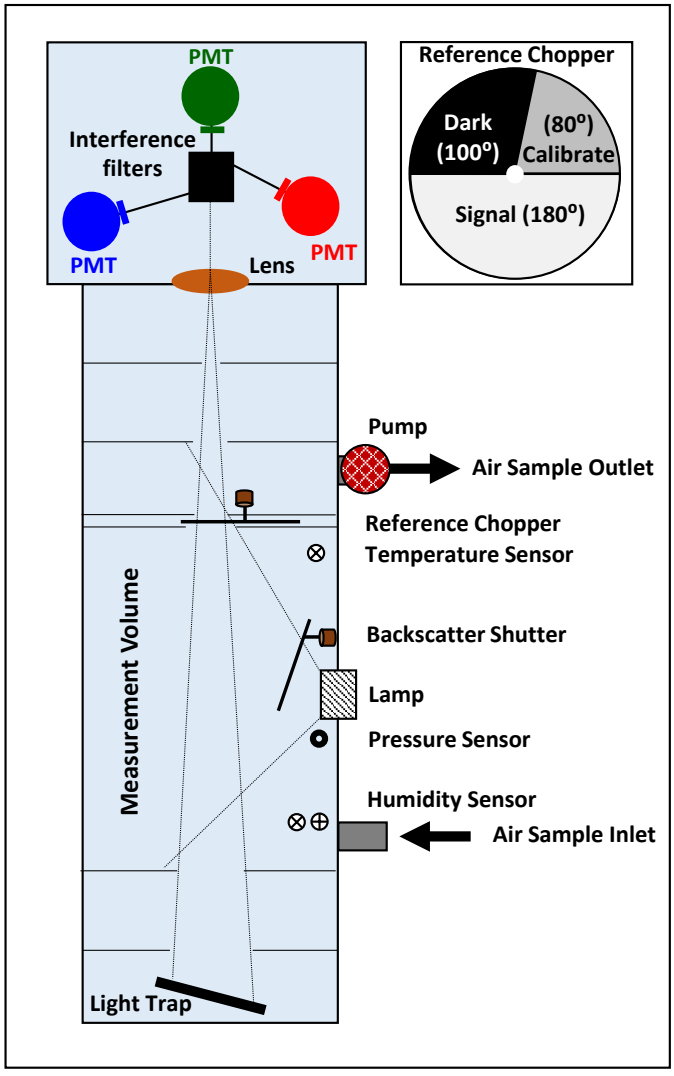

Figure 2.1: *Schematic of the Integrating Nephelometer (Model No. 3563, TSI Inc., USA). (Source: The Integrating Nephelometer, Operation manual, TSI).*

Table 2.1: *Characteristics of nephelometer TSI 3563*

Parameters	Specifications
Light source	Incandescent halogen lamp
Diffuser	Lambertian opal glass
Detectors	Photomultiplier tubes
Wavelengths	0.45, 0.55, and 0.70 μm
Filters	Interference filters
Band-width FWHM	50 nm
Backscatter	Continuous
Total scattering angular range	7-170°
Backscattering angular range	90-170°
Response time	<10 sec
Range	1-1000 Mm^{-1} ($1M = 10^6$)
Particle transport efficiency	>95% from 0.05 to 5.0 μm diameter

It consists of a reference chopper with three sections for signal (passes all light), dark (blocks light for background measurement) and calibrate (measure the lamp stability). Inside the measurement chamber the pressure and temperature are measured to compute the scattering by air molecules which is then subtracted from measured total scattering to estimate aerosol scattering coefficient. The total scattered signal is integrated over an angular range of 7-170° from the forward direction, whereas backscattered signal is integrated over 90-170°. Nephelometer is configured for an hourly auto zero calibration using a high efficiency particulate air (HEPA) filter in order to detect the background signal in the operational environment condition. In addition, the instrument is routinely calibrated for span using ultra high pure CO_2 gas and filtered ambient air using HEPA filter. Nephelometers #70522074 and #71018002 were used to measure aerosol scattering coefficients at Ahmedabad and Gurushikhar, respectively the characteristics of which are given in Table 2.1. The scattering coefficient of aerosols is obtained from the total light extinction inside the measurement chamber of the nephelometer using Beer-Lambert law as,

$$I = I_o \, exp(-\beta_{ext} \, l) \tag{2.1}$$

where I and I_o are the intensity of the light at detector and of the incident light respectively. l is the length of the measurement volume and β_{ext} is the extinction (sum of scattering and absorption) coefficients. The contribution of absorption coefficient is negligible due to the non-absorbing calibration method utilising air and CO_2 in nephelometer (*Abu-Rahmah et al.*, 2006). Inside the measurement volume the intensity of the scattered light is integrated over close to 4π steradians and it provides a good approximation of the scattering component of extinction. The nephelometer measured raw photon counts are converted into scaled count rate and then corrected for dead time as

$$C_s = \frac{360\ C\ S}{G\ N} \tag{2.2}$$

$$F = C_s\ (C_s\ K_1 + 1) \tag{2.3}$$

where C is raw photon count, S is the chopper speed (22.994 Hz), G is gate width (40^o for calibrate, 140^o for signal, and 60^o for dark), N is the number of revolutions , C_s is scaled count rate (Hz), F is corrected count rate (Hz), and K_1 is pulse width constant. The aerosol scattering coefficient (β_{sca}) is estimated from the dead time corrected count rate as

$$\beta_{sca} = B_a - W - R_a \tag{2.4}$$

where B_a is raw aerosol scatter signal, W is wall scatter for filtered air ($W = B_f - R_f$), R_a is Rayleigh scatter of unfiltered air, B_f is filtered air raw scatter signal, and R_f is Rayleigh scatter of filtered air.

$$\beta_{sca} = B_a - (B_f - R_f) - R_a \tag{2.5}$$

$$\beta_{sca} = K2\frac{S_a - D_a}{C_a - D_a} - \left(K2\frac{S_f - D_f}{C_f - D_f} - K3\frac{P_f T_s}{T_f P_s}\right) - K3\frac{P_a T_s}{T_a P_s} \tag{2.6}$$

where S_a, D_a and C_a are signal, dark and calibrate scaled count rates for aerosol respectively, S_f, D_f and C_f are signal, dark and calibrate scaled count rates

for filtered air respectively, T_s and P_s are standard temperature (273.15 K) and pressure (1013.25 hPa) respectively, T_f and P_f are temperature and pressure of filtered air respectively, T_a and P_a are temperature and pressure of unfiltered air respectively, $K2$ is span gas constant, and $K3$ is Rayleigh scatter constant. From the above equations aerosol backscattering coefficient can be calculated as

$$\beta_{bsca} = B_a - (B_f - K4R_f) - K4R_a \tag{2.7}$$

The above equations use the calibration constants, $K2$ and $K4$ (m^{-1}) which are obtained from the two point calibration (filtered ambient air as low span gas and CO_2 as high span gas). The calibration constants, $K2$ and $K4$ (m^{-1}) obtained during the study period at three wavelengths (0.45, 0.55, and 0.70 μm) are given in Table 2.2.

Table 2.2: *Calibration constants $K2$ and $K4$ (m^{-1}) for nephelometers (# 71018002 and # 70522074) during 2015-2016 at 0.45, 0.55, and 0.70 μm using two point calibration (filtered ambient air as low span gas and CO_2 as high span gas). Month/year of calibration is given as mm/yyyy.*

	Nephelometer #71018002					
	K2 (10^{-3} m^{-1})			K4 (10^{-1} m^{-1})		
Date	0.45 μm	0.55 μm	0.70 μm	0.45 μm	0.55 μm	0.70 μm
07/2014	1.957	2.155	1.829	5.109	4.958	5.115
02/2015	1.856	2.138	1.856	5.236	5.311	5.478
07/2015	1.834	2.029	1.717	5.260	5.260	4.930
01/2016	1.818	2.038	1.833	5.230	5.290	5.600
07/2016	1.808	2.055	1.799	5.229	5.029	4.954
	Nephelometer #70522074					
	K2 (10^{-3} m^{-1})			K4 (10^{-1} m^{-1})		
Date	0.45 μm	0.55 μm	0.70 μm	0.45 μm	0.55 μm	0.70 μm
07/2014	2.571	2.725	2.101	5.190	5.120	5.200
02/2015	2.480	2.877	2.171	5.010	5.020	4.960
10/2015	2.481	2.897	2.079	5.240	5.116	5.108
01/2016	2.028	2.334	1.965	5.120	5.000	4.830
09/2016	2.020	2.304	1.821	5.040	5.090	4.990

The raw scattering coefficient ($\beta_{sca(raw)}$) is corrected for the truncation (missing

forward scattering) error ($\beta_{sca(t)}$) using *Anderson and Ogren* (1998) as

$$\beta_{sca(t)} = \beta_{sca(raw)}\ (a + b\ \alpha_{sca}(\lambda)) \tag{2.8}$$

where α_{sca} is the scattering Ångström exponent and is expressed as

$$\alpha_{sca} = \frac{-ln[\beta_{sca}(\lambda_1)/\beta_{sca}(\lambda_2)]}{ln[\lambda_1/\lambda_2]}, \tag{2.9}$$

and the values of coefficients a is 1.337 and b is -0.138 (at 0.55 μm) (*Anderson and Ogren*, 1998). The variations in ambient pressure and temperature from the standard pressure (1013.25 hPa) and temperature (273.15 K) are further corrected in β_{sca} as

$$\beta_{sca} = \beta_{sca(t)}\ \frac{P}{1013.25}\frac{273.15}{T} \tag{2.10}$$

where P is ambient pressure (hPa) and T is ambient temperature (K).

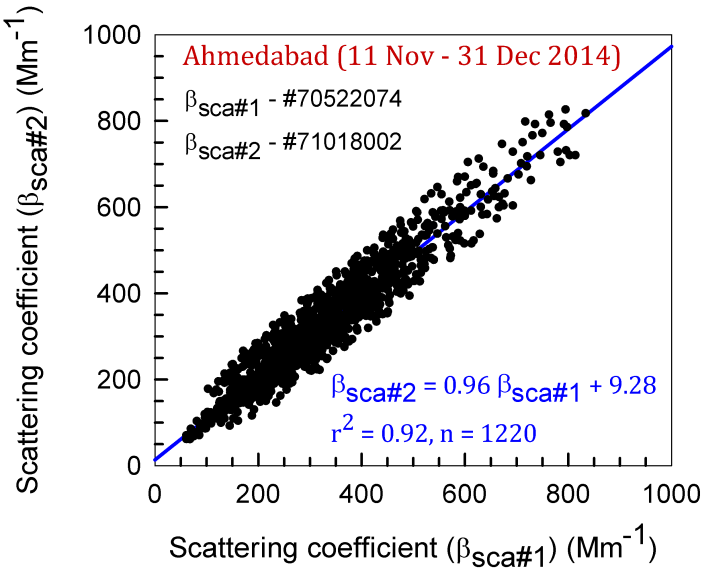

Figure 2.2: *Hourly scattergram of aerosol scattering coefficients (β_{sca}, Mm^{-1}) measured by TSI 3563, nephelometers (#70522074 and #71018002) at Ahmedabad during 11 Nov - 31 Dec 2014. The blue line shows the linear fit, where n (=1220) is the number of measurements of β_{sca} and r^2 (=0.92) is the coefficient of determination.*

An intercomparison exercise of aerosol scattering coefficient was conducted during 2014 (November - December, ambient relative humidity $<30\%$) using more than 13400 measurements at 5 minute interval or 1220 measurements hourly over Ahmedabad spanning over 50 days. The scatter plot reveals a good correlation (r^2=0.92) between the scattering coefficient (β_{sca}) measured using nephelometers (#71018002 and #70522074) (Figure 2.2).

Aerosol scattering coefficient (β_{sca}) strongly depends on the ambient relative humidity (*RH*), and the effects of *RH* on β_{sca} becomes significant when the *RH* exceeds 30%. Hence, the β_{sca} is corrected for the variation in the sample *RH* using hygroscopic *scaling factor* (*SF*) (*Ramachandran and Rajesh*, 2008). *SF* is expressed as the ratio of measured β_{sca} (at ambient *RH*) to estimated β_{sca} at 30% *RH*. Ahmedabad, an urban location can be well represented using an urban aerosol type (*Hess et al.*, 1998), whereas a high altitude remote location,

Table 2.3: *Hygroscopic Scaling factors (SF) at 0.45, 0.55, and 0.70 μm estimated using Optical Properties of Aerosols and Clouds (OPAC) model for an urban and continental clean aerosol types at different RH (30-95%).*

Relative humidity (%)	Scaling factors					
	Urban			Continental clean		
	0.45 μm	0.55 μm	0.70 μm	0.45 μm	0.55 μm	0.70 μm
30	1.00	1.00	1.00	1.00	1.00	1.00
35	1.04	1.04	1.04	1.04	1.04	1.04
40	1.08	1.08	1.08	1.09	1.09	1.09
45	1.12	1.12	1.12	1.13	1.13	1.13
50	1.16	1.16	1.17	1.18	1.18	1.18
55	1.22	1.23	1.23	1.24	1.25	1.25
60	1.28	1.29	1.30	1.31	1.31	1.32
65	1.34	1.35	1.36	1.38	1.38	1.39
70	1.40	1.42	1.43	1.45	1.45	1.46
75	1.53	1.55	1.57	1.59	1.60	1.61
80	1.66	1.69	1.72	1.74	1.75	1.77
85	1.98	2.03	2.08	2.09	2.12	2.16
90	2.30	2.37	2.45	2.44	2.50	2.55
95	3.29	3.46	3.65	3.55	3.68	3.83

Gurushikhar can be represented based on continental clean aerosol type (*Hess et al.*, 1998). The *scaling factor* for an urban and continental clean aerosol types are estimated using Optical Properties of Aerosols and Clouds (OPAC) model (*Hess et al.*, 1998) at 0.45, 0.55, and 0.70 μm (Table 2.3). Scaling factors are in agreement with the values reported by *Charlson et al.* (1984). The aerosol scattering coefficients (β_{sca}) were measured at an averaging time of 300 seconds with an hourly zero calibration over Ahmedabad and Gurushikhar, and corrected for the influence of *RH* using scaling factors as given in Table 2.3. The total uncertainty in β_{sca} due to above errors is found to be $\sim$15% (*Ramachandran and Rajesh*, 2008).

2.1.2 Aethalometer

Aethalometer uses optical attenuation technique for the measurement of black carbon (BC) mass concentration in ambient air (*Hansen et al.*, 1984). The technique assumes that BC mass deposited on the filter is proportional to light attenuation through the filter. Aethalometer measures the attenuation of light through a particle laden and particle free filter spot on the filter (*Weingartner et al.*, 2003). The change in attenuation is utilised to estimate the attenuation coefficient (ATN), which is further used to derive the absorption coefficient (β_{abs}). For low attenuation values the relation between ATN and BC mass loading is found to be linear. However, for higher attenuation values the relation becomes non-linear. This non-linearity is due to filter loading effect (*Gundel et al.*, 1984), which further cause an underestimation of black carbon mass concentrations (*Weingartner et al.*, 2003; *Arnott et al.*, 2005; *Schmid et al.*, 2006; *Virkkula et al.*, 2007; *Collaud Coen et al.*, 2010). Hence, the BC measurements need to be compensated for this loading effect (*Arnott et al.*, 2005; *Weingartner et al.*, 2003; *Arnott et al.*, 2005; *Schmid et al.*, 2006; *Jimenez et al.*, 2007; *Virkkula et al.*, 2007; *Collaud Coen et al.*, 2010; *Park et al.*, 2010; *Hyvärinen et al.*, 2013). Algorithms proposed by *Weingartner et al.* (2003) and *Virkkula et al.* (2007) are extensively used for filter loading effect compensation. Recently, a dual spot attenuation measurement technique based instru-

ment (aethalometer model no. AE33, Magee Scientific) has been developed to take care of the non-linearity in the real-time estimation of BC mass concentration (*Drinovec et al.*, 2015). The dual spot instrument simultaneously measures the attenuation through both the particle loaded sample spots on the filter with different flow rates. The present study utilises BC mass concentrations obtained from aethalometer AE31 (single spot) and AE33 (dual spot) (Table 2.4), and discussed.

Table 2.4: *Characteristics of aethalometers AE31 and AE33*

Parameters	AE31	AE33
Spot	Single	Dual
Spot shape	Extended Oval	Circle
Nominal Spot size (sq. cm)	1.67	0.785
Filter material	Quartz	Teflon coated glass fiber
Length of the filter (cm)	300	300
Width of the filter (cm)	2.5	3.0
ATN threshold (default)	75	120
Resolution (ng m^{-3})	1	1
Detection limit (ng m^{-3})	200	5
Mean ratio	0.87	NA
Filter loading effect compensation	No	Yes
Enhancement parameter	2.14	1.57

2.1.2.1 Single spot aethalometer

The single spot aethalometer (AE31) simultaneously measures the light attenuation through aerosol loaded and aerosol free spots (reference area) on the filter, and estimates the black carbon mass concentration at seven wavelengths (0.37, 0.47, 0.52, 0.59, 0.66, 0.88, and 0.95 μm). The detectors measure the attenuation (ATN) of the light through the sample and reference spots on the filter (Figure 2.3a), which is estimated as

$$ATN = -100 \ ln(I/I_o) \tag{2.11}$$

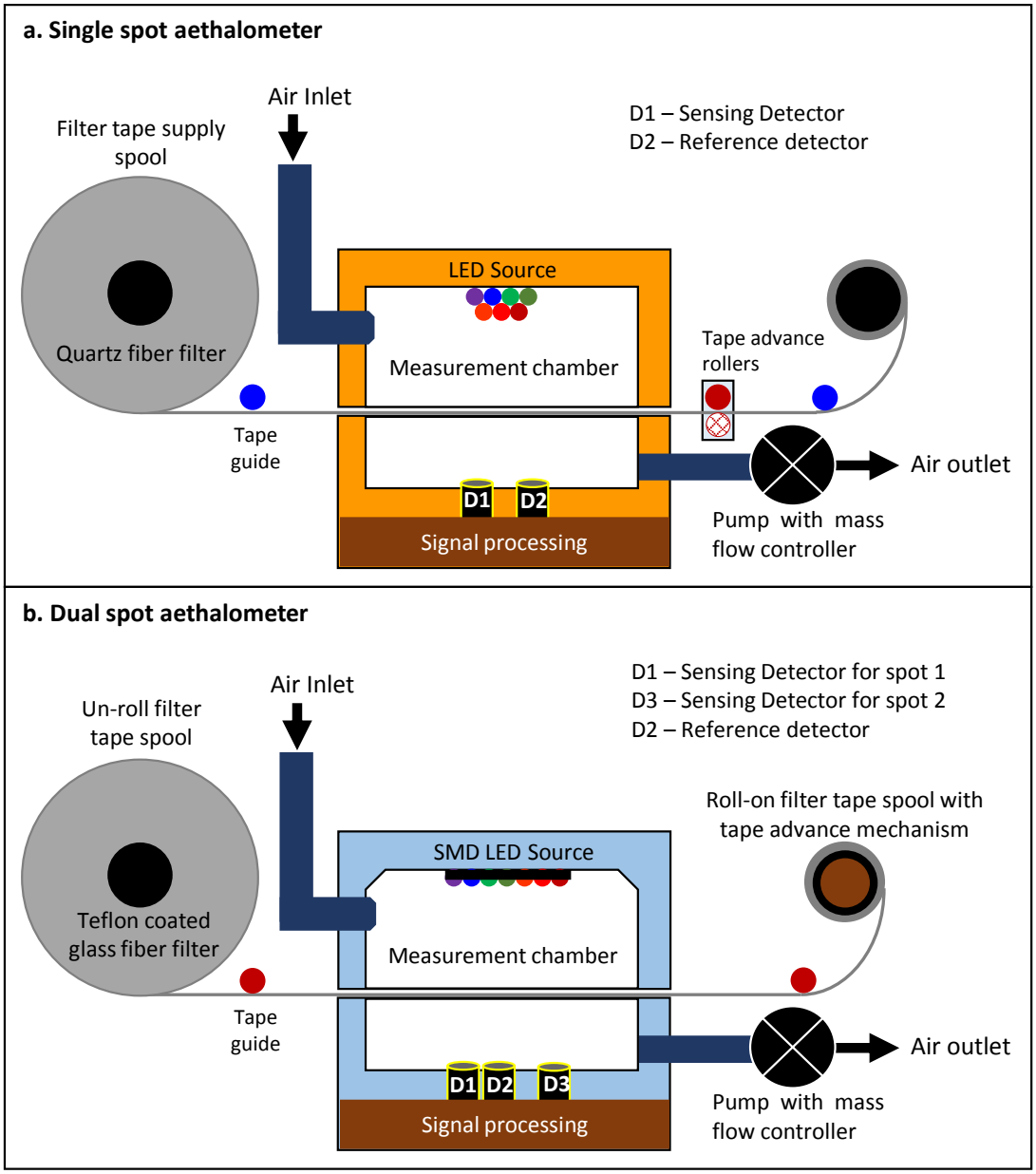

Figure 2.3: *Schematic of (a) aethalometer AE31 (single spot) and (b) aethalometer AE33 (dual spot).*

where I_0 and I are the signals from reference and sample spots respectively. The BC mass is related to rate of change in attenuation as

$$BC = \frac{d(ATN)}{\sigma}\frac{A}{V} \tag{2.12}$$

where BC, σ, A, and V represent black carbon mass concentration, mass specific attenuation cross section ($m^2 g^{-1}$) (Table 2.5), spot area, and volume of air passed through the spot respectively.

Table 2.5: *Mass specific attenuation cross section (σ) for aethalometers AE31 and AE33.*

Wavelength (μm)	Mass specific attenuation cross section ($m^2\ g^{-1}$)	
	AE31	AE33
0.37	39.50	18.47
0.47	31.10	14.54
0.52	28.10	13.14
0.59	24.80	11.58
0.66	22.20	10.35
0.88	16.60	7.77
0.95	15.40	7.16

The aerosol absorption coefficient (β_{abs}, Mm^{-1}) is computed as

$$\beta_{abs} = \frac{BC\ \sigma}{C\ R(ATN)} \tag{2.13}$$

where C represents the enhancement parameter and depends on the filter material (for quartz filter C = 2.14), and $R(ATN)$ is a correction for filter loading effect and is empirically estimated following *Weingartner et al.* (2003) as

$$R(ATN) = \left(\frac{1}{f} - 1\right)\frac{ln(ATN) - ln(10)}{ln(50) - ln(10)} + 1 \tag{2.14}$$

where f represents the compensation parameter for filter loading and is estimated using *Weingartner et al.* (2003) (Table 2.6).

Table 2.6: *Filter loading compensation parameter (f) obtained using (Weingartner et al., 2003) as function of wavelength for aethalometer AE31*

Wavelength (μm)	0.37	0.47	0.52	0.59	0.66	0.88	0.95
f	1.322	1.292	1.254	1.233	1.230	1.212	1.210

The ambient air aerosol sample is accumulated on the filter spot with an extended range sampling head (oval shape spot area of 1.67 sq. cm) (Figure 2.4a, Table 2.4). The deposition rate of BC aerosol on the filter spot is proportional to the sample flow rate and to the BC mass concentration.

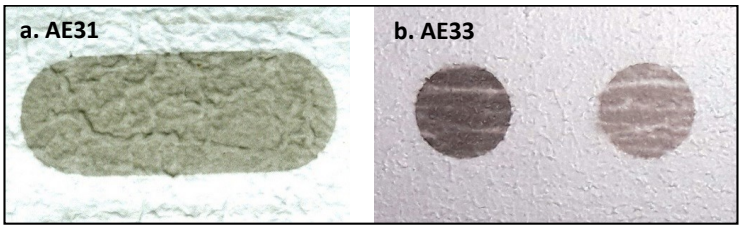

Figure 2.4: *Spot images of (a) aethalometer AE31 and (b) AE33 (not to scale).*

2.1.2.2 Dual spot aethalometer

The dual spot aethalometer (AE33) simultaneously measures the attenuation of light through two distinct circular sample spots (Figure 2.4b) at different flow rates and a particle free spot on the filter (Teflon coated fiber filter) at seven wavelengths (0.37, 0.47, 0.52, 0.59, 0.66, 0.88, and 0.95 μm) (Figure 2.3b) (*Drinovec et al.*, 2015). The detector outputs from the sample spots are used to remove the non-linearity effect, and estimate the BC mass concentration in real-time (*Drinovec et al.*, 2015). The attenuation of light is represented by a non-linear relation (empirical) as given by *Gundel et al.* (1984)

$$ATN_1 = \frac{1}{k}\left(1 - exp(-k\ B_1\ \sigma)\right) \tag{2.15}$$

$$ATN_2 = \frac{1}{k}\left(1 - exp(-k\ B_2\ \sigma)\right) \tag{2.16}$$

where ATN_1 and ATN_2 correspond to the attenuation of light through the sample spots 1 and 2 respectively, B_1 and B_2 represent the aerosol deposition on the sample spots 1 and 2 respectively, and k is filter loading effect compensation factor which is determined as

$$\frac{F_2}{F_1} = \frac{ln(1 - k\ ATN_2)}{ln(1 - k\ ATN_1)} \tag{2.17}$$

where F_1 and F_2 are the volumetric flows through the sample spots 1 and 2 respectively. Then, the BC mass concentration after compensating for filter loading effect is estimated in real-time from the sample spot with higher flow rate as

$$BC = \frac{A\ [d(ATN)/100]}{F_1(1-\phi)\ \sigma\ C(1 - k\ ATN_1)\ dt} \tag{2.18}$$

where A is sample spot area, ϕ represents lateral airflow and is estimated using input (F_{input}) and output (F_{output}) flow rates ($F_{input} = F_{output}(1-\phi)$), C is enhancement parameter (for Teflon coated fiber filter C = 1.57), and σ represents the mass specific attenuation cross section (Table 2.5). BC is also corrected for change in ambient temperature and pressure from standard temperature (293 K) and pressure (1017 hPa) as

$$BC = BC_{raw}\frac{P}{1017}\frac{293}{T} \tag{2.19}$$

where BC_{raw} represents measured BC, P is ambient pressure (hPa), and T is ambient temperature (K). Aerosol absorption coefficient (β_{abs}, $10^6 m^{-1}(Mm^{-1})$) can be further computed as $\beta_{abs} = BC\,\sigma$. The scatter plot between the off-line compensated AE31 BC mass concentrations and on-line compensated AE33 BC data shows an excellent linear agreement (coefficient of determination = 0.98) (Figure 2.5) (*Rajesh and Ramachandran*, 2018). In the present study the BC mass concentration from aethalometer AE31 were taken care of loading effect following *Weingartner et al.* (2003), and the aethalometer AE33 BC data were compensated on-line using the AE33 onboard algorithm given by *Drinovec et al.* (2015) (*Rajesh and Ramachandran*, 2018).

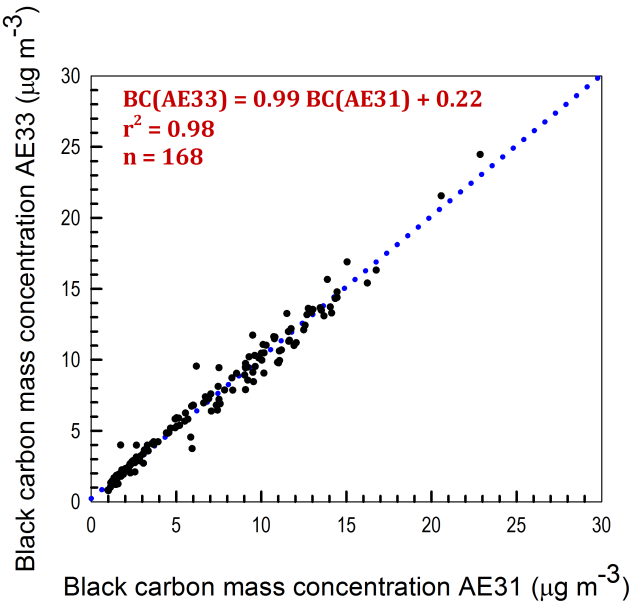

Figure 2.5: *Correlation of the daily averaged black carbon (BC) mass concentration ($\mu g\, m^{-3}$) data from aethalometer AE31 and AE33 at 0.88 μm over Ahmedabad. The blue line (dotted) shows the linear fit, n (=168) is the number of days of observations from aethalometer AE31 and AE33, and coefficient of determination as r^2 (=0.98).*

2.1.2.3 Black carbon aerosols - Fossil fuel and Biomass burning components

A two wavelength aethalometer model is utilised to estimate the relative contribution of traffic emissions (fossil fuel) and biomass emissions (wood burning) based on light attenuation measurements at ultraviolet (0.37 μm) and infrared (0.95 μm) wavelengths (*Sandradewi et al.*, 2008). The model assumes that the fossil fuel (traffic emissions) and wood burning (biomass emissions) are the potential and dominating sources of BC aerosols (*Herich et al.*, 2011). The BC aerosol from fossil fuel has greater absorption at 0.95 μm as compared to BC from wood burning (*Sandradewi et al.*, 2008). The aerosol absorption coefficients (β_{abs}) is proportional to $\lambda^{-\alpha}$, where α represents the absorption exponent and λ is wavelength. Previous studies have documented absorption exponent for fossil fuel (α_{FF}) and wood burning (α_{WB}) to be 1.1 and 2.0 respec-

tively; these values for α_{FF} and α_{WB} were retrieved from various laboratory and field measurements (*Kirchstetter et al.*, 2004; *Bond and Bergstrom*, 2006; *Day et al.*, 2006; *Lewis et al.*, 2008; *Sandradewi et al.*, 2008; *Favez et al.*, 2010; *Fuller et al.*, 2014). The aerosol absorption coefficient (β_{abs}) is the sum of the absorption coefficient from fossil fuels and wood burning component of BC aerosol (*Sandradewi et al.*, 2008), and is expressed as

$$\beta_{abs}(\lambda) = \beta_{abs}(\lambda, FF) + \beta_{abs}(\lambda, WB) \tag{2.20}$$

Aerosol absorption coefficient (β_{abs}), absorption exponent, and the wavelengths are related for fossil fuel and wood burning as

$$\frac{\beta_{abs}(0.37\ \mu m, FF)}{\beta_{abs}(0.95\ \mu m, FF)} = \left[\frac{0.37}{0.95}\right]^{-\alpha_{FF}} \tag{2.21}$$

$$\frac{\beta_{abs}(0.37\ \mu m, WB)}{\beta_{abs}(0.95\ \mu m, WB)} = \left[\frac{0.37}{0.95}\right]^{-\alpha_{WB}} \tag{2.22}$$

where α_{FF} and α_{WB} are absorption exponents computed using β_{abs} at 0.37 and 0.95 μm wavelengths, respectively. BC_{FF} can be computed following the above equations as

$$BC_{FF} = BC\frac{\beta_{abs}(0.95\ \mu m, FF)}{\beta_{abs}(0.95\ \mu m)}, \tag{2.23}$$

and the remaining BC concentration corresponds to BC_{WB} as the total BC mass concentrations is the summation of the BC contributions from fossil fuel and wood burning (*Sandradewi et al.*, 2008).

2.2 Remote sensing data

In the present study data retrieved from the following satellite sensors, namely, MODerate resolution Imaging Spectroradiometer (MODIS), Ozone Monitoring Instrument (OMI), Atmospheric InfraRed Sounder (AIRS) and Tropical Rainfall Measuring Mission (TRMM) have been used for the analysis of aerosol characteristics and their spatial and temporal variability over the study loca-

tions. The details of the satellite data sets used are discussed below.

2.2.1 MODerate resolution Imaging Spectroradiometer

The MODerate resolution Imaging Spectroradiometer (MODIS) is a remote sensing instrument aboard the Terra and Aqua satellites that measures atmospheric aerosols, cloud cover, surface reflectance, vegetation indices, thermal anomalies, etc. with high accuracy on a global scale (*Kaufman et al.*, 1997; *Remer et al.*, 2008). MODIS satellites operate in sun-synchronous, near-polar, circular orbits at an altitude of 705 km above the Earth. The Terra and Aqua spacecraft cross the equator at about 1030 (descending northward) and 1330 LST (ascending southward) respectively with a swath of 2330 km (cross track) by 10 km (along track at nadir). The aerosol products over land from MODIS are being extensively used to study the spatio-temporal variations in aerosol properties (*Levy et al.*, 2007; *Remer et al.*, 2008). The uncertainty in MODIS retrieved aerosol optical depth (*AOD*) is $\pm$ 0.05 + 0.15*AOD* over land (*Remer et al.*, 2008). In the present study, MODIS Level 2 10 km $\times$ 10 km Collection 5.1 (C5.1) daily aerosol optical depth (AOD) at 0.55 μm, and Ångström exponent (α) are utilized (*Remer et al.*, 2008). The newly released MODIS Collection 6 (C6) aerosol products are also available which has some improvements compared to MODIS C5.1 products (*Fan et al.*, 2017). The intercomparison of MODIS C5.1 and C6 *AOD* products reveals that for 10 km products, the C6 algorithm has slightly increased accuracy, with about 3-12% more data falling within the expected error envelope (*Fan et al.*, 2017). The Ångström exponent (α) is further used to derive AOD spectra in the wavelengths range of 0.4-1.0 μm using Ångström power law ($\tau(\lambda) = \beta\lambda^{-\alpha}$, $\tau(\lambda)$ is the aerosol optical depth at wavelength λ (in μm), and β represents the turbidity coefficient (*Ångström*, 1961)). The MODIS data has been downloaded from https://giovanni.gsfc.nasa.gov/giovanni. The daily MODIS *AODs* (Terra and Aqua) are further utilised to estimate the monthly mean *AODs* over the study locations.

2.2.2 Ozone Monitoring Instrument

The Ozone Monitoring Instrument (OMI) is onboard the Earth Observing System (EOS) Aura satellite. OMI is a spectrograph with high resolution used for the measurement of the upwelling radiance in ultraviolet and visible regimes (0.27-0.50 μm) at the top of the Earth's atmosphere. OMI satellite operates in sun-synchronous, near-polar orbit at an altitude of 705 km above the Earth with a sixteen-day repeat cycle and 233 revolutions per cycle. The OMI spacecraft crosses the equator at approximately 1:45 PM (ascending northward) with a swath of 2600 km (114^o across track viewing angle). It measures ozone, aerosols and other gases in the atmosphere. The monthly mean columnar ozone and single scattering albedo at 0.50 μm over the study locations was obtained from the daily mean OMI data. OMI Level 3 data at a lat-lon resolution of $1^o \times 1^o$ centered around the study locations are utilised. The OMI data has been downloaded from https://giovanni.gsfc.nasa.gov/giovanni.

2.2.3 Atmospheric Infrared Sounder

The Atmospheric InfraRed Sounder (AIRS) is on board the EOS Aqua satellite. AIRS satellite operates in sun-synchronous, near-polar, circular orbits at an altitude of 705 km above the Earth. It provides the physical state of the Earth's atmospheric column (air temperature, water vapor, clouds) and the distribution of trace gas constituents (ozone, carbon monoxide, carbon dioxide and methane) on a daily global scale. In the present study the columnar water vapor data from AIRS satellite at a lat-lon resolution of $1^o \times 1^o$ centered around the study locations were downloaded from https:// giovanni.gsfc.nasa.gov/giovanni and utilised.

2.2.4 Tropical Rainfall Measuring Mission

The Tropical Rainfall Measuring Mission (TRMM) satellite is used to measure tropical and subtropical rainfall through microwave and visible infrared sensors. TRMM satellite operates in non-sun-synchronous, near-circular orbit

at an altitude of 402 km above the Earth. TRMM's orbit ranges between 35^o N and 35^o S of the equator and has spatial and temporal resolutions of 0.25^o and 92.5 minute, respectively. The TRMM rainfall data were downloaded from https://giovanni.gsfc.nasa.gov/giovanni.

2.3 Meteorological data/datasets

2.3.1 Weather station

A weather station consists of combination of several meteorological sensors for the measurement of ambient air temperature, relative humidity (RH), pressure, wind speed, wind direction, and precipitation. In the present study we have used Vaisala weather station, model no. WXT520, which can measure the above meteorological parameters. It uses capacitive silicon BAROCAP, capacitive ceramic THERMOCAP, capacitive thin film polymer HUMICAP, and WINDCAP sensors for pressure, temperature, relative humidity, and wind (speed and direction) measurements respectively. The measurement principle of the pressure (BAROCAP), temperature (THERMOCAP), and relative humidity (HUMICAP) sensors are based on the RC oscillators and two reference capacitors against which the capacitance of the sensors are continuously measured. The wind sensor (WINDCAP) has an array of three equally spaced ultrasonic transducers on a horizontal plane and the wind parameters (speed and direction) are estimated by measuring the time it takes the ultrasound to travel from each transducer to the other two. The meteorological data measured at a temporal resolution of 10 s during 2015-2016 over the study locations are used.

2.3.2 National Center for Environmental Prediction

The National Center for Environmental Prediction (NCEP)/National Center for Atmospheric Research (NCAR) reanalysis meteorological dataset represents the state of the Earth's atmosphere utilising various meteorological observations (approximately 7-9 million observations) and numerical weather predic-

tion model output. The reanalysis data are available for various meteorological parameters (temperature, relative humidity, wind, vertical velocity, pressure, etc.) at 17 pressure and 28 sigma levels as 6-hourly, daily and monthly mean observations. The NCEP/NCAR reanalysis data can be downloaded from https://www.esrl.noaa.gov/psd/data/gridded/ data.ncep.reanalysis.html. The present study utilises the NCEP/NCAR reanalysis monthly average synoptic wind patterns over India and surrounding regions.

2.3.3 European Centre for Medium-Range Weather Forecast

The European Centre for Medium-Range Weather Forecast (ECMWF) is one of the world's largest archive of numerical weather prediction data. Numerical weather prediction (NWP) requires meteorological data measured by various Earth (surface and vertical) observation systems (like automatic and manned weather stations, aircraft, ships, weather balloons, radar, wind profiler, and satellites). These observed data are assimilated to generate an initial state of a computer model of the atmosphere. The ECMWF provides the various atmospheric parameters like temperature, wind, boundary layer height, clear sky surface photosynthetically active radiation, convective precipitation, downward UV radiation at the surface, cloud cover, mean sea level pressure, sea surface temperature, sunshine duration, surface net solar radiation, incident solar radiation, total column ozone, total column water vapor, total precipitation, etc. The ECMWF dataset at a spatial resolution of $0.25^o \times 0.25^o$ has been downloaded from https://www.ecmwf.int/. In the present study the atmospheric boundary layer height data is used for Ahmedabad only (because of plane topography) from the ECMWF reanalysis data.

2.3.4 Hybrid Single-Particle Lagrangian Integrated Trajectory

The Hybrid Single-Particle Lagrangian Integrated Trajectory (HYSPLIT) model is a mathematical tool for computing air mass transport, dispersion, and deposition simulations (*Draxler and Hess*, 1998). The model uses the Lagrangian approach (dynamic frame of reference is used for the computation of advec-

tion and diffusion processes as the air parcels are non-stationary), and the Eulerian approach (stationary 3D gridded frame of reference for the estimation of pollutant concentrations) in the computational process. This model is being used widely to investigate the air mass trajectories and source receptor relationships. It uses meteorological data from the Global Data Assimilation System (GDAS) model. GDAS is an atmospheric model which utilises the available/reported various surface (land and sea) and vertical (meteorological balloon, wind profiler, aircraft, ship, radar, and satellite) meteorological data and assimilate them with the computation of numerical weather prediction models. The online and computer based HYSPLIT models are available at https://ready.arl.noaa.gov/HYSPLIT.php. In order to examine the potential source areas and their transport route over the study locations, 7 day (mean residence time of aerosols in the lower atmosphere) back trajectory analysis is undertaken using the Hybrid Single Particle Lagrangian Integrated Trajectory (HYSPLIT) model (version 4.9) corresponding to an altitude of 500 m above ground level (*Draxler and Hess*, 1998). Surface effects can dominate the back trajectory below 500 m, and therefore, back trajectory at 500 m was chosen to examine the influence of transport. The daily trajectory in each month was assigned to clusters according to their magnitude and direction using the k-mean cluster algorithm in the HYSPLIT model. Trajectory clustering minimizes the variability among the trajectories within a cluster, and maximizes the variability between the clusters (*Toledano et al.*, 2009). The k-mean cluster algorithm used in this work is a widely employed technique to quantify transport patterns and potential sources of both anthropogenic pollution and natural aerosols (*Wang et al.*, 2010). The optimal number of significant clusters is obtained from the total spatial variance plot against the number of clusters, and in the present study it is found that 5 clusters can best represent the meteorological features.

2.3.5 Fire count

The Moderate Resolution Imaging Spectroradiometer (MODIS) views the entire Earth's surface every 1-2 days and acquires data in 36 spectral bands. It has a 1 km resolution in the mid and longwave infrared bands, which are used to detect actively burning fires. MODIS fire and thermal anomalies product is a hotspot detection product to estimate the occurrence of fire and hot objects on Earth's surface. The spatial distribution of biomass burning, which is one of the potential source of black carbon aerosols, is examined by analysing the MODIS cloud corrected fire count version 5 monthly data available at $1^o \times 1^o$ resolution.

2.4 Radiative forcing estimation

The spectral optical properties are derived using Optical Properties of Aerosols and Clouds (OPAC) model *Hess et al.* (1998), which are needed as inputs for the estimation of aerosol radiative forcing using Santa Barbara DISORT Atmospheric Radiative Transfer (SBDART) model (*Ricchiazzi et al.*, 1998).

2.4.1 Optical Properties of Aerosols and Clouds

The Optical Properties of Aerosols and Clouds (OPAC) model (*Hess et al.*, 1998) provides the microphysical and optical properties of atmospheric particulate matter in the wavelength range of 0.25 to 40 μm. OPAC is a software package that consists of dataset (of optical and physical properties of cloud and aerosol at 8 humidities (0, 50, 70, 80, 90, 95, 98, and 99%)), and a Mie scattering FORTRAN code (to extract the optical and physical properties of species from the dataset, to compute additional spectral optical properties, and to estimate the optical properties of mixtures of aerosol components). OPAC consists of ten major aerosol components viz., water soluble aerosols (typically nitrate and sulfate aerosols of anthropogenic origin), insolubles (typically soil particles), black carbon (anthropogenic origin), sea salts (natural origin in accumulation and coarse mode), mineral dust (natural origin from arid surface

in three modes), mineral-transported and sulfate droplets (*Hess et al.*, 1998). It also quantifies the various aerosol types (Continental clean, Continental average, Continental polluted, Urban, Desert, Maritime clean, Maritime polluted, Maritime tropical, etc.) with different aerosol components and corresponding particle number density (*Hess et al.*, 1998). The model can be used to construct new mixtures from the available aerosol components to match the observations. The model sensitivity and its role are discussed in Chapter 5.

2.4.2 Santa Barbara DISORT Atmospheric Radiative Transfer

Aerosol radiative forcing (ARF) is computed using Santa Barbara DISORT Atmospheric Radiative Transfer (SBDART), 1998) code in the shortwave (0.25-4.0 μm) as well as longwave (4.0-40.0 μm) range (*Ricchiazzi et al.*, 1998). SBDART algorithm is being widely used for the estimation of radiation budget of the Earth-atmosphere system. It calculates the plane-parallel radiative transfer equations both in clear and cloudy sky conditions for the Earth-atmosphere system. It uses the low resolution band models of LOWTRAN-7 atmospheric transmission code for molecular absorption. Radiative transfer equations are numerically integrated using Discrete Ordinate Radiative Transfer (DISORT) module (*Stamnes et al.*, 1988). The DISORT presents a stable solution to the plane-parallel radiative transfer equations in the Earth-atmosphere system. SBDART can be configured for 65 atmospheric layers and 40 radiation streams; in the present study we have used 65 atmospheric layers and 20 radiation streams in the shortwave (Chapter 1, Section 1.3) radiative transfer calculations at the surface, top of the atmosphere, and atmosphere. The model sensitivity and radiative forcing estimates are discussed in Chapter 5.

2.5 Observational locations

The aerosol measurements were carried out at Physical Research Laboratory (PRL), Ahmedabad (23.03^{o}N, 72.55^{o}E, 55 m above mean sea level (AMSL)), and at Optical Aeronomy Laboratory, IR Observatory, Gurushikhar, Mt. Abu

(24.65^{o}N, 72.78^{o}E, 1680 m AMSL) in western India (Figure 2.6). Ahmedabad is an urban, semi-arid, densely populated (population in excess of 7 million), and one of the industrially developed districts of Gujarat state in western India. Ahmedabad is located in Central Gujarat and has several micro, small, medium and large industries of various types (related to textiles, chemicals, machinery, metal products, pharmaceutical, engineering, plastics, electrical appliances, electronics, automobiles etc.). Two thermal power plants (coal-based) are placed in the vicinity (10-25 km away) of the observational location in Ahmedabad. The other observational site is a high altitude remote site in mountain region (Gurushikhar), and is about 200 km away from Ahmedabad in western India (Figure 2.6). Gurushikhar is is the highest point of the Aravalli Range and a pristine site in the Arbuda Mountains of Rajasthan in western India. The city of Mount Abu (1180 m AMSL) lies downhill from Gurushikhar at a distance of 15 km on a high rocky plateau and surrounded by forests. The city of Mount Abu is a popular hill station and a tourist destination in the Aravalli range. To the northwest of the Gurushikhar location lies Abu road (280 m AMSL) at a distance of 40 km in the hills of the Aravalli range and has significant anthropogenic activity. The population from the city of Mount Abu which is located at an elevation of 1180 m AMSL up to Gurushikhar is of the order to 25000. The high altitude site can be characterised as a remote location because of very negligible anthropogenic emissions within the immediate vicinity. Hence, aerosol measurements over this site represent background condition on a regional scale. Both the observational sites (Ahmedabad and Gurushikhar) are influenced by mineral dust from the Thar Desert, sea salt from the Arabian Sea, and black carbon aerosols from the Indo Gangetic Plain (north-northeastern part of India) during the year (Figure 2.6).

Depending on the prevailing meteorology over the study region the entire year is divided as winter (December-January-February), premonsoon (March-April-May), monsoon (June-July-August-September) and postmonsoon (October-November) seasons. Maximum ambient air temperature is observed during premonsoon (32 and 22°C) followed by monsoon (31 and 20°C),

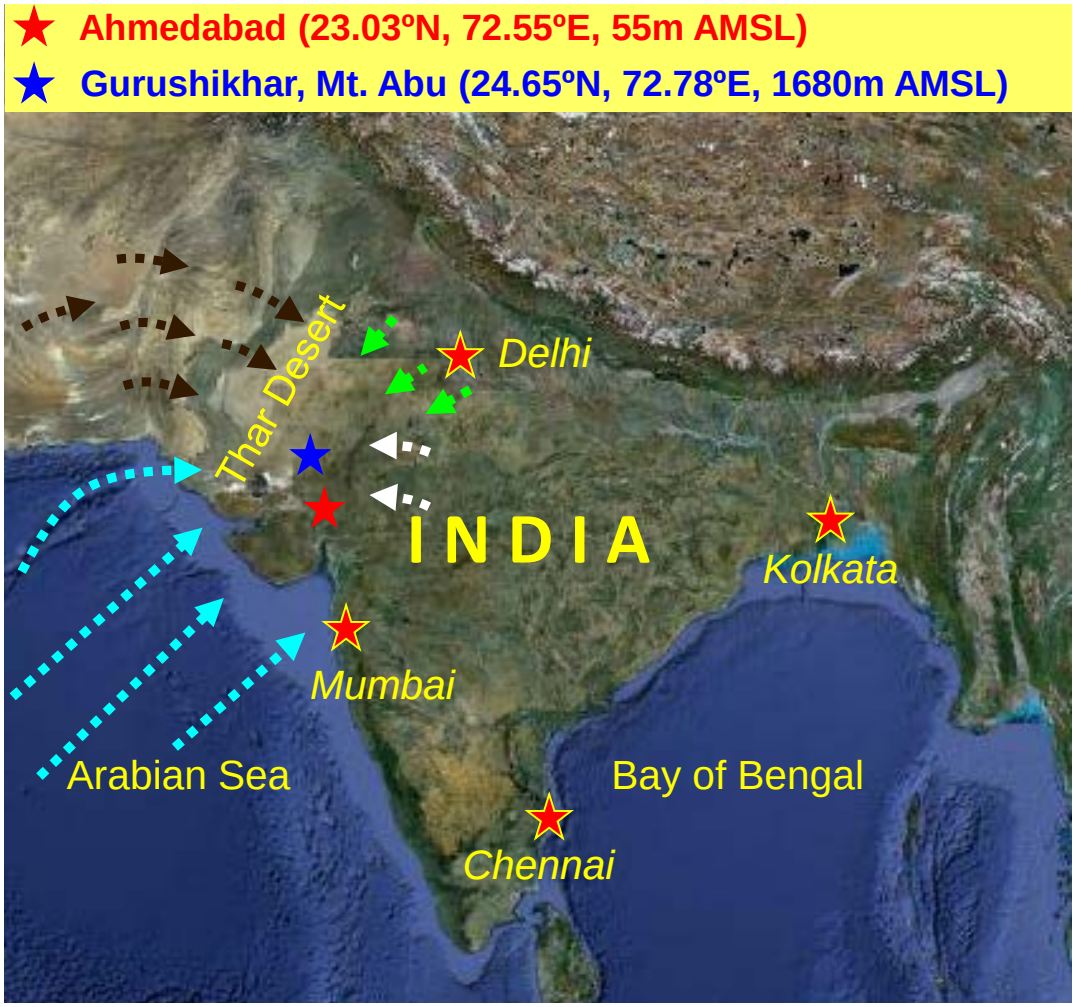

Figure 2.6: *Map of India showing the study locations (Ahmedabad and Gurushikhar) in the western India region (Google Earth Images). Delhi, Mumbai, Chennai, and Kolkata, metro cities in India, are also shown. The synoptic wind patterns during winter, premonsoon, monsoon, and postmonsoon are shown in green, brown, blue, and white respectively. Latitude, longitude, and altitude (above mean sea level (AMSL)) of Ahmedabad and Gurushikhar are given above.*

postmonsoon (27 and 17°C) and winter (22 and 14°C) at the observational sites (Ahmedabad and Gurushikhar). The monthly mean air temperature shows the highest value during May and lowest values during January (Figure 2.7a). The relative humidity (RH) is highest during monsoon (68 and 69%) with maximum RH in August (Figure 2.7b). The mean surface wind speeds consistently

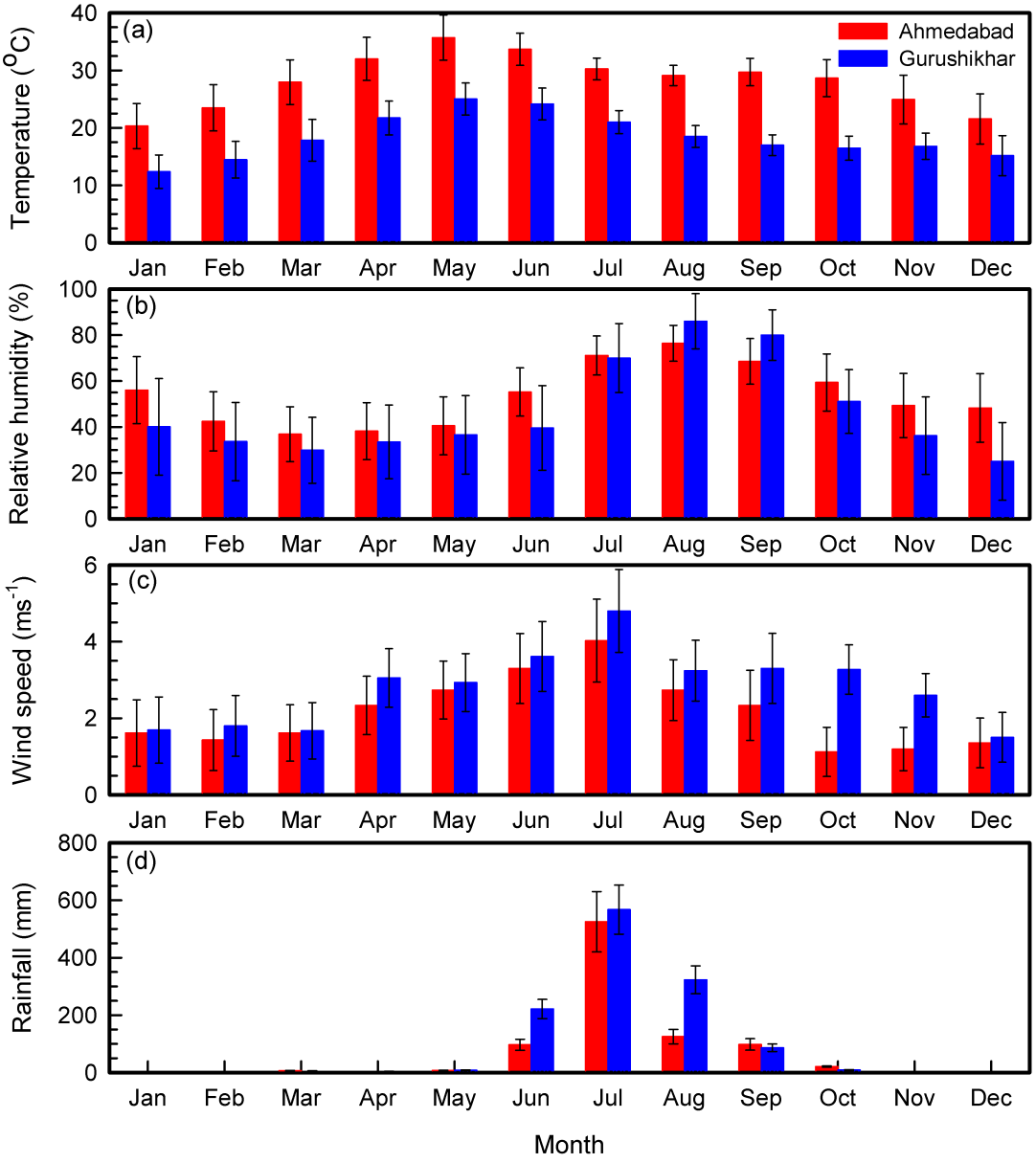

Figure 2.7: *Monthly average (a) temperature (^{o}C), (b) relative humidity (RH, %), (c) wind speed (ms^{-1}), and rainfall (mm) over Ahmedabad and Gurushikhar during 2015-2016. Vertical bars show $\pm 1\sigma$ variation from the mean.*

increase from winter (1.5 and 1.7 ms^{-1}) to monsoon (3.1 and 3.7 ms^{-1}), and then decrease. The maximum mean surface wind speeds are observed dur-

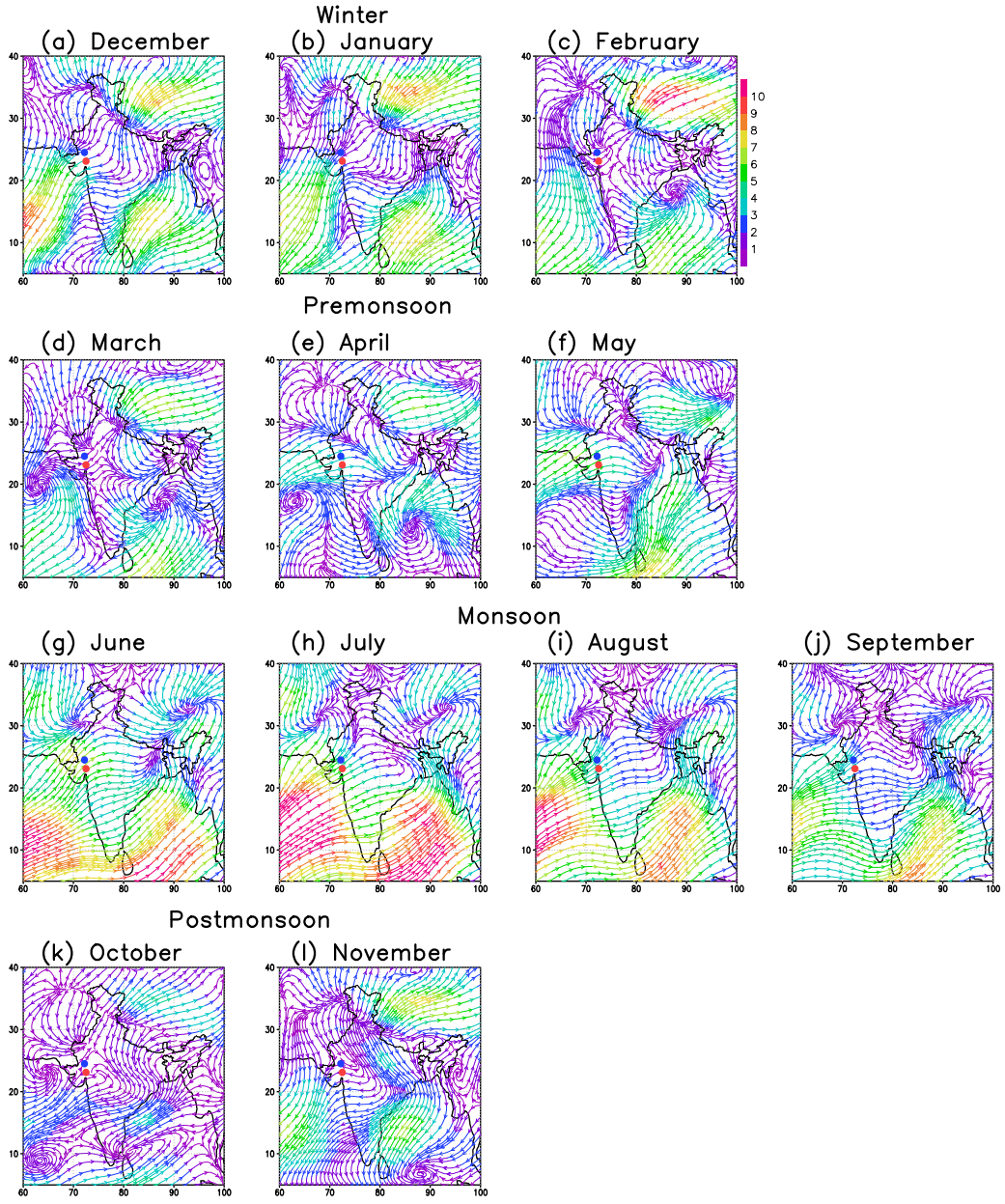

Figure 2.8: *Synoptic average wind stream* (ms^{-1}) *over India during winter (Dec (a), Jan (b), and Feb (c)), premonsoon (Mar (d), Apr (e), and May (f)), monsoon (Jun (g), Jul (h), Aug (i), and Sep (j)), and postmonsoon (Oct (k), and Nov (l)) for 2015 - 2016. The wind field data are obtained from NCEP/NCAR reanalysis. Filled red and blue circles represent Ahmedabad and Gurushikhar respectively.*

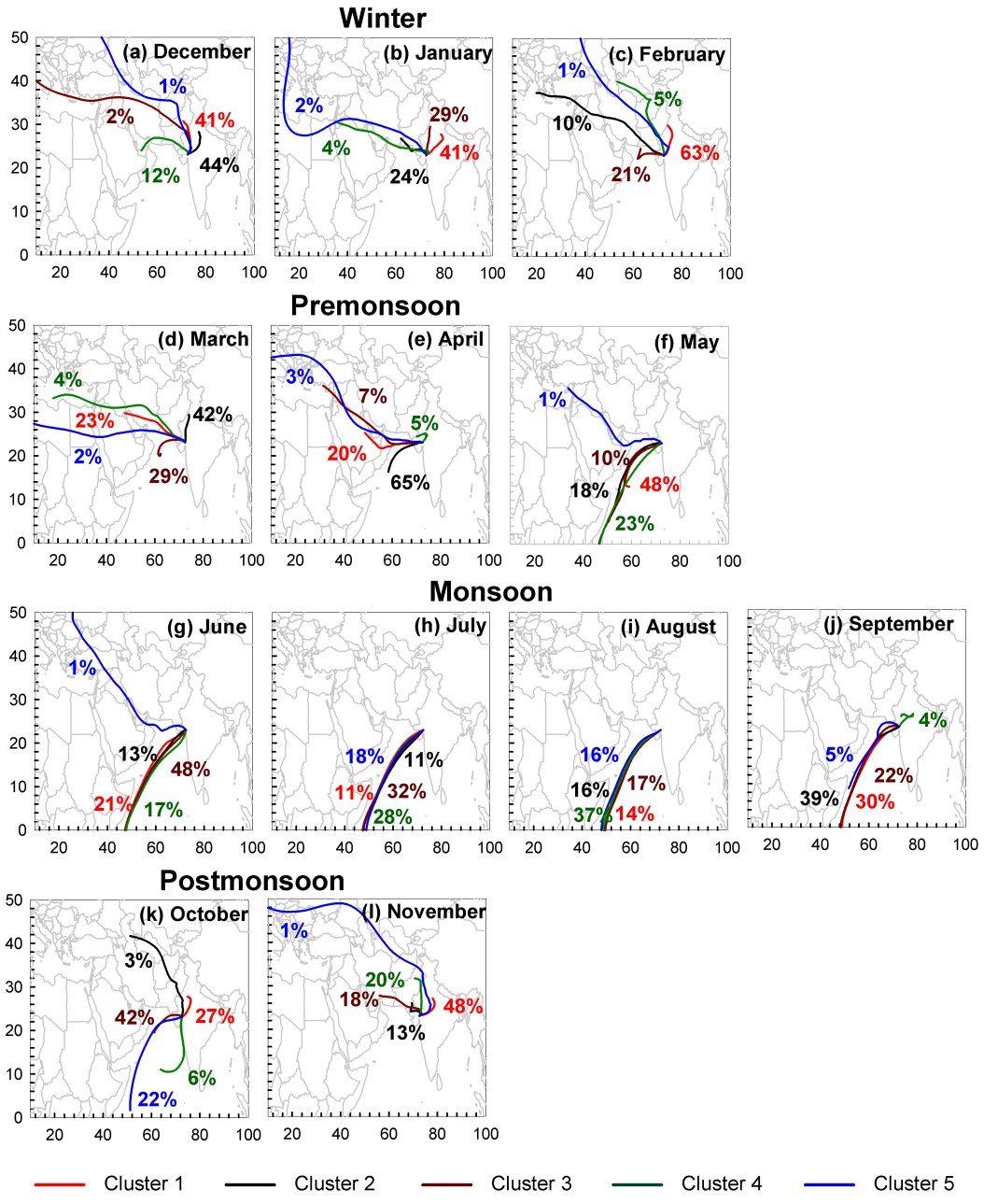

Figure 2.9: *Monthly trajectory cluster plot over Ahmedabad during winter (Dec (a), Jan (b), and Feb (c)), premonsoon (Mar (d), Apr (e), and May (f)), monsoon (Jun (g), Jul (h), Aug (i), and Sep (j)), and postmonsoon (Oct (k), and Nov (l)) at 500 m above ground level for 2015 and 2016. The cluster numbers 1, 2, 3, 4 and 5 are plotted in colors red, black, brown, green and blue respectively.*

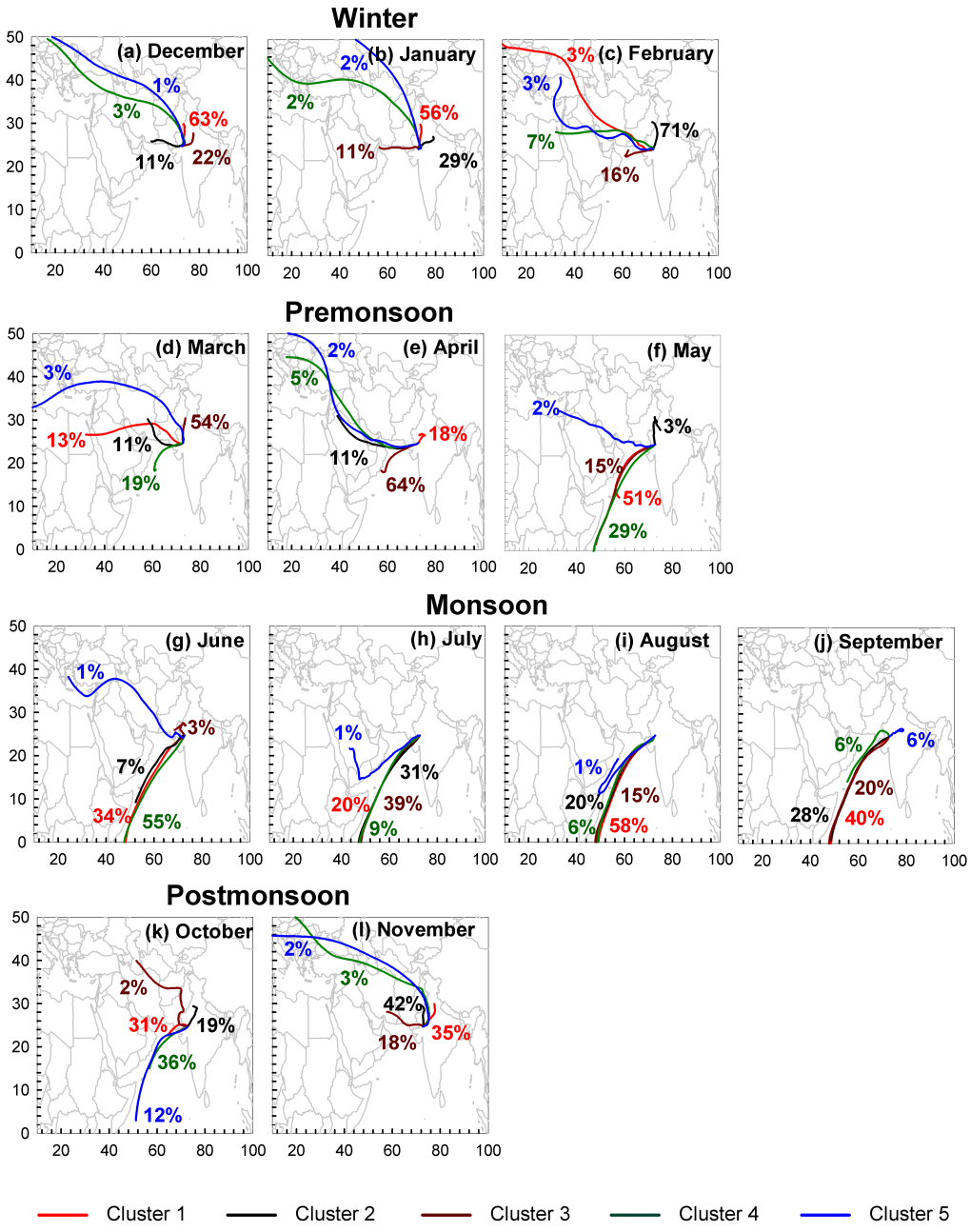

Figure 2.10: *Monthly trajectory cluster plot over Gurushikhar during winter (Dec (a), Jan (b), and Feb (c)), premonsoon (Mar (d), Apr (e), and May (f)), monsoon (Jun (g), Jul (h), Aug (i), and Sep (j)), and postmonsoon (Oct (k), and Nov (l)) at 500 m above ground level for 2015 and 2016. The cluster numbers 1, 2, 3, 4 and 5 are plotted in colors red, black, brown, green and blue respectively.*

ing July (4.0 and 4.8 ms^{-1}) at the observation locations (Ahmedabad and Gurushikhar, Mt. Abu) (Figure 2.7c). About 97% of the rainfall over Ahmedabad and Gurushikhar is distributed over the monsoon period of June (97 and 221 mm), July (525 and 567 mm), August (125 and 323 mm), and September (82 and 10 mm) (Figure 2.7d) during 2015-2016. The mean synoptic surface winds over the study locations exhibit significant variability in wind speed and wind direction (Figure 2.8). During premonsoon the winds (dry and moderate speed) are from the west, while the winds (moist and stronger) are from the Arabian Sea and west during monsoon. The wind starts changeover from southwest to northeast during postmonsoon, whereas during winter the winds (dry and calm) are from north-northeasterly. The cluster mean trajectories and their contributions (percentage) are computed for each month at both the observational locations. The cluster mean trajectories are similar over Ahmedabad and Gurushikhar, which, however, exhibit significant seasonal variability (Figures 2.9 and 2.10) similar to wind patterns (Figure 2.8).

Chapter 3

Optical and physical characteristics of aerosols over urban and high altitude remote locations

The optical properties of aerosol describe the interaction between aerosol and electromagnetic radiation. Scattering is a process through which when a particle interacts with an incident electromagnetic wave it extracts energy from the incident wave and reradiates the incident energy in 4π directions. Scattering can be classified into two categories (i) *elastic scattering* (the wavelength of the scattered radiation is same as the incident radiation), and (ii) *inelastic scattering* (the wavelength of the scattered radiation is different from that of the incident radiation). Depending on the size of the particle as compared to the wavelength of the incident radiation the elastic scattering is further classified into two categories (i) *Rayleigh scattering* and, (ii) *Mie scattering*. When the particle radius is much smaller than the incident wavelength ($< 0.03\ \lambda$, λ is the wavelength), the scattering is called *Rayleigh scattering*. Air molecules are the chief Rayleigh scatterers in the atmosphere. Rayleigh scattering varies inversely as the fourth power of the wavelength, with equal amount of fluxes scattered in both forward and backward hemispheres, and therefore, the scattering is symmetric. As the particle radius becomes comparable to the incident wavelength the scattering process is no more symmetric and is described by *Mie scattering*. In Mie scattering more radiation is scattered in the forward direction than in the backward direction. Aerosols are the chief Mie scatterers in

the atmosphere. The energy scattered (I_{sca}) or absorbed (I_{abs}) by the particles is directly proportional to the incident intensity (I_0), and given as

$$I_{sca,abs} = K_{sca,abs}\, I_0 \tag{3.1}$$

where K_{sca} and K_{abs} are the single particle scattering and absorption cross sections (m^2) respectively. Scattering or absorption cross section of a particle is a measure of the probability of scattering or absorption process, and depends on its geometrical cross section and the scattering (Q_{sca}) or absorption (Q_{abs}) efficiency. The scattering (Q_{sca}) or absorption (Q_{abs}) efficiency is defined as the ratio of scattering or absorption cross section to the geometrical cross section of the spherical particle, and is given as

$$Q_{sca,abs} = \frac{K_{sca,abs}}{\pi r^2} \tag{3.2}$$

Extinction efficiency (Q_{ext}) of the particle is the sum of the scattering and absorption efficiencies

$$Q_{ext} = Q_{sca} + Q_{abs}. \tag{3.3}$$

According to Mie theory, scattering efficiency of a spherical particle depends on the size parameter x (= $\frac{2\pi r}{\lambda}$, where λ is the wavelength of the incident radiation and r is the particle radius) and complex refractive index $m = p \pm iq$ (where *p* (real part) and *q* (imaginary part) represent the scattering and absorption properties of aerosols respectively). The aerosol scattering, absorption, and extinction coefficients are estimated using the number size distribution of aerosol population and its efficiency of interaction with radiation. For a monochromatic beam of radiation, scattering (β_{sca}) and absorption (β_{abs}) coefficients (*Bohren and Huffman*, 1983) are defined as

$$\beta_{sca,abs}(\lambda) = \int_{r_1}^{r_2} \pi r^2\, Q_{sca,abs}\,(x,m)\, n(r)\, dr \tag{3.4}$$

where $n(r)$ is the number distribution of aerosols per unit volume per radius range between r_1 and r_2. The extinction (β_{ext}) coefficient is defined as the sum

of the scattering and absorption coefficients and is written as

$$\beta_{ext}(\lambda) = \beta_{sca}(\lambda) + \beta_{abs}(\lambda). \tag{3.5}$$

Aerosol optical depth (*AOD*) is a quantitative measure of the extinction (scattering + absorption) of solar radiation due to aerosols when the solar radiation passes through the atmosphere and reaches the Earth's surface. It is the most important parameter in the radiative transfer calculations and represents the columnar aerosol loading. The total optical depth (τ) following Beer Lambert's law is given as

$$\tau(\lambda) = -\frac{1}{m} ln \frac{I(\lambda)}{I_0(\lambda)} \tag{3.6}$$

where I is the surface measured direct solar irradiance, I_0 is extraterrestrial solar irradiance, m is the air mass or relative path length and τ is the total optical depth at wavelength λ is expressed as the sum of the $\tau_{Rayleigh}$ (Rayleigh optical depth due to air molecule scattering), $\tau_{aerosol}$ (aerosol optical depth, *AOD*), and τ_{mol} (optical depth due to molecular (ozone, nitrogen dioxide or water vapor) absorptions)

$$\tau(\lambda) = \tau_{Rayleigh}(\lambda) + \tau_{aerosol}(\lambda) + \tau_{mol}(\lambda). \tag{3.7}$$

Aerosol optical depth (*AOD*, $\tau_{aerosol}$) is determined by subtracting $\tau_{Rayleigh}$ and τ_{mol} from τ and is given as

$$\tau_{aerosol}(\lambda) = \tau(\lambda) - \tau_{Rayleigh}(\lambda) - \tau_{mol}(\lambda). \tag{3.8}$$

Typically, the *AOD* values (a unitless quantity) range from 0.02 for a very clean area to 0.6 for fairly polluted area and it can be as high as 1.5 during heavy biomass burning or dust event.

The probability of a photon to be scattered rather than absorbed while interacting with a particle is defined as the *single scattering albedo* (*SSA*) of that particle, and is represented as

$$SSA = \frac{\beta_{sca}(\lambda)}{\beta_{ext}(\lambda)} = 1 - \frac{\beta_{abs}(\lambda)}{\beta_{ext}(\lambda)}, \tag{3.9}$$

The single scattering albedo can vary from 0 (perfect absorber) to 1 (perfect scatterer). *SSA* of black carbon is 0.23 while *SSA* of sulfate and sea salt is $\sim$1 at 0.55 μm (*Hess et al.*, 1998).

The spectral scattering coefficients can be further analyzed to get an insight into the sizes of particles (smaller or larger) which dominate the aerosol size distribution. *Ångström exponent* (α) describes the dependence of aerosol scattering coefficient on wavelength and can be expressed for the wavelength range 0.45 to 0.7 μm as

$$\alpha = \frac{-ln[\beta_{sca}(0.70)/\beta_{sca}(0.45)]}{ln[0.70/0.45]}. \tag{3.10}$$

The parameter α provides qualitative information of the particle sizes that dominate the aerosol size distribution. Higher α values indicate the dominance of smaller particles in scattering while smaller values arise due to increase of larger particles in an aerosol size distribution. Typically, α values approaching 4 represent air molecules (particle sizes being much smaller than the incident wavelength), whereas, α values near zero represent particles much larger than the wavelength.

The angular distribution of light intensity scattered by a particle at a given wavelength is known as the *phase function* (P). It is defined as the ratio of the energy scattered by aerosols per unit solid angle in a given direction (θ) with respect to the incident direction, to the average energy scattered per unit solid angle in all directions and is written as

$$P(\theta) = \frac{I(\theta)}{\int_0^\pi I(\theta) sin\theta \, d\theta} \tag{3.11}$$

where $I(\theta)$ is the intensity of scattered radiation in the direction θ. The aerosol *asymmetry factor* (g) is defined as the cosine-weighted average of the phase

function $P(\theta)$ and is written as

$$g = \frac{\int_0^\pi P(\theta) cos\theta \, d(cos\theta)}{\int_0^\pi P(\theta) \, d(cos\theta)} \tag{3.12}$$

The asymmetry factor is important in radiative transfer models of the atmosphere which take into account the angular scattering of radiation. The value of g ranges from -1 for complete back scattering to +1 for complete forward scattering. g = 0 for isotropic scattering (e.g., air molecules). Globally, g values are heterogeneous, and vary from 0.5 (polluted) to 0.75 (dust/seasalt dominated) for aerosols at 0.55 μm. For pristine (aerosol free) environment values are close to 0.1. To date there exists no experimental method for the direct measurement of asymmetry parameter of aerosols. *Andrews et al.* (2006) has given an empirical relation between hemispheric backscatter fraction (*b*) and *g* based on the plot of *Wiscombe and Grams* (1976), and used the equation to derive *g*,

$$g = -7.143889\, b^3 + 7.464439\, b^2 - 3.96356\, b + 0.9893. \tag{3.13}$$

Hemispheric backscatter fraction (*b*) is a unitless parameter and is defined as the ratio of light scattered into the backward (90^o-180^o scattering angles) hemisphere (β_{bsca}) to total light scattered (0^o-180^o scattering angles) (β_{sca}) (*Charlson et al.*, 1984). It can be measured directly with an integrating nephelometer equipped with backscatter shutter. The backscatter fraction is 0.5 for Rayleigh scattering. This factor is found to be largely a function of the composition of the particulate matter and the value decreases as the particle size increases.

3.1 Optical and physical characteristics of aerosols over an urban location: Ahmedabad

The aerosol scattering (β_{sca}) and absorption (β_{abs}) coefficient measurements were conducted over an urban location, Ahmedabad using nephelometer (TSI 3563) and aethalometer (AE31) respectively during 2015-2016 (Chapter 2). As

a quality control, data collected during the local festivals (Diwali, Holi, Navratri) days have not been utilised in the present study, because, the magnitudes of β_{sca} and β_{abs} were quite high (2-5 times) during these festivals. During these festivals an unusual, and a significant increase in the vehicular traffic and accompanying emissions modulate the optical and physical properties of aerosol patterns and their levels (*Ramachandran and Rajesh*, 2007).

Table 3.1: *Number of days of aerosol scattering (β_{sca}) and absorption (β_{abs}) coefficient measurements over Ahmedabad during 2015-2016. Total number of days of β_{sca} and β_{abs} measurements are 684 and 685 days. The data gaps are due to maintenance of the instruments over Ahmedabad.*

	Ahmedabad	
Month	β_{sca}	β_{abs}
Jan	62	60
Feb	56	53
Mar	55	55
Apr	60	60
May	59	62
Jun	56	59
Jul	62	62
Aug	62	62
Sep	58	58
Oct	45	45
Nov	47	47
Dec	62	62

Total of 684 and 685 days of β_{sca} and β_{abs} measurements at a temporal resolution of 5 min over Ahmedabad during 2015-2016 were used in the present study (Table 3.1). The intra-seasonal variability in observed optical properties of aerosol over the study locations was higher than the inter-annual variability, hence in the present work, optical and physical properties of aerosols are computed as a function of 2 year mean (2015-2016) for each month over Ahmedabad.

3.1.1 Aerosol scattering and absorption coefficients

Temporal variations

The aerosol optical properties (scattering (β_{sca}) and absorption (β_{abs}) coefficients at 0.55 μm) exhibit typical diurnal variability (Figures 3.1 and 3.2) with two maxima and two minima over Ahmedabad. The diurnal variation of β_{sca} and β_{abs} over Ahmedabad are primarily influenced by the atmospheric boundary layer dynamics (Figure 3.3). Atmospheric boundary layer shows typical diurnal variability (Figure 3.3) with a maxima during noontime. The parameters β_{sca} and β_{abs} show first maxima during morning (07-09 hrs) due to a substantial increase in the anthropogenic activities and the atmospheric boundary layer dynamics. Typically, atmospheric boundary layer is convective during daytime (Figure 3.3), when the Sun rises and heats the Earth surface, which emits the terrestrial radiation which in turn heats the lowest layer of the atmosphere. After 09 hrs, Earth's surface insolation increases which increases the atmospheric boundary layer height and increases the convective mixing of air which transports aerosols to higher altitudes (Figure 1.2) in the atmosphere thereby causing a dilution of aerosol concentration near the Earth's surface. The parameters β_{sca} and β_{abs} decrease as day advances (Figure 3.3) and attains a minimum around 15-16 hrs due to *ABL* evolution as well as decrease in aerosol emissions. The second maxima is found during late evening (19-21 hrs) due to combined effects of the increase in production of aerosols due to various anthropogenic emissions and the atmospheric boundary layer dynamics. After late evening, in addition to increase in the production of aerosols, formation of inversion layer inhibits convective mixing of air and therefore aerosols get piled up near the Earth's surface.

During nighttime, the atmospheric boundary layer is generally stable and cools the lowest layer of the atmosphere. After around 21 hrs, although aerosol production starts declining from most of these sources, their removal (mostly by gravitational settling) remains active. This removal process exists the whole

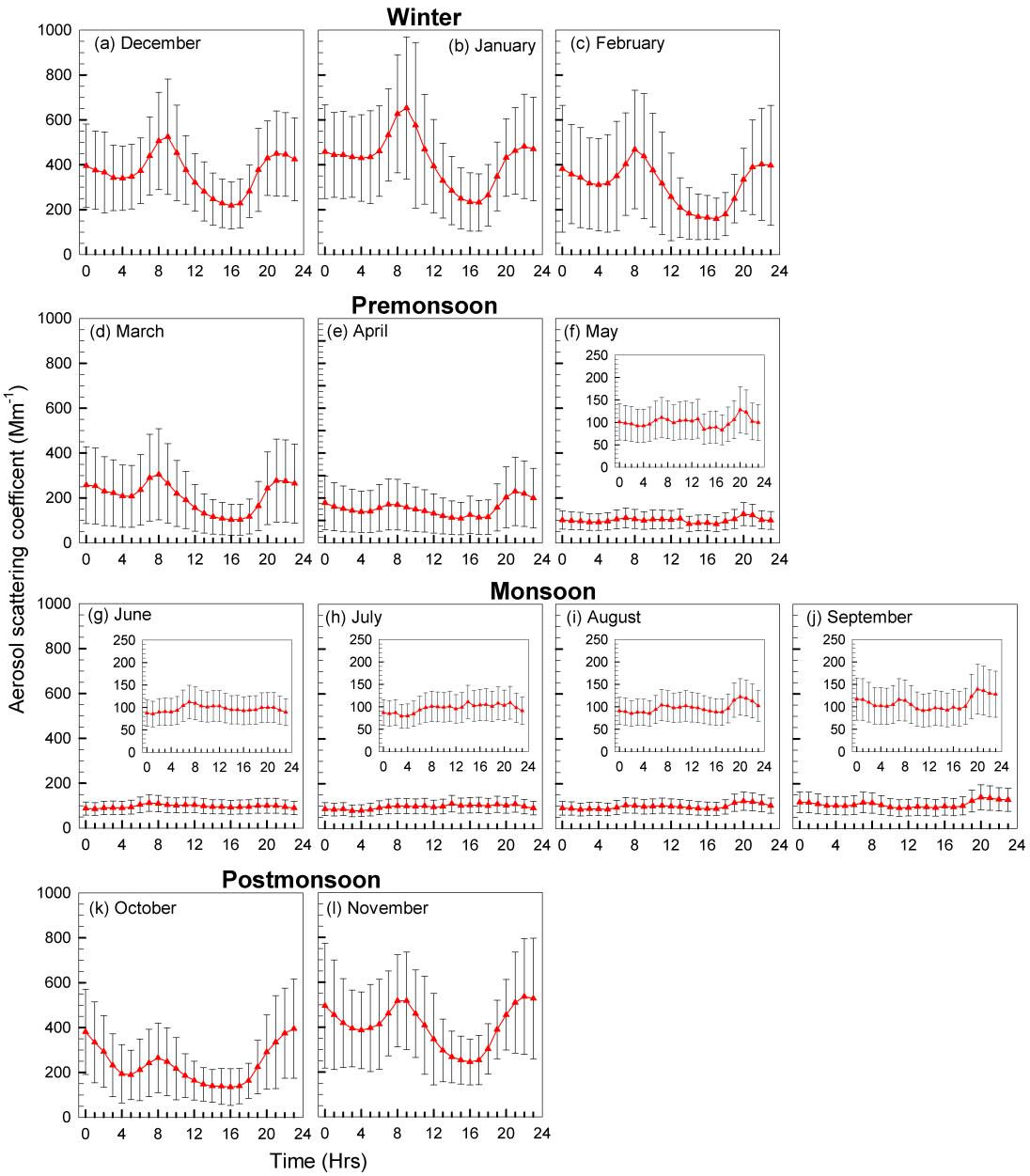

Figure 3.1: *Diurnal evolution of aerosol scattering coefficient (β_{sca}, Mm^{-1}) over Ahmedabad during winter (Dec (a), Jan (b), and Feb (c)), premonsoon (Mar (d), Apr (e), and May (f)), monsoon (Jun (g), Jul (h), Aug (i), and Sep (j)), and post-monsoon (Oct (k), and Nov (l)) at 0.55 μm. Vertical bars represent $\pm 1\sigma$ deviation from the mean.*

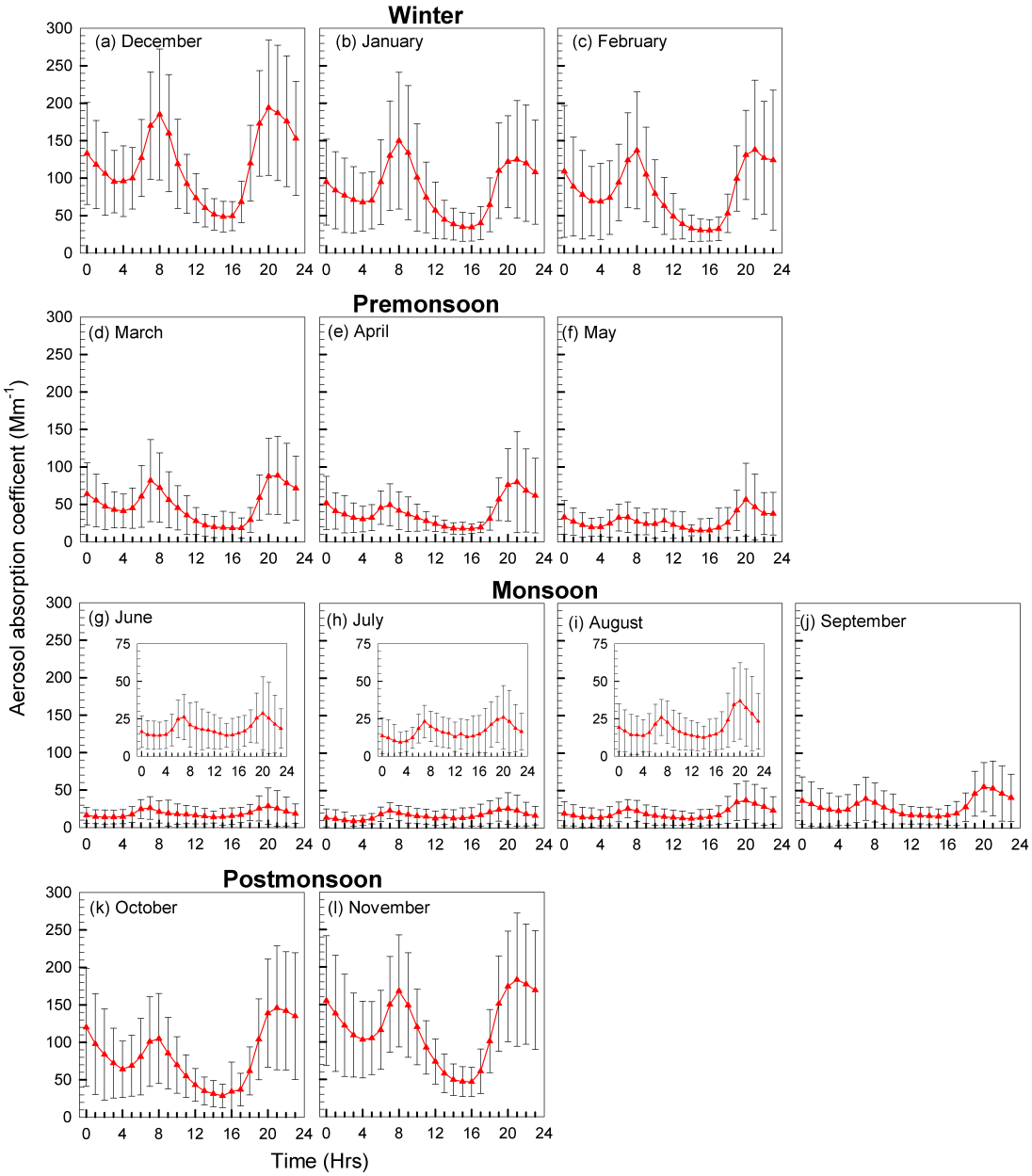

Figure 3.2: *Diurnal evolution of aerosol absorption coefficient (β_{abs}, Mm^{-1}) over Ahmedabad during winter (Dec (a), Jan (b), and Feb (c)), premonsoon (Mar (d), Apr (e), and May (f)), monsoon (Jun (g), Jul (h), Aug (i), and Sep (j)), and post-monsoon (Oct (k), and Nov (l)) at 0.55 μm. Vertical bars represent $\pm 1\sigma$ deviation from the mean.*

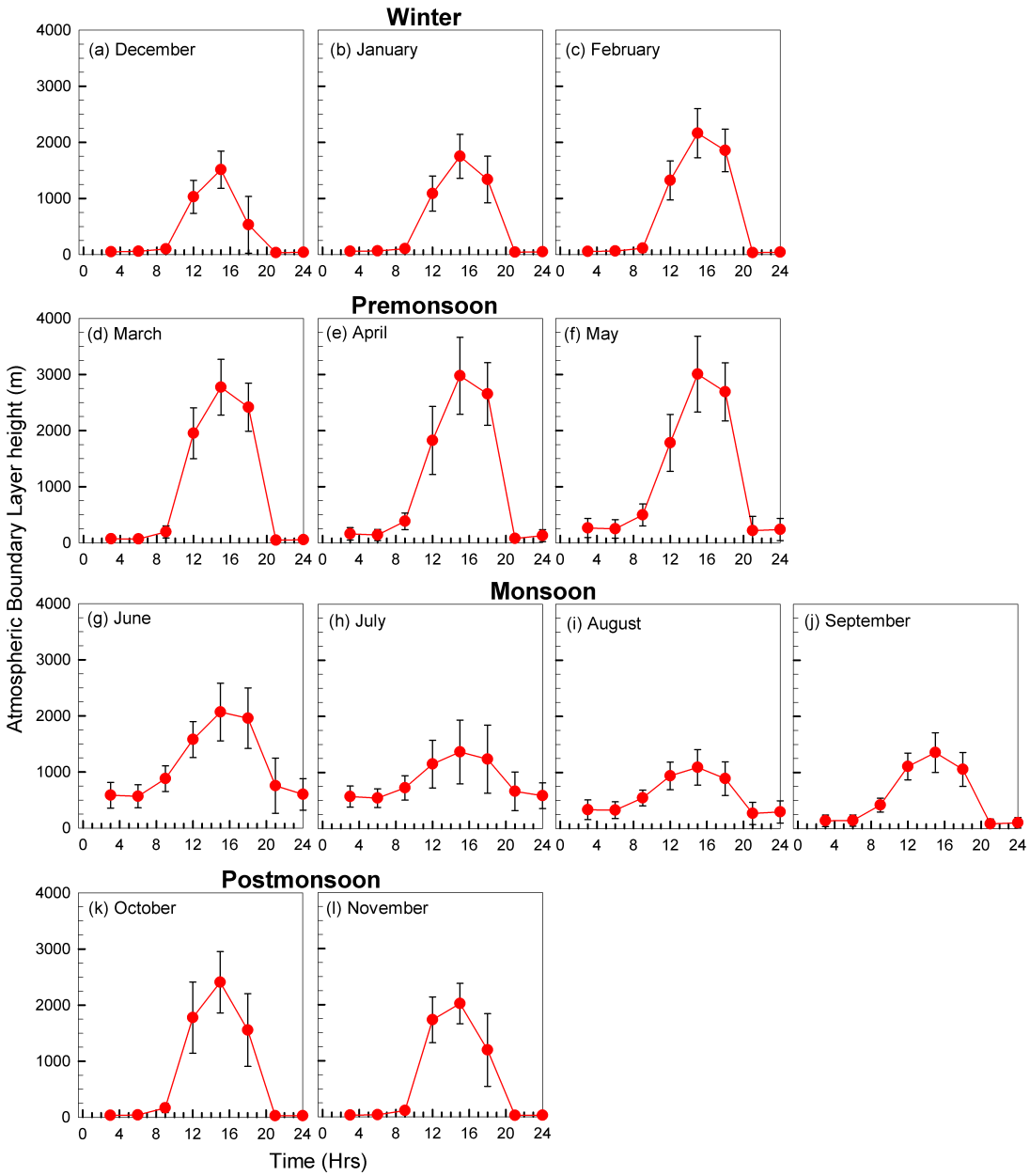

Figure 3.3: *Diurnal evolution of atmospheric boundary layer (ABL, m) over Ahmedabad during winter (Dec (a), Jan (b), and Feb (c)), premonsoon (Mar (d), Apr (e), and May (f)), monsoon (Jun (g), Jul (h), Aug (i), and Sep (j)), and post-monsoon (Oct (k), and Nov (l)) for 2015 and 2016. Vertical bars represent* $\pm 1\sigma$ *deviation from the mean.*

night, and β_{sca} and β_{abs} reach minima between 04-05 hrs. The parameters β_{sca} and β_{abs} show similar variations over Ahmedabad (Figures 3.1 and 3.2), however, β_{sca} is higher than β_{abs} by a factor of 5 throughout the year. The significant maxima and minima in the diurnal variation of β_{sca} and β_{abs} are observed during winter (December, January, and February) and postmonsoon (October and November). During monsoon β_{sca} and β_{abs} exhibit a very weak diurnal variation as compared to other seasons as aerosols are removed because of wet deposition. There exists a small phase lag between the diurnal variation of β_{abs} and β_{sca} (Figures 3.1 and 3.2), because β_{abs} is estimated using aethalometer which measures the attenuation due to particles from vehicular exhausts or biomass/biofuel burning which is directly released into the atmosphere, whereas β_{sca} measured using nephelometer which measures scattering type aerosols which are secondary aerosols formed by gas-to-particle conversion processes. Although most of these precursor gases are emitted at the same time along with absorbing aerosols, as is seen it takes slightly longer time for the formation of secondary aerosols in the submicron size.

The maximum amplitude of diurnal variation in β_{sca} and β_{abs} are 421 and 147 respectively during January and December. During winter, because of low ambient temperature people burn biomass materials to make them comfortable which results in higher anthropogenic emissions, in addition, the atmospheric boundary layer is low (Figure 3.3) and surface wind speed is also low (Figure 2.7); all these factors contribute to a significant increase in the near surface aerosol optical properties. The minimum amplitude of diurnal variation in β_{sca} and β_{abs} are 27 and 15 during June respectively. The amplitude variation in β_{sca} and β_{abs} are < 50 and 40 respectively during monsoon. The typical diurnal variation of β_{sca} and β_{abs} can be attributed to a variety of factors that include production mechanisms, variations in their source strengths, removal mechanisms, variations in atmospheric boundary layer height and surface meteorology.

The parameters β_{sca} and β_{abs} show a right-skewed distribution (Figures

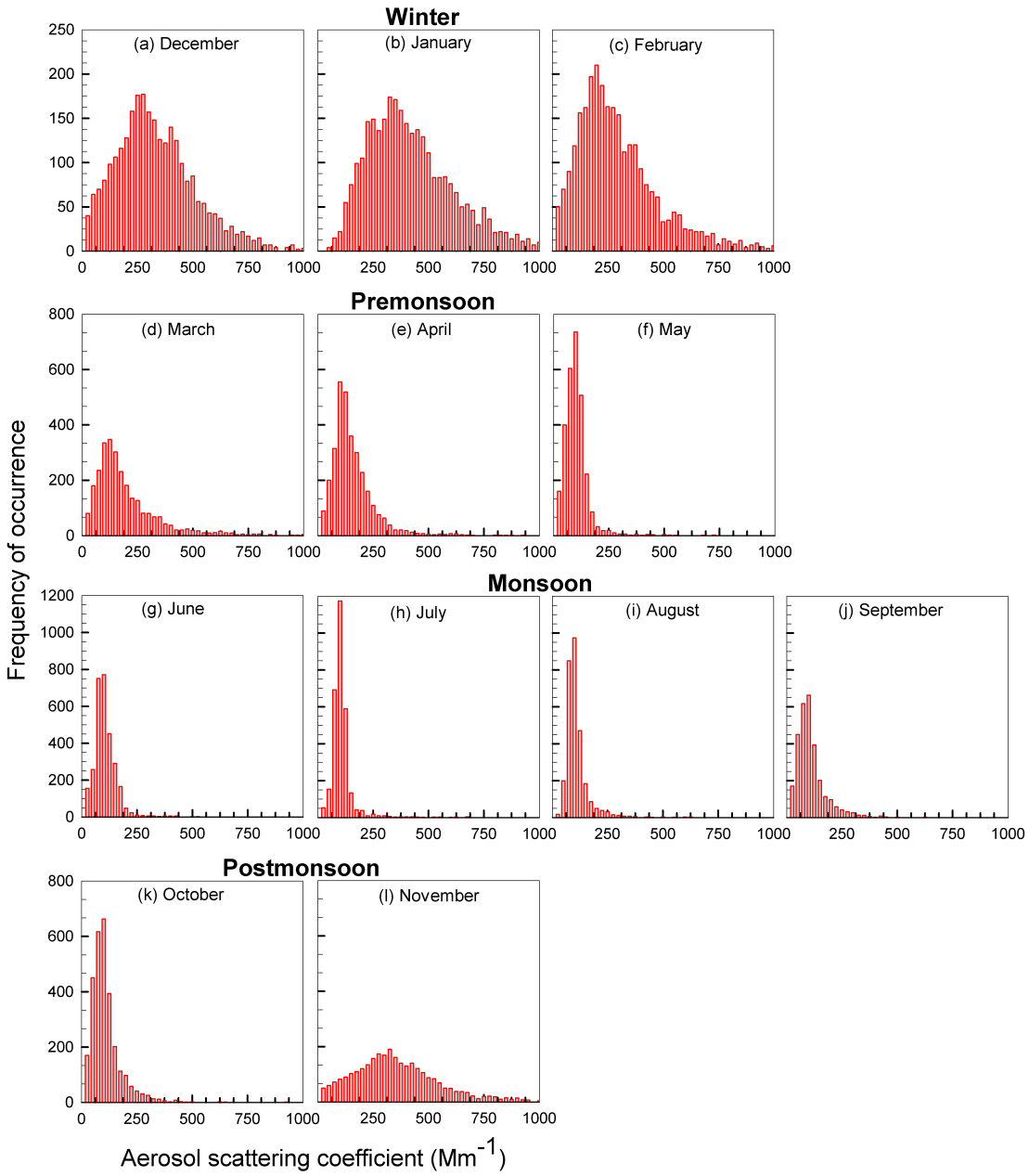

Figure 3.4: *Frequency distribution of nephelometer measured hourly aerosol scattering coefficient (β_{sca}, Mm^{-1}) over Ahmedabad during winter (Dec (a), Jan (b), and Feb (c)), premonsoon (Mar (d), Apr (e), and May (f)), monsoon (Jun (g), Jul (h), Aug (i), and Sep (j)), and postmonsoon (Oct (k), and Nov (l)).*

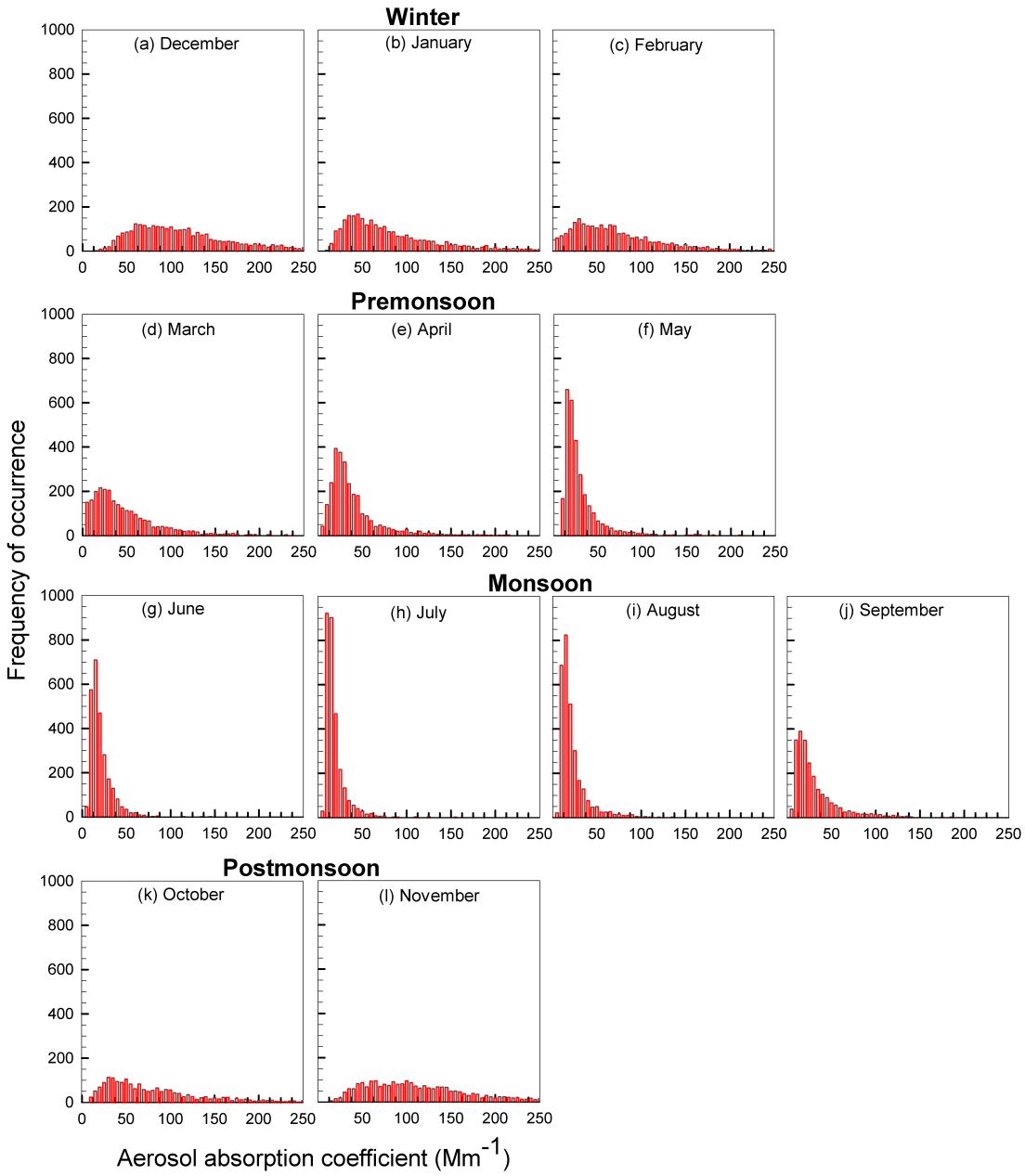

Figure 3.5: *Frequency distribution of aethalometer measured hourly aerosol absorption coefficient (β_{abs}, Mm^{-1}) over Ahmedabad during winter (Dec (a), Jan (b), and Feb (c)), premonsoon (Mar (d), Apr (e), and May (f)), monsoon (Jun (g), Jul (h), Aug (i), and Sep (j)), and postmonsoon (Oct (k), and Nov (l)).*

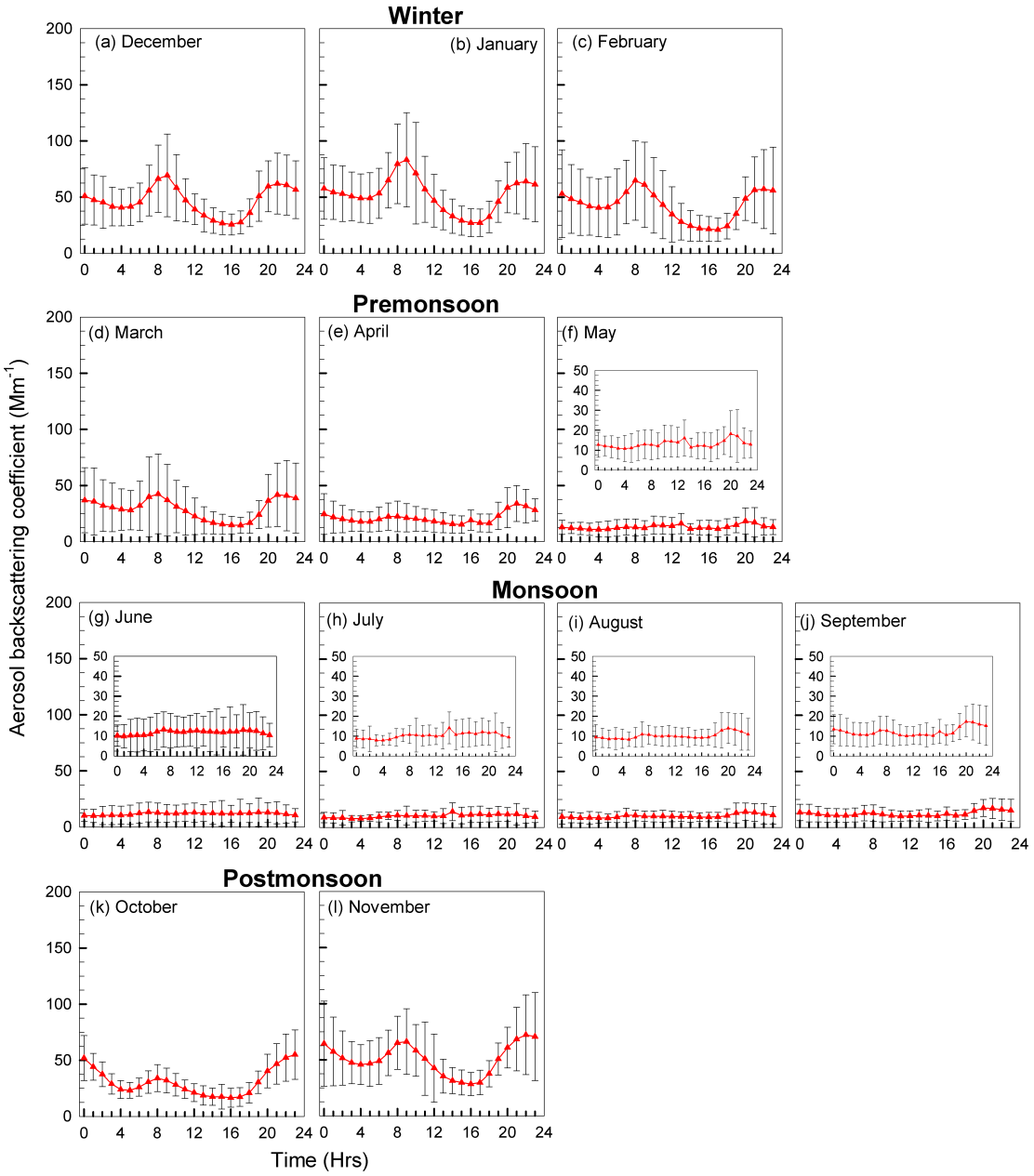

Figure 3.6: *Diurnal evolution of backscattering coefficient (β_{bsca}, Mm^{-1}) over Ahmedabad during winter (Dec (a), Jan (b), and Feb (c)), premonsoon (Mar (d), Apr (e), and May (f)), monsoon (Jun (g), Jul (h), Aug (i), and Sep (j)), and post-monsoon (Oct (k), and Nov (l)) at 0.55 μm. Vertical bars represent $\pm 1\sigma$ deviation from the mean.*

3.4 and 3.5). The observed mode in β_{sca} is between 100-150 Mm^{-1} during March - October, which shifts to higher modes during November - January. The mode in β_{abs} is found between 15-20 Mm^{-1} during March - September, which shifts to higher modes during October - February. The frequency distribution of β_{sca} and β_{abs} is found to be broader during winter (December, January, February) and postmonsoon (October and November) owing to low surface wind speed and shallow atmospheric boundary layer which traps the pollutants near Earth's surface. Back scattering coefficient (β_{bsca}) at 0.55 μm shows similar variations (Figure 3.6) as β_{sca} over Ahmedabad.

Monthly and Seasonal variations

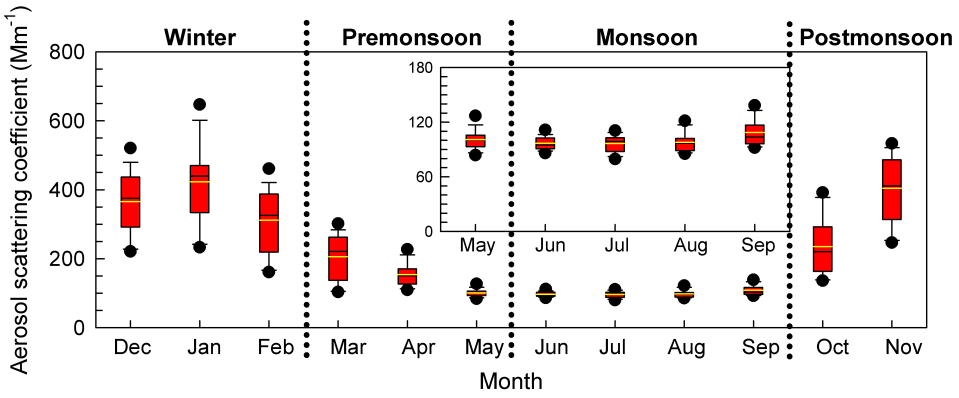

Figure 3.7: *Box and whisker plots of aerosol scattering coefficient (β_{sca}, Mm^{-1}) measured using nephelometer over Ahmedabad during 2015-2016 as function of season (winter, premonsoon, monsoon, and postmonsoon). The range of the box represent the limits of the 25^{th} and 75^{th} percentile data. The whiskers spreading from the box illustrate the limits of the 10^{th} and the 90^{th} percentile data. Yellow lines show the average of the data. The maximum and minimum and maximum in each box are represented by dots.*

Aerosol scattering (β_{sca}) and absorption (β_{abs}) coefficients exhibit significant monthly and seasonal variations over Ahmedabad. As β_{sca} and β_{abs} exhibit a right-skewed distribution the monthly mean is visualised using box and whisker plots (Figures 3.7 and 3.8). The highest β_{sca} is found during January,

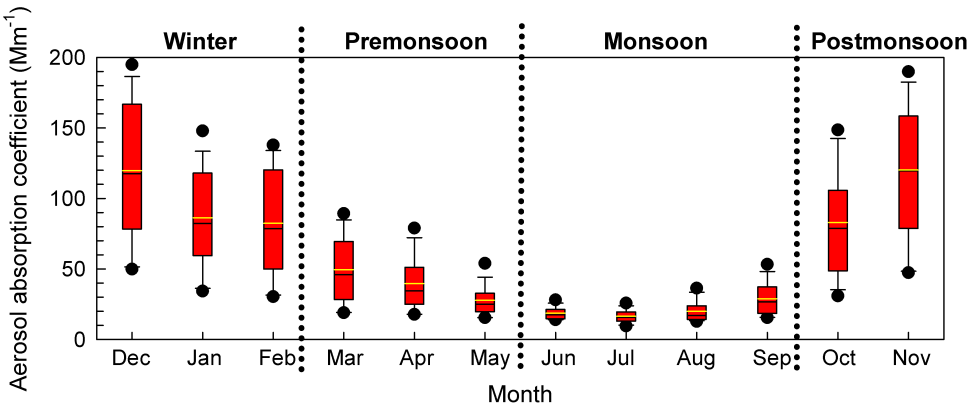

Figure 3.8: *Box and whisker plots of aerosol absorption coefficient (β_{abs}, Mm^{-1}) measured using aethalometer over Ahmedabad during 2015-2016 as function of season (winter, premonsoon, monsoon, and postmonsoon). The range of the box represent the limits of the 25^{th} and 75^{th} percentile data. The whiskers spreading from the box illustrate the limits of the 10^{th} and the 90^{th} percentile data. Yellow lines show the average of the data. The maximum and minimum and maximum in each box are represented by dots.*

and β_{sca} gradually decreases and is lowest during July (Figure 3.7). β_{abs} gradually decreases from January and is minimum during July. Then, β_{abs} increases till November and December β_{abs} values are comparable with November values (Figure 3.8). The maximum β_{abs} is found during November over Ahmedabad. A systematic seasonal variation is seen in β_{sca} and β_{abs}, with winter maximum and monsoon minimum (Table 3.2). β_{sca} and β_{abs} show a decreasing trend from winter to monsoon (Table 3.2). Higher values of β_{sca} and β_{abs} could arise owing to shallow atmospheric boundary layer (ABL), and increase in anthropogenic emissions during winter and postmonsoon, which contribute significantly to the production of both scattering and absorbing type atmospheric aerosols. During premonsoon and monsoon, the air masses originate/travel from/over Arabian Sea bringing in relatively clean air masses with less continental influence to the observational site, which results in decrease in these values. The minimum β_{sca} and β_{abs} are found during monsoon over Ahmedabad. During monsoon, β_{sca} is found to be a factor of 4 lower than winter,

whereas β_{abs} is a factor of 5 lower than postmonsoon values. As the β_{sca} and β_{abs} exhibit a right-skewed distribution (non-Gaussian distribution), the median and mean of the distribution agree within 10% throughout the year over Ahmedabad. In a Gaussian or normal distribution the median is equal to the mean of distribution.

3.1.2 Single scattering albedo

Temporal variations

The typical diurnal variation seen in surface single scattering albedo (*SSA*) is a combined effect of scattering and absorption by aerosols in the atmosphere (Figure 3.9). Surface *SSA* is estimated using β_{sca} and β_{abs} obtained from nephelometer and aethalometer respectively. *SSA* shows two minima during the morning (07-09 hrs) and evening (19-21 hrs) coinciding with the β_{sca} and β_{abs} peaks in the morning and evening due to the dominance of absorbing aerosols from the anthropogenic emissions, and an afternoon maxima over Ahmedabad (emissions are significantly low) (Figure 3.9). The diurnal variation in *SSA* is anti-correlated to the β_{sca} and β_{abs} over an urban location, Ahmedabad. The morning and evening dips in *SSA* (Figure 3.9) throughout the year suggest a consistent and significant presence of absorbing aerosols from various fossil fuel and biomass burning over Ahmedabad. Higher diurnal variation in *SSA* is found during monsoon due to the dominance of scattering type aerosols (sea salt) over Ahmedabad, which further decreases during postmonsoon and winter due to the dominance of absorbing type aerosols (Figure 3.9).

Monthly and Seasonal variations

The *SSA* near surface exhibits significant monthly and seasonal variations over Ahmedabad. *SSA* is found to vary from 0.67 to 0.89 over Ahmedabad during the study period. Higher *SSA* signifies the dominance of scattering type aerosols, whereas lower *SSA* reveals the dominance of absorbing type aerosols. Maxi-

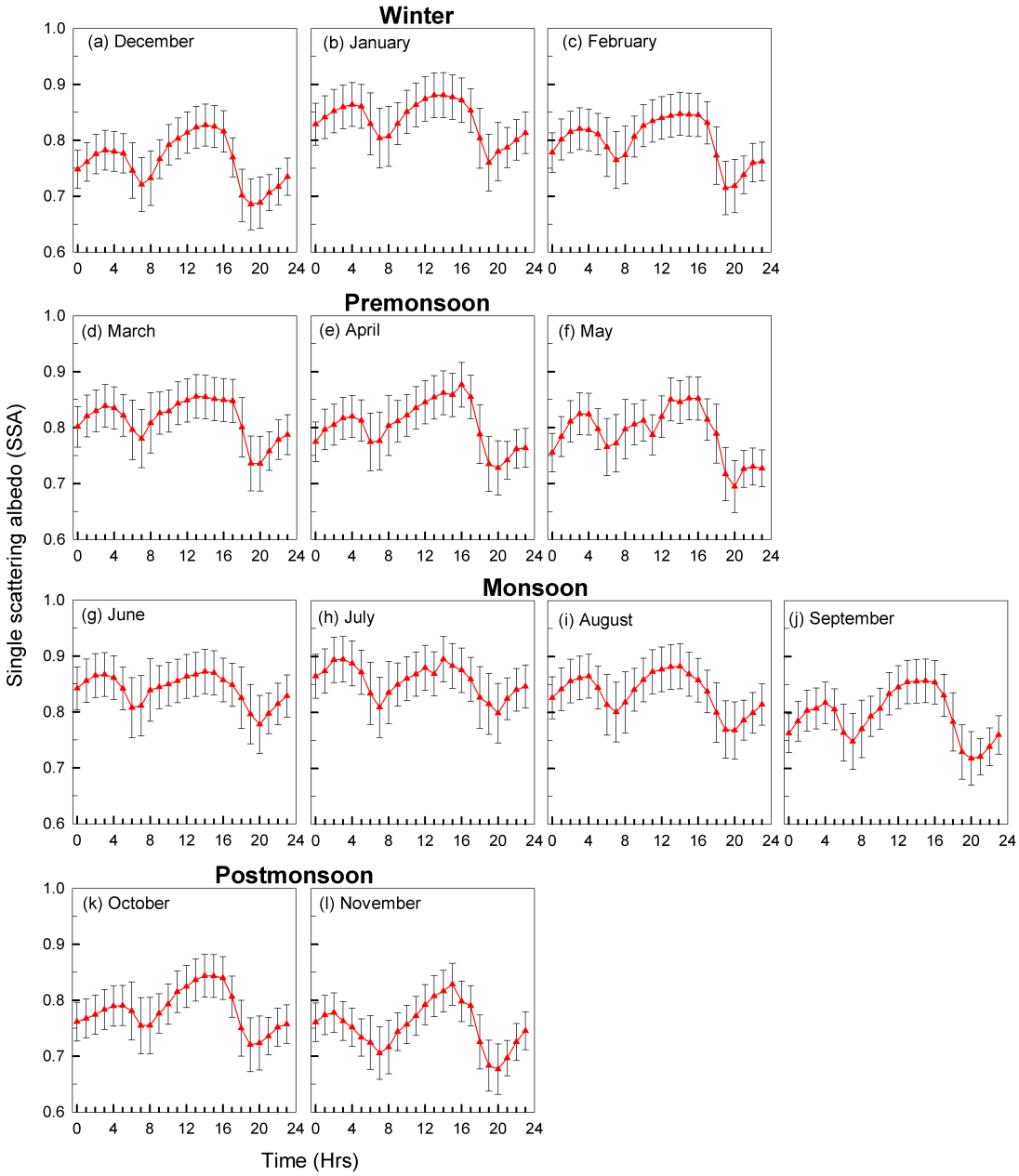

Figure 3.9: *Diurnal evolution of single scattering albedo (SSA) over Ahmedabad during winter (Dec (a), Jan (b), and Feb (c)), premonsoon (Mar (d), Apr (e), and May (f)), monsoon (Jun (g), Jul (h), Aug (i), and Sep (j)), and postmonsoon (Oct (k), and Nov (l)) at 0.55 μm. Vertical bars represent $\pm 1\sigma$ deviation from the mean.*

mum and minimum *SSA* are observed during July and November (Figure 3.10). Surface *SSA* decreases from January to May, then it gradually increases to reach a maximum during July and afterwards it decreases (Figure 3.10). The highest surface *SSA* is found during monsoon (Table 3.2) because of the dominance of scattering type aerosols as air masses that travel over Arabian Sea bring in scattering type aerosols (sea salt) to the observational site (Figure 2.9). The lowest surface *SSA* is observed during postmonsoon due to the dominance of absorbing type aerosols over Ahmedabad (Table 3.2). Surface *SSA* is found to increase from winter to monsoon (Table 3.2) corroborating the increase in the dominance of scattering type aerosols. The year-to-year variation in *SSA* during 2015-2016 is $< 10\%$ (Figure 3.14) which is within the measurement uncertainties (15%).

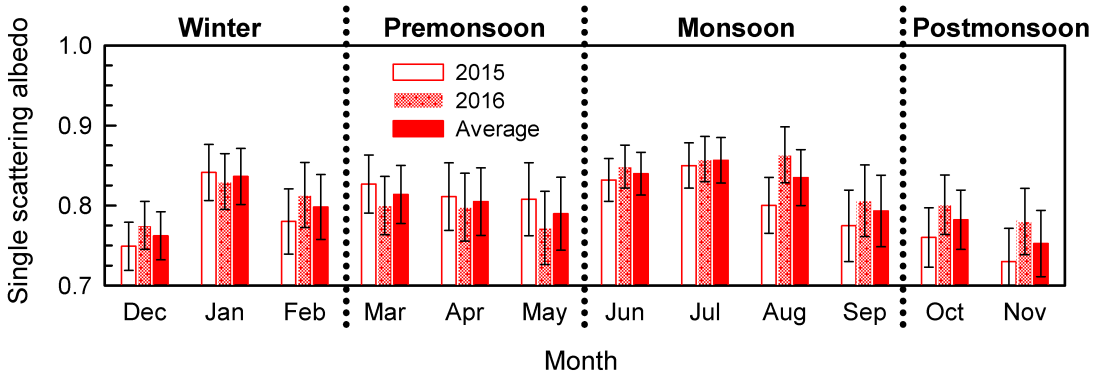

Figure 3.10: *Monthly mean surface single scattering albedo at 0.55 μm for 2015, 2016, and average of 2015 - 2016 as function of season (winter, premonsoon, monsoon, and postmonsoon) over Ahmedabad. Vertical bars indicate $\pm 1\sigma$ variation with respect to mean.*

The columnar *SSA* derived from OMI also increases from winter to premonsoon although the magnitude of columnar *SSA* is higher than the surface derived *SSA* throughout the year (Figure 3.11) (Table 3.2). The surface *SSA* is lower than the columnar *SSA* as most of the black carbon (which are absorbing species) are concentrated near the surface, hence, the aerosol absorption coefficients near the surface will be higher when compared to the column. The annual mean surface and column *SSA* are found to be 0.81 $\pm$ 0.03 and 0.91 $\pm$

0.01 respectively over Ahmedabad.

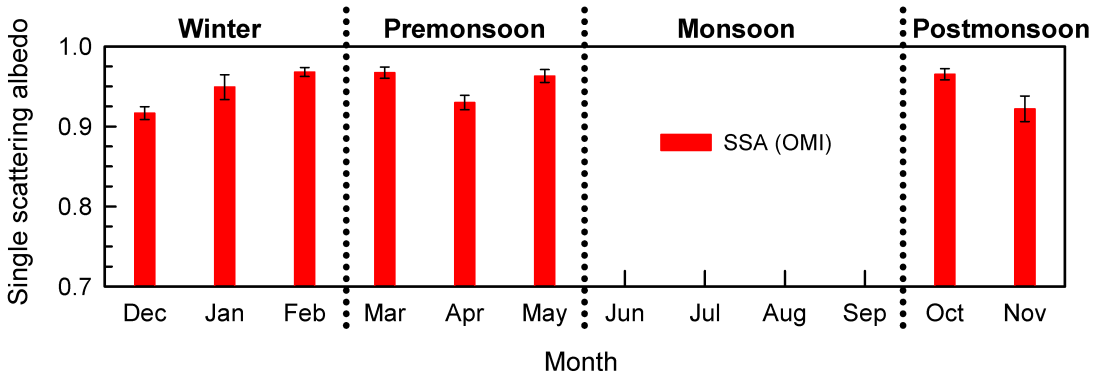

Figure 3.11: *Monthly mean columnar single scattering albedo at 0.50 μm during 2015-2016 as function of season (winter, premonsoon, monsoon, and postmonsoon) over Ahmedabad. Vertical bars indicate $\pm 1\sigma$ variation with respect to mean.*

3.1.3 Ångström exponent, Backscatter fraction, and Asymmetry parameter

Temporal variations

The diurnal variations in *Ångström exponent* (α) and *backscatter fraction* (b) exhibit morning and evening peaks (Figures 3.12 and 3.13), whereas, the *asymmetry parameter* (g) shows corresponding dips (Figure 3.14) which coincide with the peaks observed in β_{sca} (Figure 3.1) and β_{bsca} (Figure 3.6). The parameters α, b, and g are derived using the aerosol scattering coefficients, and are found to vary in the range of 0.5 to 2.0, 0.10 to 0.15, and 0.53 to 0.69 respectively over Ahmedabad. Higher α and b, and lower g indicate the dominance of smaller size particles, whereas, lower α and b, and higher g indicate the dominance of larger size particles. The morning and evening peaks in α and b, and dips in g suggest the dominance of smaller size aerosols over Ahmedabad occurring due to vehicular and domestic emissions, and α and b track each other (Figures 3.12 and 3.13). These results suggest that as backscattering increases the size distribution shifts to smaller particles resulting in higher α values. The

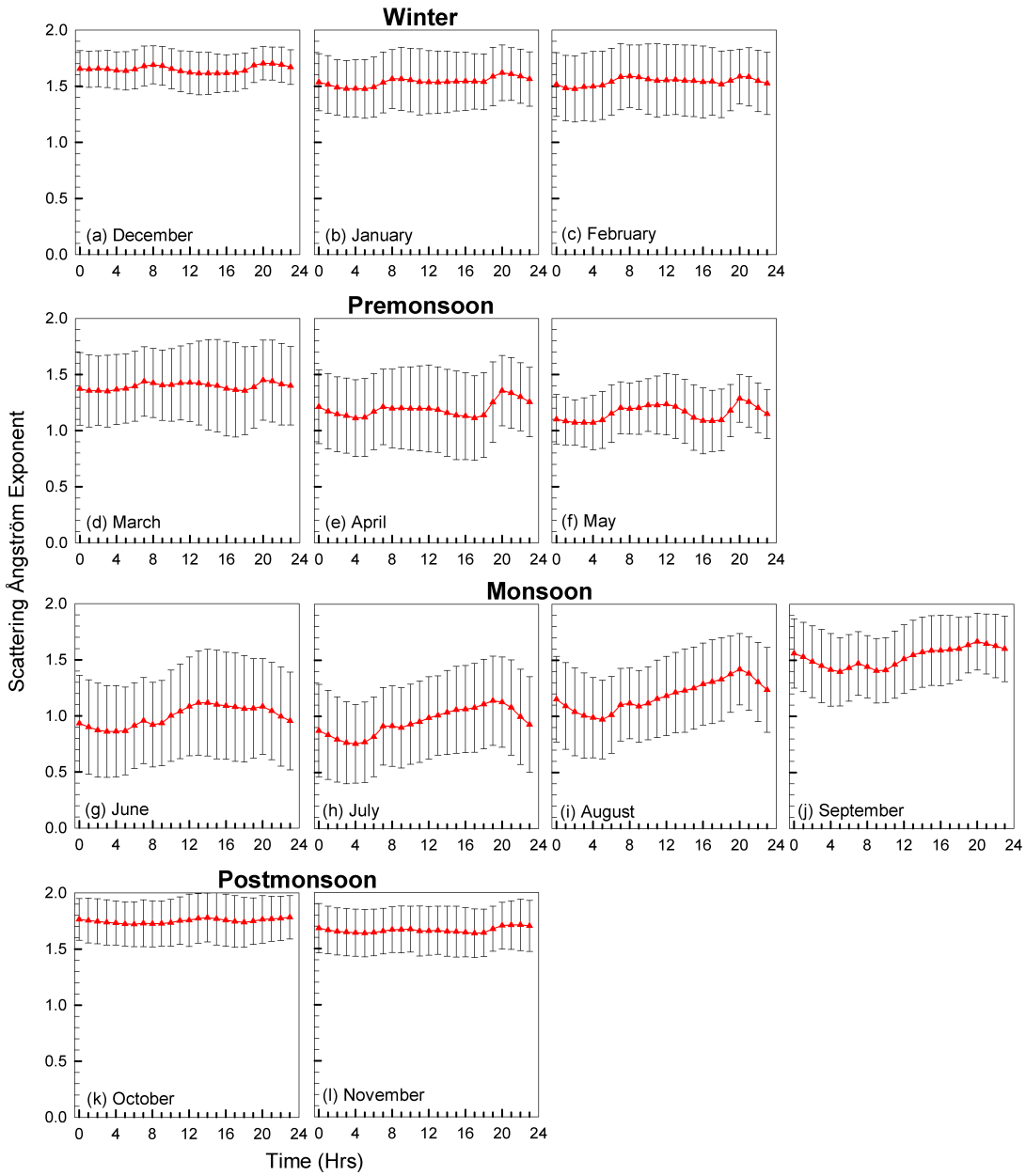

Figure 3.12: *Diurnal evolution of scattering Ångström exponent (α) over Ahmedabad during winter (Dec (a), Jan (b), and Feb (c)), premonsoon (Mar (d), Apr (e), and May (f)), monsoon (Jun (g), Jul (h), Aug (i), and Sep (j)), and post-monsoon (Oct (k), and Nov (l)) using β_{sca} measured at 0.45, 0.55 and 0.70 μm. Vertical bars represent $\pm 1\sigma$ deviation from the mean.*

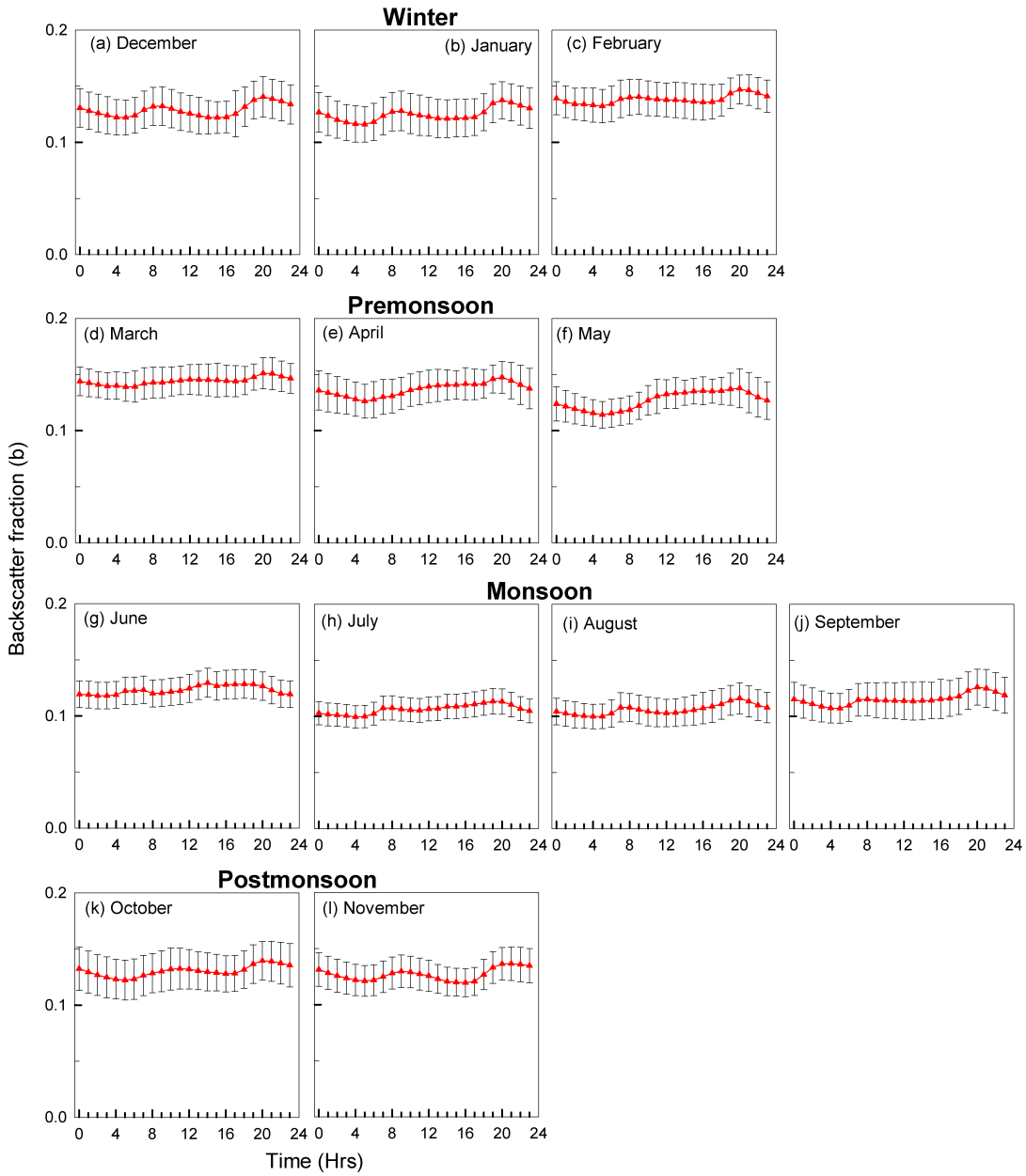

Figure 3.13: *Diurnal evolution of aerosol backscatter fraction (b) over Ahmedabad during winter (Dec (a), Jan (b), and Feb (c)), premonsoon (Mar (d), Apr (e), and May (f)), monsoon (Jun (g), Jul (h), Aug (i), and Sep (j)), and postmonsoon (Oct (k), and Nov (l)) at 0.55 μm. Vertical bars represent $\pm 1\sigma$ deviation from the mean.*

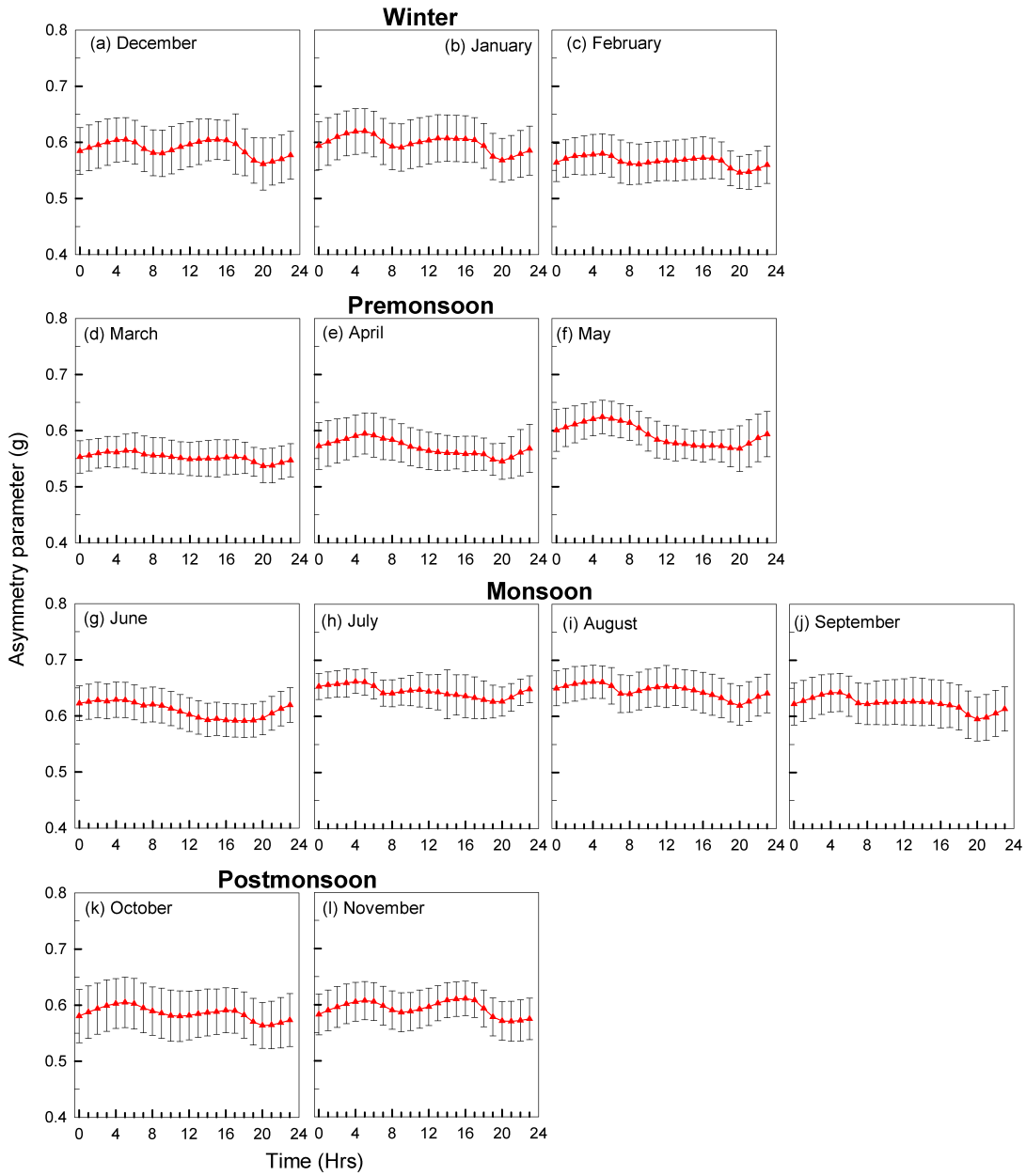

Figure 3.14: *Diurnal evolution of asymmetry parameter (g) over Ahmedabad during winter (Dec (a), Jan (b), and Feb (c)), premonsoon (Mar (d), Apr (e), and May (f)), monsoon (Jun (g), Jul (h), Aug (i), and Sep (j)), and postmonsoon (Oct (k), and Nov (l)) at 0.55 μm. Vertical bars represent $\pm 1\sigma$ deviation from the mean.*

parameter *g* increases with size of the particle and α decreases leading to an anti-correlation between α and *g* (Figures 3.12 and 3.14).

Monthly and Seasonal variations

The *Ångström exponent* (α), *backscatter fraction* (*b*), and *asymmetry parameter* (*g*) exhibit significant monthly variations over Ahmedabad (Figure 3.15). The parameter α is estimated using β_{sca} measured at 0.45, 0.55 and 0.70 μm, whereas the parameters *b* and *g* are derived using β_{sca} and β_{bsca} measured at 0.55 μm. The *Ångström exponent* and *backscatter fraction* decrease from January to July then increase afterwards (Figures 3.15a and 3.15b), whereas, the *asymmetry parameter* increases from January to July then gradually decreases (Figure 3.15c). The maximum α and *b*, and minimum *g* are found during November which suggests the dominance of smaller size particles due to relative increase in the anthropogenic emissions (Figure 3.15) and the longrange transported biomass components from the residue crop burning areas of India (Figure 3.16) under the favorable wind conditions (Figure 2.9). The minimum α and *b*, and maximum *g* are estimated during July (Figure 3.15) which reveals the dominance of larger particle (sea salt), as the air is transported from the Arabian sea to the observational location (Figure 2.9). As discussed, the maximum and minimum in SSA are found during July and November, and these results confirm the variation in the type and size of the particles in the atmosphere over Ahmedabad.

The *Ångström exponent* (α), *backscatter fraction* (*b*), and *asymmetry parameter* (*g*) also show a strong seasonal variations over Ahmedabad (Table 3.2). The highest α and *b* and lowest *g* are observed during postmonsoon (Table 3.2) suggest the dominance of smaller size aerosols from the anthropogenic emissions, whereas, the lowest α and *b* and highest *g* are found in monsoon (Table 3.2) reveal the dominance of larger particles reaching the observational site from the Arabian Sea (Figure 2.9). The aerosol *backscatter fraction* values found over Ahmedabad are less than the near surface mean *b* values re-

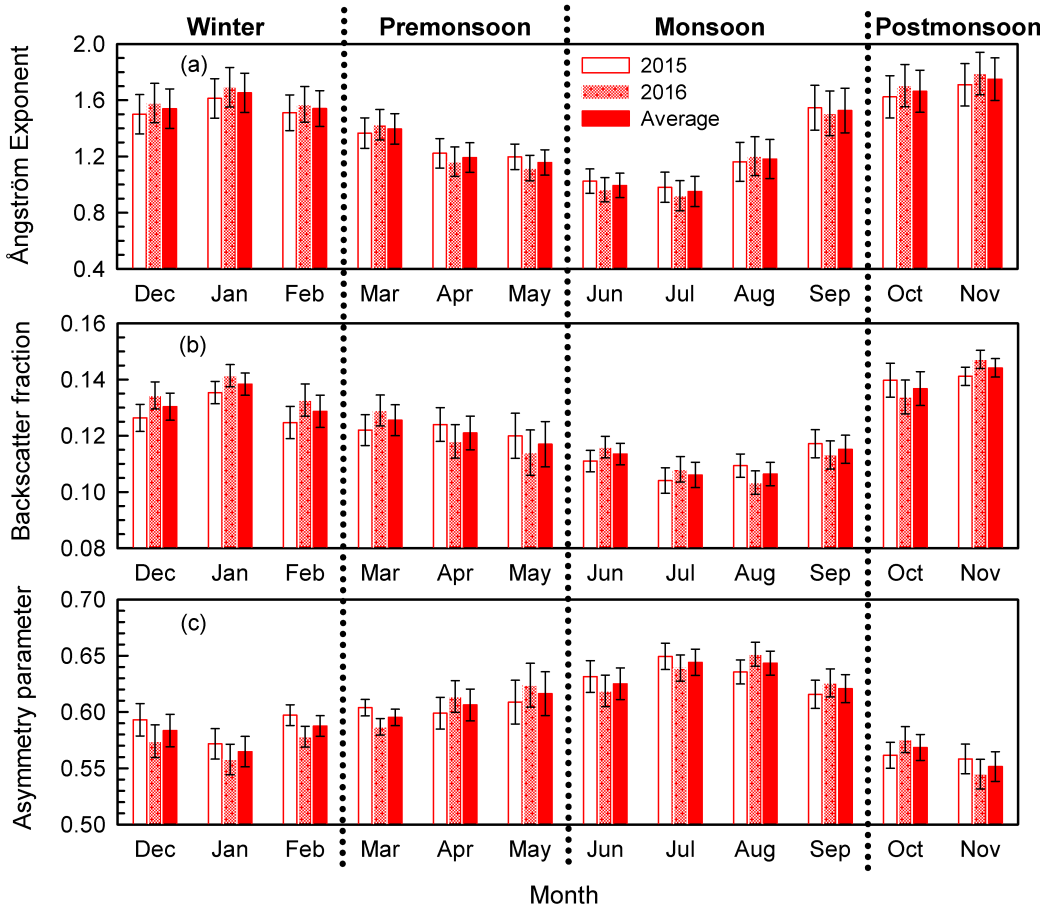

Figure 3.15: *Monthly mean (a) Ångström exponent, (b) backscatter fraction, and (c) asymmetry parameter at 0.55 μm over Ahmedabad during 2015-2016 as function of season (winter, premonsoon, monsoon, and postmonsoon). Vertical bars indicate $\pm 1\sigma$ variation with respect to mean.*

ported over Bhubaneshwar (0.14), Chennai (0.15), Trivandrum (0.18), and Goa (0.21) during premonsoon (*Ramachandran and Rajesh*, 2008). The observed monthly mean variation in g is opposite to that of b (Figures 3.15b and 3.15c). Lower g values suggest that smaller size aerosols dominate the size distribution corroborating the higher α and b value obtained. As the particle size increases g will increase and α and b will decrease leading to an anti-correlation between α and g, and b and g (Figure 3.15). The parameters α, b, and g show $<$ 10% difference between 2015 and 2016 (Figure 3.15) which is within the measurement uncertainties (15%). Hence, α, b, and g do not exhibit any significant

inter-annual variability over Ahmedabad.

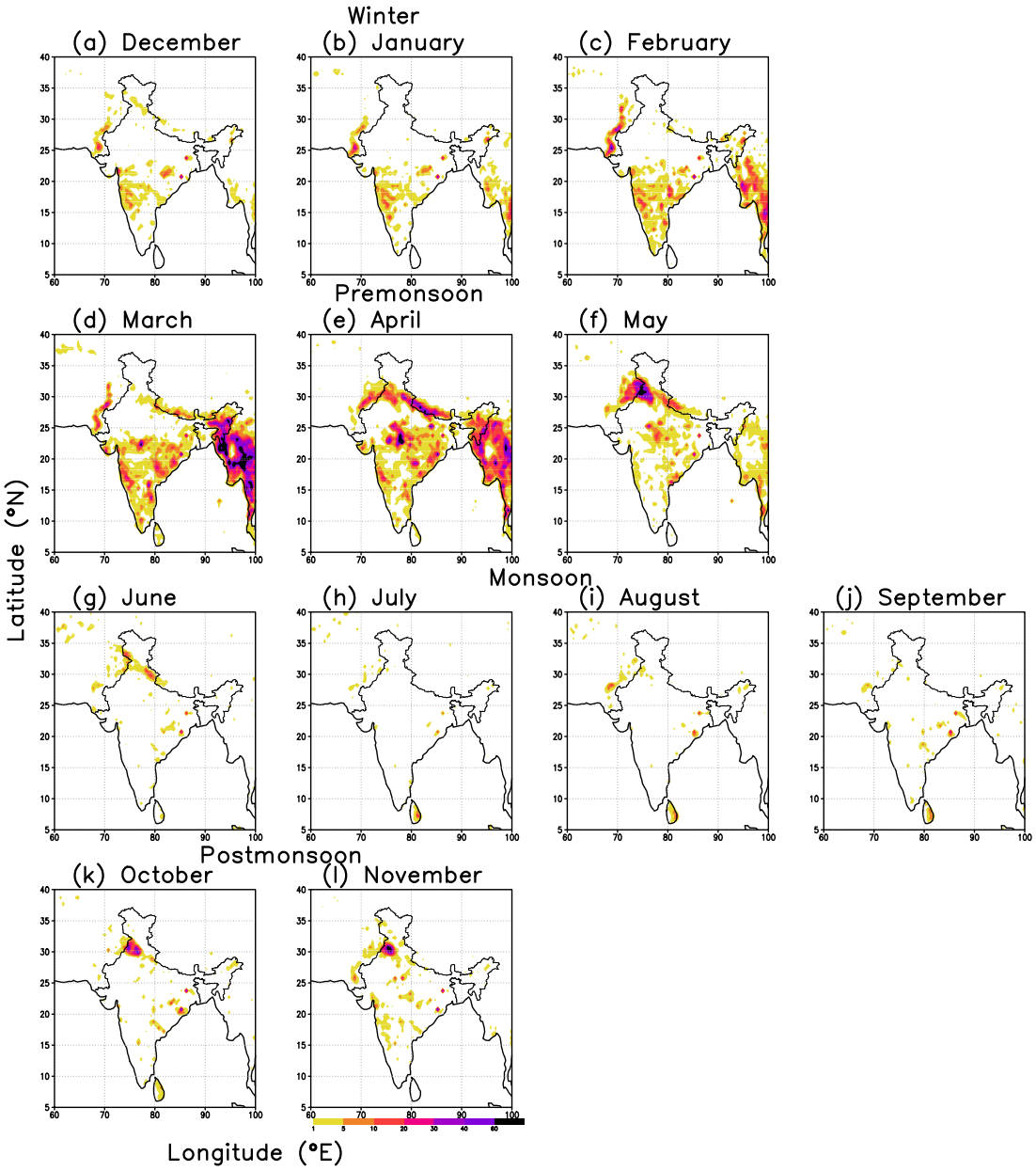

Figure 3.16: *Spatial distribution of MODIS cloud corrected fire counts over India during winter (Dec (a), Jan (b), and Feb (c)), premonsoon (Mar (d), Apr (e), and May (f)), monsoon (Jun (g), Jul (h), Aug (i), and Sep (j)), and postmonsoon (Oct (k), and Nov (l)) averaged for the years 2015 and 2016.*

Table 3.2: *Seasonal variations of aerosol scattering (β_{sca}, Mm^{-1}) and absorption (β_{abs}, Mm^{-1}) coefficients, surface single scattering albedo (SSA), Ångström exponent (α), backscatter fraction (b), asymmetry parameter (g), aerosol optical depth (AOD), and columnar single scattering albedo (SSA (OMI)).*

Parameters	Winter	Premonsoon	Monsoon	Postmonsoon
β_{sca}	366.5 ± 107.9	153.4 ± 60.5	99.9 ± 11.5	319.5 ± 122.5
β_{abs}	96.1 ± 42.9	38.9 ± 19.8	21.0 ± 8.8	101.5 ± 45.8
SSA	0.80 ± 0.04	0.80 ± 0.03	0.83 ± 0.03	0.77 ± 0.02
α	1.58 ± 0.06	1.25 ± 0.13	1.16 ± 0.26	1.71 ± 0.06
b	0.13 ± 0.01	0.12 ± 0.01	0.11 ± 0.01	0.14 ± 0.01
g	0.58 ± 0.02	0.61 ± 0.02	0.63 ± 0.02	0.56 ± 0.01
AOD	0.37 ± 0.10	0.39 ± 0.09	-	0.47 ± 0.03
$SSA(OMI)$	0.91 ± 0.01	0.92 ± 0.02	-	0.91 ± 0.01

3.1.4 Aerosol optical depth

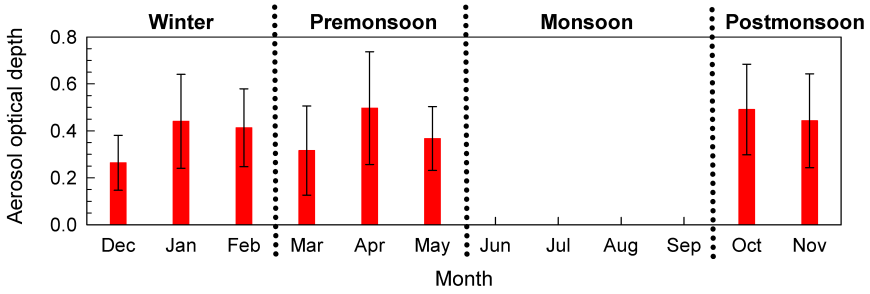

Figure 3.17: *Mean (of MODIS Terra and Aqua) $AODs$ at 0.55 μm over Ahmedabad as function of season (winter, premonsoon, monsoon, and postmonsoon). Vertical bars denote $\pm 1\sigma$ deviation from the monthly mean.*

AOD is found to be in the 0.2-0.7 range at 0.55 μm during the study period. *AOD* decreases from January to March, and is maximum during April (Figure 3.17). *AOD* decreases during October to December and is minimum during December (Figure 3.17). The highest *AOD* is found during postmonsoon followed by premonsoon and winter (Table 3.2). The annual mean *AOD* over Ahmedabad is 0.41 ± 0.09. In comparison, the annual mean *AOD* over Kanpur (an urban location) and Gandhi College (a rural location) in the densely populated Indo Gangetic Plains were higher with values of 0.62 ± 0.11 and $0.66 \pm$

0.07 respectively (*Ramachandran and Kedia*, 2012).

3.2 Optical and physical characteristics of aerosols over a high altitude remote location: Gurushikhar, Mt. Abu

The aerosol scattering (β_{sca}) and absorption (β_{abs}) coefficients of aerosols were measured simultaneously over a high altitude remote location, Gurushikhar, Mt. Abu using nephelometer (TSI 3563) and aethalometer (AE33) respectively during 2015-2016. Total of 523 and 536 days of β_{sca} and β_{abs} measurements at a temporal resolution of 5 min over Gurushikhar, Mt. Abu during 2015-2016 were utilised in the present work (Table 3.3).

Table 3.3: *Number of days of aerosol scattering (β_{sca}) and absorption (β_{abs}) coefficients measurements over Gurushikhar during 2015-2016. Total number of days of β_{sca} and β_{abs} measurements are 523 and 536 days over Gurushikhar. The data gaps are due to raw power failure, UPS failure, and maintenance of the instruments.*

	Gurushikhar	
Month	β_{sca}	β_{abs}
Jan	45	46
Feb	57	56
Mar	55	55
Apr	48	40
May	51	45
Jun	38	04
Jul	47	44
Aug	26	46
Sep	00	53
Oct	49	49
Nov	48	48
Dec	59	50

3.2.1 Aerosol scattering and absorption coefficients

Temporal variations

The aerosol optical properties (scattering (β_{sca}) and absorption (β_{abs}) coefficients at 0.55 μm) exhibit an atypical diurnal variability (Figures 3.18 and 3.19) different than the diurnal variability observed over Ahmedabad (Figures 3.1 and 3.2). β_{sca} and β_{abs} over Gurushikhar show a late afternoon maxima and a midnight minimum. This odd diurnal feature in aerosol characteristics arises due to the evolution of the atmospheric boundary layer which transports the pollutants from the foothills to the observational location during the afternoon hour (Figure 3.3). During daytime, after the sunrise, the land gets heated up which results in the convective motion of the air parcel (*Kovalev et al.*, 2004), which increases the vertical mixing of air and results in the higher values of β_{sca} and β_{abs} at the study location. The observations reveal that vertical transport of pollutants from the valley regions by the evolving atmospheric boundary layer modulates the aerosol concentration at the observational peak. Hence, the observed β_{sca} and β_{abs} during the afternoon hours are higher than forenoon (Figures 3.18 and 3.19). β_{sca} and β_{abs} show similar variations over the measurement location (Figures 3.18 and 3.19), however, β_{sca} is higher than β_{abs} by a factor of 6 throughout the year. The maximum amplitude of diurnal variation in β_{sca} and β_{abs} are $\sim$ 54 and 10 respectively during January. The minimum amplitude of diurnal variation in β_{sca} and β_{abs} are $\sim$ 6 and 2 during March respectively (Figures 3.17 and 3.18) when the observational site is least affected by the evolution of the atmospheric boundary layer.

The parameters β_{sca} and β_{abs} show a right-skewed distribution (Figures 3.20 and 3.21). The observed mode in β_{sca} is between 40-60 Mm^{-1} during February - April, which shifts to higher modes during May - June, and October - November. During December and January the modes in β_{sca} is observed between 5-15 Mm^{-1} (Figure 3.20). The mode in β_{abs} is found between 10-12 Mm^{-1} during February - October, except during July and August when the

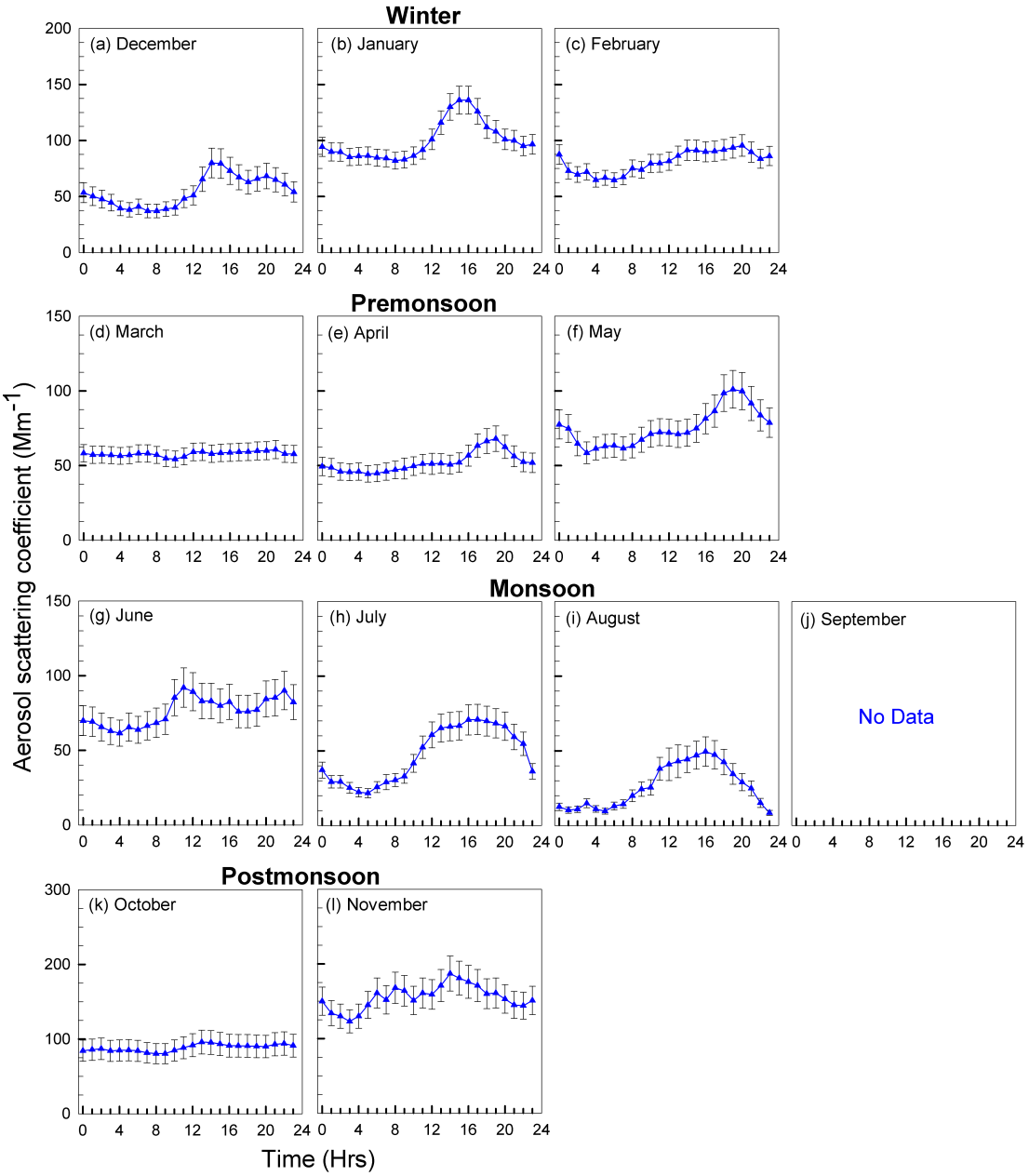

Figure 3.18: *Diurnal evolution of aerosol scattering coefficient (β_{sca}, Mm^{-1}) over Gurushikhar during winter (Dec (a), Jan (b), and Feb (c)), premonsoon (Mar (d), Apr (e), and May (f)), monsoon (Jun (g), Jul (h), Aug (i), and Sep (j)), and postmonsoon (Oct (k), and Nov (l)) at 0.55 μm for 2015 and 2016. Vertical bars represent $\pm 1\sigma$ deviation from the mean.*

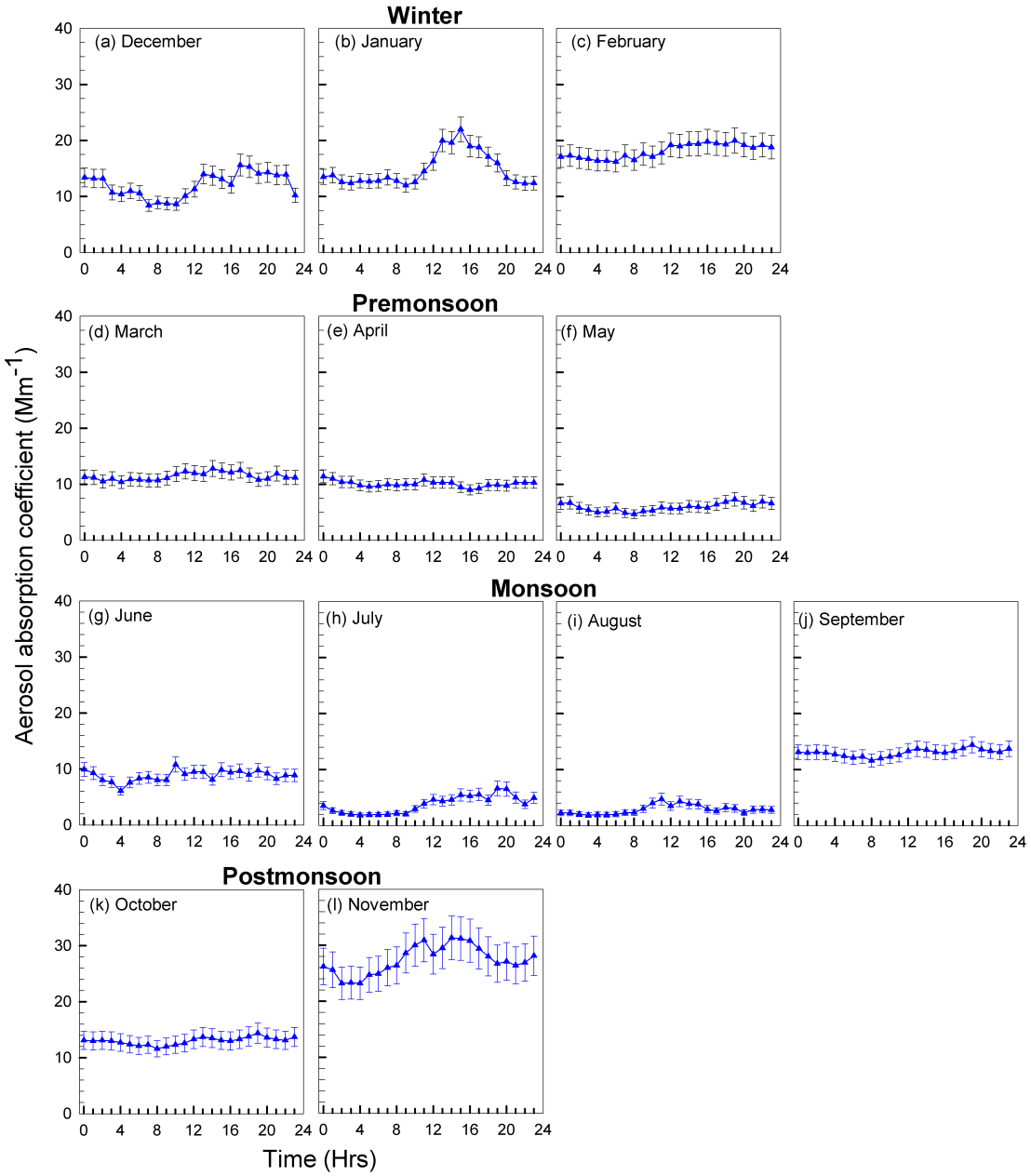

Figure 3.19: *Diurnal evolution of aerosol absorption coefficient (β_{abs}, Mm^{-1}) over Gurushikhar during winter (Dec (a), Jan (b), and Feb (c)), premonsoon (Mar (d), Apr (e), and May (f)), monsoon (Jun (g), Jul (h), Aug (i), and Sep (j)), and postmonsoon (Oct (k), and Nov (l)) at 0.55 μm for 2015 and 2016. Vertical bars represent $\pm 1\sigma$ deviation from the mean.*

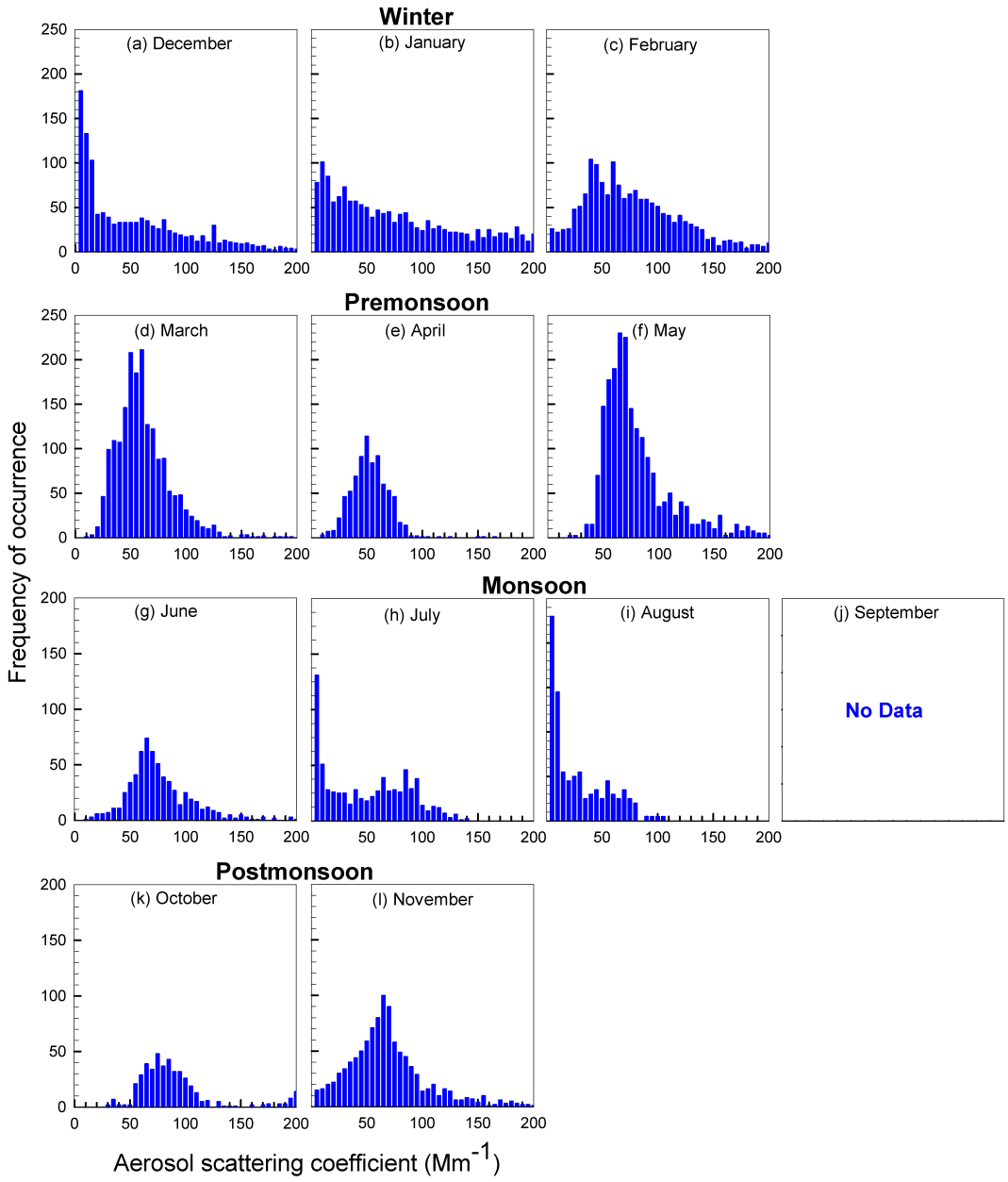

Figure 3.20: *Frequency distribution of nephelometer measured hourly aerosol scattering coefficient (β_{sca}, Mm^{-1}) over Gurushikhar during winter (Dec (a), Jan (b), and Feb (c)), premonsoon (Mar (d), Apr (e), and May (f)), monsoon (Jun (g), Jul (h), Aug (i), and Sep (j)), and postmonsoon (Oct (k), and Nov (l)) for 2015 and 2016. Vertical bars represent $\pm 1\sigma$ deviation from the mean.*

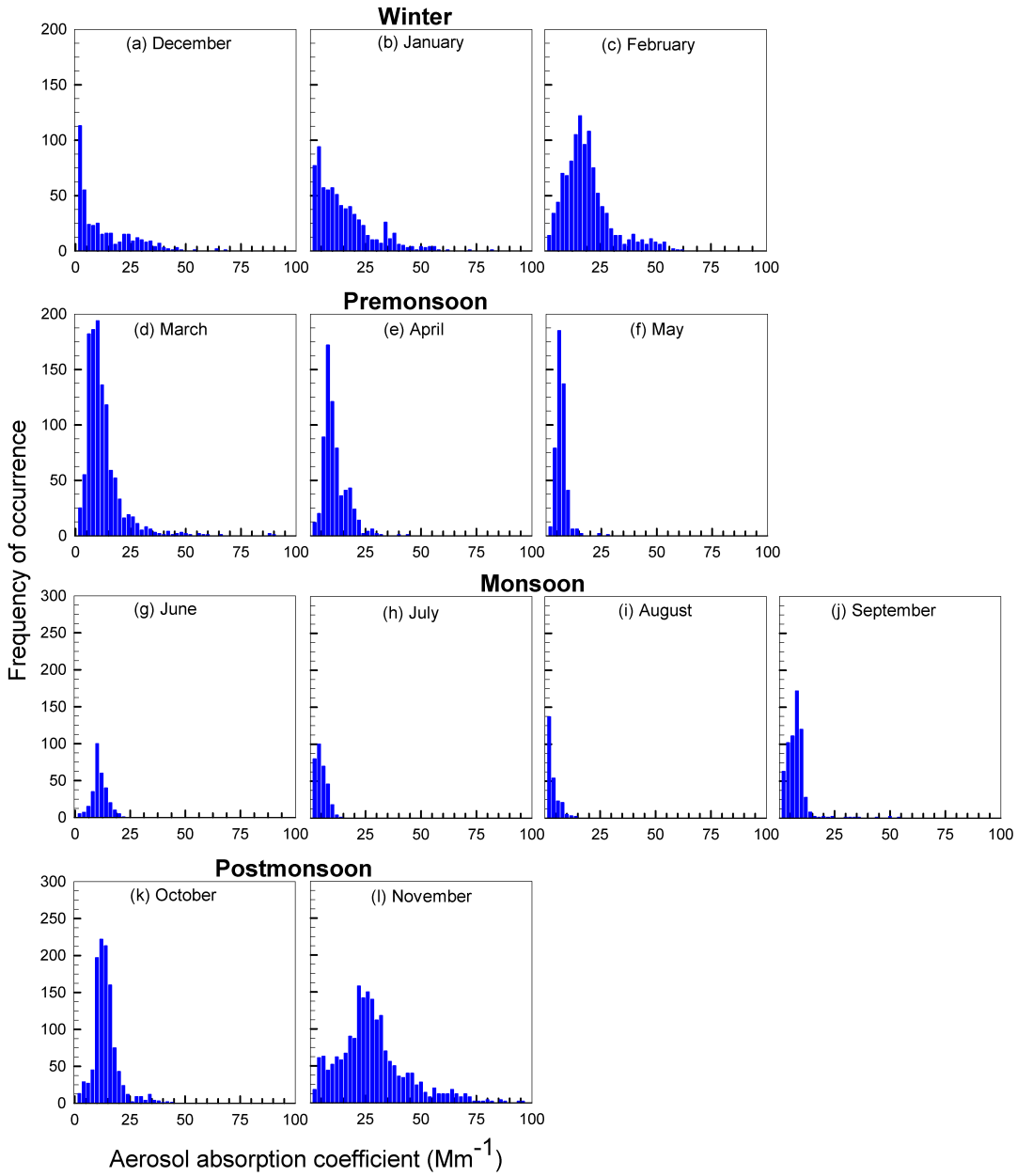

Figure 3.21: *Frequency distribution of aethalometer measured hourly aerosol absorption coefficient (β_{abs}, Mm^{-1}) over Gurushikhar during winter (Dec (a), Jan (b), and Feb (c)), premonsoon (Mar (d), Apr (e), and May (f)), monsoon (Jun (g), Jul (h), Aug (i), and Sep (j)), and postmonsoon (Oct (k), and Nov (l)) for 2015 and 2016. Vertical bars represent $\pm 1\sigma$ deviation from the mean.*

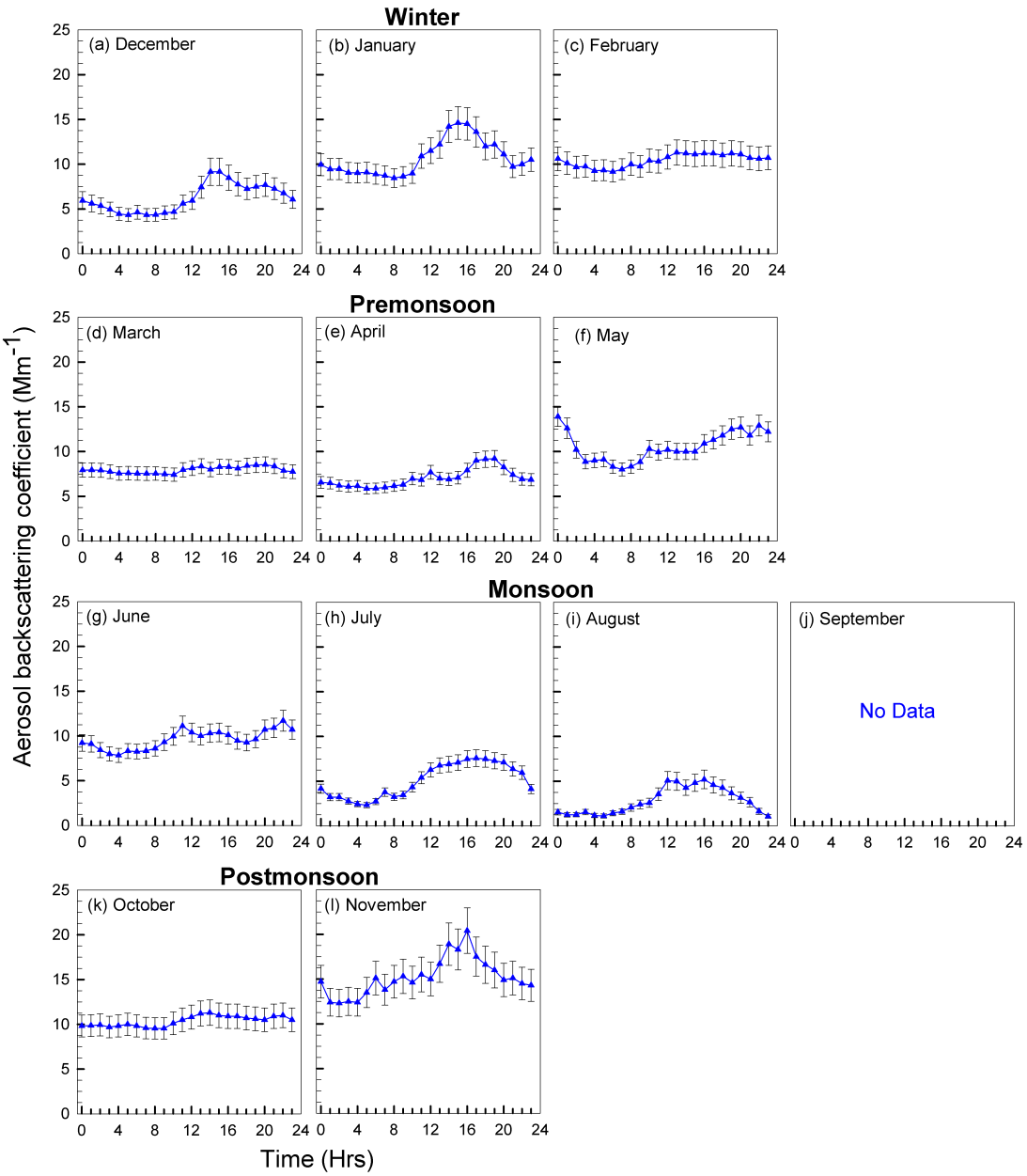

Figure 3.22: *Diurnal evolution of backscattering coefficient (β_{bsca}, Mm^{-1}) over Gurushikhar during winter (Dec (a), Jan (b), and Feb (c)), premonsoon (Mar (d), Apr (e), and May (f)), monsoon (Jun (g), Jul (h), Aug (i), and Sep (j)), and postmonsoon (Oct (k), and Nov (l)) at 0.55 μm for 2015 and 2016. Vertical bars represent $\pm 1\sigma$ deviation from the mean.*

modes are $< 5\ Mm^{-1}$ (Figure 3.21). The mode shifts to higher modes during November. During December and January the modes in β_{abs} are $< 5\ Mm^{-1}$ (Figure 3.21). Backscattering coefficient (β_{bsca}) at 0.55 μm shows similar variations as β_{sca} over Gurushikhar (Figure 3.22). β_{bsca} is found to be lower by a factor of 10 than β_{sca}.

Monthly and Seasonal variations

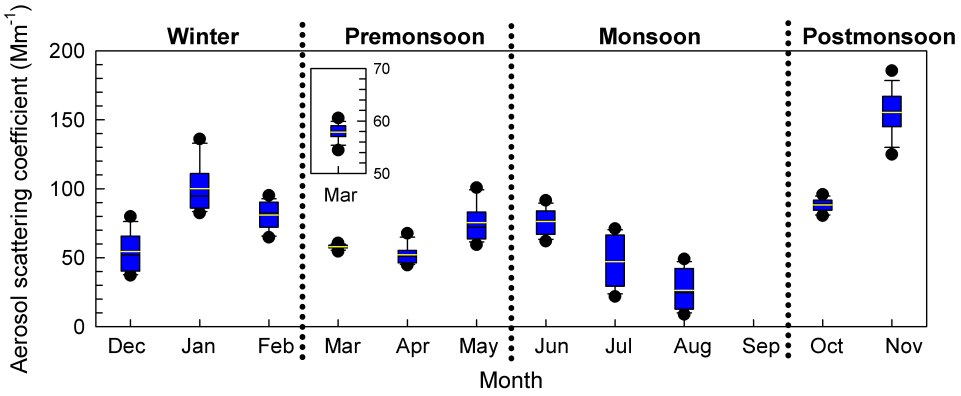

Figure 3.23: *Box and whisker plots of aerosol scattering coefficient (β_{sca}, Mm^{-1}) measured using nephelometer over Gurushikhar during 2015-2016 as function of season (winter, premonsoon, monsoon, and postmonsoon). The range of the box represent the limits of the 25^{th} and 75^{th} percentile data. The whiskers spreading from the box illustrate the limits of the 10^{th} and the 90^{th} percentile data. Yellow lines show the average of the data. The maximum and minimum and maximum in each box are represented by dots.*

The aerosol scattering (β_{sca}) and absorption (β_{abs}) coefficients (0.55 μm) over a high altitude remote location, Gurushikhar do not exhibit any systematic monthly variations as compared to an urban location, Ahmedabad (Figures 3.23 and 3.24). The parameters β_{sca} and β_{abs} decrease from January to April and then peak during May and June, which again decrease afterward till August and then increase from October to November before becoming low in December (Figures 3.23 and 3.24). The maximum β_{sca} and β_{abs} are observed during November as in addition to the anthropogenic emission from the nearby re-

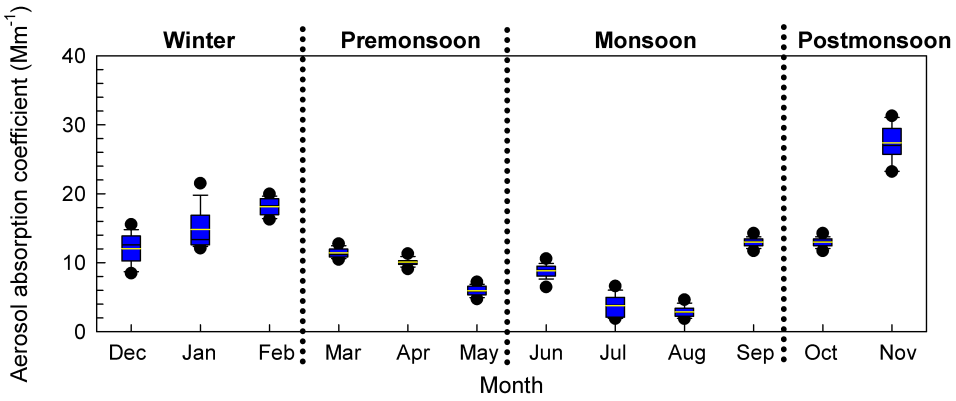

Figure 3.24: *Box and whisker plots of aerosol absorption coefficient (β_{abs}, Mm^{-1}) measured using aethalometer over Gurushikhar during 2015-2016 as function of season (winter, premonsoon, monsoon, and postmonsoon). The range of the box represent the limits of the 25^{th} and 75^{th} percentile data. The whiskers spreading from the box illustrate the limits of the 10^{th} and the 90^{th} percentile data. Yellow lines show the average of the data. The maximum and minimum and maximum in each box are represented by dots.*

gion, it is strongly influenced by the longrange transport (77%) from the northern part of India (Figure 2.10). The minimum β_{sca} and β_{sca} are observed during August as a result of wet removal. The parameters β_{sca} and β_{abs} exhibit a significant seasonal variation over Gurushikhar, where β_{sca} and β_{abs} are highest during postmonsoon followed by winter (Table 3.4), as the location is affected by convection from the foothills and significantly influenced by the advection process through the longrange transport mechanism (Figure 2.10). In addition, during postmonsoon and winter there is an increase in biomass burning, and tourist activities in the region. β_{sca} and β_{abs} decrease during premonsoon owing to the shift in the wind direction and source region. The minimum β_{sca} and β_{abs} are observed during monsoon due to the wet removal. The annual mean β_{sca} and β_{abs} found to be 78.0 $\pm$ 31.5 and 12.4 $\pm$ 6.6 Mm^{-1} respectively over Gurushikhar. It is interesting to note that monthly mean variability of β_{sca} is different than that of β_{abs}, but the seasonal mean β_{sca} and β_{abs} go hand in hand with each other. The median and mean of β_{sca} and β_{abs} distribution agree within 10% throughout the year over Gurushikhar.

The parameters β_{sca} and β_{abs} do not exhibit any significant inter-annual variability. The observed monthly percentage change in β_{sca} and β_{abs} between 2015 and 2016 is $< 15\%$ which is within the uncertainty in the measurements of these parameters. The seasonal mean β_{sca} values observed over Gurushikhar are significantly lower than Ahmedabad by a factor of 3 during winter and by a factor of 2 during premonsoon, monsoon and postmonsoon seasons (Tables 3.2 and 3.4). A similar pattern in β_{sca} and β_{abs} was observed over another urban location (Delhi) in the Indo Gangetic Plains with very high magnitude during winter (8 and 12 times higher than Gurushikhar β_{sca} and β_{abs} values respectively) (*Soni et al.*, 2010).

3.2.2 Single scattering albedo

Temporal variations

The surface single scattering albedo (*SSA*) exhibits a rare diurnal variability (Figure 3.25) at 0.55 μm over Gurushikhar when compared to an urban region. The diurnal variation is minimal consistent with minimal variations seen in β_{sca} and β_{abs}. Gurushikhar shows afternoon/evening small peak in *SSA* during some months (December, April, and August) due to the influence of the atmospheric boundary layer dynamics. The study confirms that Gurushikhar is significantly influenced by the local and longrange transported aerosols through convection and advection processes.

Monthly and Seasonal variations

Surface single scattering albedo (*SSA*) estimated from surface measured aerosol scattering and absorption coefficients also exhibits a significant seasonal variation (Figure 3.26). The maximum *SSA* is observed during May as 95% of the longrange transported air are from the arid regions and Arabian Sea (Figure 2.10) which bring in more scattering type aerosols relative to the anthro-

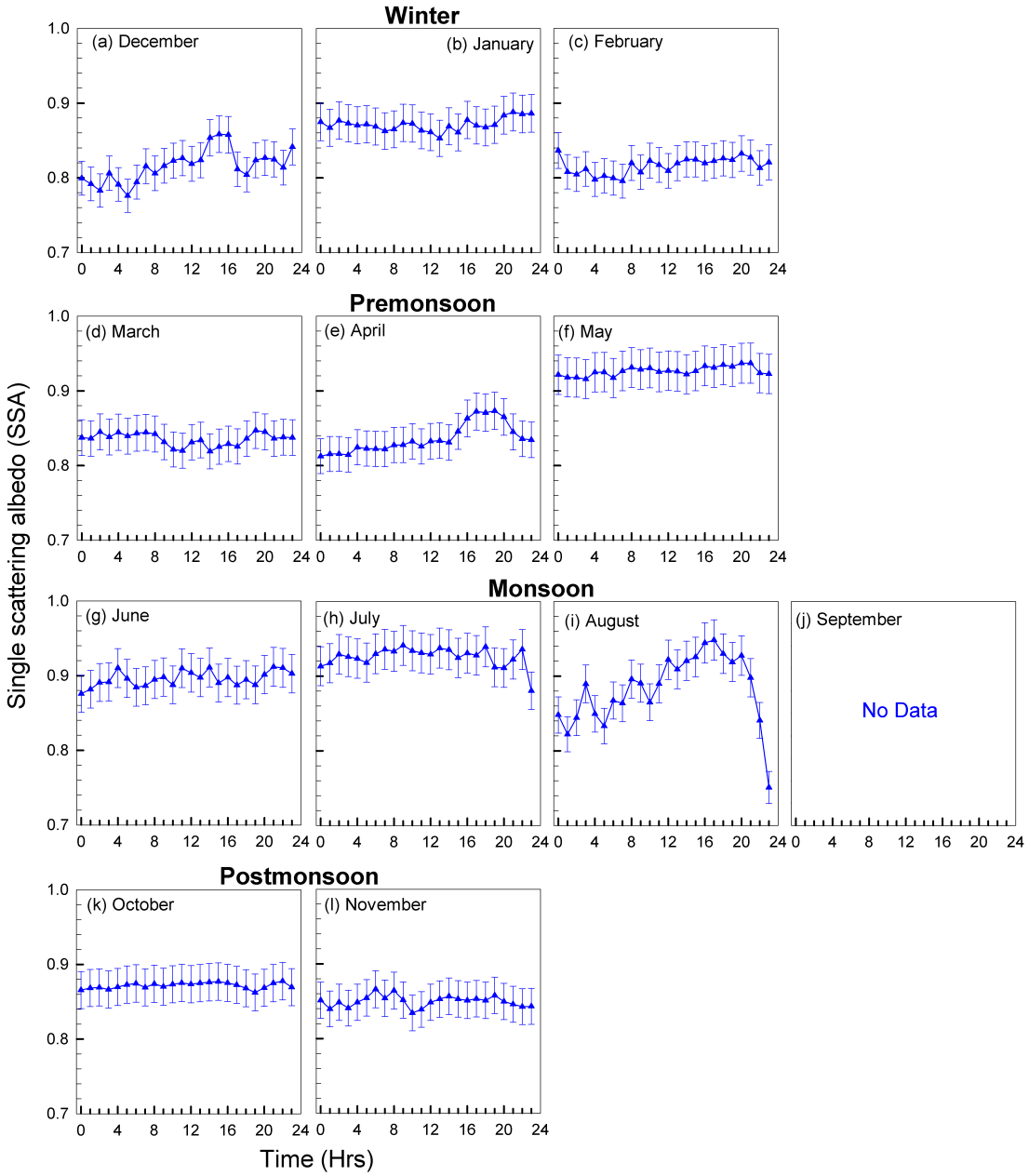

Figure 3.25: *Diurnal evolution of single scattering albedo (SSA) over Gurushikhar during winter (Dec (a), Jan (b), and Feb (c)), premonsoon (Mar (d), Apr (e), and May (f)), monsoon (Jun (g), Jul (h), Aug (i), and Sep (j)), and postmonsoon (Oct (k), and Nov (l)) at 0.55 μm for 2015 and 2016. Vertical bars represent $\pm 1\sigma$ deviation from the mean.*

pogenic emissions from the valley regions. Whereas, the minimum *SSA* is found during December as 85% of the longrange transported air are from the northern region of India (Figure 2.10) which brings in more absorbing type aerosols (black carbon) as compared to the contributions from the nearby valley regions. *SSA* decreases from July to December indicating a transition from the dominant scattering type aerosols to absorbing type aerosol. Fire counts exhibit large spatial variations over India (Figure 3.16). The area infested by forest fires and biomass burning is high during winter and premonsoon as compared to monsoon and postmonsoon. During postmonsoon, Punjab and Haryana show high fire counts due to relative dominance of biomass burning (residue crop burning). In addition, premonsoon shows higher fire counts in the Indo Gangetic Plains due to residue crop burning during this period over Punjab and Haryana (Figure 3.16). The wind patterns play an important role in transporting the biomass components from the biomass burning regions to the observational site through advection process (Figure 2.10). Low *SSA* during March and April reveals the dominance of absorbing type aerosols which get transported from the residue crop burning areas in Punjab and Haryana. On a relative scale, March shows lower *SSA* than April because 54% of air trajectories originate from the residue crop burned source region during March when compared to April (Figure 2.10). The MODIS fire count map shows highest fire density during May in the Punjab and Haryana region of northern India but this signature is not observed over Gurushikhar as only 3% of the air parcels reaching the observational site are from this hot spot region, and 95% of the air trajectories are from the arid regions and Arabian Sea (Figure 2.10). Highest *SSA* is observed during monsoon followed by premonsoon and postmonsoon (Table 3.3). Minimum *SSA* is observed during winter as a result of the abundance of the absorbing aerosols arriving to the observational site from the northern region of India.

The surface *SSA* over Gurushikhar is found to be higher than Ahmedabad *SSA* due to the dominance of absorbing aerosols over Ahmedabad from the anthropogenic emissions. The surface *SSA* over Gurushikhar is found to be lower

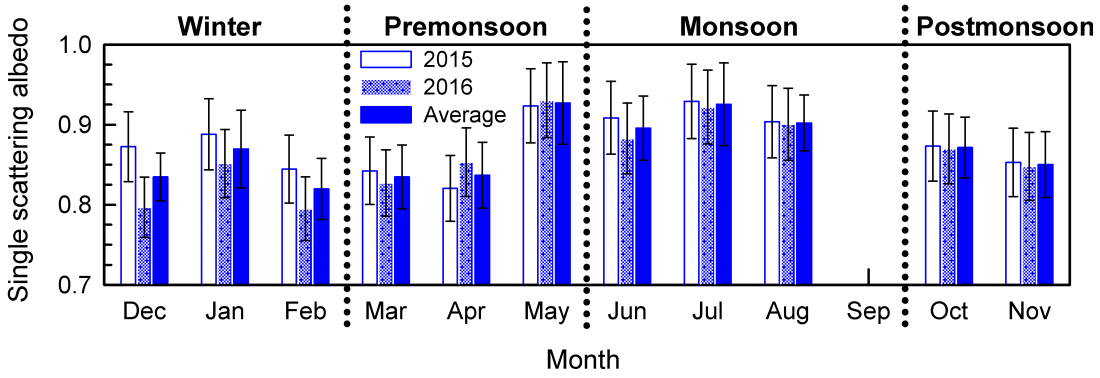

Figure 3.26: *Monthly mean surface single scattering albedo at 0.55 μm for 2015, 2016, and average of 2015 - 2016 as function of season (winter, premonsoon, monsoon, and postmonsoon) over Gurushikhar. Vertical bars indicate $\pm 1\sigma$ variation with respect to mean.*

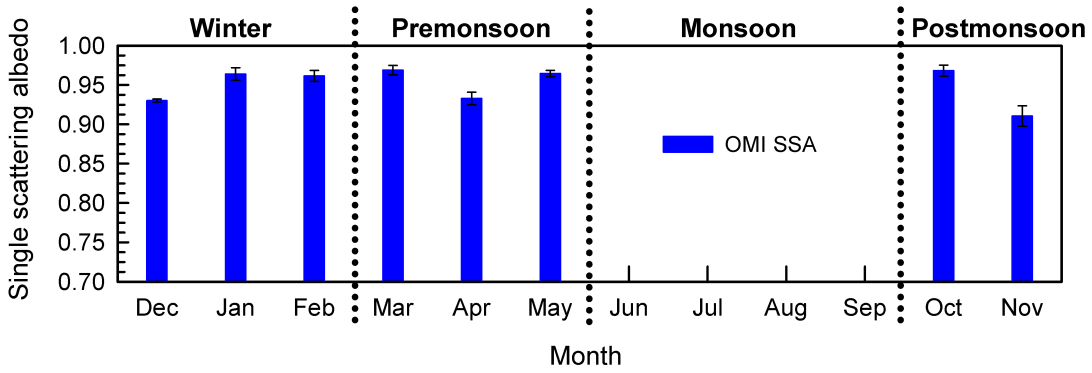

Figure 3.27: *Monthly mean columnar single scattering albedo at 0.50 μm during 2015-2016 as function of season (winter, premonsoon, monsoon, and postmonsoon) over Gurushikhar. Vertical bars indicate $\pm 1\sigma$ variation with respect to mean.*

than columnar *SSA* derived from OMI (Figures 3.26 and 3.27) because most of the absorbing aerosols which are transported from the nearby foothills are concentrated near the surface, hence, the aerosol absorption coefficients near the surface will be higher when compared to the column. The annual mean surface and column *SSA* are found to be 0.87 $\pm$ 0.04 and 0.95 $\pm$ 0.01 respectively over Gurushikhar. The *SSA* derived from the measured aerosol scattering and absorption coefficients exhibits $<$ 10% difference between 2015 and 2016 (Figure 3.26).

The *SSA* during December is lower than the *SSA* reported over a cleaner site Manora Peak, a high altitude site in the central Himalayas (0.90) (*Pant et al.*, 2006). Annual mean *SSA* over Gurushikhar is significantly higher than Ahmedabad, Delhi (0.70) (*Soni et al.*, 2010), and Visakhapatnam (0.76) (*Niranjan et al.*, 2011). *SSA* shows $< 10\%$ difference between 2015 and 2016 over Gurushikhar. Less significant inter-annual variability in aerosol optical properties indeed confirms that Gurushikhar is a regional representative background site for aerosols.

3.2.3 Ångström exponent, Backscatter fraction, and Asymmetry parameter

Temporal variations

The diurnal variation in *Ångström exponent* (α), *backscatter fraction* (*b*), and *asymmetry parameter* (*g*) over Gurushikhar do not exhibit any morning or evening peaks (Figures 3.28 - 3.30) as observed over an urban region (Ahmedabad) (Figure 3.9). On the relative scale, the α, *b*, and *g* show large diurnal variability during July and August probably as the observational location is influenced by the maximum surface wind speed (Figure 2.7) during these months. The lowest mean diurnal variability in the α and *b*, and maximum *g* are found during monsoon indicate the dominance of larger size aerosols in the size distribution over Gurushikhar (Figures 3.28 - 3.30). The highest average diurnal variability in the α and *b*, and lowest *g* are found during winter and postmonsoon suggesting the dominance of smaller size aerosols (Figures 3.28 - 3.30).

Monthly and Seasonal variations

The near surface *Ångström exponent* (α), *backscatter fraction* (*b*), and *asymmetry parameter* (*g*) exhibit monthly variations over a high altitude remote location, Gurushikhar (Figure 3.31). The parameter α, an atmospheric aerosol

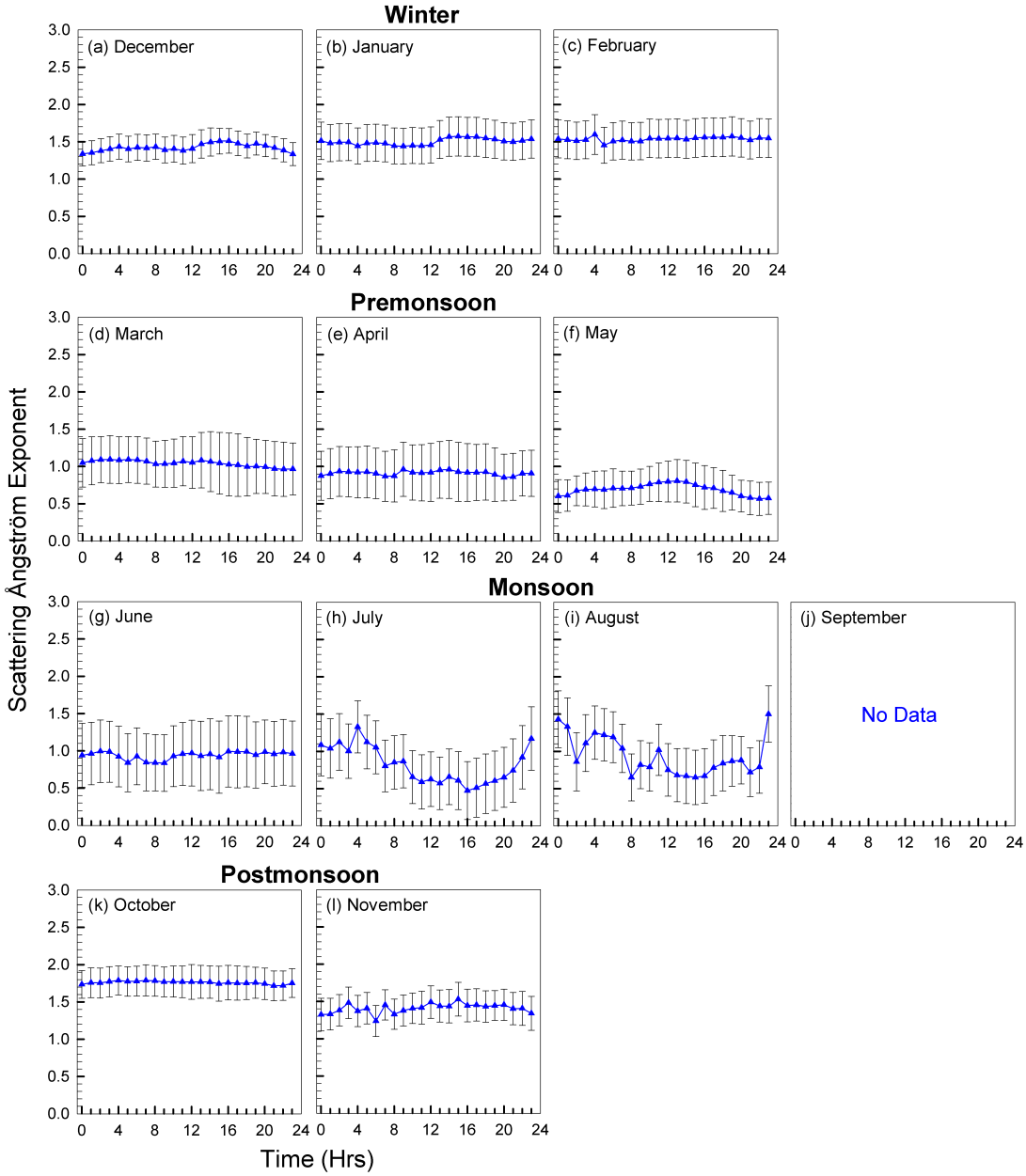

Figure 3.28: *Diurnal evolution of scattering Ångström exponent (α) over Gurushikhar during winter (Dec (a), Jan (b), and Feb (c)), premonsoon (Mar (d), Apr (e), and May (f)), monsoon (Jun (g), Jul (h), Aug (i), and Sep (j)), and postmonsoon (Oct (k), and Nov (l)) using β_{sca} measured at 0.45, 0.55 and 0.70 μm during 2015 and 2016. Vertical bars represent $\pm 1\sigma$ deviation from the mean.*

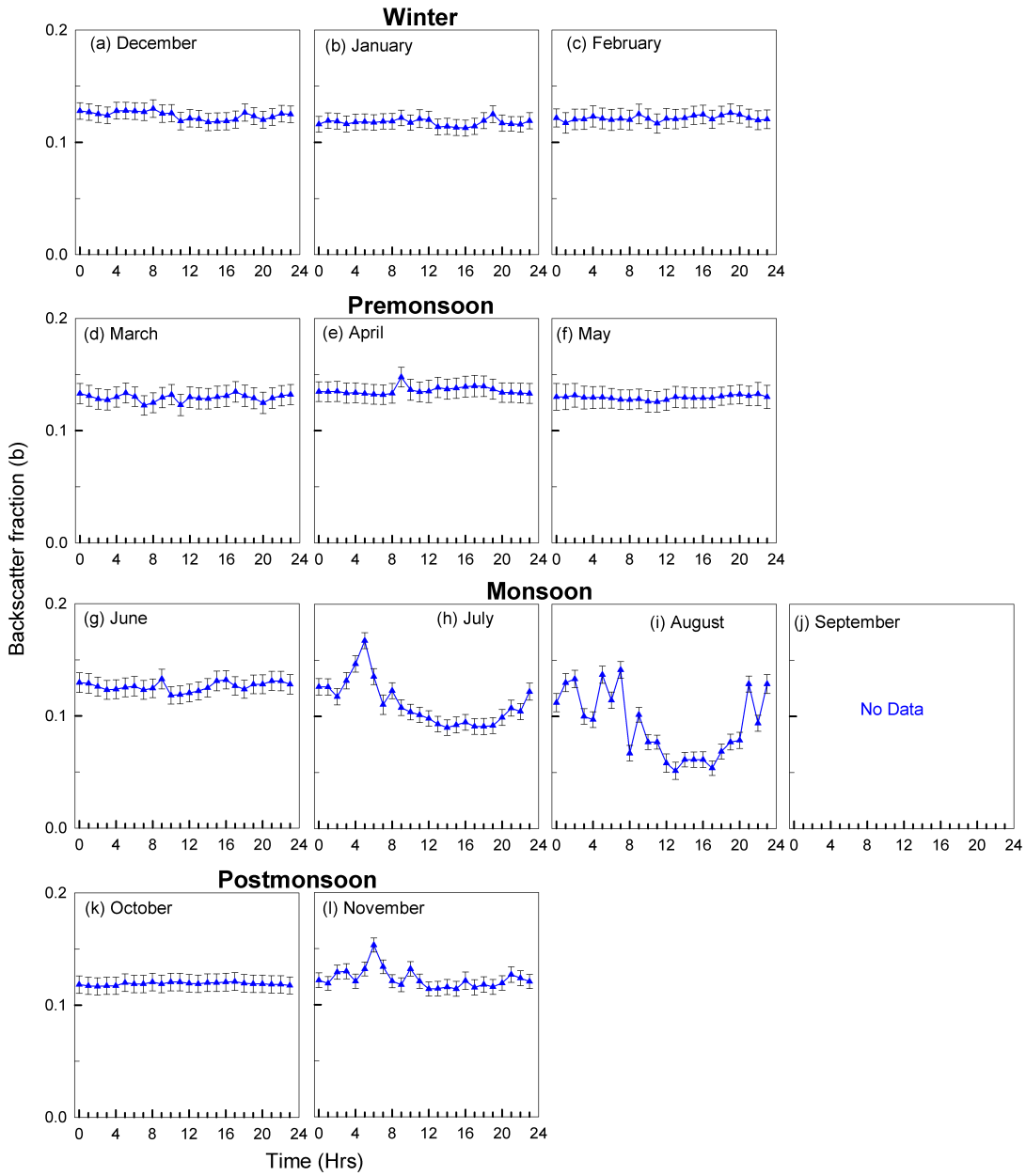

Figure 3.29: *Diurnal evolution of aerosol backscatter fraction (b) over Gurushikhar during winter (Dec (a), Jan (b), and Feb (c)), premonsoon (Mar (d), Apr (e), and May (f)), monsoon (Jun (g), Jul (h), Aug (i), and Sep (j)), and postmonsoon (Oct (k), and Nov (l)) at 0.55 μm for 2015 and 2016. Vertical bars represent $\pm 1\sigma$ deviation from the mean.*

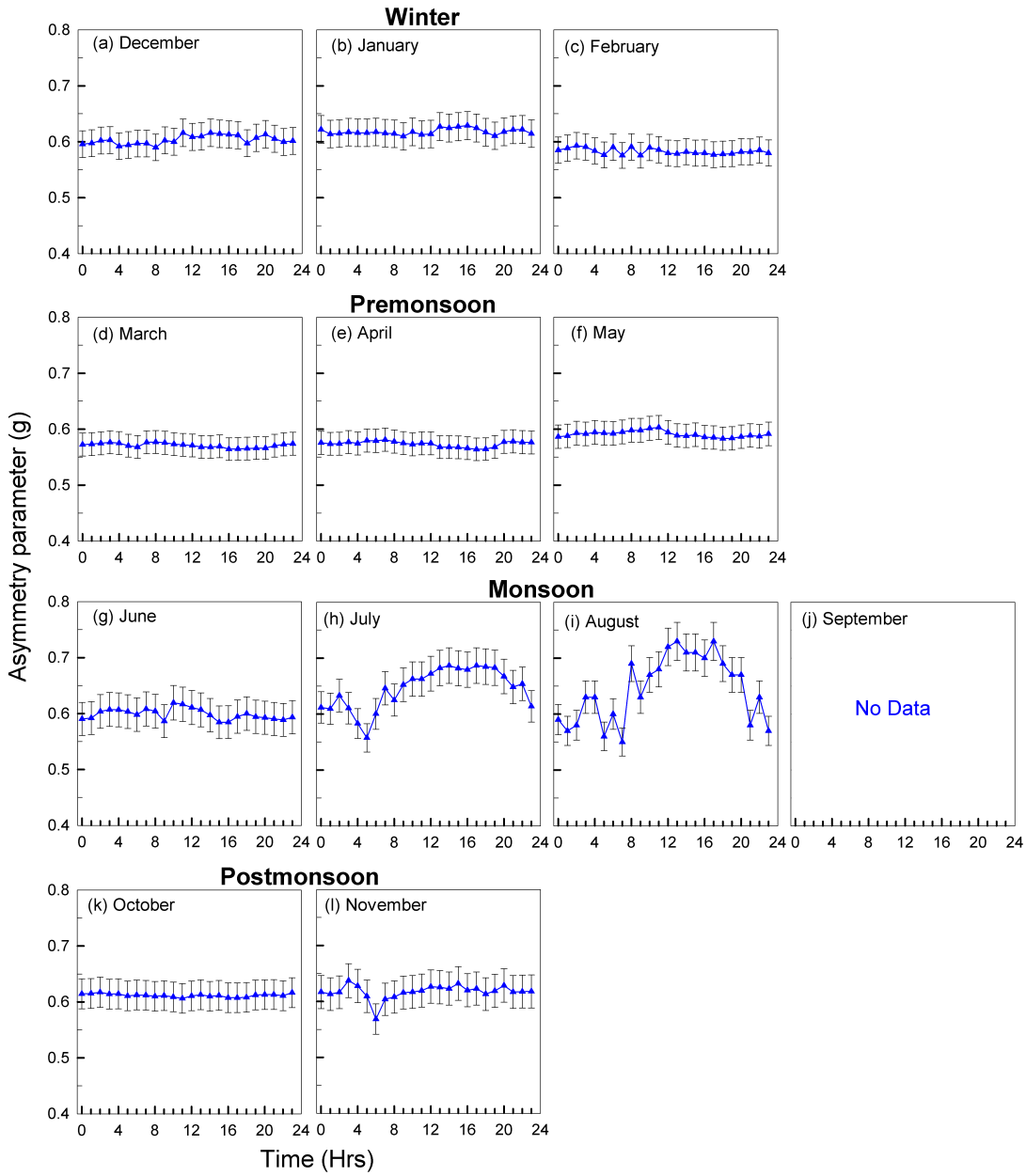

Figure 3.30: *Diurnal evolution of asymmetry parameter (g) over Gurushikhar during winter (Dec (a), Jan (b), and Feb (c)), premonsoon (Mar (d), Apr (e), and May (f)), monsoon (Jun (g), Jul (h), Aug (i), and Sep (j)), and postmonsoon (Oct (k), and Nov (l)) at 0.55 μm for 2015 and 2016. Vertical bars represent $\pm 1\sigma$ deviation from the mean.*

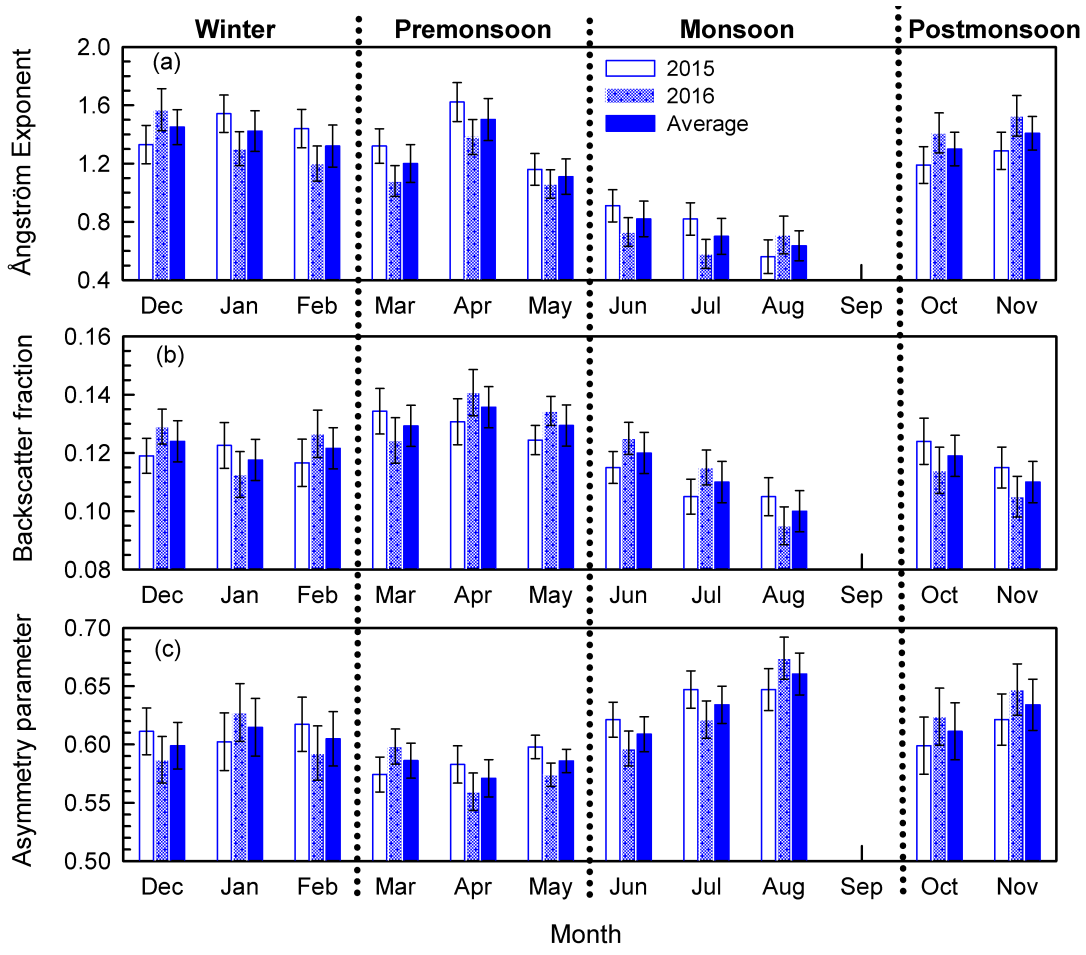

Figure 3.31: *Monthly mean (a) Ångström exponent, (b) backscatter fraction, and (c) asymmetry parameter at 0.55 μm over Gurushikhar during 2015-2016 as function of season (winter, premonsoon, monsoon, and postmonsoon). Vertical bars indicate $\pm 1\sigma$ variation with respect to mean.*

size indicator decreases from January to August except during April (Figure 3.31a). The *backscatter fraction* increases from January to April and decreases afterward (Figure 3.31b), whereas, the *asymmetry parameter* decreases from January to April then gradually increases to reach maximum during August (Figure 3.31c). During April, maximum α and b, and minimum g are found which suggest the dominance of smaller size particles due to the influence of the biomass burning from the northern part of India (Figure 3.16) being transported through advection (Figure 2.10) to the observational location. The min-

imum α and *b*, and maximum *g* are observed during August due to the dominance of higher size particle transported from the Arabian Sea (Figure 2.10).

The parameters α, *b*, and *g* derived from the surface measured β_{sca} and β_{bsca} data over Gurushikhar exhibit $< 10\%$ difference during the measurement period (2015-2016) (Figure 3.31) which is within the uncertainty of the measurements (15%). Hence, α, *b*, and *g* do not exhibit any significant inter-annual variability over the high altitude remote location, Gurushikhar. Typically, urban emissions are influenced by anthropogenic activities. The high altitude remote region is influenced by local and longrange transported aerosols through convective and advective processes. When the high altitude remote location is in the same region as that of an urban aerosol source region, and is governed by the same meteorology and atmospheric dynamics, then aerosol measurements over the high altitude region can serve as regional representative background which is the case here.

3.2.4 Aerosol optical depth

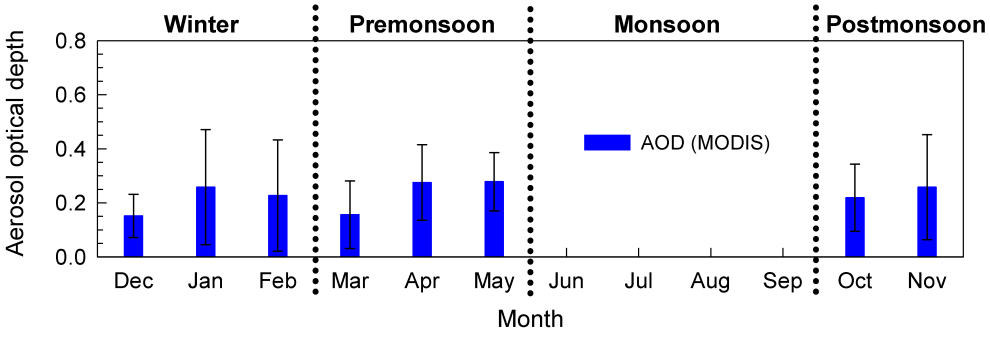

Figure 3.32: *Mean (of MODIS Terra and Aqua) AODs at 0.55 μm over Gurushikhar, Mt. Abu as function of season (winter, premonsoon, monsoon, and postmonsoon). Vertical bars denote $\pm 1\sigma$ deviation from the monthly mean.*

Aerosol optical depth (*AOD*) shows significant monthly and seasonal variations (Figure 3.32) in Gurushikhar. The estimated *AOD* over a high altitude

Table 3.4: *Seasonal variations of aerosol scattering (β_{sca}, Mm^{-1}) and absorption (β_{abs}, Mm^{-1}) coefficients, surface single scattering albedo (SSA), Ångström exponent (α), backscatter fraction (b), asymmetry parameter (g), aerosol optical depth (AOD), and columnar single scattering albedo (SSA (OMI)) at Gurushikhar during January 2015 - December 2016.*

Parameters	Winter	Premonsoon	Monsoon	Postmonsoon
β_{sca}	78.5 ± 22.9	61.8 ± 12.2	49.9 ± 25.1	121.8 ± 47.4
β_{abs}	15.0 ± 3.0	9.1 ± 2.9	5.1 ± 3.2	20.2 ± 10.2
SSA	0.84 ± 0.03	0.87 ± 0.05	0.91 ± 0.02	0.86 ± 0.01
α	1.40 ± 0.04	1.27 ± 0.36	0.72 ± 0.06	1.35 ± 0.15
b	0.12 ± 0.01	0.13 ± 0.01	0.11 ± 0.01	0.11 ± 0.01
g	0.61 ± 0.02	0.58 ± 0.01	0.63 ± 0.01	0.62 ± 0.01
AOD	0.21 ± 0.05	0.24 ± 0.07	-	0.25 ± 0.03
SSA (OMI)	0.95 ± 0.02	0.96 ± 0.02	-	0.94 ± 0.04

remote location, Gurushikhar is found to be lower than an urban location, Ahmedabad in western India, as Ahmedabad is consistently influenced by the high magnitude of anthropogenic emissions, whereas Gurushikhar is influenced by the local and longrange transported aerosols through convection and advection. The parameter *AOD* decreases from January to March, and increases afterward. *AOD* is found to be maximum during May (Figure 3.32) probably due to the presence of dust from the nearby arid regions. During October - November *AOD* increases and is found to be minimum during December (Figure 3.32). The highest *AOD* is found during postmonsoon followed by premonsoon and winter (Table 3.4). The annual mean *AOD* over Gurushikhar is 0.23 ± 0.05, which is found to be a factor of 2 lower than Ahmedabad.

Chapter 4

Black carbon aerosol characteristics over urban and high altitude remote locations

Most of the black carbon (BC) aerosols in the atmosphere are anthropogenic in nature as they are emitted from the burning of fossil fuel and biomass. Fossil fuel emissions consists of large fraction of black carbon than organic carbon (OC) and absorb in the near infrared regime, whereas biomass (wood) burning consists dominantly organic carbon and exhibit strong absorption in the ultraviolet regime (*Sandradewi et al.*, 2008). BC aerosol mass concentrations are underestimated over source regions (urban), especially in Asia (*IPCC*, 2013). The underestimation of BC mass concentration can be attributed to the lack of systematic BC measurements, and proper emission inventories (*Ramachandran et al.*, 2015). The measurement of BC mass concentration over high altitude remote location is sparse, and is required along with BC over the source regions in order to reduce the uncertainty due to BC emissions, and the resultant radiative effects of BC aerosols. BC mass concentration from a high altitude remote location represents the background BC concentration for the corresponding region. BC characteristics and its source apportionment have been examined over an urban (Ahmedabad) and a high altitude remote (Gurushikhar) locations in western India.

4.1 BC aerosol characteristics over an urban location: Ahmedabad

The BC mass concentration measurements were conducted over an urban location, Ahmedabad during January 2015 to December 2016 using multiwavelength aethalometer AE31. Total of 680 days of BC mass concentrations data at a temporal resolution of 5 min were used in the present study (Table 3.1). The BC data during the local festival (Diwali, Holi, Navratri) have not been utilised in the present study (Chapter 3, section 3.1).

4.1.1 Diurnal variations

The temporal variation in the near surface BC mass occurs owing to the evolution of atmospheric boundary layer (Figure 3.3), various BC emission sources and their strengths. BC shows a consistent diurnal pattern over Ahmedabad with two minima and two maxima (Figure 4.1). BC mass concentrations show the first maxima around 07-09 hrs as a result of the combination of increase in anthropogenic activities and fumigation effect (*Stull*, 1988) of the ABL. BC concentration then decreases owing to increase in ABL (Figure 4.1) (*Rajesh and Ramachandran*, 2017). BC concentrations are minimum (second minima for the day) between 15 and 16 hrs as a result of fully evolved ABL and decline in the emissions associated with road traffic. The second maxima in BC concentrations (around 19-21 hrs) is attributed due to declining atmospheric boundary layer and increasing road traffic. After 21 hrs, the road traffic decreases and hence the production of BC aerosol declines. The BC aerosols from the atmosphere are removed by gravitational settling which results in a minima around 04-05 hrs (first minima) (Figure 4.1). BC mass are significantly affected by the atmospheric dynamics (ABL and surface winds) and anthropogenic sources. The peak intensity is influenced by the source and removal processes of black carbon aerosols and the meteorological dynamics. The morning and nocturnal peaks in BC mass concentration show maximum strength during December - March. The peak intensity decreases due to advection by strong wind

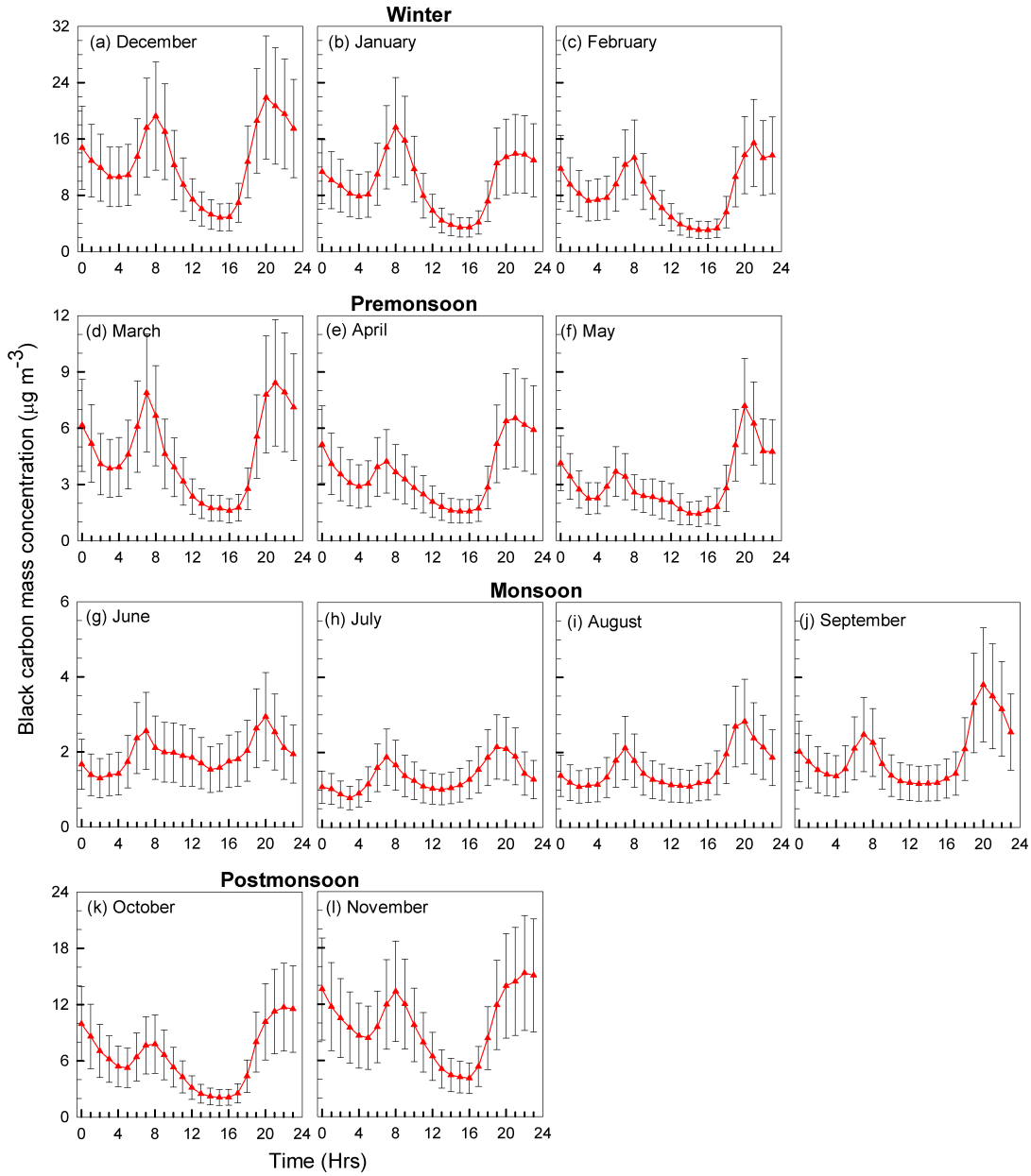

Figure 4.1: *Monthly diurnal variation of black carbon (BC) mass concentrations ($\mu g\, m^{-3}$) over Ahmedabad during winter (Dec (a), Jan (b), and Feb (c)), premonsoon (Mar (d), Apr (e), and May (f)), monsoon (Jun (g), Jul (h), Aug (i), and Sep (j)), and postmonsoon (Oct (k), and Nov (l)) for 2015 and 2016. Vertical bars indicate $\pm 1\sigma$ variation from the mean.*

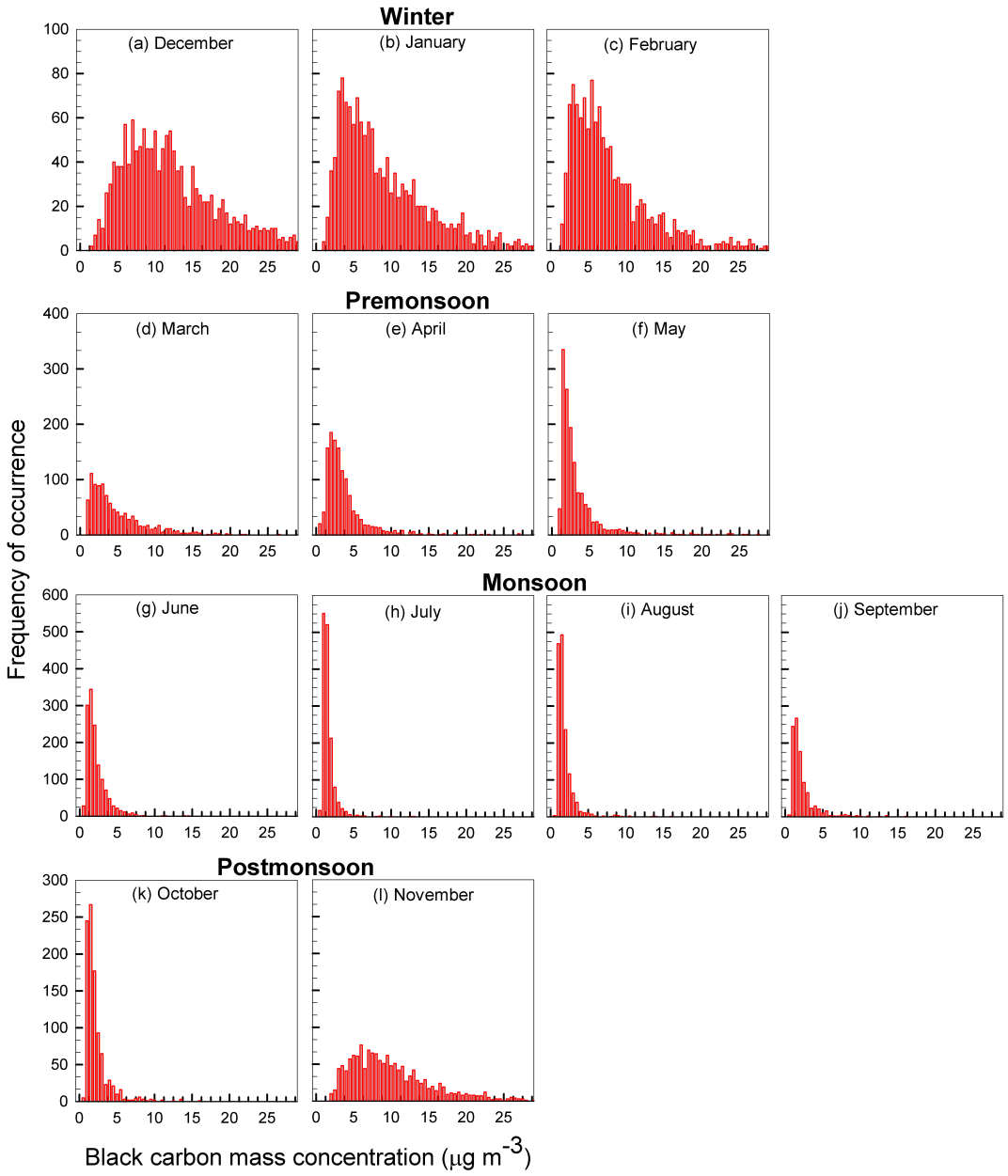

Figure 4.2: *Frequency distribution of black carbon (BC) mass concentrations ($\mu g\ m^{-3}$) over Ahmedabad during winter (Dec (a), Jan (b), and Feb (c)), premonsoon (Mar (d), Apr (e), and May (f)), monsoon (Jun (g), Jul (h), Aug (i), and Sep (j)), and postmonsoon (Oct (k), and Nov (l)) for 2015 and 2016.*

and stronger thermal convection (high surface temperature resulted in higher

ABL height) during April - September. During June - September due to precipitation BC aerosols were washed out from the atmosphere and hence the observed magnitude of diurnal variation was small. During October - November and December - February, the observed BC mass concentration increased due to shallow ABL height and low surface wind speed, which holds the BC aerosol for a longer period. Highest diurnal BC mass concentrations were observed during winter followed by postmonsoon and premonsoon. Lowest diurnal BC mass concentration were observed during monsoon when the rainfall is maximum.

The BC mass concentration shows a right-skewed or skewed to the right distribution (Figure 4.2). The observed mode is between 1 - 3 μg m^{-3} during March - September, which shifts to 2 - 4 μg m^{-3} during January - October. Higher modes are observed during February, November and December (Figure 4.3). Frequency distribution of BC mass concentration exhibits a significant seasonal variation (Figure 4.2). The frequency distribution of BC mass concentration is broader during winter (December, January, February) and postmonsoon (October, November) as a result of shallow atmospheric boundary layer, low surface wind speed and significant increase in biomass burning which holds the aerosol near Earth's surface (Figure 4.2). During monsoon, the maximum frequency occurs when BC values are low (1 - 2 μg m^{-3}) owing to wet removal and transition in the direction of the wind (arid to marine). While the maximum frequency occurs in the range of higher BC mass concentrations during winter and postmonsoon (Figure 4.2).

In order to quantify the observed temporal behavior of BC mass concentration, the average diurnal pattern of BC mass has been classified into specific time periods viz, morning (05:00 to 10:55 hrs), afternoon (11:00 to 15:55 hrs), evening (16:00 to 20:55 hrs) and night (21:00 to 04:55 hrs) (Figure 4.3a) (*Rajesh and Ramachandran*, 2017). The BC mass corresponding to morning, afternoon, evening and nighttime periods are represented as *BC(M)*, *BC(A)*, *BC(E)*, and *BC(N)* respectively. *BC(M)*, *BC(A)*, *BC(E)*, and *BC(N)* mass concen-

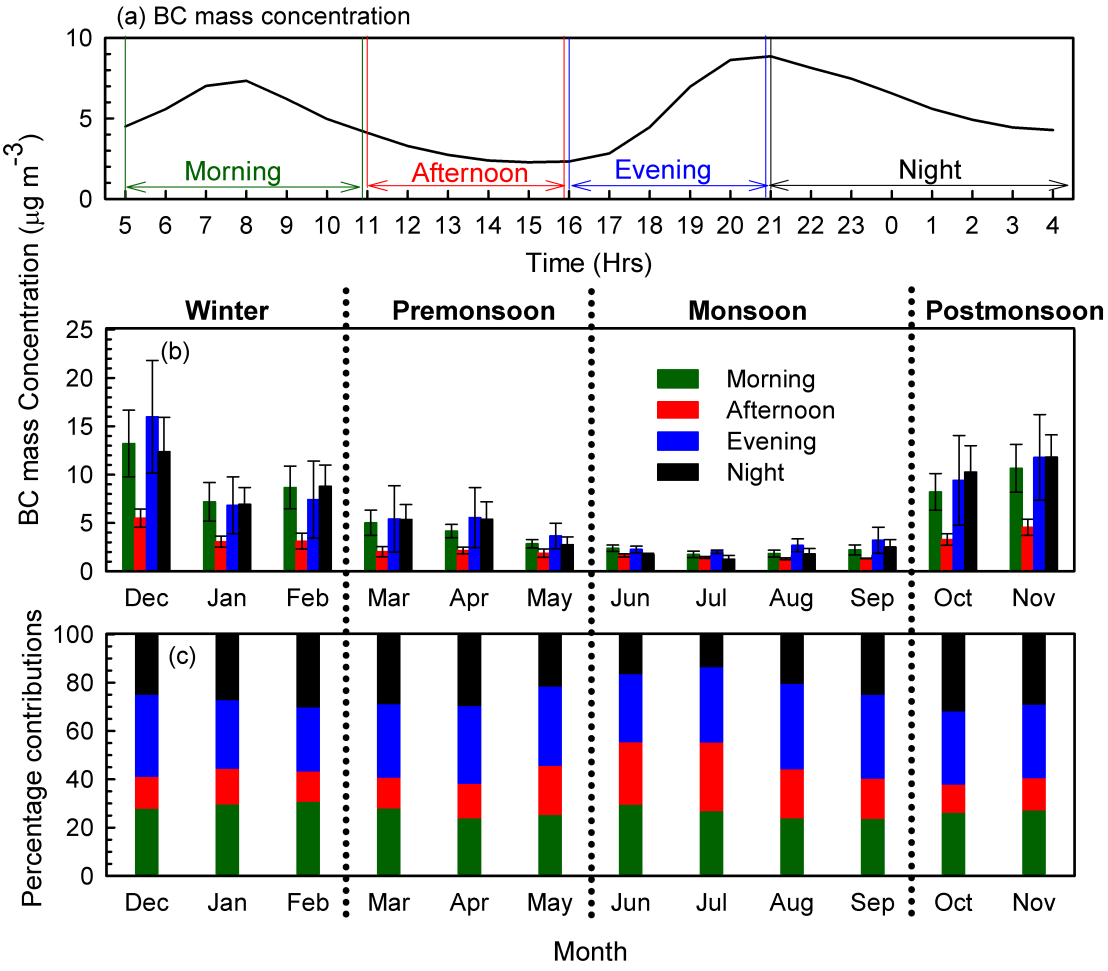

Figure 4.3: *(a) Average diurnal variation of black carbon (BC) mass concentration ($\mu g\ m^{-3}$) with specific time periods quantified as morning (05:00 to 10:55 hrs), afternoon (11:00 to 15:55 hrs), evening (16:00 to 20:55 hrs) and night (21:00 to 04:55 hrs). Monthly (b) BC mass concentrations and (c) percentage contributions at specific time periods (morning - night) over Ahmedabad during 2015 to 2016 as function of season (winter, premonsoon, monsoon, and postmonsoon). Vertical bars indicate $\pm 1\sigma$ variation with respect to mean.*

tration exhibit significant and large variations during the morning, afternoon, evening and night period (Figure 4.3b). The BC values are comparable during morning, evening and night period throughout the year (Figure 4.3c). During the afternoon period the BC values are minimum (17%) throughout the year (Figure 4.3c). *BC(M)* and *BC(E)* mass concentration exhibit significant varia-

tion throughout the year, while *BC(A)* mass shows the maximum change followed by *BC(N)* mass which occurs due to the influence of the atmospheric boundary layer dynamics and the anthropogenic emissions.

Table 4.1: *Mean sunrise and sunset time for each month at Ahmedabad during January 2015 - December 2016.*

Month	Sunrise (hrs)	Sunset (hrs)
Jan	7.37	18.25
Feb	7.20	18.58
Mar	6.82	18.80
Apr	6.32	19.00
May	5.98	19.22
Jun	5.88	19.43
Jul	6.03	19.47
Aug	6.25	19.20
Sep	6.43	18.72
Oct	6.60	18.23
Nov	6.87	17.92
Dec	7.20	17.93

Day and nighttime variations in the BC mass were further investigated to study the BC characteristics during the day and night time. The BC mass during daytime, *BC(Day)*, is defined as the BC mass within sunrise and sunset time and the remaining BC mass is nighttime BC, *BC(Night)*. The sunrise and sunset times exhibit variation for each month (Table 4.1). The length of the day (hrs) is calculated as the time interval between sunrise and sunset, and the remaining time is the length of the night (24 - the length of the day). The variability in the length of the day and night occurs owing to the 23.5^{o} inclination in the Earth's axis of rotation (Figure 4.4a). During summer - monsoon solstice the days are longest with higher ABL, whereas during winter solstice the days are shortest with lower ABL height. BC mass concentrations show significant seasonal variations during daytime and nighttime (Figure 4.4b). *BC(Night)* mass is found to be higher than *BC(Day)* over Ahmedabad. *BC(Day)* and *BC(Night)* mass concentrations are maximum during December and minimum during July (*Rajesh and Ramachandran*, 2017). Typically, the mean *BC(Night)* mass

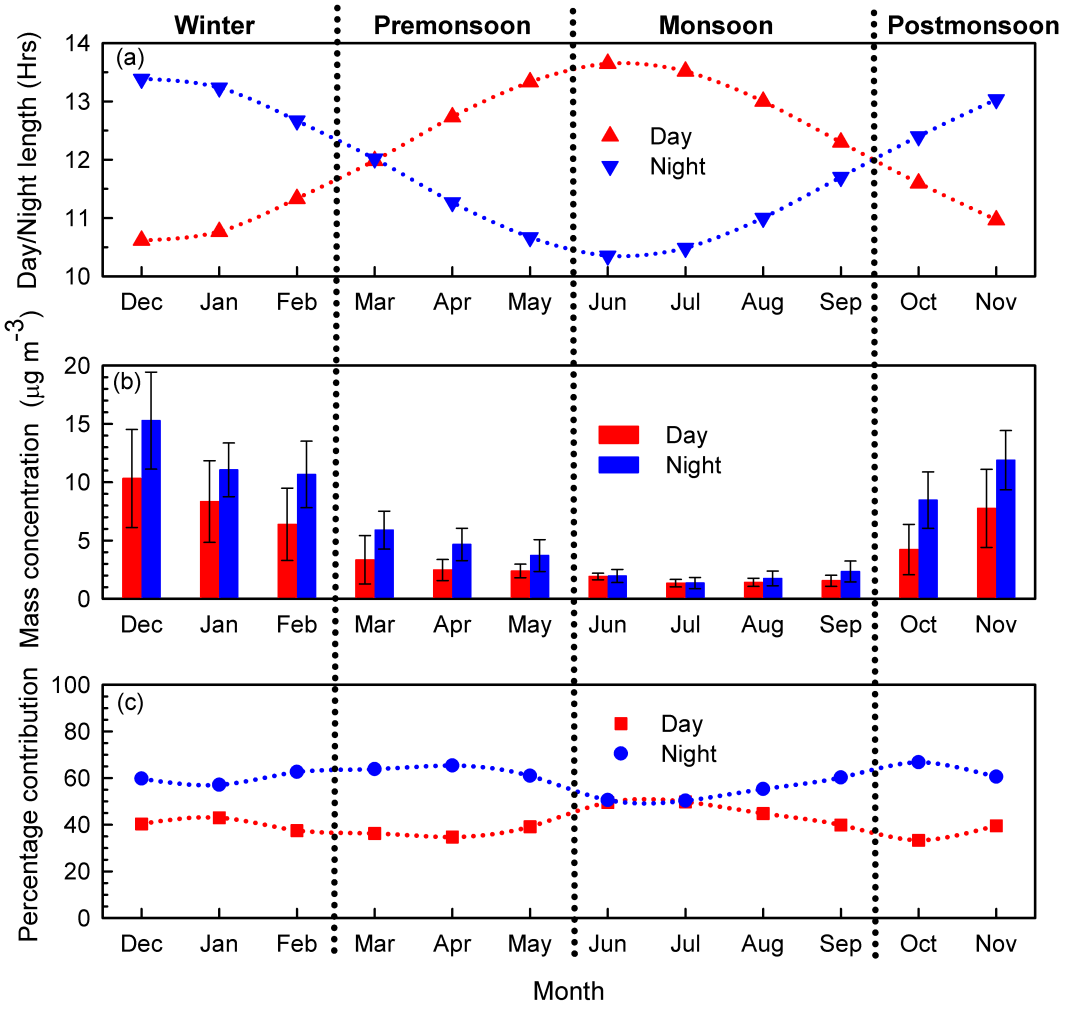

Figure 4.4: *Monthly variations in (a) length of the day and night (hrs), (b) BC mass concentrations ($\mu g\ m^{-3}$) during day BC(Day) and nighttime BC(Night), and (c) contributions (%) of day and nighttime BC mass concentration over Ahmedabad during 2015 - 2016 as function of season (winter, premonsoon, monsoon, and postmonsoon). Vertical bars indicate $\pm 1\sigma$ variation with respect to mean.*

is about 1.5 times higher than *BC(Day)* as the ABL is shallow during nighttime which traps the pollutants to a confined volume causing an increase in the surface BC mass concentration. The contribution (%) of *BC(Night)* to total BC mass dominates except, during June and July as during these months the *BC(Night)* and *BC(Day)* contributions are comparable probably due to the longer length of the day resulting in more anthropogenic emissions (Figure

4.4c). The annual average contribution (%) of *BC(Day)* and *BC(Night)* to total BC mass is 40 and 60% respectively.

4.1.2 Weekly variations

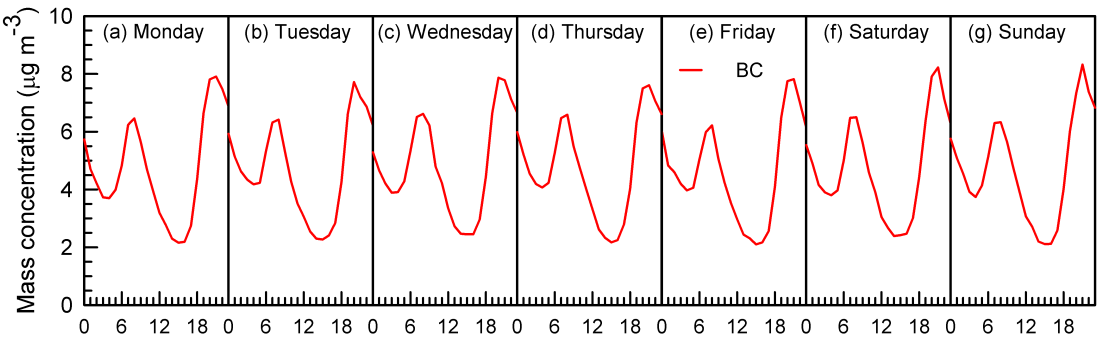

Figure 4.5: *Diurnal variation in black carbon (BC) mass ($\mu g\ m^{-3}$) as a function of weekdays (Monday - Friday) and weekends (Saturday - Sunday) over Ahmedabad during 2015 - 2016.*

The BC mass diurnal variations during weekday (Monday - Friday) and weekend (Saturday - Sunday) are found to be almost the same (Figure 4.5) over Ahmedabad during 2015-2016. The diurnal variation throughout the week shows a pronounced evening BC peak (Figure 4.5) owing to significant and dominant vehicular/traffic activity. The observed weekly variation in BC mass may be a typical characteristic feature of Ahmedabad, where BC sources during weekday and weekend are similar.

4.1.3 Monthly and Seasonal variations

BC mass is found to be maximum and minimum during December and July respectively. BC mass concentration is higher during postmonsoon and winter (Table 4.3), as a result of shallow atmospheric boundary layer and weaker surface winds which trap the particles in a confined volume near the Earth's surface as compared to premonsoon and monsoon, and the BC aerosol from biomass burning increases. During premonsoon, BC mass decreases owing to

shift in the wind direction and hence the source region (arid to marine) (*Rajesh and Ramachandran*, 2017). BC mass decreases to minimum during monsoon (Table 4.3) as a result of the precipitation which removes the aerosols from the atmosphere. The mean and median agree within 5% during winter and post-monsoon when observed BC mass is high, whereas they (mean and median) differ by 10% during premonsoon and monsoon when observed BC mass is relatively low. The annual mean black carbon mass concentration is found to be $5.4 \pm 3.6\ \mu g\ m^{-3}$ over Ahmedabad.

BC(M), *BC(A)*, *BC(E)*, and *BC(N)* also exhibit similar monthly variation as BC mass concentration. Highest *BC(M)* ($9.7\ \mu g\ m^{-3}$) and *BC(A)* ($3.9\ \mu g\ m^{-3}$) mass concentrations are found during winter, whereas *BC(E)* ($10.6\ \mu g\ m^{-3}$) and *BC(N)* ($11.0\ \mu g\ m^{-3}$) are found highest during postmonsoon. During monsoon, *BC(M)*, *BC(A)*, *BC(E)*, and *BC(N)* are found to be minimum as a result of precipitation which removes BC aerosol from the atmosphere. The highest percentage contribution of *BC(M)*, *BC(A)*, *BC(E)*, and *BC(N)* are found during winter, monsoon, monsoon, and postmonsoon respectively (Table 4.2). *BC(Day)* and *BC(Night)* exhibit similar monthly and seasonal variation as BC mass concentration. The maximum *BC(Day)* and *BC(Night)* are observed during December due o shallow atmospheric boundary layer and in addition; the winds are from north-northeast regions which brings anthropogenically produced black carbon to the measurement location. The highest percentage contribution of *BC(Day)* in total BC mass concentration is during Monsoon, while *BC(Night)* shows maximum during postmonsoon (Table 4.2). During postmonsoon and winter, *BC(Day)* contributions are low because the variations in surface wind speed and ABL height are least significant. The contribution of *BC(Night)* dominates throughout the season. The annual mean *BC(Night)* is about 1.5, 1.7, 1.2 and 1.7 times larger than *BC(Day)* during winter, premonsoon, monsoon and postmonsoon respectively.

Black carbon mass concentrations over Ahmedabad are higher than Trivandrum (coastal urban (*Moorthy et al.*, 2007)), Hyderabad (tropical urban

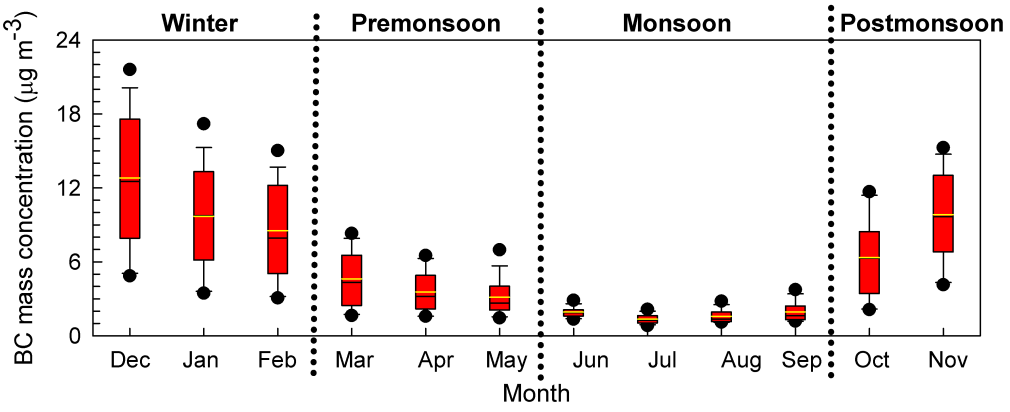

Figure 4.6: *Box and Whisker plots of black carbon (BC) mass ($\mu g\ m^{-3}$) during 2015-2016 over Ahmedabad as function of season (winter, premonsoon, monsoon, and postmonsoon). The range of the box represent the limits of the 25^{th} and 75^{th} percentile data. The whiskers spreading from the box illustrate the limits of the 10^{th} and the 90^{th} percentile data. Yellow lines show the average of the data. The maximum and minimum and maximum in each box are represented by dots.*

Table 4.2: *Variations (seasonal) in the contribution (%) of BC(Day) and BC(Night) in total BC at Ahmedabad during 2015-2016.*

Contribution (%)	Winter	Premonsoon	Monsoon	Postmonsoon
BC(Day)	40	37	46	36
BC(Night)	60	63	54	64
BC(M)	29	26	26	27
BC(A)	12	13	18	11
BC(E)	31	32	33	30
BC(N)	28	29	23	32

(*Dumka et al.*, 2013)), Pune (tropical urban (*Safai et al.*, 2013)), and Dhanbad (urban coal capital of India (*Singh et al.*, 2015)), and lower than metropolitan cities (Delhi (*Tiwari et al.*, 2013), Chennai (*Aruna et al.*, 2013)), urban Indo Gangetic Plain regions (Kanpur (*Nair et al.*, 2007), Varanasi (*Singh et al.*, 2015)) (Table 4.3). For the various urban sites (Ahmedabad, Trivandrum, Hyderabad, Pune, Dhanbad, Delhi, Chennai, Kanpur, and Varanasi) the maximum BC mass concentrations are observed during winter (Table 4.3).

Table 4.3: *Seasonal variation of BC mass concentration ($\mu g\ m^{-3}$) measured at various urban locations in India*

Location (Latitude, Longitude)	BC mass concentrations ($\mu g\ m^{-3}$) Winter	Premonsoon	Monsoon	Postmonsoon
Ahmedabad (23.03^{o}N, 72.55^{o}E)	10.3 ± 3.6	3.8 ± 1.2	1.7 ± 0.6	8.1 ± 2.9
Chennai (12.81^{o}N, 80.03^{o}E)	11.2	5.5	5.4	2.1
Delhi (28.35^{o}N, 77.12^{o}E)	12.0 ± 5.4	4.7 ± 1.6	2.8 ± 0.2	9.1 ± 3.7
Dhanbad (23.47^{o}N, 86.30^{o}E)	8.2 ± 2.8	5.5 ± 1.9	4.6 ± 1.7	6.4 ± 2.6
Hyderabad (17.50^{o}N, 78.60^{o}E)	6.7 ± 1.2	4.9 ± 1.0	3.0 ± 0.6	3.6 ± 0.8
Kanpur (26.40^{o}N, 80.30^{o}E)	9.8 ± 2.7	4.3 ± 1.8	-	-
Pune (18.53^{o}N, 73.80^{o}E)	6.3 ± 1.7	2.7 ± 1.1	1.3 ± 0.4	4.9 ± 1.5
Trivandrum (08.55^{o}N, 76.90^{o}E)	5.7	2.6	2.0	3.5
Varanasi (25.20^{o}N, 83.00^{o}E)	18.4 ± 7.6	5.8 ± 2.4	6.3 ± 2.2	18.1 ± 9.2

4.1.4 Source apportionment of black carbon aerosols

Diurnal variations

The diurnal variation of equivalent BC mass concentration of fossil fuel (BC_{FF}) and wood burning (BC_{WB}) persistently shows two maxima and two minima (Figure 4.7). BC_{FF} is maximum during day, which reveals the consistent anthropogenic activity at the study location (*Rajesh and Ramachandran*, 2017). The higher contribution of BC_{FF} in BC mass is found during early morning and nighttime due to surface inversion which holds the pollutants. The contributions of BC_{WB} to total BC mass increases during morning and evening hrs due to an increase in biomass (wood) emissions. During daytime contributions of BC_{FF} and BC_{WB} in total BC are governed by the diurnal evolution of

atmospheric boundary layer. The BC_{FF} contribution was found to be higher by a factor of 2-6 than BC_{WB}, and BC_{FF} contributes maximum to BC mass over Ahmedabad.

The differences in the contributions (%) of BC_{WB} and BC_{FF} to the BC mass exist as a result of the emissions from wood burning and fossil fuel combustion respectively (Figure 4.8). The contribution (%) of BC_{FF} mass dominates around the year over Ahmedabad. During winter, premonsoon, and postmonsoon the diurnal contribution (%) of BC_{FF} is minimum at around noontime owing to ABL evolution. After sunrise the contribution (%) of BC_{WB} increases owing to an increase in emissions from industrial and household activities, and is maximum during afternoon (Figure 4.8). During monsoon, the contribution (%) of BC_{FF} is found to be maximum due to significant decrease in the usage of biomass (wood) burning. Hence, emissions from fossil fuel contribute a larger part of BC mass during monsoon.

$BC(M)_{FF}$, $BC(A)_{FF}$, $BC(E)_{FF}$, $BC(N)_{FF}$, $BC(M)_{WB}$, $BC(A)_{WB}$, $BC(E)_{WB}$ and $BC(N)_{WB}$ mass concentration show large variations during the morning (05:00 to 10:55 hrs), afternoon (11:00 to 15:55 hrs), evening (16:00 to 20:55 hrs) and night (21:00 to 04:55 hrs) period (Figures 4.9a-b). During afternoon, the BC_{FF} and BC_{WB} mass concentrations are minimum (Figures 4.9a-b). During morning, BC_{WB} is maximum owing to significant household activity. The contribution of BC_{FF} in total BC mass is found maximum during nighttime. During monsoon, the contribution of BC_{FF} is maximum around afternoon probably as a result of the larger influence of emissions from fossil fuel combustion than biomass (wood) burning which is minimal because of wet conditions. During monsoon, the BC aerosols are removed from the atmosphere by precipitation, however, BC emissions in the atmosphere occur continuously due to predominant use of fossil fuel over an urban region, as observed (Figures 4.9 a-b). The annual mean percentage contribution of $BC(E)_{FF}$ is maximum and $BC(A)_{FF}$ exhibit a minimum during the study period. The contribution of $BC(E)_{FF}$ dominates throughout the season (Figure 4.9c). The contribution

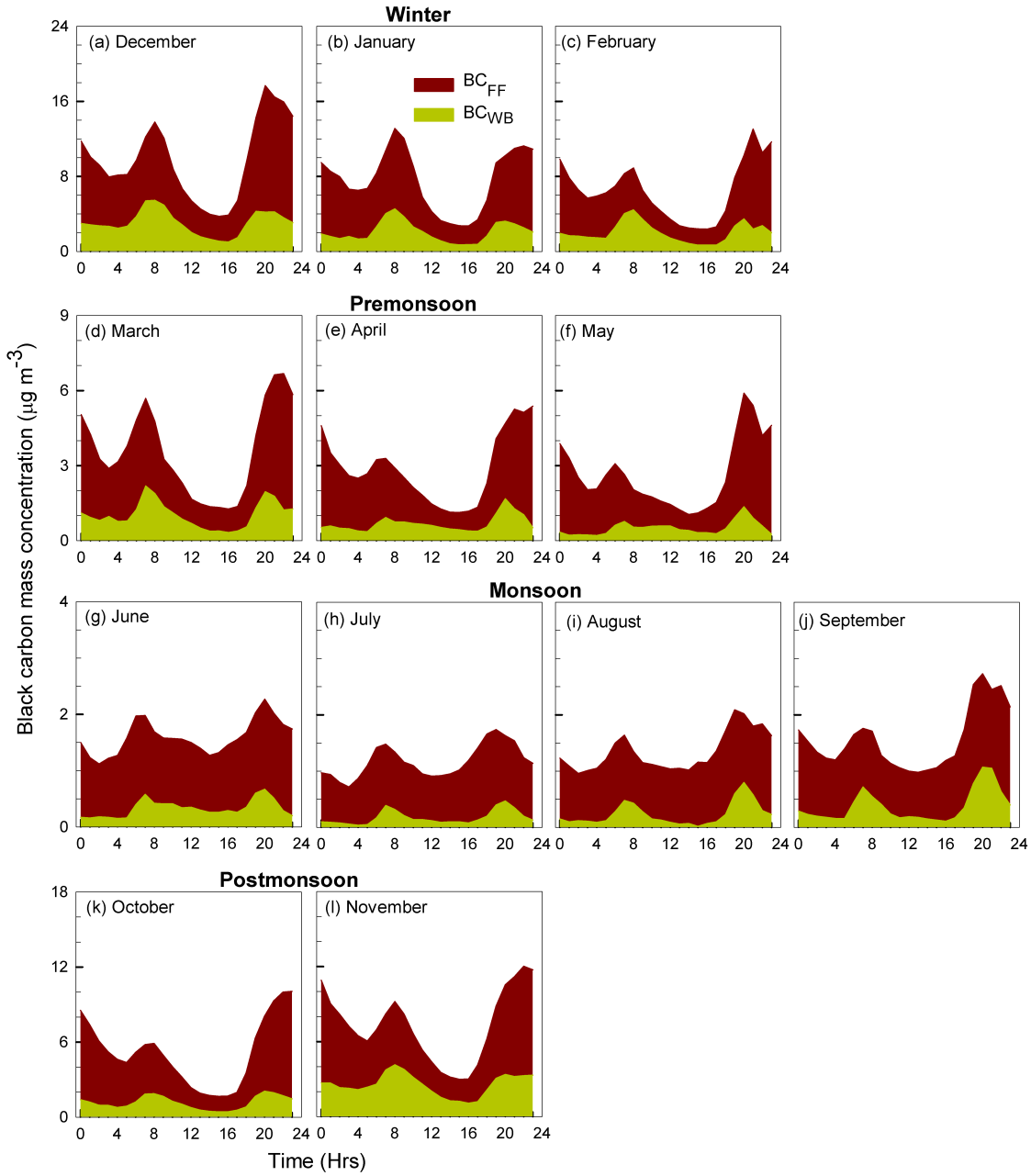

Figure 4.7: *Monthly diurnal variation of BC_{FF} ($\mu g\ m^{-3}$) and BC_{WB} ($\mu g\ m^{-3}$) in black carbon (BC) mass during winter (Dec (a), Jan (b), and Feb (c)), premonsoon (Mar (d), Apr (e), and May (f)), monsoon (Jun (g), Jul (h), Aug (i), and Sep (j)), and postmonsoon (Oct (k), and Nov (l)) over Ahmedabad for 2015 and 2016.*

of $BC(A)_{WB}$ in total BC mass concentration is found minimum throughout the

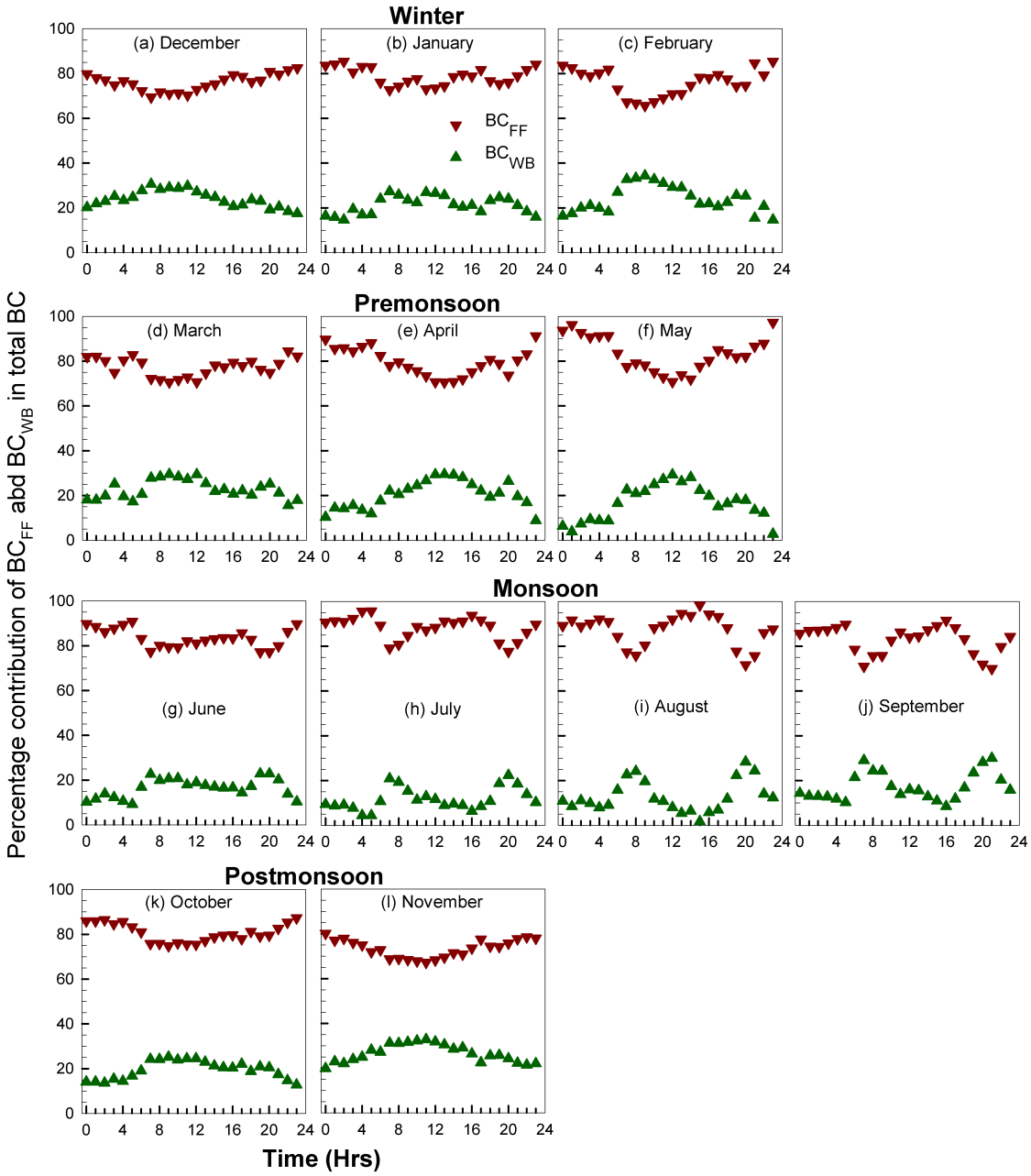

Figure 4.8: *Monthly diurnal variation of percentage contributions of BC_{FF} and BC_{WB} in black carbon (BC) mass during winter (Dec (a), Jan (b), and Feb (c)), premonsoon (Mar (d), Apr (e), and May (f)), monsoon (Jun (g), Jul (h), Aug (i), and Sep (j)), and postmonsoon (Oct (k), and Nov (l)) over Ahmedabad for 2015 and 2016.*

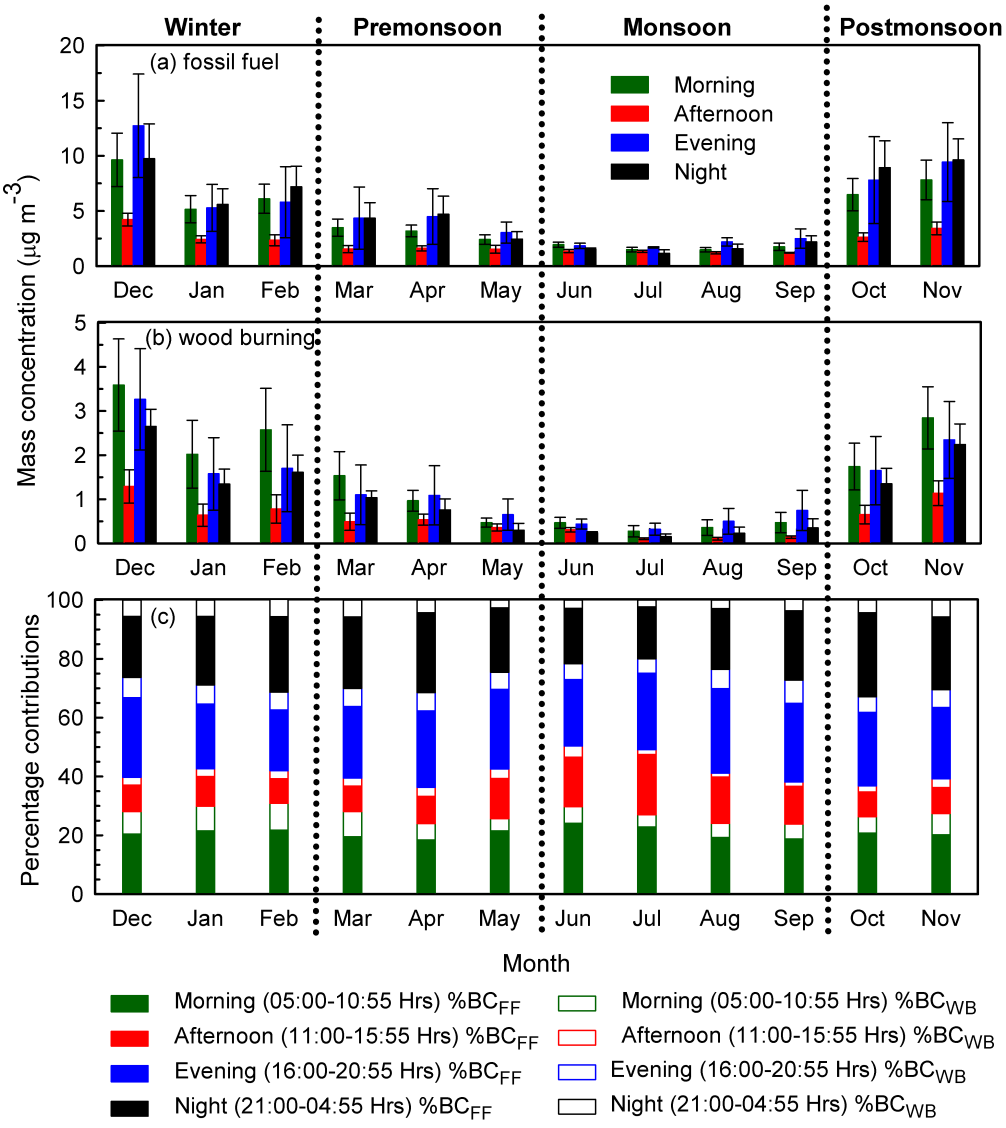

Figure 4.9: *Monthly variations in (a) equivalent BC concentrations from fossil fuel (BC_{FF}, $\mu g\ m^{-3}$) (b) wood burning (BC_{WB}, $\mu g\ m^{-3}$), (c) percentage contributions of BC_{FF} and BC_{WB} in BC mass during morning (05:00 to 10:55 hrs), afternoon (11:00 to 15:55 hrs), evening (16:00 to 20:55 hrs), and night (21:00 to 04:55 hrs) period over Ahmedabad as function of season (winter, premonsoon, monsoon, and postmonsoon). Vertical bars indicate $\pm 1\sigma$ variation with respect to mean.*

year (Table 4.4) due to the decrease in the anthropogenic emissions during afternoon and fully evolved atmospheric boundary layer.

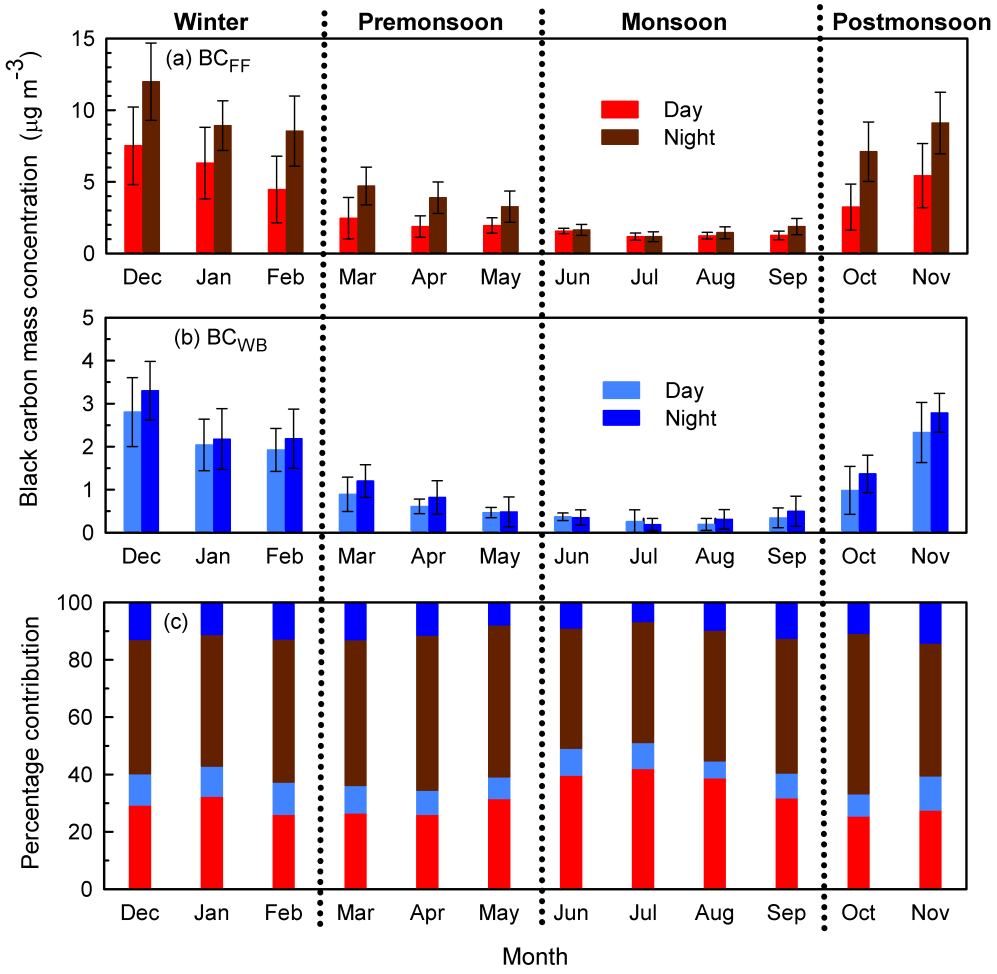

Figure 4.10: *Monthly variations in (a) fossil fuel BC concentration during day (BC(Day)$_{FF}$, $\mu g\ m^{-3}$) and nighttime (BC(Night)$_{FF}$, $\mu g\ m^{-3}$), (b) wood burning BC concentration during daytime (BC(Day)$_{WB}$, $\mu g\ m^{-3}$) and nighttime (BC(Night)$_{WB}$, $\mu g\ m^{-3}$), and (c) day (BC(Day))and nighttime (BC(Night)) contributions (%) in total BC mass during 2015-2016 over Ahmedabad. Vertical bars indicate $\pm 1\sigma$ variation with respect to mean.*

During December, *BC(Day)$_{FF}$*, *BC(Day)$_{WB}$*, *BC(Night)$_{FF}$*, and *BC(Night)$_{WB}$* are found maximum, while the minimum are observed during July (Figure 4.10) (*Rajesh and Ramachandran*, 2017). The percentage contribution of *BC(Night)$_{FF}$* and *BC(Night)$_{WB}$* dominates throughout the year when compared to *BC(Day)$_{FF}$* and *BC(Day)$_{WB}$* respectively, confirming the significant influence of nighttime black carbon mass concentration from biomass (wood)

and fossil fuel emissions over Ahmedabad. BC_{FF} and BC_{WB} mass concentration show significant seasonal variations during daytime and nighttime (Figures 4.10a-b).

Weekly variations

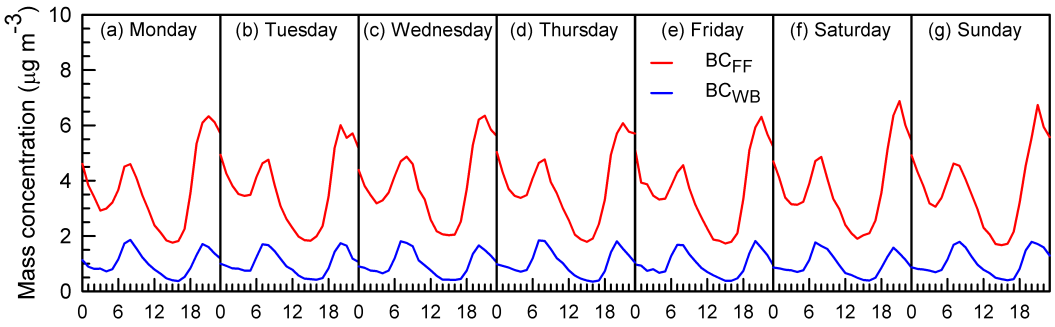

Figure 4.11: *Weekly diurnal variation of equivalent BC concentrations from fossil fuel (BC_{FF}, $\mu g\ m^{-3}$), and wood burning (BC_{WB}, $\mu g\ m^{-3}$) in black carbon (BC) mass as a function of weekdays (Monday - Friday) and weekends (Saturday - Sunday) during 2015-2016 over Ahmedabad.*

The equivalent BC concentrations from fossil fuel (BC_{FF}) and wood burning (BC_{WB}) during weekday (Monday - Friday) and weekend (Saturday - Sunday) are found to be similar (Figure 4.11) over Ahmedabad during 2015-2016. The weekly diurnal variation in BC_{FF} exhibits a pronounced evening BC_{FF} peak (Figure 4.11) due to the dominant vehicular emissions, whereas, BC_{WB} shows similar morning and evening BC_{WB} peak throughout the week (Figure 4.11) due to the consistent biomass burning from household and industry activities. The observed weekly variation in BC_{FF} and BC_{WB} may be a typical BC characteristic feature of an urban region (Ahmedabad) where there are no significant differences in BC emissions between weekdays and weekends.

Monthly and seasonal variations

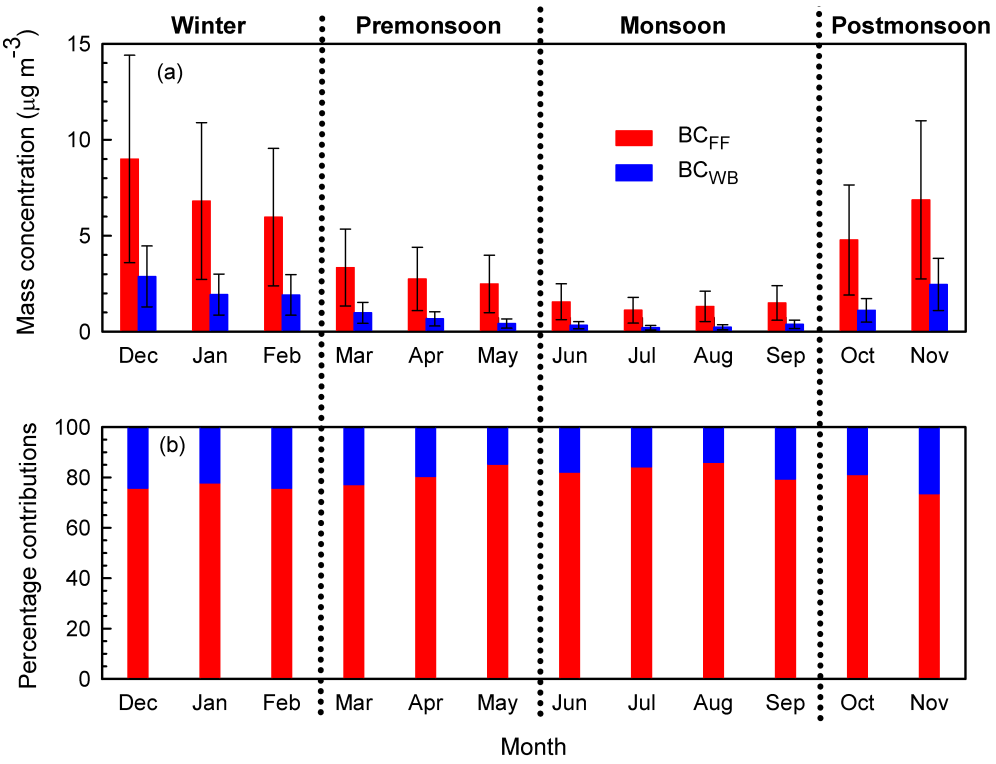

Figure 4.12: *Monthly mean (a) equivalent black carbon (BC) concentrations from fossil fuel (BC_{FF}, $\mu g\ m^{-3}$) and wood burning (BC_{WB}, $\mu g\ m^{-3}$), and (b) percentage contributions of BC_{FF} and BC_{WB} in BC over Ahmedabad during January 2015 to December 2016 as function of season (winter, premonsoon, monsoon, and postmonsoon). Vertical bars indicate $\pm 1\sigma$ variation with respect to mean.*

A complimentary variation is found in the monthly contributions of BC_{FF} and BC_{WB} as a result of the influence of different types of emission sources over Ahmedabad (Figure 4.12a). The contributions of BC_{FF} in BC mass dominates around the year and is found maximum and minimum during August and November respectively, whereas the BC_{WB} contributes maximum and minimum during November and August respectively (Figure 4.12b). BC_{FF} and BC_{WB} exhibit a significant seasonal variation over urban location (Ahmedabad). During monsoon, the highest contribution of BC_{FF} to the total BC mass is seen as the emission from fossil fuel combustion contributes significantly to the total BC emission. The contribution of BC_{WB} is observed highest during winter as a result of the significant increase in wood burning

over Ahmedabad.

Table 4.4: *Variations (seasonal) of the contribution (%) of BC_{FF}, BC_{WB}, BC(Day)$_{FF}$, BC(Day)$_{WB}$, BC(Night)$_{FF}$, BC(Night)$_{WB}$, BC(M)$_{FF}$, BC(M)$_{WB}$, BC(A)$_{FF}$, BC(A)$_{WB}$, BC(E)$_{FF}$, BC(E)$_{WB}$, BC(N)$_{FF}$ and BC(N)$_{WB}$ in BC mass over Ahmedabad during 2015 - 2016.*

Contribution (%)	Winter	Premonsoon	Monsoon	Postmonsoon
BC_{FF}	77	80	84	78
BC_{WB}	23	20	16	22
BC(Day)$_{FF}$	29	28	38	27
BC(Day)$_{WB}$	11	9	8	10
BC(Night)$_{FF}$	47	52	44	50
BC(Night)$_{WB}$	12	11	10	13
BC(M)$_{FF}$	21	20	21	20
BC(M)$_{WB}$	8	6	5	6
BC(A)$_{FF}$	9	11	16	9
BC(A)$_{WB}$	3	3	2	3
BC(E)$_{FF}$	23	26	26	25
BC(E)$_{WB}$	7	6	6	6
BC(N)$_{FF}$	23	24	20	27
BC(N)$_{WB}$	6	4	3	5

The larger part of the BC mass comes from fossil fuel combustion during monsoon as the usage of biomass (wood) for burning is minimal due to the wet condition (Table 4.4). The *BC(Day)* and *BC(Night)* exhibit significant seasonal variation over Ahmedabad (Table 4.4). BC_{FF} and BC_{WB} are maximum during monsoon and winter respectively over Ahmedabad (Table 4.4). The BC(Day)$_{FF}$ and BC(Day)$_{WB}$ peak during monsoon and winter respectively, whereas BC(Night)$_{FF}$ and BC(Night)$_{WB}$ are found maximum during premonsoon and postmonsoon respectively. Results reveal that BC_{FF} contributes the maximum to BC mass over Ahmedabad. Annual average BC_{FF} and BC_{WB} contribute to 80 and 20% respectively in total BC mass concentrations over Ahmedabad. The source apportionment investigation of black carbon aerosols brings out the temporal, monthly and seasonal equivalent contribution of BC mass concentration from fossil fuel (BC_{FF}) and wood burning (BC_{WB}) to total BC mass over an urban location (Ahmedabad).

4.2 BC aerosol characteristics over a high altitude remote location: Gurushikhar, Mt. Abu

The BC mass concentration measurements were conducted over a high altitude remote location, Gurushikhar, Mt. Abu using multiwavelength aethalometer AE33. Total of 536 days of BC mass concentrations data at a temporal resolution of 5 min were used over Gurushikhar during 2015-2016 (Table 3.1).

4.2.1 Diurnal variations

At the outset, BC mass concentrations observed at a remote high altitude location, Gurushikhar is significantly lower than an urban location, Ahmedabad. Secondly, no significant diurnal variation in BC mass concentration is observed over Gurushikhar (Figure 4.13) as compared to Ahmedabad similar to β_{abs} (Chapter 3). Diurnal variation of BC mass concentrations over the high altitude remote site, Gurushikhar does not exhibit any significant morning and nocturnal peaks like observed over Ahmedabad (Figure 4.1). However, atypical diurnal behavior in BC mass concentration has been observed throughout the year, with the increase in BC concentration during the noontime due to strong thermal convection during this time and rising up of pollutants to the observational location from the foothills. This effect is significant during strong thermal convection period, whereas during the weak thermal convection period the ABL height is less than the observational site altitude and the pollutants from the foothills could not reach the observational site. In addition, the longrange transport of pollutants always contribute during the strong and weak thermal convection period and the net resultant effect is observed in the diurnal variation of BC mass concentration (Figure 4.13). During winter, the BC values measured at Gurushikhar are factor of 8 lower than Ahmedabad BC (Figure 4.1), whereas during monsoon the values are lower by a factor of 3. During premonsoon and postmonsoon, the observed BC concentration at Gurushikhar was lower by a factor of 6 than Ahmedabad BC mass concentration. The BC values observed at Gurushikhar is mostly transported from nearby ur-

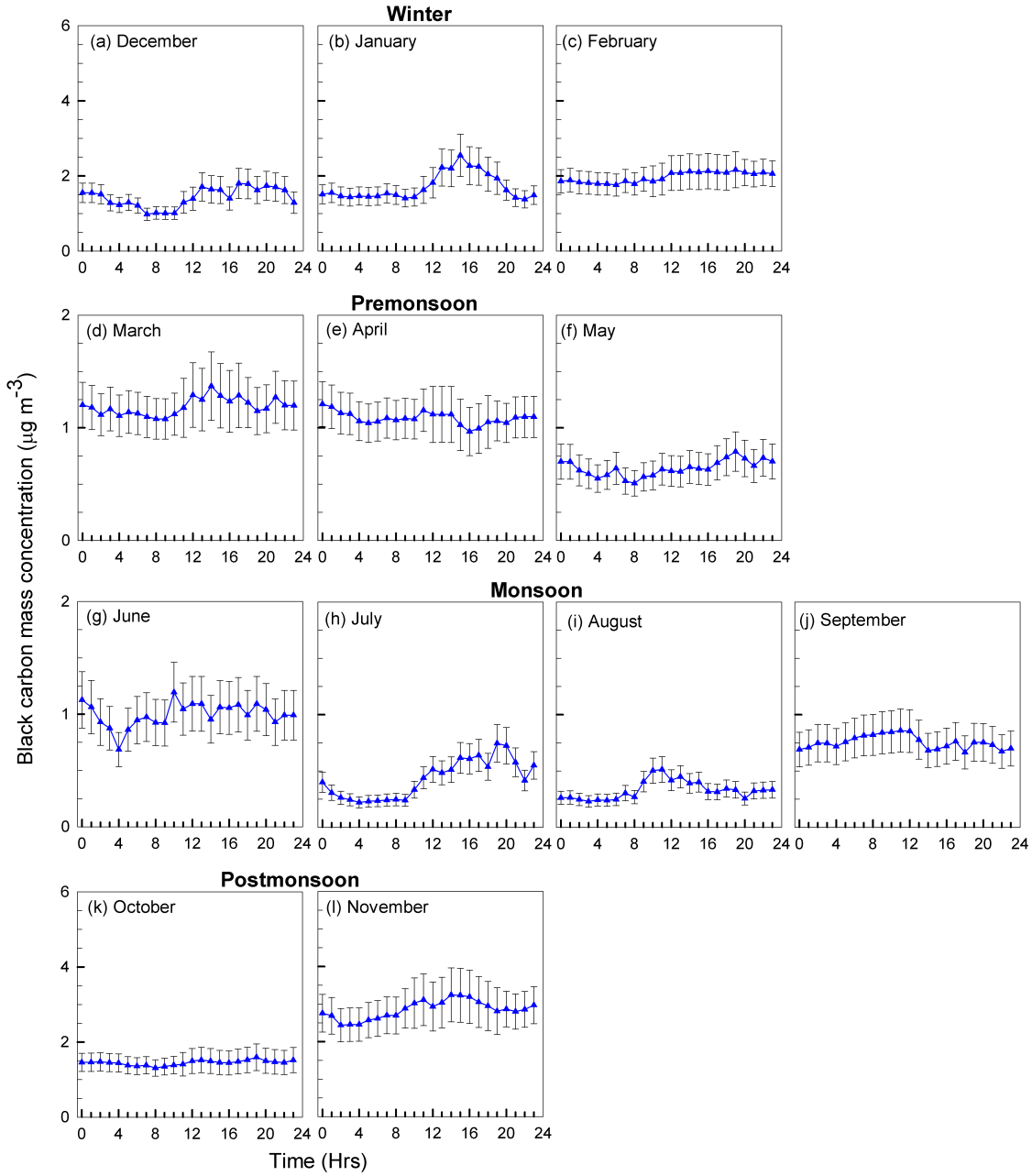

Figure 4.13: *Monthly diurnal variation of black carbon (BC) mass concentrations ($\mu g\ m^{-3}$) over Gurushikhar, Mt. Abu during winter (Dec (a), Jan (b), and Feb (c)), premonsoon (Mar (d), Apr (e), and May (f)), monsoon (Jun (g), Jul (h), Aug (i), and Sep (j)), and postmonsoon (Oct (k), and Nov (l)) for 2015 and 2016. Vertical bars indicate $\pm 1\sigma$ variation with respect to mean.*

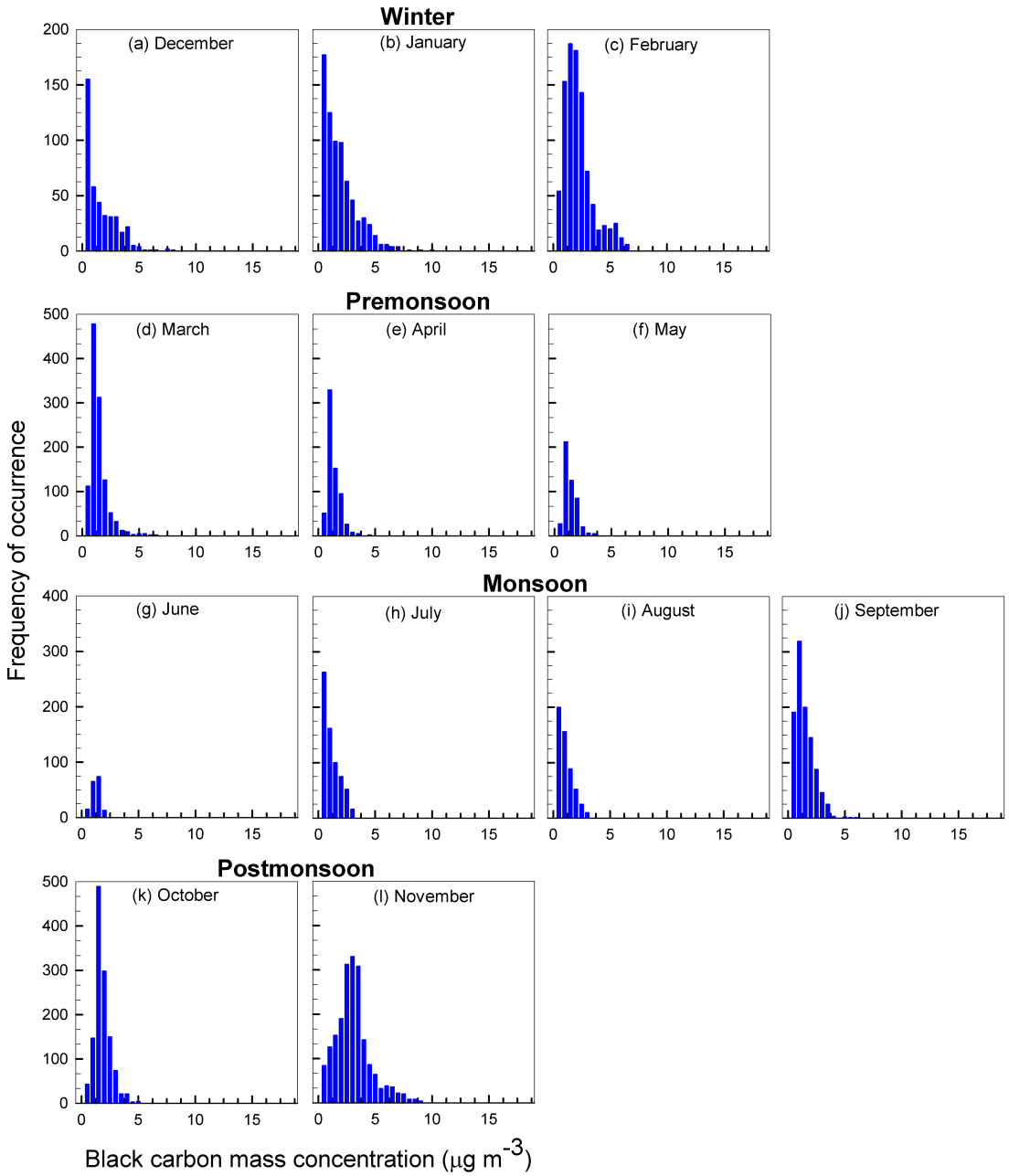

Figure 4.14: *Frequency distribution of black carbon (BC) mass concentrations ($\mu g\ m^{-3}$) over Gurushikhar, Mt. Abu during winter (Dec (a), Jan (b), and Feb (c)), premonsoon (Mar (d), Apr (e), and May (f)), monsoon (Jun (g), Jul (h), Aug (i), and Sep (j)), and postmonsoon (Oct (k), and Nov (l)) for 2015 and 2016.*

ban and industrial areas.

The BC mass concentration shows a right-skewed distribution over Gurushikhar (Figure 4.14). The observed mode is between 0.2-2 μg m^{-3} March to September, which shifts to 0.5-3 μg m^{-3} during October and winter. The higher mode is observed during November (Figure 4.14). The frequency distribution of BC mass is broader during winter (December, January, February) and postmonsoon (October, November) due to meteorological dynamics, the significant influence of longrange transport and increase in biomass burning which holds the pollutants near Earth's surface. During monsoon the peak in frequency occurs at low BC mass concentrations because of wet removal and transition in wind directions. During winter and postmonsoon the frequency peaks at high BC values (Figure 4.14). The median and mean agree within 3% throughout the year except during January when it differs by $\sim$ 12%. As no significant and consistent diurnal variations are observed over Gurushikhar, the quantification of the temporal characteristics of BC mass concentration during distinct time periods (morning, afternoon, evening, and night) did not result in distinctly varying numbers.

Table 4.5: *Mean sunrise and sunset time (hrs) for each month at Gurushikhar, Mt. Abu during January 2015 - December 2016.*

Month	Sunrise (hrs)	Sunset (hrs)
Jan	7.42	18.18
Feb	7.22	18.55
Mar	6.80	18.78
Apr	6.28	19.02
May	5.92	19.25
Jun	5.83	19.48
Jul	5.98	19.50
Aug	6.22	19.22
Sep	6.42	18.72
Oct	6.60	18.20
Nov	6.90	17.87
Dec	7.25	17.88

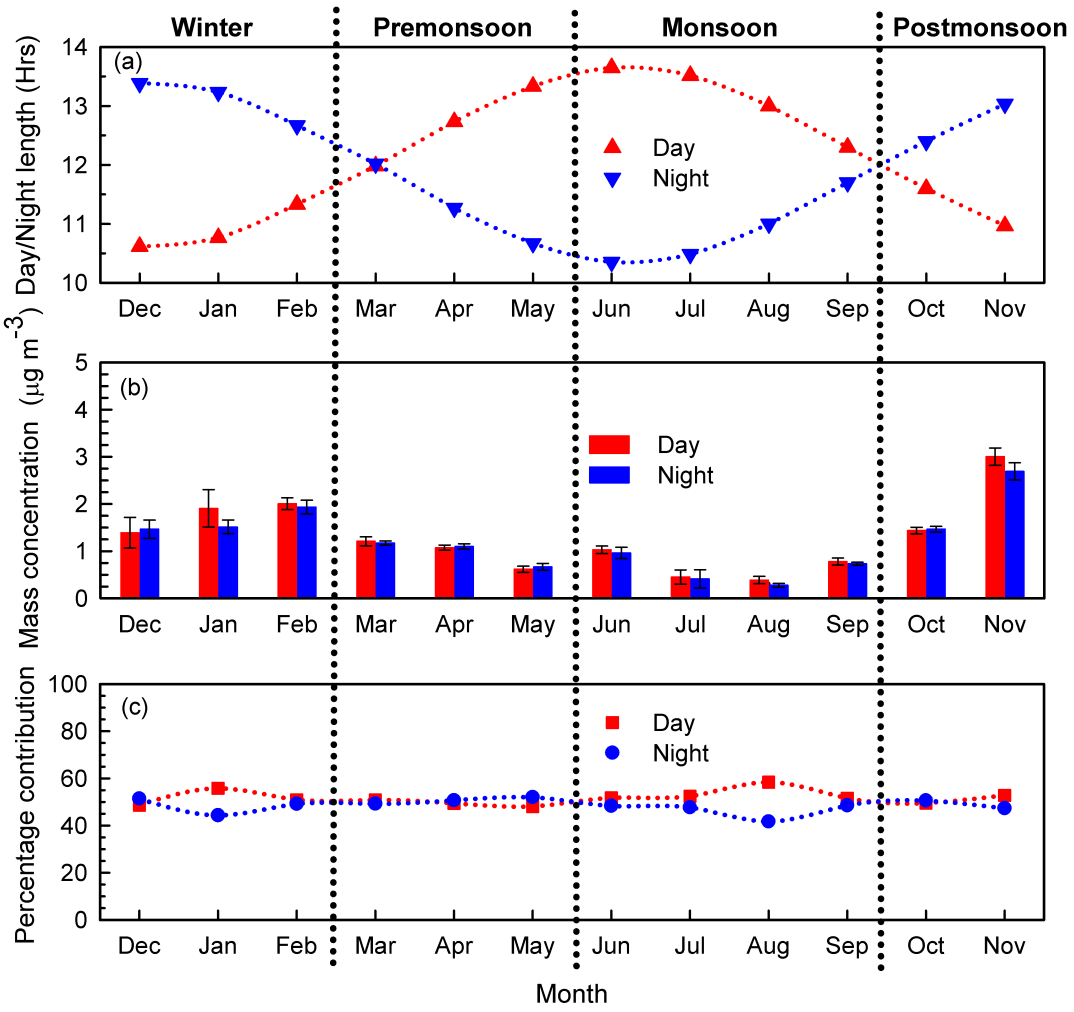

Figure 4.15: *Monthly variations in (a) length of the day and night (hrs), (b) BC mass concentrations ($\mu g\ m^{-3}$) during day BC(Day) and nighttime BC(Night), and (c) contributions (%) of day and nighttime BC mass concentration over Gurushikhar during 2015-2016 as function of season (winter, premonsoon, monsoon, and postmonsoon). Vertical bars indicate $\pm 1\sigma$ variation with respect to mean.*

Day and nighttime variations in BC mass concentrations over a high altitude remote location are governed by the meteorological dynamics, temporal variation in emission sources and longrange transport. The days are the longest during summer monsoon solstice and the day is shorter during the winter solstice (Table 4.5). At Gurushikhar, BC_{Day} and BC_{Night} contributions are more or less equal throughout the year (Figure 4.15), suggesting

that this could be the characteristics feature over a background region of an aerosol component produced by anthropogenic sources. In contrast, over Ahmedabad, BC_{Night} is higher than BC_{Day} (Figure 4.4). In January and August BC_{Day} is >55% in Gurushikhar; in January and August daytime BC are higher than nighttime BC, and the gradient between BC_{Night} and BC_{Day} is relatively steeper when compared to the other months of the year (Figure 4.15). During the other months of the year, the day-night BC values are more or less the same (Figure 4.15) over Gurushikhar. The annual average contribution (%) of *BC(Day)* and *BC(Night)* is 52 and 48% respectively.

4.2.2 Monthly and Seasonal variations

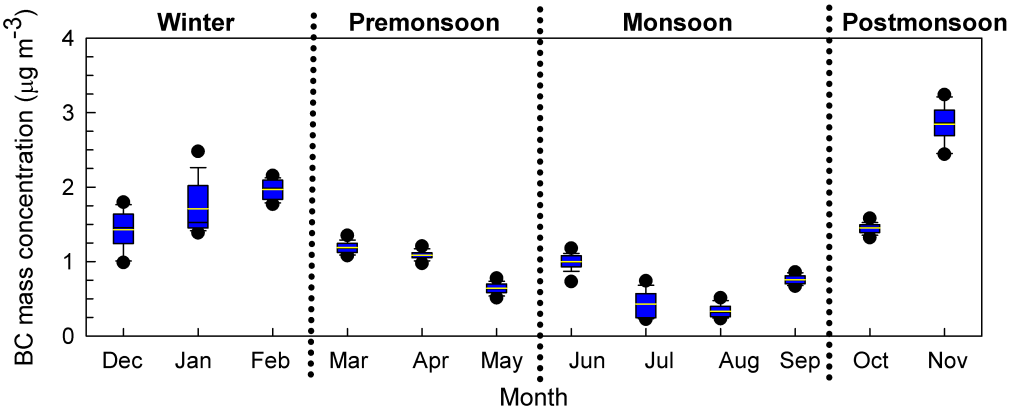

Figure 4.16: *Box and Whisker plots of black carbon (BC) mass concentrations ($\mu g\ m^{-3}$) over Gurushikhar, Mt. Abu during 2015 - 2016 as function of season (winter, premonsoon, monsoon, and postmonsoon). The range of the box represent the limits of the 25^{th} and 75^{th} percentile data. The whiskers spreading from the box illustrate the limits of the 10^{th} and the 90^{th} percentile data. Yellow lines show the average of the data. The maximum and minimum and maximum in each box are represented by dots.*

Over Gurushikhar, the monthly mean BC mass concentration is found to decrease from February to May and then it increases from August to November (Figure 4.16). The maximum BC mass concentration is observed during November (Figure 4.16) as in addition to the anthropogenic emission from the nearby region, it is strongly influenced by the longrange transport (77%)

from the northern part of India (Figure 2.11). The minimum BC mass concentration is observed during August due to the removal of aerosols by precipitation (Figure 4.16). *BC(Day)* and *BC(Night)* contributions are more or less same throughout the season. The maximum The percentage contribution of *BC(Day)* is observed maximum during monsoon (Table 4.6), while the contribution of *BC(Night)* is found maximum during winter (Table 4.6) because the lengths of the day and night are maximum during respective season (Table 4.6). *BC(Day)* and *BC(Night)* contributions are comparable over Gurushikhar. BC mass concentration shows a strong seasonal variation over Gurushikhar. BC mass is highest during postmonsoon followed by winter (Table 4.7), as the location is affected by convection from the foothills and significantly influenced by the advection process through the longrange transport mechanism (Figure 2.11). In addition, during postmonsoon and winter there is an increase in biomass burning, and tourist activities in the region. During premonsoon, BC mass decreases owing to a shift in the wind direction (Table 4.7). The minimum BC (Table 4.7) is observed during monsoon due to the wet removal. The annual mean BC mass concentration is found to be 1.5 ± 0.8 μg m^{-3} over Gurushikhar.

Table 4.6: *Variations (seasonal) in the contribution (%) of BC(Day) and BC(Night) in total BC mass over Gurushikhar, Mt. Abu during 2015-2016.*

Contribution (%)	Winter	Premonsoon	Monsoon	Postmonsoon
BC(Day)	52	50	53	52
BC(Night)	48	50	47	48

BC mass exhibits similar seasonal variation pattern at other high altitude locations in India with differences in their magnitude (Table 4.7). The measured BC values over Gurushikhar are found to be higher than Hanle (Western Himalaya (*Babu et al.*, 2011)), Ooty (Nilgiris mountain range in southern India (*Udayasoorian et al.*, 2014)), Nainital (central Himalayas (*Dumka et al.*, 2010)), Manora Peak (Himalayan foothills (*Srivastava et al.*, 2012)) and Mukteshwar (Himalayan mountain terrain (*Panwar et al.*, 2013)), and lower than Sinhagad (South west India (*Raju et al.*, 2011)), Darjeeling (Eastern Himalaya

Table 4.7: *Seasonal (Winter, Premonsoon, Monsoon, and Postmonsoon) variation of BC mass concentration ($\mu g\ m^{-3}$) measured at various high altitude locations in India.*

Location, Altitude (Latitude, Longitude)	BC mass concentrations ($\mu g\ m^{-3}$) Winter	Premonsoon	Monsoon	Postmonsoon
Sinhagad, 1450 m (18.50^{o}N, 73.50^{o}E)	2.2	0.9	-	-
Gurushikhar, 1680 m (24.64^{o}N, 72.68^{o}E)	2.1 ± 1.0	1.0 ± 0.3	0.7 ± 0.2	2.3 ± 1.1
Nainital, 1958 m (29.40^{o}N, 79.50^{o}E)	1.1	1.3	0.5	1.0
Manora Peak, 2000 m (29.4^{o}N, 79.5^{o}E)	1.02 ± 0.81	1.55 ± 0.63	-	-
Mukteshwar, 2180 m (29.78^{o}N, 80.5^{o}E)	0.8 ± 0.4	1.2 ± 0.3	0.5 ± 0.2	1.0 ± 0.2
Darjeeling, 2200 m (27.02^{o}N, 88.25^{o}E)	3.9 ± 2.2	5.0 ± 1.1	1.7 ± 0.7	2.9 ± 1.0
Ooty, 2520 m (11.23^{o}N, 76.43^{o}E)	0.8	1.0	0.2	0.4
Hanle, 4520 m (32.78^{o}N, 78.95^{o}E)	0.07	0.11	0.06	0.07

(*Sarkar et al.*, 2015))(Table 4.8). Most of the high altitude sites (Gurushikhar, Hanle, Nainital, Ooty, Darjeeling, Manora Peak and Mukteshwar) exhibit the maximum BC mass concentration during premonsoon except over Sinhagad where the maximum is observed during winter season (Table 4.8). BC mass concentration observed over Darjeeling in Eastern Himalaya is higher than the other high altitude sites (Table 4.7) due to high population density, high anthropogenic emissions from tourist activities, orography and land use pattern which inhibits the dispersion of aerosols (*Sarkar et al.*, 2015). Typically, the observed variation of BC mass concentration in the high altitude remote site may be due to the prevailing local sources, meteorology and the longrange transport of pollutants over the observational location.

The maximum and minimum in aerosol concentration are predomi-

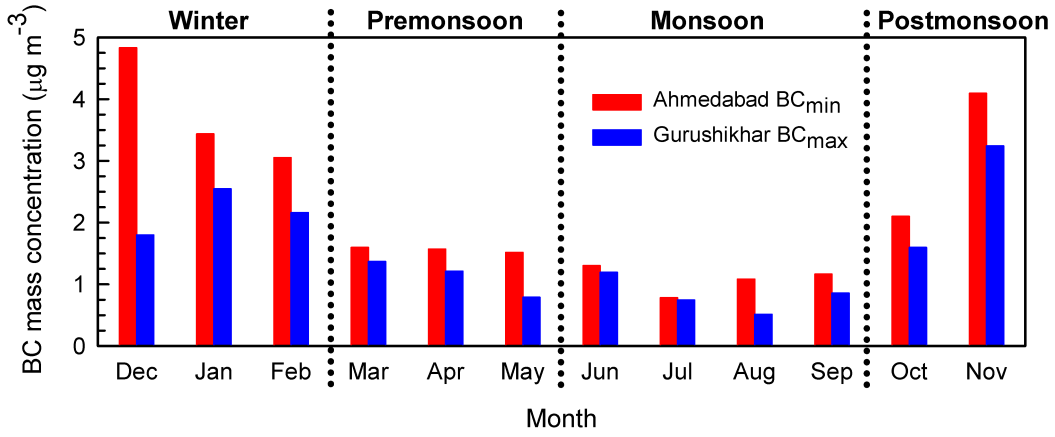

Figure 4.17: *Monthly variations in measured BC_{min} ($\mu g\ m^{-3}$) in Ahmedabad and BC_{max} ($\mu g\ m^{-3}$) in Gurushikhar during 2015 - 2016 as function of season (winter, premonsoon, monsoon, and postmonsoon).*

nantly controlled by aerosol emissions, and evolution of ABL which transports aerosol upwards and/or to nearby locations. Long range transport could be a vital factor that influences aerosol mass concentrations during favorable temporal conditions. It is quite interesting to note that BC_{max} mass concentrations in Gurushikhar are comparable with BC_{min} mass concentrations in Ahmedabad (Figure 4.17). BC_{max} in Gurushikhar and BC_{min} in Ahmedabad occur during the same time frame of the day. BC is maximum in Gurushikhar when the ABL is fully evolved which aids the upward transport of anthropogenic emissions from the surrounding foothill regions, while the BC mass is minimum in Ahmedabad when the ABL is fully evolved and the anthropogenic emission sources are at their minimum. This result highlights the variation in the diurnal evolution of an atmospheric species emitted by anthropogenic activities over an urban source (Ahmedabad) and a background (Gurushikhar, Mt. Abu) region, and the differences in the magnitudes of mass concentration due to the evolution of atmospheric boundary layer.

4.2.3 Source apportionment of black carbon aerosols

Diurnal variations

The BC_{FF} and BC_{WB} exhibit an atypical diurnal variation throughout the year over Gurushikhar (Figure 4.18). BC_{FF} is found to contribute maximum to the BC mass around the day, which suggests consistent BC aerosols over Gurushikhar due to the dominant aerosol transport mechanism (convection and advection). BC_{FF} and BC_{WB} do not exhibit any consistent diurnal variability as observed in Ahmedabad (Figure 4.7). The higher contribution of BC_{FF} in BC is observed during 12-18 hrs due to the fully evolved ABL when the observation location lies within the atmospheric boundary layer (Figure 4.19). The contribution of BC_{WB} in BC was higher during the April and November as the black carbon aerosols are transported from the residue crop burning areas of Punjab and Haryana (Figures 2.11 and 2.12). HYSPLIT model computed monthly mean 7 day back trajectory using cluster analysis at 500 m reveals the sources of these aerosols, their origin, pathways and percentage contributions over Gurushikhar (Figure 2.11). The daytime and nighttime BC_{FF} and BC_{WB} mass concentration show significant seasonal variations (Figure 4.20). BC_{FF} and BC_{WB} are found maximum during monsoon and pre-monsoon respectively (Table 4.8). The maximum and minimum $BC(Day)_{FF}$, $BC(Day)_{WB}$, $BC(Night)_{FF}$ and $BC(Night)_{WB}$ mass concentrations are observed during November and August respectively (Figure 4.20). $BC(Day)_{FF}$ dominates throughout the year and is highest during monsoon (Table 4.8). $BC(Day)_{FF}$ and $BC(Night)_{FF}$ contributions are comparable (Table 4.8). $BC(Day)_{FF}$ contributes 60% or more to the BC mass over Gurushikhar (Table 4.8). The annual average contributions (%) of day (*BC(Day)*) and nighttime (*BC(Night)*) BC mass concentrations are 52 and 48% respectively over Gurushikhar while they are 60 and 40% over Ahmedabad.

BC_{FF} and BC_{WB} exhibit similar monthly variation as BC mass concentration (Figure 4.21a). The maximum BC_{FF} and BC_{WB} (Figure 4.21) are ob-

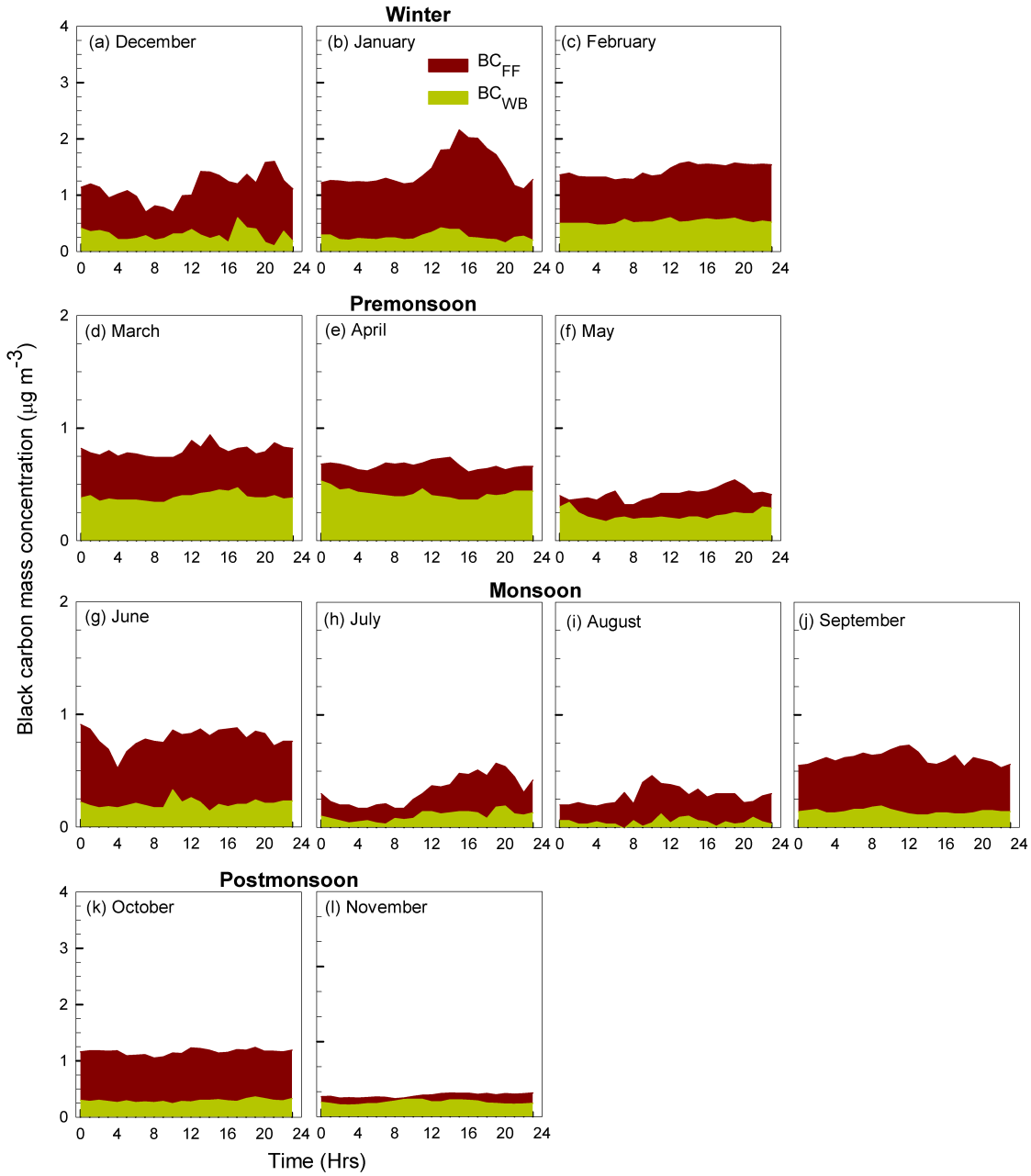

Figure 4.18: *Monthly diurnal variation of BC_{FF} ($\mu g\, m^{-3}$) and BC_{WB} ($\mu g\, m^{-3}$) in total black carbon (BC) mass concentrations over Gurushikhar, Mt. Abu during winter (Dec (a), Jan (b), and Feb (c)), premonsoon (Mar (d), Apr (e), and May (f)), monsoon (Jun (g), Jul (h), Aug (i), and Sep (j)), and postmonsoon (Oct (k), and Nov (l)) for 2015 and 2016.*

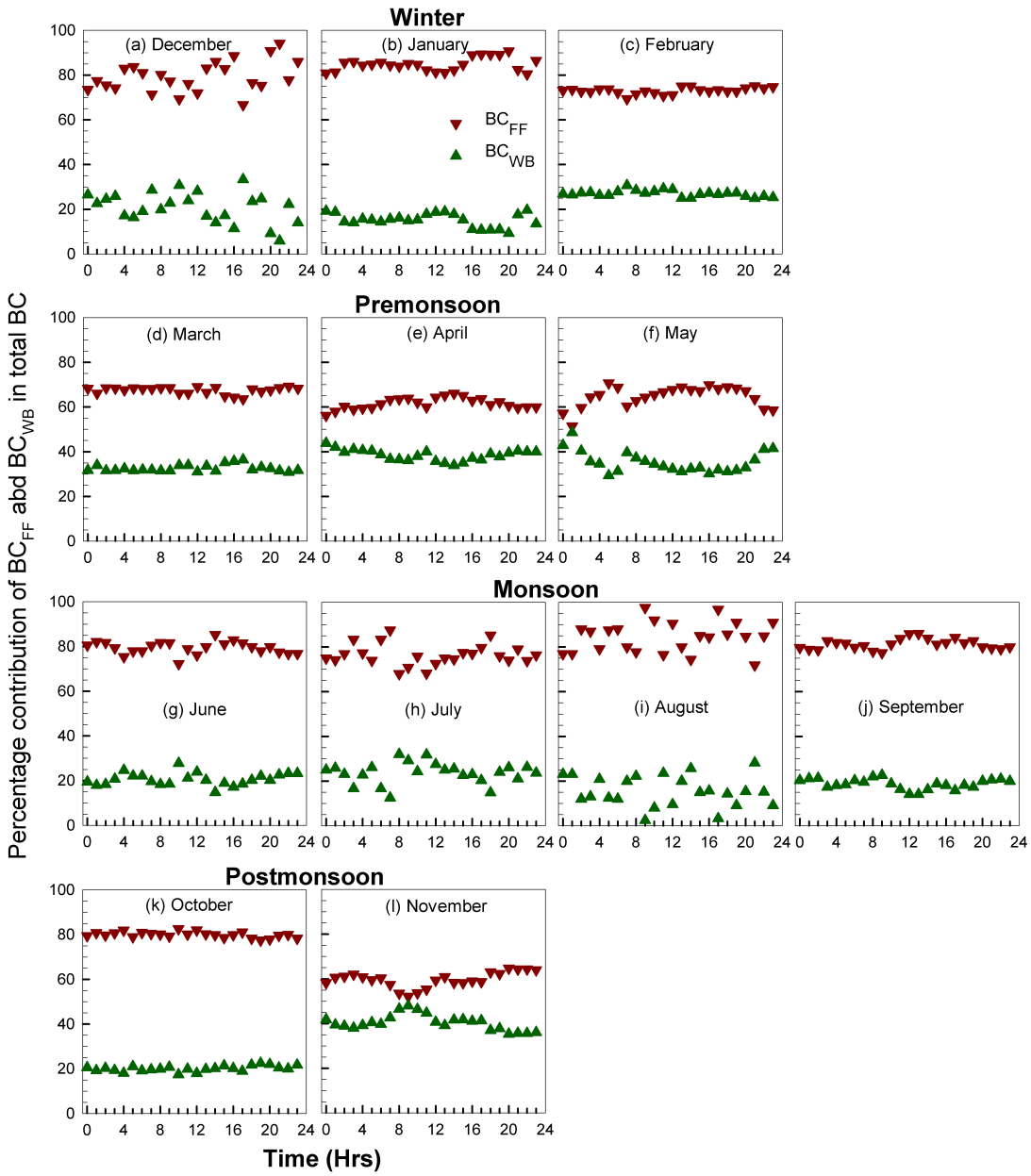

Figure 4.19: *Monthly diurnal variation of percentage contributions of BC_{FF} and BC_{WB} in total black carbon (BC) mass concentrations over Gurushikhar, Mt. Abu during winter (Dec (a), Jan (b), and Feb (c)), premonsoon (Mar (d), Apr (e), and May (f)), monsoon (Jun (g), Jul (h), Aug (i), and Sep (j)), and postmonsoon (Oct (k), and Nov (l)) for 2015 and 2016 as function of season (winter, premonsoon, monsoon, and postmonsoon).*

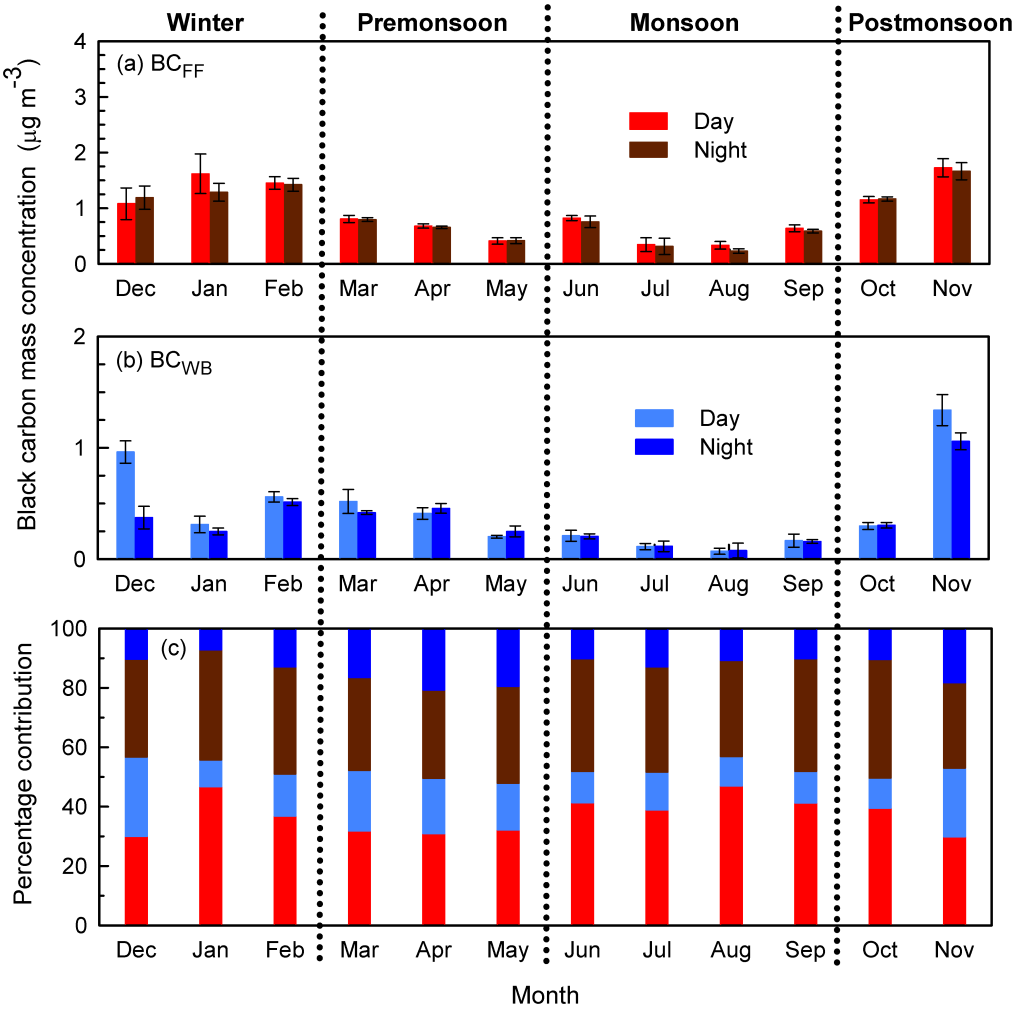

Figure 4.20: *Monthly variations in (a) equivalent BC concentrations from fossil fuel (BC_{FF}, $\mu g\ m^{-3}$), and (b) wood burning (BC_{WB}, $\mu g\ m^{-3}$) during day and nighttime. Vertical bars indicate $\pm 1\sigma$ variation with respect to mean. (c) Contributions (%) of BC components (fossil fuel and biomass) during the daytime and nighttime over Gurushikhar, Mt. Abu.*

served during November as in addition to the anthropogenic emission from the nearby region, it is strongly influenced by the longrange transport (77%) from the northern part of India. The residue crop burning in Punjab and Haryana produce black carbon aerosols which get transported to the observational site. The contributions of BC_{FF} in BC mass dominates around the year and is found highest during January over Gurushikhar (Figure 4.21). The high-

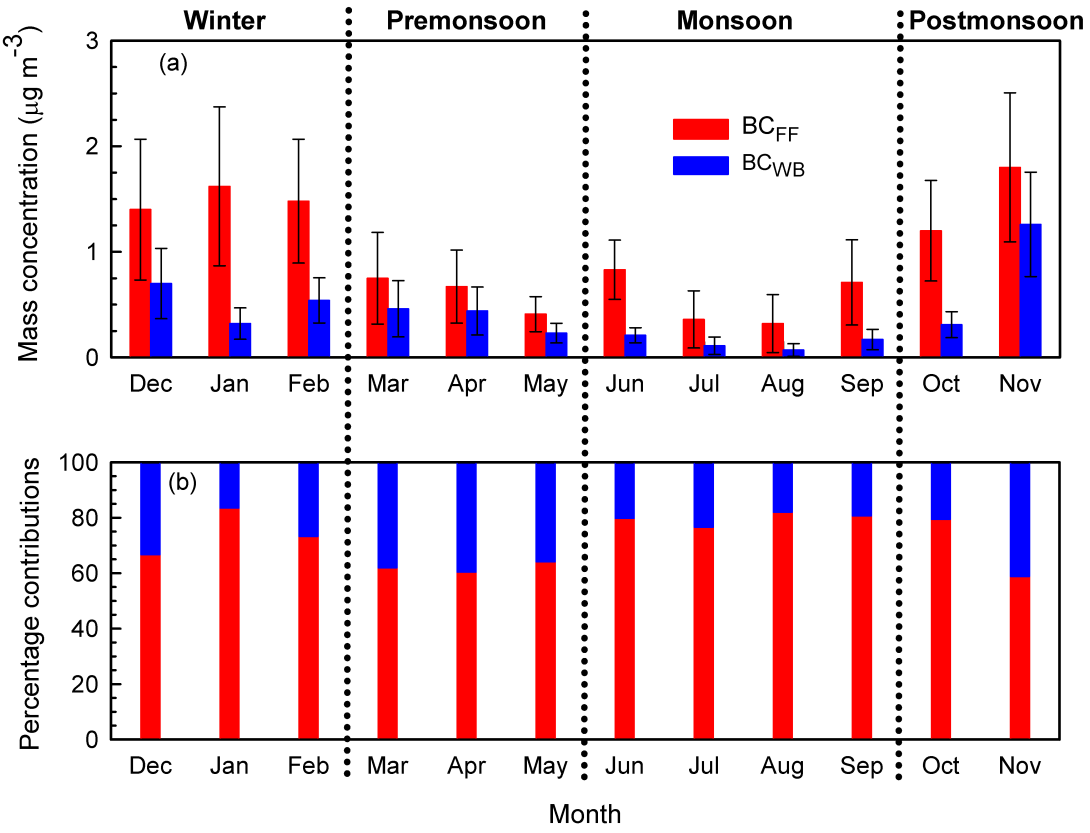

Figure 4.21: *Monthly mean (a) equivalent black carbon concentrations from fossil fuel (BC_{FF}, $\mu g\ m^{-3}$) and wood burning (BC_{WB}, $\mu g\ m^{-3}$). Vertical bars respresent $\pm 1\sigma$ variation with respect to mean. (b) Percentage contributions of BC_{FF} and BC_{WB} in BC over Gurushikhar, Mt. Abu as function of season (winter, premonsoon, monsoon, and postmonsoon).*

est BC_{FF} contribution to BC is observed during monsoon over Gurushikhar because of reduction in the use of biomass for various burning activities. The maximum BC_{WB} contributions to the total BC at Gurushikhar is observed during premonsoon followed by postmonsoon (Table 4.8) due to the longrange transport of the pollutants from the residue crop burning areas of Punjab and Haryana to the observational location. The analysis reveals that BC_{FF} dominates the contribution to BC mass even over a high altitude remote site. The annual mean contribution of 72% to total BC confirms that BC mass concentrations from fossil fuels dominate over Gurushikhar while it is 80% for Ahmedabad. The contribution of biomass burning component of BC is found

to be higher over Gurushikhar (28%) in comparison to Ahmedabad (20%) due to the significant influence of the longrange transport.

Table 4.8: *Variations (seasonal) in the contribution (%) of BC_{FF}, BC_{WB}, BC(Day)$_{FF}$, BC(Day)$_{WB}$, BC(Night)$_{FF}$, and BC(Night)$_{WB}$ in BC mass over Gurushikhar during 2015-2016.*

Contribution (%)	Winter	Premonsoon	Monsoon	Postmonsoon
BC_{FF}	74	62	82	66
BC_{WB}	26	38	18	34
BC(Day)$_{FF}$	38	31	41	33
BC(Day)$_{WB}$	17	19	11	19
BC(Night)$_{FF}$	35	31	37	32
BC(Night)$_{WB}$	10	19	11	16

In summary, BC, BC_{FF} and BC_{WB} mass concentrations exhibit strong diurnal variations over Ahmedabad compared to Gurushikhar due to the combined effects of the diurnal evolution of atmospheric boundary layer and consistent anthropogenic emissions. A distinct BC variation is observed over Gurushikhar with an increase in BC concentration during noontime due to strong thermal convection whereby pollutants from the foothills rise up to the measurement site. The diurnal contribution of BC_{FF} in total BC dominates throughout the day at both the observational sites. The annual mean contribution of BC_{FF} to total BC mass concentration is 80 and 72% respectively over Ahmedabad and Gurushikhar. The study illustrates that Gurushikhar is influenced by local and longrange transported aerosols through convection and advection processes. These results correspond to regional background value for western India region, and can be used as a representative inputs in various regional and global climate models for the estimation of climate forcing.

Chapter 5

Aerosol radiative forcing over urban and high altitude remote locations

Aerosols from natural (sea salt, biogenic, mineral dust, and volcanic ash) and anthropogenic (combustion of fossil/bio fuel from industrial processes, biomass burning from domestic and industrial, etc) sources produce a cooling on the Earth-atmosphere system via direct and indirect effects which partially counteracts the warming induced by greenhouse gases (*IPCC*, 2007). Because of the short residence times of aerosols, and varied sources aerosol properties (optical, physical, and chemical) and aerosol radiative forcing exhibit strong seasonal and regional variations. However, the effect of different aerosol species on Earth's climate need not be cumulative because of the (i) inhomogeneity in the aerosol distributions both in space and time, (ii) uncertainty in their mixing states, (iii) differences in the surface albedo, and (iv) differences in the vertical distribution of aerosols (*Haywood and Ramaswamy*, 1998; *Jacobson*, 2001). The aerosol forcing of climate can vary due to regional variations in aerosol chemical composition, columnar concentration, and its residence time in the atmosphere (*Spencer et al.*, 2008). The emissions from anthropogenic activities can alter the composition of the atmosphere which play a significant role in the climate change, and the climate change through changes in atmospheric dynamics, temperature, atmospheric stability, hydrological cycle, and biosphere-atmosphere interactions can influence the atmospheric composition (*Isaksen et al.*, 2009).

Typically, aerosols are found near source regions but they get transported due to changes in the mean atmospheric circulation patterns which significantly impact the global climate. The present chapter documents the monthly and seasonal variations in clear sky shortwave aerosol radiative forcing over an urban location (as discussed in Chapters 3 and 4) and a high altitude remote location in western India (as discussed in Chapters 3 and 4). Measured surface and columnar aerosol properties with radiative transfer models are used to compute the aerosol radiative forcing. This study will give an insight into the aerosol radiative effects over a source (Ahmedabad) and a background region (Gurushikhar).

5.1 Aerosol radiative forcing

Aerosol radiative forcing is computed using Santa Barbara DISORT Atmospheric Radiative Transfer (SBDART) code in the shortwave (0.25 - 4.0 μm) regions (Chapter 2, Section 2.4.2). The contribution of aerosol radiative forcing in longwave range is $< 10\%$ to the net aerosol radiative forcing (Chapter 1, Section 1.3), hence, in the present work, aerosol radiative forcing is estimated and discussed only in shortwave range for clear sky conditions over the study locations. The details of the principal aerosol parameters, and other additional inputs that are required to estimate aerosol radiative forcing follow.

5.1.1 Principal inputs

Aerosol optical depth, single scattering albedo and asymmetry parameter are the principal input parameters required for the computation of aerosol radiative forcing. In the present study, MODerate resolution Imaging Spectroradiometer (MODIS) Level 2 10 km $\times$ 10 km Collection 5.1 daily aerosol optical depth (*AOD*) at 0.55 μm, and Ångström exponent (α) are utilised (*Remer et al.*, 2008). The Ångström exponent (α) is further used to derive *AOD* spectra (0.4-1.0 μm) using Ångström power law ($\tau(\lambda) = \beta\lambda^{-\alpha}$, $\tau(\lambda)$ is the aerosol optical depth at wavelength λ (in μm), and β represents the turbidity coefficient

(*Ångström*, 1961)). The monthly mean *SSA* at 0.50 μm is from Ozone Monitoring Instrument (OMI) sensor onboard the AURA satellite over the study locations is utilised. Since measurements of *AOD*, and *SSA* correspond to a particular wavelength, and as spectral aerosol optical properties in the wavelength range of 0.25 - 4.0 μm are necessary to estimate aerosol radiative forcing, the Optical Properties of Aerosols and Clouds (OPAC) model (*Hess et al.*, 1998) is utilised. The necessary spectral (0.25 - 4.0 μm) aerosol optical properties (*AOD*, *SSA*, and *g*) are obtained over the study locations as a function of relative humidity.

In the present work, Optical Properties of Aerosols and Clouds (OPAC) model (Chapter 2, Section 2.4.1) is used to reproduce the observed aerosol properties by changing the number concentration of the aerosol species that contribute to the aerosol properties over the measurement location. The Optical Properties of Aerosols and Clouds (OPAC) model developed by *Hess et al.* (1998) provides the microphysical and optical properties of atmospheric particulate matter in the wavelength range of 0.25 to 40 μm. OPAC software package consists of a dataset of optical and physical properties aerosols at 8 humidities (0, 50, 70, 80, 90, 95, 98, and 99%)), and a Mie scattering FORTRAN code (to extract the optical and physical properties of species from the dataset, to compute spectral optical properties, and to estimate the optical properties of mixtures of different aerosol components). The OPAC aerosol dataset consists of water soluble (mostly gas-to-particle transformed like sulfates, nitrates, etc.), water insoluble (largely soil particles with organic material), black carbon, sea salt (coarse and accumulation), mineral dust (nucleation, accumulation and coarse), etc. The mixture of these aerosol components are used to define different type of aerosols as continental clean (water insoluble and soluble; with total particle number density of 2600 cm^{-3}), continental average (water insoluble, water soluble, and black carbon; 15300 cm^{-3}), continental polluted (water insoluble, water soluble, and black carbon; 50000 cm^{-3}), urban (water insoluble, water soluble, and black carbon; 158000 cm^{-3}), desert (water soluble and minerals; 2300 cm^{-3}), maritime clean (water soluble and

sea salts; 1520 cm^{-3}), maritime polluted (water soluble, sea salts, and black carbon; 9000 cm^{-3}), maritime tropical (water soluble and sea salts; 600 cm^{-3}) (*Hess et al.*, 1998). This model can be used to generate new mixtures using the available aerosol components to match the observations. OPAC computes various spectral (0.25 - 40 μm) optical properties of aerosol viz., extinction, scattering, absorption coefficients, single scattering albedo, aerosol optical depth, asymmetry parameter, and phase function as a function of relative humidity (0, 50, 70, 80, 90, 95, 98, and 99%) assuming aerosols to be spherical (*Hess et al.*, 1998). Depending on the source regions of aerosol and its prominent pathways the most suitable aerosol components over the study locations (Ahmedabad and Gurushikhar) are found to be water insoluble, water soluble, black carbon, sea salt, and mineral dust (*Ganguly and Jayaraman*, 2006; *Ramachandran and Kedia*, 2010). The concentrations (number) of the above aerosol species are adjusted to obtain the monthly average *AOD* spectra derived using MODIS retrieved Ångström exponent, and *SSA* at ambient relative humidity condition. The number concentration of each component is varied iteratively until the following criteria are fulfilled: (1) root mean square (RMS) variation between the OPAC *AOD* and MODIS *AOD* spectra is $<$0.03, (2) OPAC BC mass concentration is the same as that of the measured BC mass concentration, and (3) Single scattering albedo (*SSA*) in OPAC best matches the surface or column *SSA* (discussed in detail in Section 5.4). The asymmetry parameter (*g*) does not produce a significant impact on *ARF* as much as *AOD* and *SSA* (*Mishchenko et al.*, 1997). Therefore, *g* in the wavelength range of 0.25 - 4.0 μm corresponding to urban aerosols are used in radiative forcing estimation as was done earlier (*Ramachandran et al.*, 2012).

Spectral (0.25 - 4.0 μm) variation of *AOD*, *SSA*, and *g* for urban and continental clean aerosol models at 0, 50, and 80% *RH* in the shortwave spectral region of 0.25 - 4.0 μm are shown in Figure 5.1 (*Hess et al.*, 1998). $AODs$ increase from continental clean to urban aerosols (Figure 5.1). *AOD*, *SSA* and *g* increase as *RH* increases. *AOD* shows a very sharp decrease for the atmosphere dominated by fine mode aerosols (Figures 5.1 a and d). The decrease

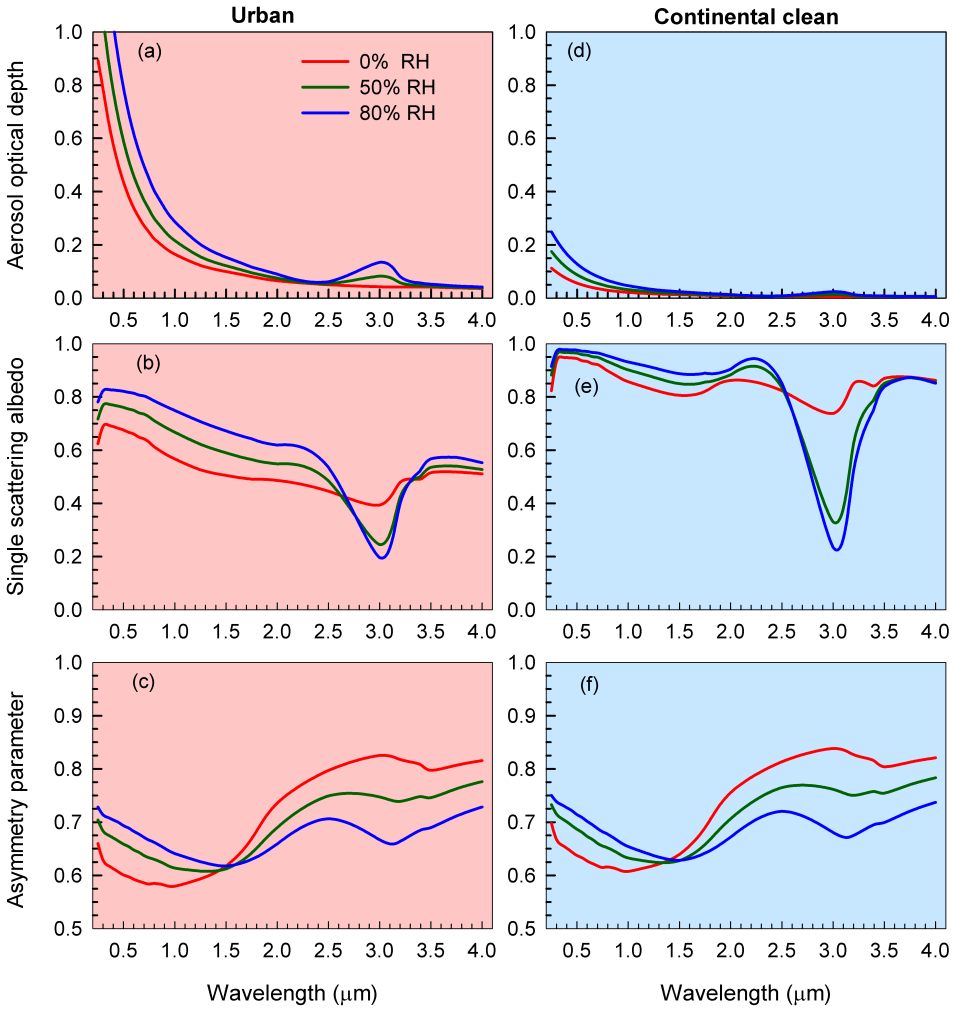

Figure 5.1: *Spectral variation of aerosol optical depth (a, d), single scattering albedo (b, e), and asymmetry parameter (c, f) for urban (a-c), and continental clean (d-f) aerosol models at 0, 50, and 80% RH in the shortwave spectral region (0.25 - 4.0 μm) estimated using Hess et al. (1998).*

in *AOD* with wavelength is more steeper as *RH* increases. *SSA* is wavelength dependent and gradually decreases with wavelength. Water soluble aerosols dominate the continental clean aerosol model, while black carbon aerosols dominate the urban aerosol leading to lower *SSA*. With increase in relative humidity the size of hygroscopic aerosol (water soluble and sea salt) increases and hence, the scattering coefficient and *SSA* are found to increase (Figures

5.1 b and e). In contrast, asymmetry parameter (g) increases as RH increases up to $\sim$ 1.0 μm, thereafter g is higher for dry aerosols than those at higher RH (Figures 5.1 c and f). The SSA and g show dips around 3 μm for urban and continental clean aerosol models (Figure 5.1) due to the enhancement in the absorptive nature of water soluble, mineral dust and sea salt (*d'Almeida et al.*, 1991).

5.1.2 Additional inputs

The other additional inputs required for the estimation of aerosol radiative forcing are atmospheric profiles of temperature and pressure, vertical profiles of aerosol, surface reflectance, columnar ozone, and water vapor. Standard tropical atmospheric profiles of temperature and pressure (*McClatchey et al.*, 1972) have been used in the radiative transfer algorithm (SBDART). Surface reflectance is not an intrinsic property of aerosol, however, but it plays a crucial role in determining the sign and magnitude of aerosol radiative forcing. Erroneous values of surface reflectance can give rise to large errors in the radiative forcing estimates (especially over land) (*Wielicki et al.*, 2005). The absorbing aerosols can exert a positive forcing over a high surface reflectance, whereas it exerts negative forcing over low surface reflectance (*Haywood and Shine*, 1995). Typically, surface reflectance is found higher for land as compared to water. The daily mean surface reflectance obtained from MODIS (Level 3 Global 500 m ISIN Grid product) at 7 wavelengths (0.469, 0.555, 0.645, 0.859, 1.240, 1.640 and 2.130 μm) are utilised to determine the mean monthly spectral surface reflectance over the study locations (Ahmedabad and Gurushikhar) (Figures 5.2 and 5.3). The uncertainty in MODIS derived surface reflectances is $\pm$2% over land (*Li et al.*, 2009) and is available at discrete wavelengths mentioned above. However, for aerosol radiative forcing estimates surface reflectances in the wavelength range of 0.25 - 4.0 μm are required. The spectral surface reflectance characteristics are obtained by the linear combination of vegetation, sand and water, so that the estimated surface reflectance spectra is in good agreement with the observed reflectance values from MODIS (Figures

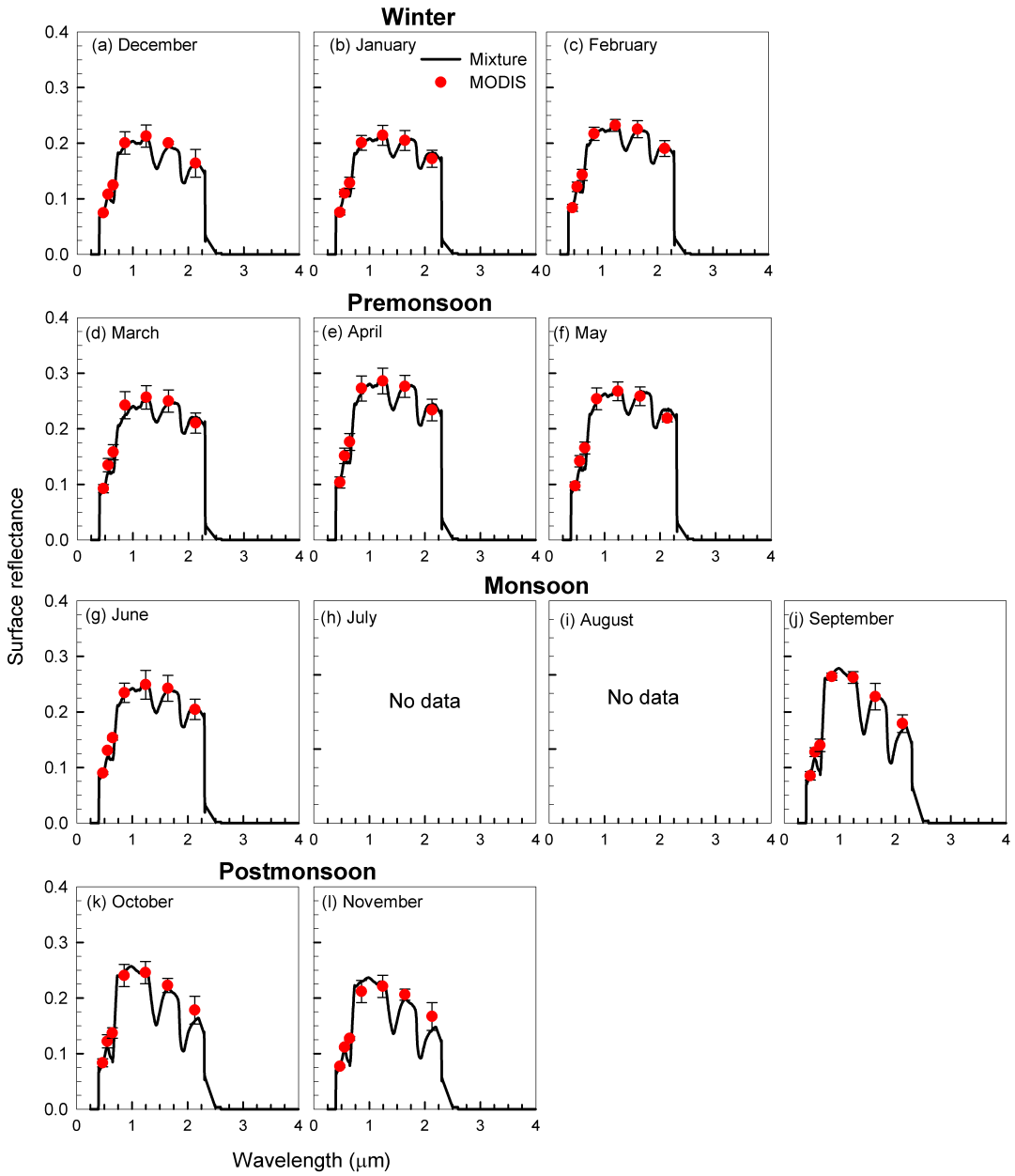

Figure 5.2: *Surface reflectance data from MODIS at 0.469, 0.555, 0.645, 0.859, 1.240, 1.640 and 2.130 μm over Ahmedabad. Combination of reflectance from different surface type (water, sand, and vegetation) are used to estimate the spectral surface albedo obtained from MODIS. Vertical bars represent $\pm 1\sigma$ variation from the mean.*

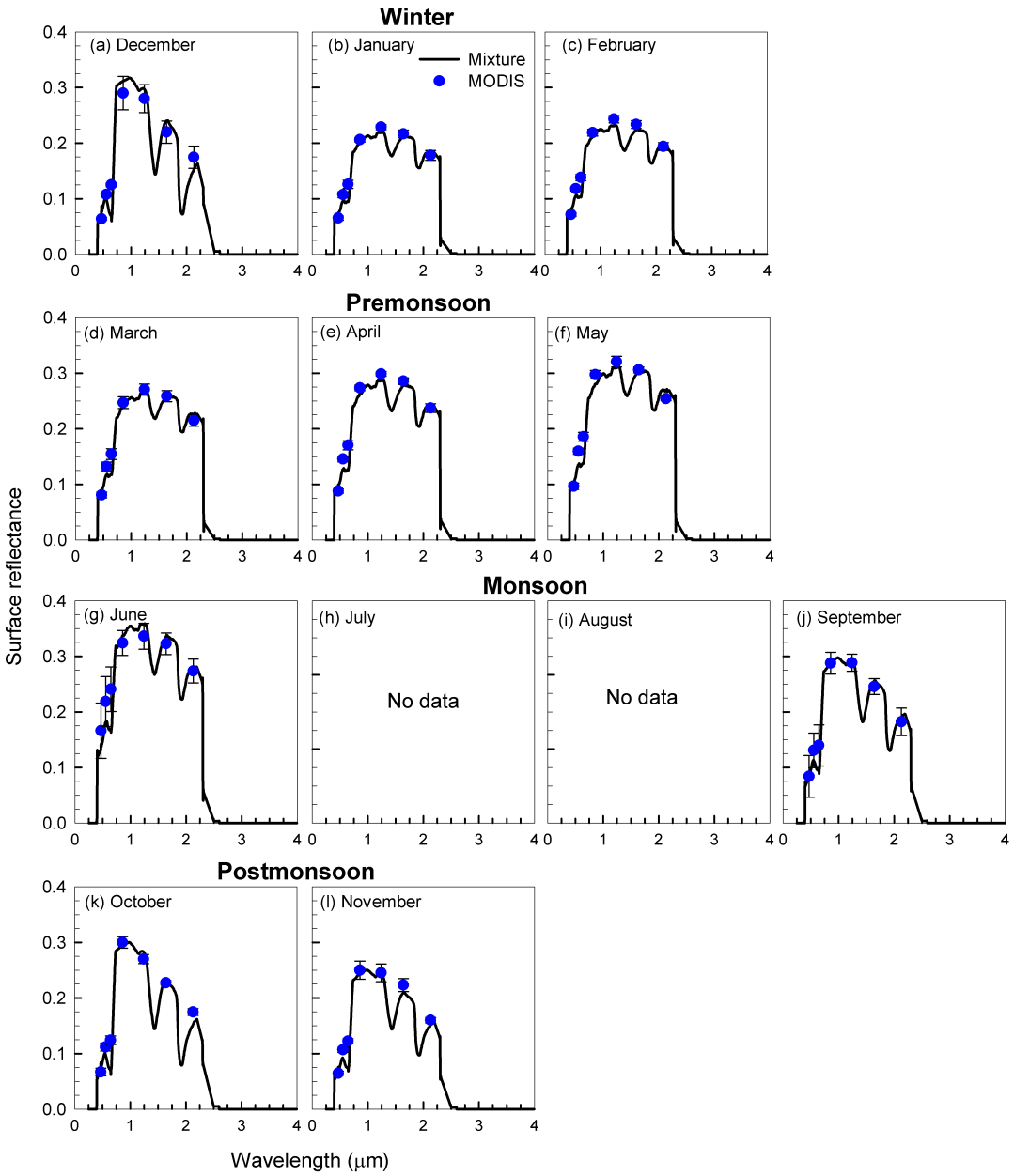

Figure 5.3: *Surface reflectance data from MODIS at 0.469, 0.555, 0.645, 0.859, 1.240, 1.640 and 2.130 μm over Gurushikhar. Combination of reflectance from different surface type (water, sand, and vegetation) are used to estimate the spectral surface albedo obtained from MODIS. Vertical bars represent $\pm 1\sigma$ variation from the mean.*

5.2 and 5.3). Surface reflectances are found to be high during premonsoon (March, April, and May) while reflectances are low during winter (December, January, and February) and postmonsoon (October and November) over both the study locations.

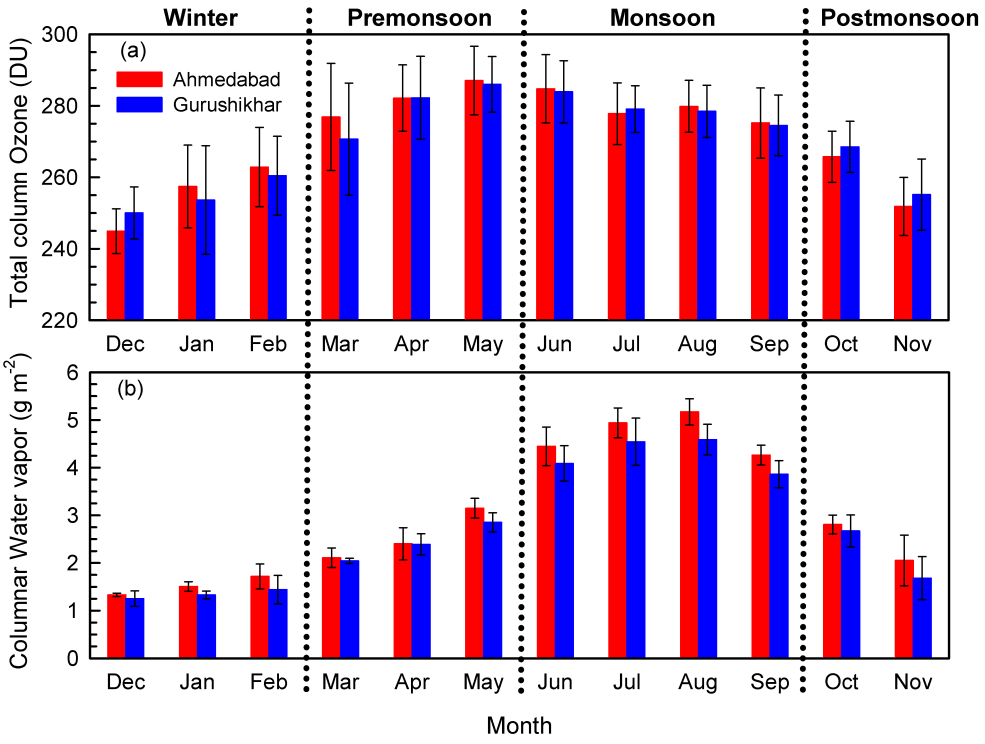

Figure 5.4: *Monthly variations in (a) columnar ozone (DU), and (b) columnar water vapor (gm^{-2}) over Ahmedabad and Gurushikhar as function of season (winter, premonsoon, monsoon, and postmonsoon). Vertical bars indicate $\pm 1\sigma$ variation with respect to mean.*

The maximum columnar ozone is found during May as the solar radiation is maximum, while the minimum is observed during December due to the minimum solar radiation available over both the study locations (Figure 5.4a). Columnar ozone is found to be higher during premonsoon (279.6 ± 7.9 and 282.0 ± 5.1 DU) and lower during winter (254 ± 5.3 and 255 ± 9.2 DU) over Ahmedabad and Gurushikhar. Typically, columnar water vapor over Ahmedabad is found to be higher than Gurushikhar (Figure 5.4b). Highest columnar

water vapor is found during August due to the presence of higher moisture content in the atmosphere, while the lowest is observed during December due to the minimum solar radiation available over Ahmedabad and Gurushikhar (Figure 5.4b). Columnar water vapor is found to be maximum during monsoon (4.7 ± 0.4 and 4.3 ± 0.4 gm^{-2}) and minimum during winter (1.5 ± 0.2 and 1.3 ± 0.1 gm^{-2}) over Ahmedabad and Gurushikhar.

Aerosol vertical profile is an important parameter required to determine the aerosol radiative forcing. The non-inclusion of aerosol vertical profile can give rise to an uncertainty in the estimation of forcing as a function of height (*IPCC*, 2007). The primary objective of the thesis is to determine the total energy content trapped in the atmosphere on regional scale due to aerosols present over distinct environments - one an urban region and other a high altitude mountain site. The total energy trapped in the atmosphere is the same with and without vertical profiles of aerosol, but exhibits variation in its vertical distribution (*Ramachandran and Kedia*, 2010). Hence, the non-inclusion of the vertical profiles of aerosol will not alter the results presented in the thesis.

5.2 Computation

5.2.1 Aerosol radiative forcing

The aerosol radiative forcing (*ARF*) is calculated using 40 streams at an interval of 1 hr for a range of solar zenith angles, and 24 hr averages are determined for each month. Direct aerosol radiative forcing at the top of the Earth's atmosphere (*TOA*) and at the Earth's surface (*SFC*) is defined as difference in the net flux with and without aerosols as

$$ARF_{TOA} = Flux(net)_{(aerosol)\,TOA} - Flux(net)_{(no\,aerosol)\,TOA} \tag{5.1}$$

$$ARF_{SFC} = Flux(net)_{(aerosol)\,SFC} - Flux(net)_{(no\,aerosol)\,SFC} \tag{5.2}$$

The atmospheric forcing (ARF$_{ATM}$) corresponds to the energy trapped in the Earth's atmosphere due to aerosols and is calculated as the difference in forcing at the *TOA* (100 km) and the *SFC*,

$$ARF_{ATM} = ARF_{TOA} - ARF_{SFC}. \tag{5.3}$$

Positive ARF$_{ATM}$ represents an increase in flux in the atmosphere leading to warming, while a negative ARF$_{ATM}$ corresponds to a decrease in flux leads to cooling. ARF$_{ATM}$ indicates the total energy trapped in the atmosphere due to aerosols. SBDART estimated radiation has been validated against the ground based observations of shortwave radiation. A good correlation (r^2 = 0.99) was found between the SBDART modeled fluxes (Wm^{-2}) and the measured fluxes over Ahmedabad (*Ramachandran et al.*, 2012). The uncertainty in the SBDART's predicted direct shortwave radiation is found to be about 1%, while the uncertainty in the diffused radiation is about 30% (*Ricchiazzi et al.*, 1998). The relative standard error in *ARF* is on the order of 15% taking into account all the uncertainties mentioned above (*Ramachandran and Kedia*, 2010).

5.2.2 Atmospheric heating rate

The *ATM* forcing (Equation 5.3) represents the total energy absorbed by aerosols, and this energy is converted into heat and termed as atmospheric heating rate (Kd^{-1}). The aerosol heating rate is calculated as

$$\frac{\partial T}{\partial t} = \frac{g}{C_p}\frac{ARF_{ATM}}{\triangle P} \tag{5.4}$$

where $\partial T/\partial t$ represents the atmospheric heating rate (Kelvin per day, Kd^{-1}), C_p represents the specific heat capacity (air) at constant pressure, $\triangle$P is the pressure difference between *TOA* and *SFC*, and *g* is the acceleration due to gravity. Most of the atmospheric aerosols are concentrated near Earth's surface up to 3 km, hence, $\triangle$P = 300 hPa (pressure difference between surface and 3 km) (*Ramachandran and Kedia*, 2010). The intra-seasonal variability in observed aerosol optical properties over the study locations was found to be

higher than the inter annual variability, hence in the present work, aerosol radiative forcing is computed as a function of 2 year mean (2015-2016) for each month. It may be noted that *ARF* is not estimated for monsoon as MODIS $AODs$ can be erroneous due to cloud contamination, and further $AODs$ were available only for a few days in the monsoon season. Further, to examine the effect of BC aerosols on the Earth-atmosphere system the shortwave *ARF* was computed for composite (total) aerosols, and for BC aerosols only over Ahmedabad and Gurushikhar.

5.3 Aerosol radiative forcing: Sensitivity studies

Aerosols can scatter and absorb the incoming solar radiation. The relative amount of aerosol and their reflectivity is controlled by its columnar extinction, single scattering albedo, asymmetry parameter, and the albedo of the underlying surface and or/atmosphere. In order to examine the effects of variations in the aerosol properties measured over the study locations, these observed/derived aerosol parameters are utilised as inputs in a radiative transfer model and *ARF* is estimated. In addition, further to understand the implications of the variabilities in aerosol parameters on aerosol radiative forcing, the sensitivity of various aerosol parameters to aerosol direct radiative forcing is examined.

5.3.1 Aerosol optical depth (*AOD*), Single scattering albedo (*SSA*), and Asymmetry parameter (*g*)

A sensitivity study has been undertaken to estimate the effects of *AOD*, *SSA* and *g* on aerosol radiative forcing for urban aerosols (*Hess et al.*, 1998), for vegetation surface albedo, and at 50% relative humidity. *AOD*, *SSA* and *g* in the wavelength range 0.25 - 4.0 μm are normalized with *AOD*, *SSA* and *g* at 0.55 μm. The resultant normalized *AOD*, *SSA* and *g* shortwave spectra are further used to estimate the aerosol radiative forcing in steps of 0.1 interval for *AOD*, *SSA* and *g*. In the sensitivity study, when *AOD* varies from 0.1 to 1 (steps of 0.1)

the other parameters (*SSA* and *g*) spectra are kept fixed. Likewise, when *SSA* and *g* are changed (steps of 0.1), *AOD* and *g* spectra, and *AOD* and *SSA* spectra respectively are fixed.

Shortwave *ARF* for the same aerosol species (same because *SSA* is fixed) is nearly linearly associated with *AODs* (Figure 5.5a). Whereas, *ARF* is non-linearly related to *SSA* (Figure 5.5b), while variations in *g* has the minimum effect on the shortwave *ARF* (Figure 5.5c). When *AOD* increases from 0.1 to 1.0 the top of the atmosphere (*TOA*) aerosol radiative forcing increases and is always positive, whereas when *SSA* increases from 0.1 to 1.0 the *TOA* forcing decreases and it changes sign from positive (+ve) to negative (-ve) (Figure 5.5). *TOA* forcing increases as *g* increases from 0.1 to 1.0 and flips its sign from -ve to +ve when *g* values are > 0.3 (Figure 5.5). The relation between *SSA* and *ARF* is found to be non-linear due to the variation in *TOA* forcing. The aerosol surface forcing is always negative which implies cooling at the surface for all *AOD*, *SSA* and *g* values (Figure 5.5). The atmospheric forcing is the difference between the top of the atmosphere and surface forcing, and it increases nearly linearly with increase in *AOD* and decrease non-linearly with increase in *SSA* (Figure 5.5). Hence, any change in aerosol distribution in the atmosphere will significantly effect the aerosol radiative forcing in the atmosphere.

5.3.2 Refractive index

In OPAC dataset the refractive index for black carbon (BC) is given as $1.75-0.44i$ at 0.55 μm. However, it has been suggested by *Bond and Bergstrom* (2006) that the usage of this refractive index should be avoided, because most of the light absorbing carbon lie on the void-fraction line (*Bond and Bergstrom*, 2006). Further, they recommended a set of refractive indices that should be used to represent BC at 0.55 μm (Table 5.1). This range of refractive index is given based on several studies listed in Table 5 of *Bond and Bergstrom* (2006), and further *Bond and Bergstrom* (2006) recommended the use of higher refractive index for BC (cases 5 and 6, Table 5.1). A sensitivity study was undertaken to

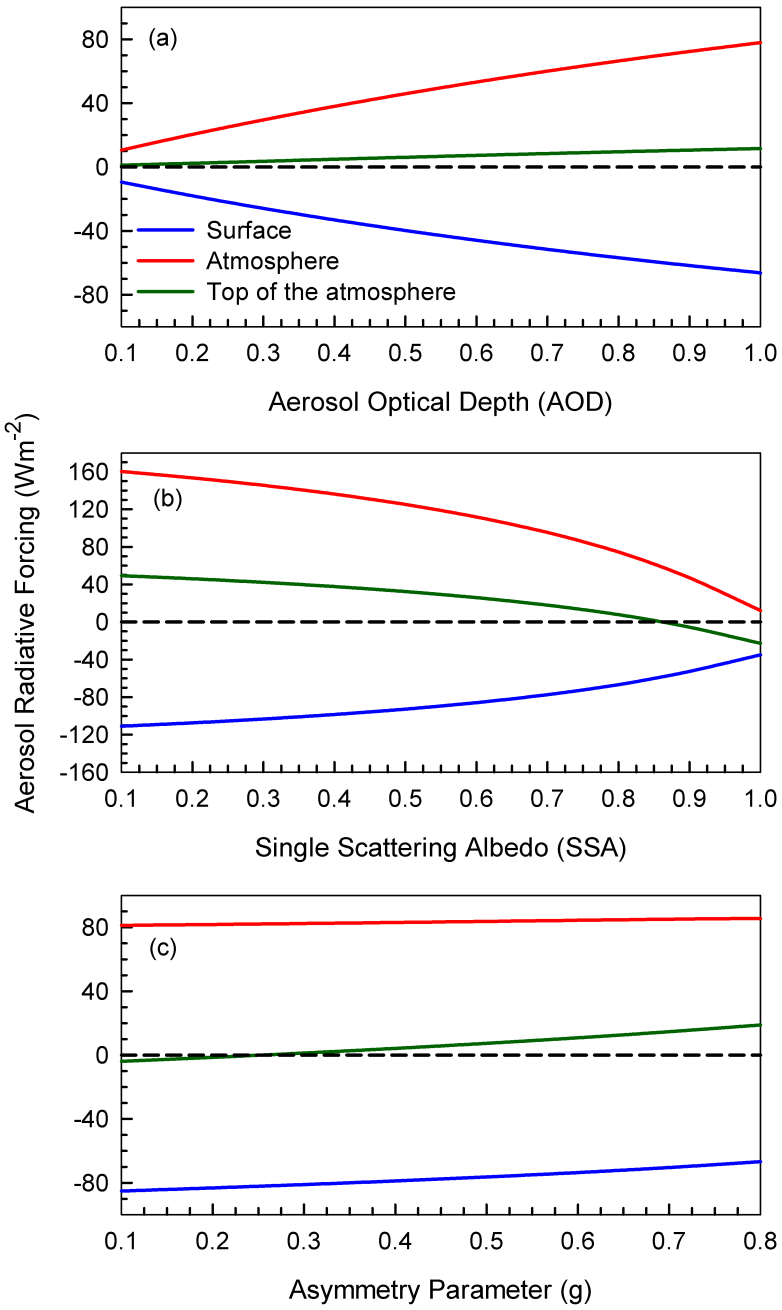

Figure 5.5: *Aerosol radiative forcing (ARF) (Wm^{-2}) at the surface, atmosphere, and top of the atmosphere due to variations in aerosol optical depth, single scattering albedo, and asymmetry parameter. Aerosol radiative forcing is estimated using urban aerosol model at 50% relative humidity (RH) and for surface albedo vegetation.*

Table 5.1: *Aerosol scattering coefficient (β_{sca}, km^{-1}), absorption coefficient (β_{abs}, km^{-1}), extinction coefficient (β_{ext}, km^{-1}), and single scattering albedo (SSA) estimated using Mie theory (Bohren and Huffman, 1983) for black carbon aerosol as a function of refractive indices at 0.55 μm. Case 1 corresponds to the OPAC dataset for black carbon at 0% relative humidity (Hess et al., 1998). Cases 2-6 represent the computed aerosol optical properties for the recommended range of refractive indices given in Bond and Bergstrom (2006). $\triangle$SSA represents the percentage change in SSA estimated with respect to SSA of case 1.*

	Refractive index		β_{sca}	β_{abs}	β_{ext}	*SSA*	$\triangle$*SSA*
Cases	Real	Imaginary	(km^{-1})	(km^{-1})	(km^{-1})		%
1	1.75	0.44	1.156E-07	4.385E-07	5.541E-07	0.209	-
2	1.75	0.63	1.278E-07	5.841E-07	7.119E-07	0.179	14
3	1.80	0.67	1.387E-07	6.002E-07	7.389E-07	0.188	10
4	1.85	0.71	1.495E-07	6.143E-07	7.638E-07	0.196	6
5	1.90	0.75	1.602E-07	6.264E-07	7.866E-07	0.204	2
6	1.95	0.79	1.706E-07	6.368E-07	8.074E-07	0.211	1

determine the influence of different refractive index values on the scattering coefficient (β_{sca}, km^{-1}), absorption coefficient (β_{abs}, km^{-1}), extinction coefficient (β_{ext}, km^{-1}), and single scattering albedo (*SSA*) of BC aerosols using Mie theory (*Bohren and Huffman*, 1983). The percentage variation in *SSA* due to the recommended refractive index values with respect to the one used in OPAC is in the 1-14% range; the percentage change for higher refractive index is $< 2\%$ (Table 5.1). Thus, this sensitivity study suggests that the change in *SSA* due to the differences in refractive index values is less than the uncertainty in *SSA* (which is estimated to be 15%), and as such is not expected to alter the results and inferences drawn.

5.3.3 Surface reflectance

The surface albedo plays a significant and important role while studying the interaction between solar radiation and the atmosphere. *ARF* depends on the aerosol types (absorbing or scattering) and reflectance of the underlying surface (lower reflectance (ocean) or higher reflectance (desert, land and snow)). A sensitivity study has been undertaken to estimate the effects of sur-

face albedo on aerosol radiative forcing when continental polluted aerosols (*Hess et al.*, 1998) are present over ocean, vegetation, and snow albedo surfaces. The components of continental polluted aerosols are same as that of urban aerosols, however, the number concentrations of components namely, water soluble, insoluble, and black carbon aerosols for continental polluted are lower than urban by a factor of 1.8, 2.5, and 3.8 respectively (*Hess et al.*, 1998). Spectral aerosol optical properties corresponding to 50 % *RH* are used. The aerosol radiative forcing in the atmosphere increases with the increase in surface reflectance. When the surface reflectance increases the *TOA* forcing becomes negative (land) or positive (snow) when compared to ocean. Whereas *TOA* forcing is always positive for greenhouse gases. The *ATM* forcing is found to increase when the *TOA* forcing becomes less negative or positive. Thus, the same aerosols can produce significantly different radiative responses (forcing) depending on the albedo of the underlying surface.

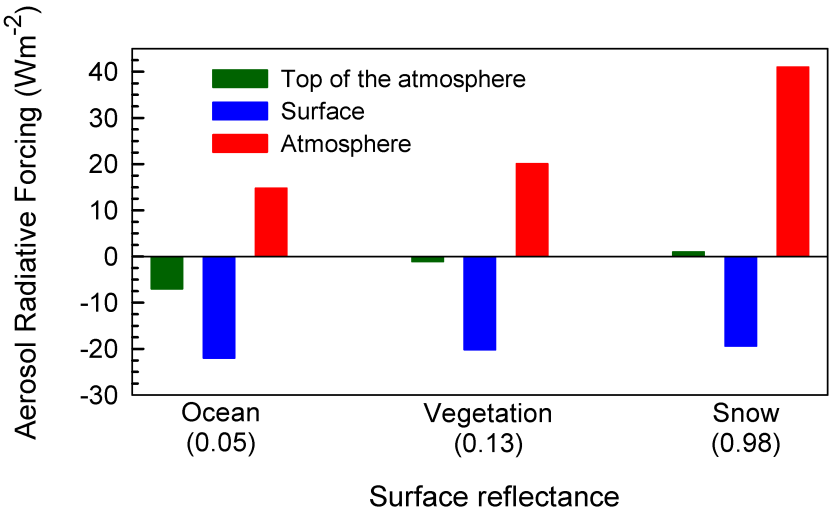

Figure 5.6: *Aerosol radiative forcing (ARF) (Wm^{-2}) at the top of the atmosphere, surface, and atmosphere, and for surface reflectance corresponding to ocean, vegetation and snow. ARF is estimated using continental polluted aerosol model corresponding to 50% RH in the 0.25 - 4.0 μm wavelength region as given in Hess et al. (1998). The reflectance of each surface at 0.55 μm are given in brackets.*

5.3.4 Relative Humidity

Aerosol radiative forcing exhibits a strong dependence on relative humidity (*RH*) because of the influence of *RH* on the aerosol properties (*Pilinis et al.*, 1995; *Penner et al.*, 1998). A sensitivity study has been undertaken to estimate the effects of *RH* on aerosol radiative forcing for urban aerosols (*Hess et al.*, 1998) and for vegetation (surface albedo). *AOD*, *SSA* and *g* in the wavelength range 0.25 - 4.0 μm are utilised at 0, 50, 70, 80, 90, 95, 98 and 99% *RH* from OPAC model. It is found that as *RH* increases *SSA* increases, resulting in an increase (-ve) in the top of the atmosphere and surface forcing (Figure 5.7).

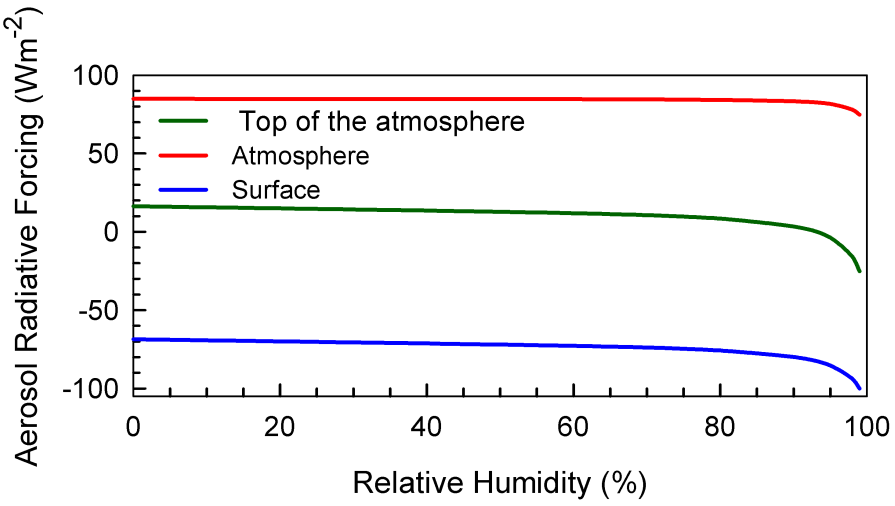

Figure 5.7: *Aerosol radiative forcing (ARF) (Wm^{-2}) at the top of the atmosphere, atmosphere, and surface as a function of relative humidity (RH). ARF is estimated using urban aerosol model for 15 January over Ahmedabad and for surface albedo vegetation. Spectral optical properties of aerosol (AOD, SSA and g) in the 0.25 - 4.0 μm wavelength region as given in Hess et al. (1998) are used to calculate shortwave aerosol radiative forcing.*

5.4 Aerosol radiative forcing over an urban location: Ahmedabad

The shortwave aerosol radiative forcing (*ARF*) is estimated using surface *SSA* (derived from the surface measurements of aerosol absorption and scattering coefficients using nephelometer and aethalometer respectively - Method 1), and using columnar *SSA* (from satellite remote sensing measurements - Method 2) for composite aerosols. Further, to investigate the effect of black carbon (BC) aerosols on the Earth-atmosphere system the shortwave *ARF* is computed for BC aerosols only and contrasted with the radiative forcing obtained for composite aerosols. The *ARF* is computed for winter (December-January-February), premonsoon (March-April-May), and postmonsoon (October-November) over Ahmedabad during 2015-2016. It may be noted that *ARF* is not estimated for monsoon (June, July, August, and September) as MODIS $AODs$ can be erroneous due to cloud contamination, and further $AODs$ were available only for a few days in the monsoon season.

5.4.1 Composite forcing

Method 1 (Surface SSA)

The *TOA* forcing ranges from 0.75 to 6.30 Wm^{-2}, while *SFC* forcing varies from -58.3 to -40.2 Wm^{-2} over Ahmedabad (Figure 5.8). *TOA* forcing is positive over Ahmedabad (Figure 5.8). The shortwave *TOA* forcing is positive when relatively more absorbing aerosols (lower *SSA*) exist over surface with higher reflectance leading to a higher positive *ATM* warming. *SFC* forcing is more negative from February to April and it becomes less negative during October - December (Figure 5.8). *ATM* forcing will increase when *TOA* forcing is more towards positive side and *SFC* forcing is highly negative. *ATM* forcing increases from February to April and gradually decreases from October to December (Figure 5.8). The maximum *ATM* forcing is found during October as *SSA* is low over Ahmedabad.

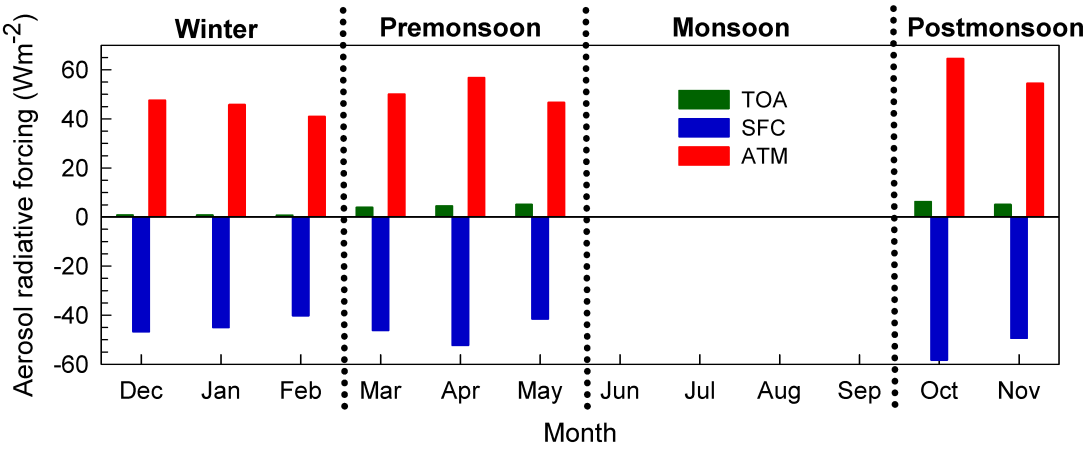

Figure 5.8: *Clear sky aerosol radiative forcing (ARF) (Wm^{-2}) at the TOA (top of the atmosphere), SFC (surface) and ATM (atmosphere) corresponding to ambient relative humidity estimated using surface SSA (Method 1) over Ahmedabad during 2015-2016 as function of season (winter, premonsoon, monsoon, and postmonsoon).*

The *ARF* exhibits a strong seasonal variability over Ahmedabad. During the study period the maximum *TOA* forcing is found during postmonsoon followed by premonsoon and winter (Table 5.2). The positive value of *TOA* forcing during all seasons is attributed to the higher concentration of absorbing aerosols over Ahmedabad (Figure 5.9). *ATM* forcing shows the maximum during postmonsoon (Table 5.2) due to the dominance of absorbing type aerosol associated with lower *SSA* in the atmosphere (Figure 5.9). The annual mean shortwave composite *ARF* at *TOA*, *SFC*, and *ATM* are found to be 3.9 $\pm$ 2.6, -48.2 $\pm$ 5.1, and 52.1 $\pm$ 7.4 Wm^{-2} over Ahmedabad when estimated using Method 1 (Table 5.2).

Method 2 (Columnar SSA)

The columnar *SSA* over Ahmedabad is remarkably higher than the *SSA* estimated using ground based measurements as most of the absorbing aerosols are concentrated near the surface (Figure 5.9). The radiative forcing at *TOA*

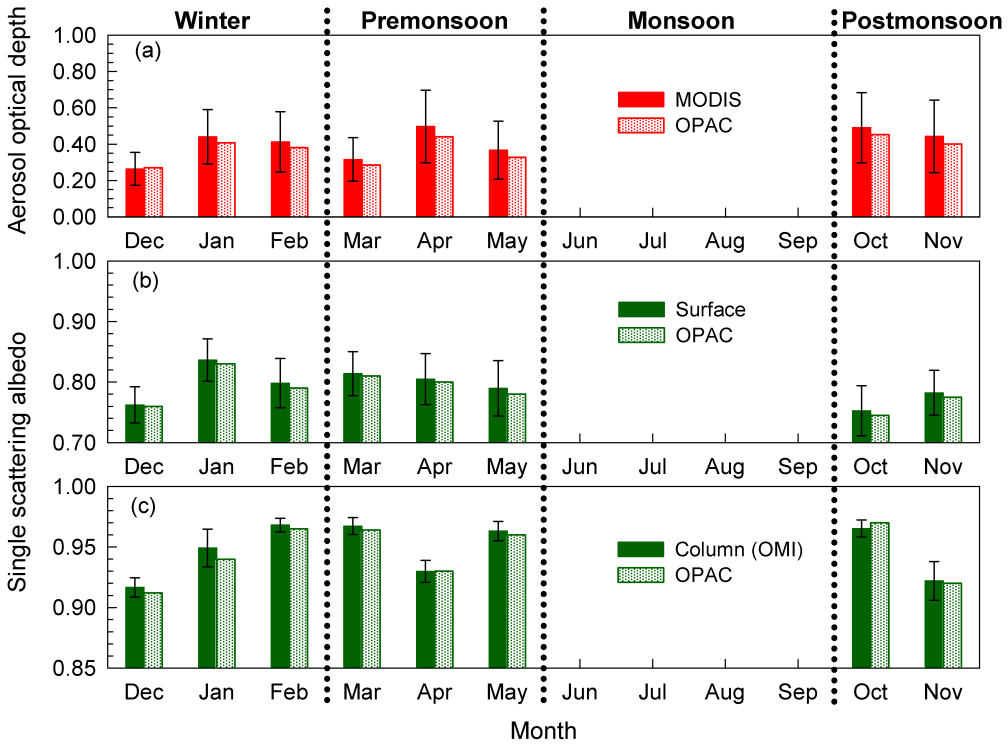

Figure 5.9: *(a) Mean AODs (of MODIS Terra and Aqua) at 0.55 μm in comparison with model (OPAC) $AODs$. Single scattering albedo (SSA) at 0.50 μm in comparison with OPAC SSA over Ahmedabad derived from (b) the surface measurements of aerosol absorption and scattering coefficients, and (c) OMI. Vertical bars denote $\pm 1\sigma$ deviation from the monthly mean. The parameters AOD and SSA are plotted as function of season (winter, premonsoon, monsoon, and postmonsoon).*

and *SFC* decreases when estimated for columnar *SSA* from January to February and then gradually increases from March to April (Figure 5.10). The maximum *TOA* and *SFC* forcing is found during April (Figure 5.10) as *AOD* is found to be maximum during this month. *TOA* forcing is negative due to higher *SSA* as compared to those used in Method 1. Several studies reported (Kanpur (*Ramachandran and Kedia*, 2012), Gandhi college (*Ramachandran and Kedia*, 2012), Dibrugarh (*Pathak et al.*, 2010), Ahmedabad (*Ramachandran and Kedia*, 2011)) negative *TOA* forcing throughout the year when estimated using Method 2 which is consistent with the present study. *SFC* forcing further decreases from October to December (Figure 5.10). *SFC* forcing (computed using

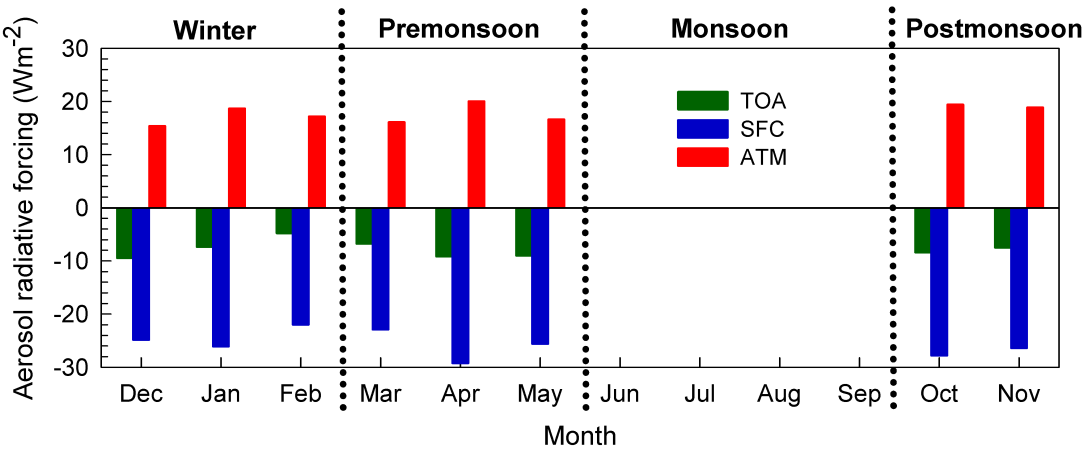

Figure 5.10: *Clear sky aerosol radiative forcing (ARF) (Wm^{-2}) at the TOA (top of the atmosphere), SFC (surface) and ATM (atmosphere) corresponding to ambient relative humidity estimated using columnar single scattering albedo (SSA) (Method 2) over Ahmedabad during 2015-2016 as function of season (winter, premonsoon, monsoon, and postmonsoon).*

Method 2) is found to be lower by a factor of 2 over Ahmedabad when compared to Method 1. *ATM* forcing decreases from January to March and then attains a maximum during April. *ATM* forcing (computed using Method 2) is also found to be lower by a factor of 2-3 compared to those estimated following Method 1. Surface (*SFC*) composite forcing is well correlated with the observed *AOD* (Figure 5.9). Higher *AOD* results in higher surface cooling thereby suggesting that *AOD* and surface forcing exhibit a linear relation (Figure 5.10). *TOA* and *SFC* forcing is negative which implies cooling, whereas the *ATM* forcing is positive (Figure 5.10).

The maximum *TOA* forcing is found during premonsoon followed by postmonsoon and winter (Table 5.2). During the study period the maximum and minimum surface cooling are estimated during postmonsoon and winter respectively. *ATM* forcing exhibits a typical variations throughout the year and shows maximum variation during postmonsoon and then followed by winter due to the significant contribution of the black carbon aerosol in the atmosphere during these seasons. The annual mean shortwave *TOA* forcing flips

the sign when compared to Method 1 due to the contribution of higher *SSA* with respect to Method 1 (Table 5.2). The *ATM* forcing is a factor of 3 lower than Method 1 (Table 5.2) over Ahmedabad. Significant differences in forcing arise due to the differences in the *SSA* as *AOD* and *g* remain the same in radiative forcing estimates.

5.4.2 Radiative forcing due to black carbon aerosols

In order to examine the effect of black carbon (BC) aerosols on the Earth-atmosphere system the ARF_{TOA}, ARF_{SFC}, and ARF_{ATM} are computed for BC aerosols only in the wavelength range of 0.25 - 4.0 μm. The radiative forcing due to black carbon aerosols are estimated using the spectral properties (*AOD*, *SSA*, and *g*) of BC aerosols only which are derived using the measured BC mass concentrations in OPAC (*Srivastava et al.*, 2012). Since, the number concentrations of a particular aerosol species (in this case BC) are modified, only *AOD* (columnar concentration) will exhibit variation, while single scattering albedo (ratio of scattering to extinction coefficients) and asymmetry parameter (angular distribution of scattering) will not exhibit any variation, throughout the year.

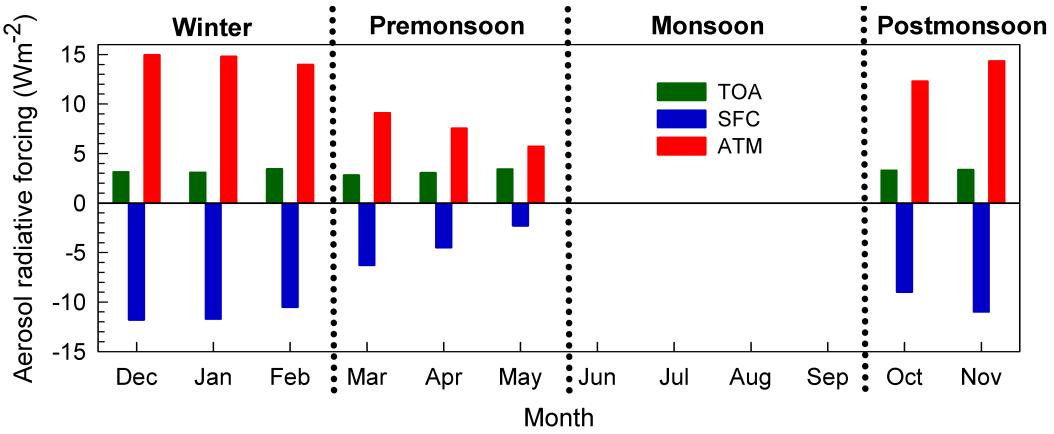

Figure 5.11: *Clear sky aerosol radiative forcing (Wm^{-2}) for black carbon (BC) aerosols only at the TOA (top of the atmosphere), SFC (surface) and ATM (atmosphere) over Ahmedabad during 2015-2016 as function of season (winter, premonsoon, monsoon, and postmonsoon).*

The monthly mean shortwave surface forcing (*SFC*) for BC aerosols only decreases from January to May and then gradually increases from October to December (Figure 5.11). The *TOA* forcing for BC only ranges from 2.8 to 3.4 Wm^{-2}, and does not show large variations as compared to the *TOA* forcing due to composite aerosols (Figure 5.11). The maximum atmospheric (*ATM*) forcing due to BC aerosol only is found in December (Figure 5.11) over Ahmedabad, which is found to be consistent with the maximum BC mass concentrations during this month. The *SFC* composite forcing is always higher than the surface forcing due to BC aerosols only. Top of the atmosphere forcing is positive for BC aerosols only, and is negative for composite aerosols. The maximum *SFC* forcing due to BC aerosols only is found during winter (-11.3 $\pm$ 0.8 Wm^{-2}) followed by postmonsoon (-10.1 $\pm$ 1.4 Wm^{-2}) and premonsoon (-4.4 $\pm$ 1.8 Wm^{-2}). During the study period the maximum and minimum *ATM* forcing due to BC aerosols only is found during winter (14.6 $\pm$ 0.5 Wm^{-2}) and premonsoon (7.5 $\pm$ 1.7 Wm^{-2}). The annual mean shortwave *ARF* due to BC aerosol only at *TOA*, *SFC*, and *ATM* are found to be 3.2 $\pm$ 0.3, -8.4 $\pm$ 3.6, and 11.6 $\pm$ 3.6 Wm^{-2} over Ahmedabad.

The *TOA* forcing estimated for BC aerosols is comparable with the *TOA* forcing from Method 1 (surface *SSA*, Table 5.2). The *SFC* forcing varies by a factor of $\sim$ 6 (Table 5.2) due to the significant contribution of *AOD*. Hence, the resultant *ATM* forcing for BC aerosols is lower by a factor of $\sim$ 4 when compared to Method 1 (Table 5.2). On the contrary, the *TOA* from Method 2 (column *SSA*) flips the sign when compared to BC aerosols only (Table 5.2). The *SFC* and *ATM* forcing for BC aerosols only are lower by a factor of $\sim$ 2 as compared to Method 2 (Table 2). The study reveals that BC aerosols alone can contribute $\sim$ 60% to the shortwave atmospheric forcing when compared to Method 2, whereas it contributes $\sim$ 20 % when compared to Method 1 over Ahmedabad, an urban region. The significant differences found in the forcing values are due to the observed differences in the *SSA*.

5.4.3 Atmospheric heating rate

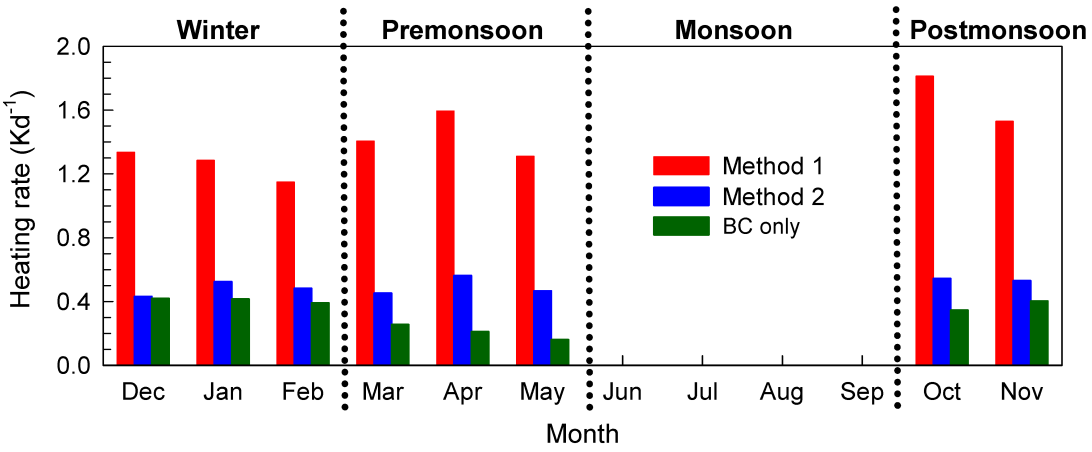

Figure 5.12: *Monthly mean heating rate (Kelvin per day, Kd^{-1}) for composite aerosols estimated using Method 1 and Method 2 over Ahmedabad during 2015 - 2016 as function of season (winter, premonsoon, monsoon, and postmonsoon).*

The monthly mean atmospheric heating rate estimated for composite aerosols using Method 1 (*SSA* derived from the surface measurements of aerosol absorption and scattering coefficients) for the shortwave *ATM* forcing exhibit strong seasonal variation. The heating rate increases from February to March and gradually decreases from October to December (Figure 5.12). Maximum heating rate is found during October over Ahmedabad (Figure 5.12), due to the abundance of absorbing aerosols (minimum surface *SSA*). The monthly mean shortwave atmospheric heating rate computed for composite aerosols using Method 2 (columnar *SSA*) is lower by a factor of 3-7 when compared to Method 1 as function of season (Figure 5.12), as columnar *SSA* is higher which decreases the forcing. The heating rate estimated from Method 2 decreases from January to March (Figure 5.12). The monthly mean heating rate estimated for composite aerosols using columnar *SSA* (Method 2) for the shortwave *ATM* forcing is found to be the highest during April over Ahmedabad (Figure 5.12), consistent with the maximum *AOD* in that month. The variations in heating rate for BC aerosols is in agreement with the variations in black carbon mass concentrations over Ahmedabad (Figure 5.12). The maximum heating

rate for BC aerosols only is found in December (Figure 5.12), consistent with the highest BC mass concentrations during December. The minimum heating rate for BC aerosols only is found during May (Figure 5.12) due to the minimum BC mass found during May.

Table 5.2: *Annual mean aerosol radiative forcing (ARF) (Wm^{-2}) at the TOA (top of the atmosphere), SFC (surface) and ATM (atmosphere) along with atmospheric heating rate (Kd^{-1}) estimated using surface SSA (Method 1), column SSA (Method 2), and BC aerosols only over Ahmedabad and Gurushikhar during 2015-2016.*

Method	Aerosol radiative forcing (Wm^{-2}) TOA	SFC	ATM	Heating rate (Kd^{-1})
Ahmedabad				
Surface *SSA* (Method 1)	3.4 $\pm$ 2.3	-47.5 $\pm$ 5.9	50.9 $\pm$ 7.4	1.43 $\pm$ 0.21
Column *SSA* (Method 2)	-7.8 $\pm$ 1.6	-25.6 $\pm$ 1.4	17.8 $\pm$ 1.1	0.50 $\pm$ 0.03
BC aerosols	3.2 $\pm$ 0.3	-8.4 $\pm$ 3.7	11.6 $\pm$ 3.8	0.33 $\pm$ 0.11
Gurushikhar				
Surface *SSA* (Method 1)	-3.2 $\pm$ 0.8	-14.6 $\pm$ 0.9	11.4 $\pm$ 1.0	0.32 $\pm$ 0.01
Column *SSA* (Method 2)	-3.5 $\pm$ 0.8	-14.2 $\pm$ 1.4	10.7 $\pm$ 0.7	0.30 $\pm$ 0.02
BC aerosols	1.3 $\pm$ 0.1	-5.4 $\pm$ 1.2	6.7 $\pm$ 1.2	0.19 $\pm$ 0.03

The maximum atmospheric heating rate is found during postmonsoon followed by premonsoon and winter (Table 5.2) over Ahmedabad from Method 1 and Method 2. During winter, the heating rate due to BC aerosols only is maximum over Ahmedabad (0.41 $\pm$ 0.01 Kd^{-1}), followed by postmonsoon (0.37 $\pm$ 0.04 Kd^{-1}) and premonsoon (0.21 $\pm$ 0.05 Kd^{-1}), which is in agreement with seasonal variation in black carbon aerosols over Ahmedabad. Atmospheric heating rate estimated using surface *SSA* (Method 1) is higher by a factor of 2-3 than the heating rate computed using columnar *SSA* (Method 2) throughout the season. The significant differences in atmospheric heating rate estimated using Method 1 and Method 2 are attributed to the differences in the *SSA* used while estimating the aerosol radiative forcing. During winter and postmonsoon, the atmospheric heating rates are higher when the BC mass concentrations are higher and *SSA* is lower over Ahmedabad. The highest annual mean heating rate is estimated using Method 1 due to lower *SSA* followed

by Method 2 and BC aerosols (Table 5.2). Such large regional atmospheric warming and surface cooling can significantly influence the atmosphere stability, cloud formation and impact the hydrological cycle (*Ramanathan et al.*, 2005).

5.5 Aerosol radiative forcing over a high altitude remote location: Gurushikhar, Mt. Abu

5.5.1 Composite forcing

Method 1 (Surface SSA)

The composite *SFC* forcing ranges from -12.3 to -16.2 Wm^{-2}, while *TOA* forcing ranges from -2.3 to -4.3 Wm^{-2} over Gurushikhar (Figure 5.13). *TOA* forcing sign is negative during the study period over Gurushikhar using Method 1 (Figure 5.13). On the contrary, the *TOA* composite forcing is always positive over Ahmedabad (Figure 5.8) during the study period due to the lower *SSA* (abundant absorbing aerosols) over Ahmedabad. The surface albedo observed over Gurushikhar and Ahmedabad are similar (Figures 5.2 and 5.3). *TOA* composite forcing increases from January to May and decreases from October to December (Figure 5.13). The maximum *TOA* composite forcing is found during May due to the maximum surface *SSA* during this month (Figure 5.14). The maximum and minimum *SFC* forcing are found during February and December respectively. Hence, the resultant composite *ATM* forcing is found to decrease from February to May (Figure 5.13). The maximum *ATM* forcing is found during February due to the corresponding minimum surface measured *SSA* (Figure 5.14). The minimum *ATM* forcing is seen during December due to the minimum *AOD* observed during this month over Gurushikhar (Figure 5.14).

The maximum *TOA* forcing is found during premonsoon followed by

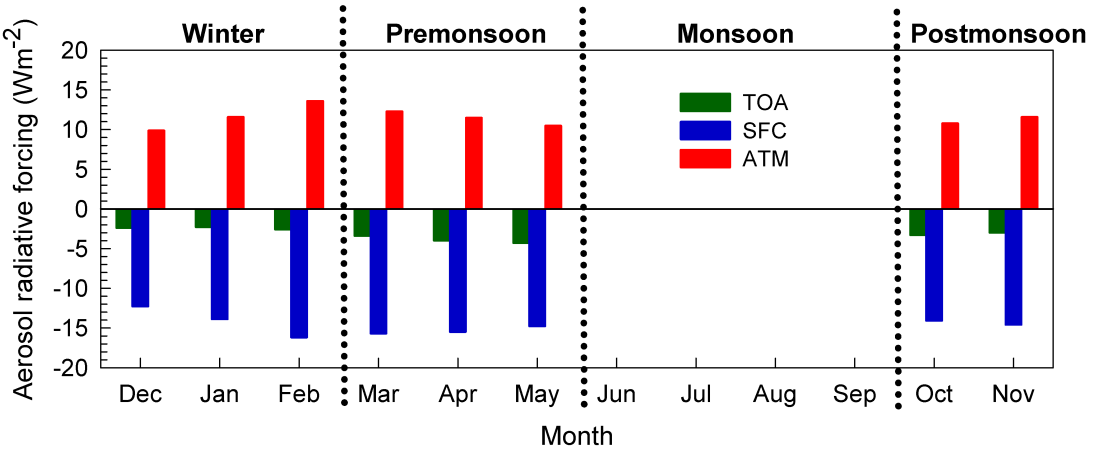

Figure 5.13: *Clear sky aerosol radiative forcing (Wm^{-2}) at the TOA (top of the atmosphere), SFC (surface) and ATM (atmosphere) corresponding to ambient relative humidity estimated using surface SSA (Method 1) over Gurushikhar during 2015-2016 as function of season (winter, premonsoon, monsoon, and postmonsoon).*

postmonsoon and winter (Table 5.2). The maximum *TOA* forcing for composite aerosols is found during premonsoon which is attributed due to the significant influence of the longrange transported scattering particles. The negative value of *TOA* forcing is attributed to the higher concentration of scattering aerosols over Gurushikhar. The maximum and minimum *SFC* forcing are found to be in premonsoon and winter respectively (Table 5.2). *ATM* forcing is found maximum during winter due to the dominance of absorbing type aerosol associated with lower *SSA* in the atmosphere. The composite surface and atmospheric forcing are found to lower by a factor of 3-4 than Ahmedabad. The annual mean shortwave composite *ARF* using surface *SSA* (Method 1) at *TOA*, *SFC*, and *ATM* are found to be -3.2 $\pm$ 0.8, -14.6 $\pm$ 0.9, and 11.4 $\pm$ 1.0 Wm^{-2} respectively over Gurushikhar. The *TOA* forcing flips sign over Gurushikhar when compared to Ahmedabad (Table 5.2). The *SFC* and *ATM* forcings are lower over Gurushikhar by a factor of $\sim$ 3 and 5 than Ahmedabad (Table 5.2). This differences in forcing is attributed due to higher *SSA* found over Gurushikhar.

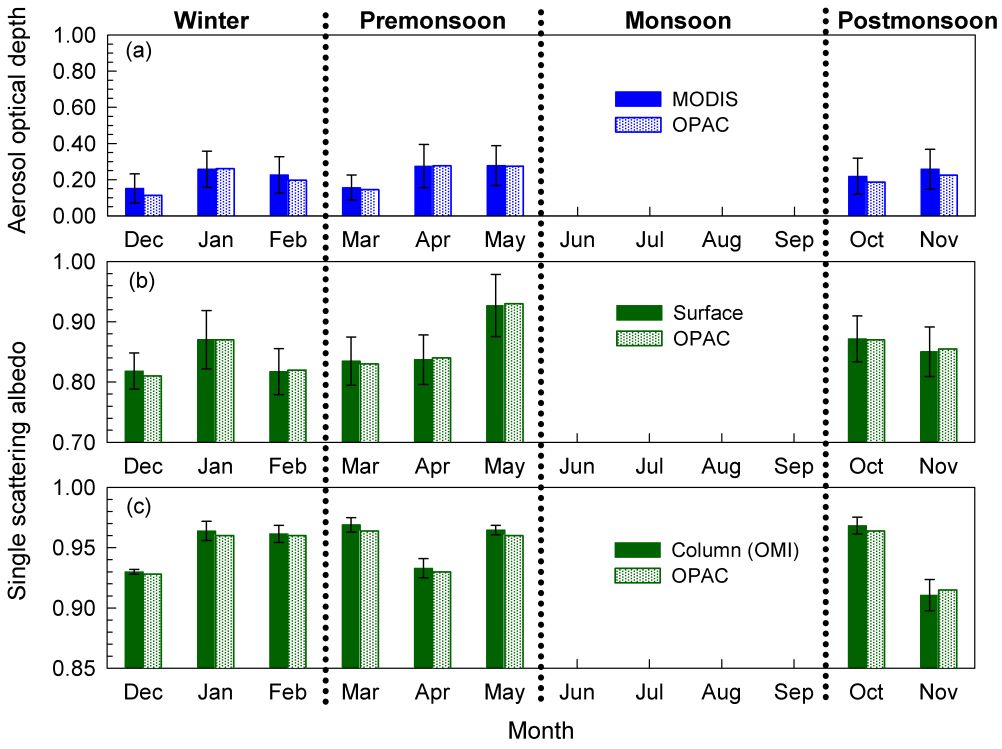

Figure 5.14: *(a) Mean AODs (of MODIS Terra and Aqua) at 0.55 μm in comparison with model $AODs$. Single scattering albedo (SSA) at 0.50 μm in comparison with OPAC SSA over Gurushikhar derived from (b) the surface measurements of aerosol absorption and scattering coefficients, and (c) OMI. Vertical bars denote $\pm 1\sigma$ deviation from the monthly mean. The parameter AOD and SSA are plotted as function of season (winter, premonsoon, monsoon, and postmonsoon).*

Method 2 (Columnar SSA)

The *TOA* composite forcing increases from January to May and from October to December using Method 2 (Figure 5.15). The maximum *TOA* forcing is found during April (Figure 5.15). The composite *TOA* forcing is always negative due to the dominance of scattering aerosols (higher *SSA*). *SFC* forcing decreases from January to March and increases afterwards till May (Figure 5.15). The maximum *SFC* forcing is found during May and the minimum is observed during December (Figure 5.15). The composite *ATM* forcing decreases from January to March then attains maximum during May (Figure 5.15). *ATM* forcing shows a minimum during December (Figure 5.15). The composite forcing

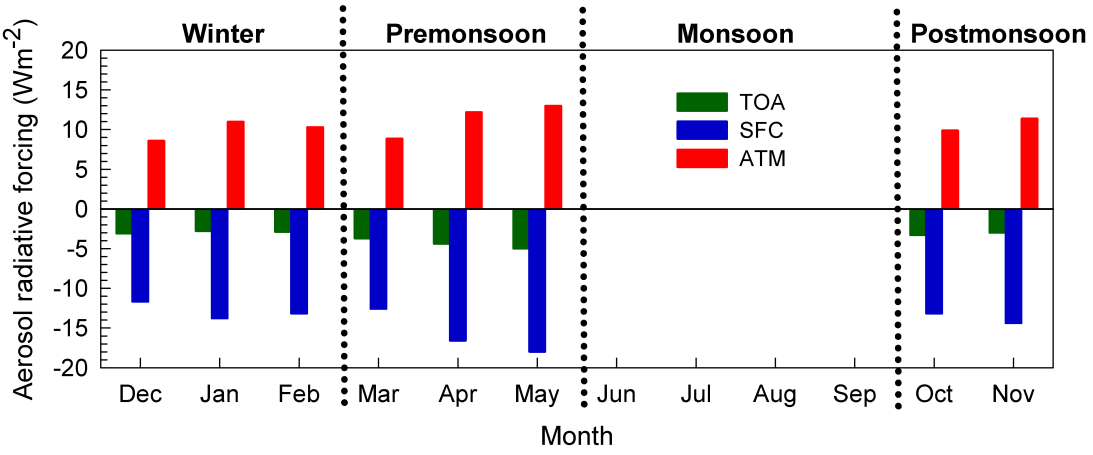

Figure 5.15: *Clear sky aerosol radiative forcing (ARF) (Wm^{-2}) at the TOA (top of the atmosphere), SFC (surface) and ATM (atmosphere) corresponding to ambient relative humidity estimated using columnar single scattering albedo (SSA) (Method 2) over Gurushikhar during 2015-2016 as function of season (winter, premonsoon, monsoon, and postmonsoon).*

values are comparable over Gurushikhar because differences in surface and columnar *SSA* are small (Table 5.2) when estimated from surface (Method 1) and columnar (Method 2) *SSA*.

Over Gurushikhar the maximum and minimum surface cooling are estimated during premonsoon and winter (Table 5.2). *ATM* forcing shows maximum variation during premonsoon (Table 5.2) owing to the presence of long-grange transported dust particles in the atmosphere. The annual mean *TOA* and *SFC* forcing are lower by a factor of 2 than Ahmedabad due to the lower *AOD* and higher columnar *SSA* (Table 5.2).

5.5.2 Radiative forcing due to black carbon aerosols

The *TOA* forcing for BC aerosols only ranges from 1.2 to 1.4 Wm^{-2} and does not show large variations as compared to composite aerosols over Gurushikhar. *TOA* forcing for BC aerosols only is also found to be a factor of 2 lower than Ahmedabad. *TOA* forcing is positive for BC aerosols only, whereas it is negative for composite aerosols. *SFC* forcing decreases from January to May and then

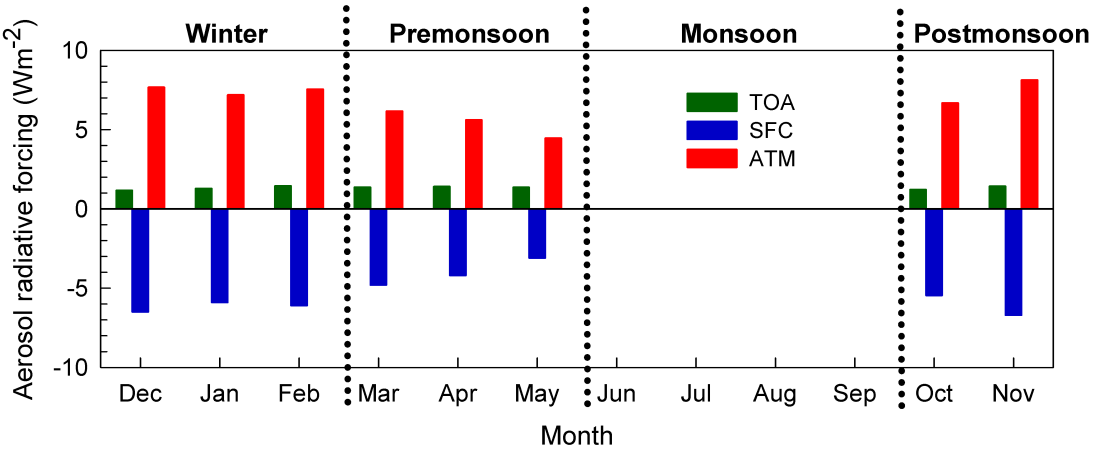

Figure 5.16: *Clear sky aerosol radiative forcing (Wm^{-2}) for black carbon aerosols only at the TOA (top of the atmosphere), SFC (surface) and ATM (atmosphere) over Gurushikhar during 2015-2016 as function of season (winter, premonsoon, monsoon, and postmonsoon).*

gradually increases from October to November (Figure 5.16). The *SFC* forcing by BC aerosols only is always lower as compared to composite aerosols (Figure 5.16). The maximum and minimum *SFC* forcing by BC aerosols is found during November and May respectively (Figure 5.16) which are consistent with the BC mass variation. The *ATM* forcing due to BC aerosols only decreases from February to May and increases from October to November (Figure 5.16). The maximum atmospheric (*ATM*) forcing due to BC aerosols only is found in November over Gurushikhar, which is found to be consistent with the maximum BC mass concentrations during this month (Figure 5.16). As the BC mass over Gurushikhar is found to be lower by a factor of 4 than Ahmedabad, the OPAC estimated *AOD* for BC aerosols only over Gurushikhar is a factor of 2-3 lower than Ahmedabad, and the resultant forcing due to BC aerosols only over Gurushikhar is found to lower by a factor of 2-3 than Ahmedabad BC forcing values. The maximum *SFC* forcing due to BC aerosols only is found during winter (-6.2 Wm^{-2}) followed by postmonsoon (-6.1 Wm^{-2}) and premonsoon (-4.0 Wm^{-2}). During the study period the maximum and minimum *ATM* forcing due to BC aerosols only is estimated during winter (7.5 Wm^{-2}) and premonsoon (5.4 Wm^{-2}). The annual mean shortwave *ARF* due to BC aerosols

only at *TOA*, *SFC*, and *ATM* are found to be 1.3 $\pm$ 0.1, -5.4 $\pm$ 1.2, and 6.7 $\pm$ 1.2 Wm^{-2} over Gurushikhar. The principal aerosol parameter that influences *ARF* in case of BC aerosols only is *AOD*, because *AODs* over Gurushikhar are lower than Ahmedabad by a factor of 2-3 while *SSA* and *g* remain the same for both locations.

The *TOA* forcing estimated for BC aerosols only is higher than the *TOA* forcing obtained from Method 1 and 2 over Gurushikhar due to the lower *SSA* for BC aerosols only (Table 5.2). The forcing due to BC aerosols only is lower by a factor of $\sim$ 2 when compared to Ahmedabad (Table 5.2) which is corroborated with the similar variations seen in *AOD*. The *SFC* forcing for BC aerosols and estimated following Methods 1 and 2, vary by a factor of $\sim$ 3 (Table 5.2) due to the significant differences in *AOD*. The study reveals that over a high altitude remote location BC aerosols alone can contribute $\sim$ 60% to the shortwave atmospheric forcing which is least affected by anthropogenic activities.

5.5.3 Atmospheric heating rate

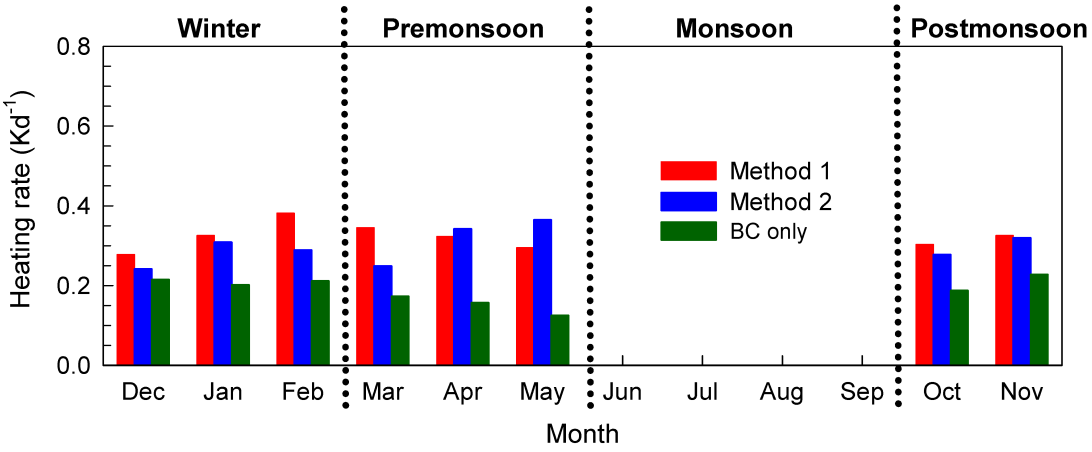

Figure 5.17: *Monthly mean heating rate (Kelvin per day, Kd^{-1}) for composite aerosols estimated using Method 1 and Method 2 over Gurushikhar during 2015 - 2016 as function of season (winter, premonsoon, monsoon, and postmonsoon).*

The atmospheric heating rate decreases from February to May and later on it decreases from November to December (Figure 5.17). November exhibits the maximum heating rate over Gurushikhar (Figure 5.17), which is consistent with the minimum *SSA* during this month. The monthly mean shortwave composite atmospheric heating rate estimated using columnar *SSA* (Method 2) is lower by a factor of 1.5 when compared to Method 1 (surface *SSA*) as function of season (Figure 5.17). The composite heating rate estimated from Method 2 decreases from January to March (Figure 5.17). The monthly mean atmospheric heating rate (Method 2) is found to be the maximum during May over Gurushikhar (Figure 5.17), consistent with the maximum *AOD* during this month. The variations in atmospheric heating rate for BC aerosols only is consistent with the variations in BC mass concentrations (Figure 5.17). The maximum heating rate for BC aerosols only is found in November (0.23 Kd^{-1}) (Figure 5.17). During winter, the heating rate due to BC aerosols only is maximum (Method 1) over Gurushikhar (0.21 Kd^{-1}), which is in agreement with seasonal variation in black carbon aerosols over Gurushikhar. The present study shows that the magnitude of atmospheric heating rate estimated using Method 1 (surface *SSA*) and Method 2 (columnar *SSA*) is comparable over a high altitude remote location (Gurushikhar). Ahmedabad heating rate is a factor of $\sim$2 higher than Gurushikhar due to higher BC concentration over Ahmedabad.

In Gurushikhar, the aerosol radiative forcing estimated using Method 1 and Method 2 are comparable because the percentage difference between the surface and columnar *SSA* is $<$ 10% as compared to Ahmedabad where it is $>$ 16%. The study reveals that BC aerosols alone contribute $\sim$60% to the shortwave atmospheric forcing over both the urban (Ahmedabad) and high altitude remote (Gurushikhar) locations. This rather unexpected result on similar percentage contribution of BC aerosols to radiative forcing suggests that even very low BC concentrations can significantly perturb the Earth-atmosphere radiative balance. The study reveals that large spatial and temporal variations in aerosol properties over urban (Ahmedabad) and high altitude remote (Gurushikhar) locations can produce significant regional variabilities in aerosol

radiative effects.

5.6 Comparison of aerosol radiative forcing

ARF_{TOA}, ARF_{SFC}, ARF_{ATM}, and atmospheric heating rate from the present study over Ahmedabad (urban location) and Gurushikhar (high altitude remote location) are compared with results obtained from earlier studies over different continental and high altitude locations in India (Table 5.3). At the outset, the forcing and heating rate show large spatial and temporal differences over different locations (Table 5.2). One of the previous studies over Ahmedabad by *Ramachandran and Kedia* (2011) estimated and reported the *ARF* during 2006-2008 using the surface measured *SSA*. They showed that the *ATM* forcing was lower during monsoon and winter, while the values were higher during premonsoon and postmonsoon (Table 5.3). The forcing and heating rate values are comparable to the present study estimated values using Method 1, however, the differences become larger when compared to the results obtained using Method 2 due to differences in the *SSA*. The atmospheric heating rate were found in the range of 1.13 to 1.51 Kd^{-1} during 2006-2008 while the values are in the range of 1.26 to 1.67 Kd^{-1} over Ahmedabad in the present study (Method 1) excluding the monsoon season. The forcing and heating rate estimated using columnar *SSA* (Method 2) over Ahmedabad are lower by a factor of two than the values obtained from Method 1 in the present study. The *ATM* forcing and heating rates over Delhi are higher than the values found over Ahmedabad (Table 5.3). The higher forcing over Delhi, an urban location is due to higher *AOD* and lower *SSA* (abundance of absorbing aerosols) throughout the year (*Singh et al.*, 2010). Over Kanpur, an urban location in Indo Gangetic Plains the forcing is estimated using columnar *SSA* and the forcing and heating rate values are higher than Ahmedabad (Method 2) due to lower *SSA* (Table 5.3) (*Ramachandran and Kedia*, 2012). The *TOA* forcing is found to be positive in the range of 0.7 to 8.4 Wm^{-2} over Visakhapatnam during all the seasons indicating higher concentration of absorbing aerosols throughout the year (*Sreekanth et al.*, 2007). The forcing and heating

Table 5.3: *Aerosol radiative forcing (ARF) (Wm^{-2}) at the TOA (top of the atmosphere), SFC (surface) and ATM (atmosphere) along with the heating rate (Kd^{-1}) over different environments in India.*

Location Region, Period *Reference*	Season	Aerosol radiative forcing (Wm^{-2})			Heating rate (Kd^{-1})
		TOA	SFC	ATM	
Ahmedabad	Winter	0.8 ± 0.1	-44.0 ± 3.4	44.8 ± 3.4	1.26 ± 0.10
Urban, 2015-16	Premonsoon	4.5 ± 0.6	-46.7 ± 5.4	51.2 ± 5.1	1.44 ± 0.14
Present study	Monsoon	-	-	-	-
(Method 1)	Postmonsoon	5.7 ± 0.9	-53.9 ± 6.3	59.6 ± 7.1	1.67 ± 0.20
Ahmedabad	Winter	-7.2 ± 2.4	-24.3 ± 2.1	17.1 ± 1.7	0.48 ± 0.05
Urban, 2015-16	Premonsoon	-8.3 ± 1.3	-25.9 ± 3.2	17.6 ± 2.1	0.49 ± 0.06
Present study	Monsoon	-	-	-	-
(Method 2)	Postmonsoon	-8.0 ± 0.6	-27.1 ± 1.1	19.1 ± 1.4	0.54 ± 0.01
Ahmedabad	Winter	0.8	-41.1	41.9	1.13
Urban, 2006-08	Premonsoon	4.4	-44.7	49.1	1.38
Ramachandran and	Monsoon	-0.7	-34.3	33.6	0.94
Kedia (2011)	Postmonsoon	5.7	-48.3	54.0	1.51
Delhi	Winter	5.0	-64.0	69.0	1.94
Urban, 2006-07	Premonsoon	2.7	-82.1	84.8	2.38
Singh et al. (2010)	Monsoon	11.7	-62.2	74.0	2.08
	Postmonsoon	5.1	-66.3	71.4	2.00
Kanpur	Winter	-9.9	-33.6	23.7	0.44
Urban, 2006-08	Premonsoon	-4.6	-40.8	36.2	0.67
Ramachandran and	Monsoon	-6.3	-30.9	24.6	0.46
Kedia (2012)	Postmonsoon	-12.0	-36.5	24.5	0.45
Visakhapatnam	Winter	8.4	-35.8	44.2	1.24
Urban, 2005-06	Premonsoon	4.0	-16.8	20.8	0.58
Sreekanth et al. (2007)	Monsoon	2.4	-9.9	12.3	0.34
	Postmonsoon	0.7	-2.8	3.5	0.10
Gurushikhar	Winter	-2.4 ± 0.2	-14.1 ± 1.9	11.7 ± 1.9	0.33 ± 0.05
Remote, 2015-16	Premonsoon	-3.9 ± 0.5	-15.3 ± 0.6	11.4 ± 0.9	0.32 ± 0.03
Present study	Monsoon	-	-	-	-
(Method 1)	Postmonsoon	-3.2 ± 0.2	-14.4 ± 0.7	11.2 ± 0.8	0.31 ± 0.02
Gurushikhar	Winter	-2.9 ± 0.8	-12.9 ± 1.1	10.0 ± 1.2	0.28 ± 0.04
Remote, 2015-16	Premonsoon	-4.4 ± 0.8	-15.7 ± 2.8	11.3 ± 2.2	0.32 ± 0.06
Present study	Monsoon	-	-	-	-
(Method 2)	Postmonsoon	-3.2 ± 0.3	-13.8 ± 0.8	10.6 ± 1.1	0.30 ± 0.03
Gurushikhar	Winter	-3.0	-7.3	4.3	0.12
Remote, 2015-16	Premonsoon	-5.0	-14.0	9.0	0.25
Ramachandran and	Monsoon	-	-	-	-
Kedia (2011)	Postmonsoon	-4.5	-10.0	5.5	0.15
Manora Peak	Winter	-0.70 ± 0.20	-6.7 ± 3.2	6.0 ± 3.0	0.17 ± 0.09
Remote, 2006-08	Premonsoon	3.50 ± 1.70	-25.0 ± 4.8	28.4 ± 4.9	0.80 ± 0.14
Srivastava et al. (2015)	Monsoon	-0.02 ± 0.70	-12.1 ± 2.1	12.1 ± 2.7	0.34 ± 0.08
	Postmonsoon	-0.70 ± 0.20	-6.9 ± 1.1	6.2 ± 1.3	0.17 ± 0.04

rate values are comparable to Ahmedabad (Method 1) (Table 5.3). The forcing estimated over Gurushikhar (a high altitude location in western India) using Method 1 and Method 2 are comparable (Table 5.3). Aerosol radiative forcing over Gurushikhar during 2015-2016 (present study) is comparable to an earlier study conducted in 2007 by *Ramachandran and Kedia* (2011). The forcing and heating rate values are found to be lower than Ahmedabad values (Table 5.3). The forcing values are found to higher than reported over Manora Peak (a high altitude location in central Himalaya) (*Srivastava et al.*, 2015). The aerosol radiative forcing exhibits a significant spatial and seasonal variation (Table 5.3).

Chapter 6

Summary and scope for future work

Aerosols can influence our planet by interacting with incoming solar and outgoing radiation, and exhibit large spatio-temporal variabilities in their optical and physical properties. The objectives of the thesis are to characterize the spatial and temporal variabilities in optical and physical properties of aerosols, apportion black carbon aerosols in terms of their sources, and estimate the aerosol radiative forcing and their seasonal variability over an urban and a high altitude remote location in western India. Aerosol characteristics were measured and analysed over an urban environment (characterized by high aerosol concentrations dominated by anthropogenic aerosols) (Ahmedabad (23.03^{o}N, 72.55^{o}E, 55 m above mean sea level (AMSL)), and a high altitude remote region (with low aerosol concentration dominated by transport) (Gurushikhar (24.65^{o}N, 72.78^{o}E, 1680 m AMSL) over western India. Both the study locations in western India were found influenced by similar meteorology. Aerosol properties (scattering and absorption coefficients, backscattering coefficient, single scattering albedo (*SSA*), Ångström exponent, backscatter fraction, asymmetry parameter, aerosol optical depth (*AOD*)), and black carbon (BC) aerosol mass concentration (and its source apportionment) have been analysed to investigate their diurnal, monthly, and seasonal variabilities over Ahmedabad and Gurushikhar. The influence of atmospheric aerosols on the Earth's radiation budget is examined using radiative transfer model. The shortwave aerosol radiative forcing is estimated using surface SSA (derived from the surface measurements of aerosol scattering and absorption coefficients using nephelometer and aethalometer respectively - Method 1), and using columnar SSA (from

remote sensing satellite measurement - Method 2). Further, to delineate the impact of black carbon (BC) aerosols on the Earth-atmosphere radiation budget the shortwave radiative forcing is computed for BC aerosols only over both the study locations. Major results obtained from these investigations are summarized below and the scope for future work are discussed.

6.1 Summary of results

6.1.1 Urban location: Ahmedabad

The major findings obtained from the study over urban, Ahmedabad are summarized as follows:

1. Aerosol scattering (β_{sca}) and absorption (β_{abs}) coefficients exhibit strong temporal variation due to diurnal variations in emission sources and their strengths, and atmospheric boundary layer. High values of β_{sca} and β_{abs} during morning and late evening hrs coincide with an increase in anthropogenic activities and atmospheric boundary layer dynamics. β_{sca} and β_{abs} decrease as day advances due to the evolution of atmospheric boundary layer and attains a minimum around afternoon when emissions are low. A systematic seasonal variation is found in β_{sca} and β_{abs}, with winter maximum and monsoon minimum. Higher values of β_{sca} and β_{abs} measured during winter and postmonsoon are attributed to shallow atmospheric boundary layer, and increase in anthropogenic emissions. During premonsoon and monsoon, the air masses originate/travel from/over Arabian Sea bringing in relatively clean air masses with less continental influence to the observational site, which results in decrease in these values. The annual mean β_{sca} and β_{abs} are found to be 235 ± 128 and 64 ± 40 Mm^{-1} respectively.

2. The diurnal variation in single scattering albedo (*SSA*, ratio of scattering to extinction coefficient) is anti-correlated with β_{sca} and β_{abs} over the urban location, Ahmedabad. The morning and evening dips in *SSA*

throughout the year suggest a consistent and significant presence of absorbing aerosols from fossil fuel and biomass burning emissions over Ahmedabad. *SSA* is maximum during monsoon (0.83 $\pm$ 0.03) due to the dominance of scattering type aerosols as air masses that travel over Arabian Sea bring in scattering type aerosols to the study location. The minimum *SSA* is observed during postmonsoon (0.77 $\pm$ 0.02) revealing the dominance of absorbing type aerosols over Ahmedabad. The surface *SSA* is lower than the columnar *SSA* as most of the black carbon (which are absorbing species) are concentrated near the surface, hence, the aerosol absorption coefficients near the surface will be higher when compared to the column. The annual mean surface and column *SSA* are found to be 0.81 $\pm$ 0.03 and 0.91 $\pm$ 0.01 respectively.

3. *Ångström exponent* (α) and *backscatter fraction* (*b*) exhibit morning and evening peaks, whereas *asymmetry parameter* (*g*) shows corresponding dips which coincide with the peaks observed in β_{sca} and β_{bsca}. As the particle size increases *g* will increase, and α and *b* will decrease leading to an anti-correlation between α and *g*, and *b* and *g*. Higher α and *b*, and lower *g* indicate the dominance of smaller size particles, whereas, lower α and *b*, and higher *g* indicate the dominance of larger size particles. The morning and evening peaks in α and *b*, and dips in *g* suggest the dominance of smaller size aerosols over urban, Ahmedabad. The parameters α, *b*, and *g* exhibit significant monthly and seasonal variations over Ahmedabad. The highest α and *b*, and lowest *g* are observed during postmonsoon corroborating the dominance of smaller size aerosols from the anthropogenic emissions, whereas the lowest α and *b*, and highest *g* are found in monsoon reveal the dominance of larger particles reaching the observational site from the marine region (Arabian Sea). The annual mean α, *b*, and *g* are found to be 1.43 $\pm$ 0.26, 0.13 $\pm$ 0.01, and 0.60 $\pm$ 0.03 respectively over Ahmedabad.

4. The aerosol optical depth (*AOD*) at 0.55 μm is found to be in the 0.2-0.7 range. The maximum and minimum *AOD* is found during April and De-

cember. The highest *AOD* is found during postmonsoon followed by premonsoon and winter. The annual mean *AOD* over Ahmedabad during 2015-2016 is 0.41 $\pm$ 0.09.

5. Black carbon (BC) aerosol mass concentration exhibits strong diurnal variation. Night time average BC values are 1.5 times higher than the day time BC values as the atmospheric boundary layer is shallow during night time resulting in trapping of pollutants in a lesser volume which leads to higher BC mass concentration. The average annual percentage contributions of day time and night time BC aerosols are 40 and 60% respectively over Ahmedabad. Maximum BC mass concentration is observed during winter due to the significant increase in the anthropogenic emissions and lower atmospheric boundary layer height, whereas the minimum is found during monsoon due to wet removal of aerosols by precipitation. The annual mean BC mass concentration is 6.0 $\pm$ 3.9 $\mu g m^{-3}$.

6. The contribution of fossil fuel (BC_{ff}) and wood burning (BC_{wb}) to total BC mass show significant diurnal, monthly and seasonal variations over Ahmedabad. The contribution of BC_{ff} was higher by a factor of 2-4 than BC_{wb}, and dominates throughout the day, which indicates persistent anthropogenic activities over Ahmedabad. Highest BC_{ff} (84%) contribution to total BC occurs during monsoon as the BC emissions from wood burning is low due to prevailing wet conditions, while highest BC_{wb} (23%) contribution to the total BC is during winter season due to significant increase in biomass (wood) burning. Annual mean contributions of BC_{ff} and BC_{wb} to total BC mass concentration are found to be 80 and 20% respectively over Ahmedabad.

7. Aerosol radiative forcing has been estimated using surface SSA derived from the measurements of aerosol scattering and absorption coefficients (Method 1) and columnar SSA from the satellite (Method 2). The *ATM* forcing following Method 2 is a factor of 3 lower than Method 1 over Ahmedabad. The significant differences in forcing are due to the differences in the *SSA* as *AOD* remains same in both the methods. The an-

nual mean shortwave *TOA* forcing (Method 2) flips its sign from 3.9 to -7.8 Wm^{-2} due to the contribution of higher *SSA* with respect to Method 1. During the study period the maximum and minimum surface cooling are estimated during postmonsoon and winter respectively. *ATM* forcing and heating rate exhibit a typical variation throughout the year and show maximum variation during postmonsoon and winter because of higher contribution of black carbon aerosols arising from anthropogenic emissions enhanced by the conducive meteorological conditions (atmospheric boundary layer and wind speed). The annual mean *TOA*, *SFC*, *ATM*, and heating rate are estimated to be 3.4, -47.5, 50.9 Wm^{-2}, and 1.43 Kd^{-1}, and -7.8, -25.6, 17.8 Wm^{-2}, and 0.50 Kd^{-1} following Methods 1 and 2 respectively.

8. The *TOA* forcing estimated for BC aerosols only is comparable with the *TOA* forcing from Method 1 because *SSA* is comparable in both the methods. The *SFC* forcing varies by a factor of ~ 6 due to the significant contribution of *AOD*. The resultant *ATM* forcing for BC aerosols is lower by a factor of ~ 4 when compared to Method 1. The *SFC* and *ATM* forcing for BC aerosols only are lower by a factor of ~ 2 as compared to Method 2. The study reveals that BC aerosols alone can contribute $\sim 60\%$ to the shortwave atmospheric forcing when compared to Method 2 (higher *SSA*), whereas it contributes ~ 20 % when compared to Method 1 (lower *SSA*) over Ahmedabad, an urban region.

6.1.2 High altitude remote location: Gurushikhar, Mt. Abu

The major findings obtained from the study over Gurushikhar, a high altitude remote site are summarized as follows:

1. Aerosol scattering (β_{sca}) and absorption (β_{abs}) coefficients exhibit peculiar diurnal variability with higher afternoon values as compared to forenoon and night because of fully evolved atmospheric boundary layer which accompanied with strong thermal convection aid an upward transport of aerosols to the mountain site from the surrounding

foothills during afternoon hours. The monthly variability of β_{sca} is different than that of β_{abs}, however, the seasonal mean β_{sca} and β_{abs} go hand in hand with each other. β_{sca} and β_{abs} exhibit a significant seasonal variability, and are highest during postmonsoon followed by winter, because the measurement site is influenced by convection from the foothills and advection through longrange transport and a significant increase in the amount of biomass burning and tourist activities in the region. The minimum β_{sca} and β_{abs} are observed during monsoon due to the wet removal. The annual mean β_{sca} and β_{abs} are estimated as 78 ± 31 and $12 \pm 6\ Mm^{-1}$ respectively over Gurushikhar, which are lower by a factor of 3 and 5 respectively than Ahmedabad.

2. The surface single scattering albedo (*SSA*) shows a rare diurnal variability over Gurushikhar when compared to Ahmedabad. Highest *SSA* is observed during monsoon due to the dominance of sea salt reaching the site from the Arabian Sea through advection. Minimum *SSA* is observed during winter due to the dominance of the absorbing type aerosols arriving to the observational site from the northern region of India. The surface *SSA* is higher over Gurushikhar than Ahmedabad *SSA* due to the dominance of absorbing aerosols over Ahmedabad from the anthropogenic emissions. The annual mean surface and column *SSA* are found to be 0.87 ± 0.04 and 0.95 ± 0.01 respectively over Gurushikhar. Over Gurushikhar, the surface *SSA* is lower than column *SSA* despite being a high altitude remote site. However, when compared to Ahmedabad surface and column *SSA* are higher over Gurushikhar, though the differences between surface and column *SSA* are lower over Gurushikhar.

3. The diurnal variation in *Ångström exponent* (α), *backscatter fraction* (*b*), and *asymmetry parameter* (*g*) over Gurushikhar do not show any morning or evening peaks as observed over Ahmedabad consistent with β_{sca} and β_{abs} variations. The low α values corroborate the low *b* values which indicate the dominance of higher size aerosols in the size distribution. However, the *b* values found over Gurushikhar are similar to the values

observed over Ahmedabad perhaps indicating the characteristic feature of the western India region. The maximum α observed during winter suggests the dominance of smaller size aerosols reaching the observational site through convection from foothills. The minimum α and *b*, and maximum *g* found during monsoon suggest the dominance of larger particles reaching the observational site from the marine region (Arabian Sea). The annual mean α, *b*, and *g* are estimated to be 1.19 $\pm$ 0.31, 0.12 $\pm$ 0.01, and 0.61 $\pm$ 0.02 respectively over Gurushikhar.

4. The aerosol optical depth (*AOD*) over Gurushikhar is lower than Ahmedabad, as Ahmedabad is consistently influenced by the high magnitude of anthropogenic emissions, whereas Gurushikhar is less influenced by the local than the longrange transported aerosols through convection and advection. The highest *AOD* is found during postmonsoon followed by premonsoon and winter. The annual mean *AOD* over Gurushikhar is 0.23 $\pm$ 0.05, which is a factor of 2 lower than Ahmedabad.

5. A distinct variation in BC mass concentration is observed over Gurushikhar with an increase in BC concentration during noontime due to strong thermal convection whereby pollutants from the foothills rise up to the site. At Gurushikhar, day time and night time BC contributions are more or less equal throughout the year, suggesting that this could be the characteristic feature of the aerosol component produced by anthropogenic sources over a background region. The annual mean percentage day time and night time BC contributions are 52 and 48% respectively. BC is highest during postmonsoon and lowest in monsoon due to meteorological dynamics (atmospheric boundary layer and wind speed) and wet removal respectively. The annual mean BC mass concentration is found to be 1.5 $\pm$ 0.8 $\mu g m^{-3}$ over Gurushikhar, which is a lower by a factor of 4 than Ahmedabad.

6. It has been found that maximum BC mass concentrations in Gurushikhar are comparable with minimum BC mass concentrations in Ahmedabad. BC is maximum in Gurushikhar when the atmospheric boundary layer

is fully evolved which aids the upward transport of anthropogenic emissions from the surrounding foothill regions, while the BC mass is minimum in Ahmedabad when the atmospheric boundary layer is fully evolved and the anthropogenic emission sources are at their minimum. This result highlights the variation in the diurnal evolution of an atmospheric species emitted by anthropogenic activities over an urban source (Ahmedabad) and a background (Gurushikhar, Mt. Abu) region, and the differences in the magnitudes of mass concentration of the aerosol species due to the evolution of atmospheric boundary layer.

7. The diurnal contribution of BC_{ff} in total BC dominates throughout the day. The annual mean contribution of BC_{ff} and BC_{wb} to total BC mass concentrations are found to be 72 and 28% respectively over Gurushikhar and dominated by fossil fuel component of BC. The study suggests that Gurushikhar despite being a high altitude remote site is influenced by fossil fuel component of black carbon aerosols through convection (local) and advection (longrange transport).

8. The composite *TOA* forcing is always negative due to the dominance of scattering aerosols (higher *SSA*). *ARF* values are comparable over Gurushikhar because of the small differences in surface and column *SSA*. The maximum and minimum surface forcing (cooling) are found during premonsoon and winter respectively. *ATM* forcing shows maximum variation during premonsoon when the atmosphere is dominated by the longrange transported dust particles. The annual mean *TOA* and *SFC* forcing over Gurushikhar are lower by a factor of 2 than Ahmedabad forcing due to lower *AOD* and higher columnar *SSA*, whereas the *ATM* forcing and heating rate estimated from Methods 1 and 2 are comparable as surface and column *SSA* are comparable.

9. The *ATM* forcing due to BC aerosols only is found to be maximum during winter while it is minimum during premonsoon. The annual mean shortwave *ARF* due to BC aerosols only at *TOA*, *SFC*, and *ATM* are found to be 1.3 ± 0.1, -5.4 ± 1.2, and 6.7 ± 1.2 Wm^{-2} over Gurushikhar. The *TOA*

forcing estimated for BC aerosols only is higher than the *TOA* forcing obtained from Method 1 and 2 over Gurushikhar due to the lower *SSA* for BC aerosols only. The forcing due to BC aerosols only is lower by a factor of $\sim$ 2 when compared to Ahmedabad which is corroborated by similar variations in *AOD*. The study reveals that even over a high altitude remote location that is less affected by anthropogenic activities BC aerosols alone can contribute $\sim$ 60% to the shortwave atmospheric forcing.

6.2 Scope for future work

The present study investigated the spatial and temporal variability in aerosol properties over an urban and a high altitude remote location in western India. As aerosol characteristics exhibit large spatial and temporal variability the precise measurements of the various aerosol properties should be continued and conducted over distinct environment in order to understand and quantify the role of anthropogenic and natural aerosols and hence better estimate their radiative effects.

The estimation of the aerosol radiative forcing was undertaken using OPAC and SBDART models which are based on several assumptions (considering aerosols of different types as external mixtures, shape of aerosol considered as spherical particles, etc.) which introduces uncertainty in the computation. Aerosols can exist as externally, and/or internally mixed state in the atmosphere. Aerosol mixing state alters the aerosol size distribution, and its chemical composition. Information about aerosol mixing state as a function of size will be useful in reducing the uncertainty in the aerosol radiative forcing estimates. Aerosol size distribution varies by orders of magnitude depending on the production and transport mechanisms, and we need to understand and correlate the aerosol size information with derived aerosol parameters such as Ångström exponent, backscatter fraction, and asymmetry parameter.

Physical and optical properties and aerosol radiative forcing can vary as

a function of relative humidity (*RH*). In order to characterize and quantify the effect of relative humidity on aerosols the optical and physical properties of aerosols should be corrected for variations in ambient relative humidity.

Atmospheric boundary layer governs the diurnal characteristics of surface aerosol characteristics, and its diurnal evolution is required to quantify its influence on surface as well as column aerosol characteristics over different environmental regimes. The information about atmospheric boundary layer is required to further delineate the contribution of aerosols from convective and advective process over a high altitude remote region which is significantly influenced by a nearby source (urban) region.

Aerosols play an important and significant role in the formation of clouds, and serves as cloud condensation nuclei around which cloud droplets are formed. Hence, the measurements of aerosols along with cloud properties are required to study aerosol-cloud interaction, and their effect on rainfall. Aerosols exhibit significant altitudinal variations and information about their vertical distribution is required to reduce the uncertainty in the atmospheric heating rate. The vertical distribution of aerosols influence the cloud formation and hence the precipitation. The columnar aerosol properties (aerosol optical depth, single scattering albedo, and asymmetry parameter) need to be simultaneously measured along with surface aerosol properties, in order to reduce the uncertainty in the direct as well as indirect aerosol radiative forcing. Further, in order to reduce the uncertainty in the aerosol radiative forcing estimates simultaneous and collocated measurements of shortwave and longwave downwelling and upwelling radiation at Earth's surface are needed.

References

Abu-Rahmah, A., W. P. Arnott, and H. Moosmüller (2006), Integrating nephelometer with a low truncation angle and an extended calibration scheme, *Meas. Sci. Tech.*, *17*(7), 1723.

Anderson, T. L., and J. A. Ogren (1998), Determining aerosol radiative properties using the TSI 3563 integrating nephelometer, *Aerosol Sci. Tech.*, *29*, 57–69.

Andrews, E., et al. (2006), Comparison of methods for deriving aerosol asymmetry parameter, *J. Geophys. Res. Atmos.*, *111*(D5), doi:10.1029/2004JD005734.

Ångström, A. (1961), Techniques of determing the turbidity of the atmosphere, *Tellus*, *13*(2), 214–223.

Arnott, W., K. Hamasha, H. Moosmüller, P. Sheridan, and J. Ogren (2005), Towards aerosol light-absorption measurements with a 7-wavelength aethalometer: Evaluation with a photoacoustic instrument and 3-wavelength nephelometer, *Aerosol Sci. Tech.*, *39*(1), 17–29.

Aruna, K., T. L. Kumar, D. N. Rao, B. K. Murthy, S. S. Babu, and K. K. Moorthy (2013), Black carbon aerosols in a tropical semi-urban coastal environment: Effects of boundary layer dynamics and long range transport, *J. Atmos. Sol. Terr. Phys.*, *104*, 116 – 125.

Babu, S. S., et al. (2011), High altitude (4520 m amsl) measurements of black carbon aerosols over western trans-Himalayas: Seasonal heterogeneity and source apportionment, *J. Geophys. Res. Atmos.*, *116*(D24), doi:10.1029/2011JD016722.

Beegum, S. N., et al. (2009), Spatial distribution of aerosol black carbon over India during pre-monsoon season, *Atmos. Environ.*, *43*, 1071–1078.

Bohren, C. F., and D. R. Huffman (1983), *Absorption and scattering of light by small particles*, John Wiley & Sons, Inc.

Bond, T. C., and R. W. Bergstrom (2006), Light absorption by carbonaceous particles: An Investigative review, *Aerosol Sci. Tech.*, *40*(1), 27–67.

Bond, T. C., D. G. Streets, K. F. Yarber, S. M. Nelson, J.-H. Woo, and Z. Klimont (2004), A technology-based global inventory of black and organic carbon emissions from combustion, *J. Geophys. Res. Atmos.*, *109*(D14), doi:10.1029/2003JD003697.

Brasseur, G. P., R. G. Prinn, and A. A. P. Pszenny (2003), *Atmospheric Chemistry in a Changing World*, Springer-Verlag.

Chameides, W. L., et al. (1999), Case study of the effects of atmospheric aerosols and regional haze on agriculture: An opportunity to enhance crop yields in China through emission controls?, *Proc. Natl. Acad. Sci.*, *96*(24), 13,626–13,633.

Charlson, R. J., D. S. Convert, and T. V. Larson (1984), Observation of the effect of relative humidity on light scattering by aerosols in Hygroscopic Aerosols, Deepak, A., Hampton, Va.

Collaud Coen, M., et al. (2010), Minimizing light absorption measurement artifacts of the aethalometer: evaluation of five correction algorithms, *Atmos. Meas. Tech.*, *3*, 457–474.

d'Almeida, G. A., P. Koepke, and E. P. Shettle (1991), *Atmospheric Aerosols: Global Climatology and Radiative Characteristics*, A. Deepak, Hampton, Virginia, USA.

Day, D. E., J. L. Hand, C. M. Carrico, G. Engling, and W. C. Malm (2006), Humidification factors from laboratory studies of fresh smoke from biomass fuels, *J. Geophys. Res. Atmos.*, *111*(D22), doi:10.1029/2006JD007221.

Draxler, R. R., and G. D. Hess (1998), An overview of the HYSPLIT_4 modelling system for trajectories, dispersion and deposition, *Aust. Meteorol. Mag.*, *47*(4), 295–308.

Drinovec, L., et al. (2015), The "dual-spot" aethalometer: an improved measurement of aerosol black carbon with real-time loading compensation, *Atmos. Meas. Tech.*, *8*(5), 1965–1979.

Dumka, U., K. K. Moorthy, R. Kumar, P. Hegde, R. Sagar, P. Pant, N. Singh, and S. S. Babu (2010), Characteristics of aerosol black carbon mass concentration over a high altitude location in the Central Himalayas from multi-year measurements, *Atmos. Res.*, *96*(4), 510 – 521.

Dumka, U., R. Manchanda, P. Sinha, S. Sreenivasan, K. Moorthy, and S. S. Babu (2013), Temporal variability and radiative impact of black carbon aerosol over tropical urban station Hyderabad, *J. Atmos. Sol. Terr. Phys.*, *105-106*, 81–90.

Fan, A., W. Chen, L. Liang, W. Sun, Y. Lin, H. Che, and X. Zhao (2017), Evaluation and comparison of long-term MODIS C5.1 and C6 products against AERONET observations over China, *Remote Sens.*, *9*(12), 1269.

Favez, O., et al. (2010), Inter-comparison of source apportionment models for the estimation of wood burning aerosols during wintertime in an Alpine city (Grenoble, France), *Atmos. Chem. Phys.*, *10*(12), 5295–5314.

Forbes, M., R. Raison, and J. Skjemstad (2006), Formation, transformation and transport of black carbon (charcoal) in terrestrial and aquatic ecosystems, *Sci. Total Environ.*, *370*(1), 190–206.

Fuller, G. W., A. H. Tremper, T. D. Baker, K. E. Yttri, and D. Butterfield (2014), Contribution of wood burning to PM10 in London, *Atmos. Environ.*, *87*(0), 87–94.

Gadhavi, H., and A. Jayaraman (2010), Absorbing aerosols: contribution of biomass burning and implications for radiative forcing, *Ann. Geophys.*, *28*(1), 103–111.

Ganguly, D., H. Gadhavi, A. Jayaraman, T. A. Rajesh, and A. Misra (2005), Single scattering albedo of aerosols over the central India: Implications for the regional aerosol radiative forcing, *Geophys. Res. Lett.*, *32*, doi:10.1029/2005GL023903.

Ganguly, D., and A. Jayaraman (2006), Physical and optical properties of aerosols over an urban location in western India: Implications for shortwave radiative forcing, *J. Geophys. Res.*, *111*(D24), doi:10.1029/2006JD007393.

Ganguly, D., A. Jayaraman, T. A. Rajesh, and H. Gadhavi (2006), Wintertime aerosol properties during foggy and nonfoggy days over urban center Delhi and their implications for shortwave radiative forcing, *J. Geophys. Res. Atmos.*, *111*(D15), doi:10.1029/2005JD007029.

Gong, X., C. Zhang, H. Chen, S. A. Nizkorodov, J. Chen, and X. Yang (2016), Size distribution and mixing state of black carbon particles during a heavy air pollution episode in Shanghai, *Atmos. Chem. Phys.*, *16*(8), 5399–5411.

Gundel, L., R. Dod, H. Rosen, and T. Novakov (1984), The relationship between optical attenuation and black carbon concentration for ambient and source particles, *Sci. Total Environ.*, *36*, 197–202.

Hansen, A. D. A., H. Rosen, and T. Novakov (1984), The Aethalometer - an instrument for the real-time measurement of optical absorption by aerosol particles, *Sci. Total Environ.*, *36*, 191–196.

Haywood, J., and V. Ramaswamy (1998), Global sensitivity studies of the direct radiative forcing due to anthropogenic sulfate and black carbon aerosols, *J. Geophys. Res. Atmos.*, *103*(D6), 6043–6058.

Haywood, J. M., and K. P. Shine (1995), The effect of anthropogenic sulfate and soot aerosol on the clear sky planetary radiation budget, *Geophys. Res. Lett.*, *22*(5), 603–606.

Heintzenberg, J. (1997), *The life cycle of the atmospheric aerosol*, Boutron.

Herich, H., C. Hueglin, and B. Buchmann (2011), A 2.5 year's source apportionment study of black carbon from wood burning and fossil fuel combustion at urban and rural sites in Switzerland, *Atmos. Meas. Tech.*, *4*(7), 1409–1420.

Hess, M., P. Koepke, and I. Schult (1998), Optical Properties of Aerosols and Clouds: The Software Package OPAC, *Bull. Am. Meteorol. Soc.*, *79*, 831–844.

Hyvärinen, A.-P., et al. (2013), Correction for a measurement artifact of the multi-angle absorption photometer (MAAP) at high black carbon mass concentration levels, *Atmos. Meas. Tech.*, *6*(1), 81–90.

IPCC (2007), Summary for policymakers, in *Climate Change 2007: The Physical Science Basis. Contribution of Working Group I to the Fourth Assessment Report of the Intergovernmental Panel on Climate Change*, edited by T. Stocker, D. Qin, G.-K. Plattner, M. Tignor, S. Allen, J. Boschung, A. Nauels, Y. Xia, V. Bex, and P. Midgley, pp. 1–18, Cambridge University Press, Cambridge, United Kingdom.

IPCC (2013), Summary for policymakers, in *Climate Change 2013: The Physical Science Basis. Contribution of Working Group I to the Fifth Assessment Report of the Intergovernmental Panel on Climate Change*, edited by T. Stocker, D. Qin, G.-K. Plattner, M. Tignor, S. Allen, J. Boschung, A. Nauels, Y. Xia, V. Bex, and P. Midgley, pp. 1–30, Cambridge University Press, Cambridge, United Kingdom.

Isaksen, I., et al. (2009), Atmospheric composition change: climate–chemistry interactions, *Atmos. Environ.*, *43*(33), 5138–5192.

Jacobson, M. Z. (2001), Strong radiative heating due to the mixing state of black carbon, *Nature*, *409*, 695–697.

Jaenicke, R. (1993), Tropospheric aerosols, in *Aerosol-Cloud-Climate Interactions*, *International Geophysics*, vol. 54, edited by P. V. Hobbs, pp. 1–31, Academic Press.

Jayaraman, A., D. Lubin, S. Ramachandran, V. Ramanathan, E. Woodbridge, W. D. Collins, and K. S. Zalpuri (1998), Direct observations of aerosol radiative forcing over the tropical Indian Ocean during the January-February 1996 pre-INDOEX cruise, *J. Geophys. Res.*, *103*, doi:10.1029/98JD00559.

Jayaraman, A., H. Gadhavi, D. Ganguly, A. Misra, S. Ramachandran, and T. A. Rajesh (2006), Spatial variations in aerosol characteristics and regional radiative forcing over India: Measurements and modeling of 2004 road campaign experiment, *Atmos. Environ.*, *40*, 6504–6515.

Jimenez, J., C. Claiborn, T. Larson, T. Gould, T. Kirchstetter, and L. Gundel (2007), Loading effect correction for real-time aethalometer measurements of fresh diesel soot, *J. Air Waste Manage. Assoc.*, *57*(7), 868–873.

Jose, S., B. Gharai, K. Niranjan, and P. Rao (2016), Investigation on seasonal variations of aerosol properties and its influence on radiative effect over an urban location in central India, *Atmos. Environ.*, *133*, 41–48.

Kant, Y., P. Patel, A. K. Mishra, D. U. Dumka, and V. Dadhwal (2012), Diurnal and seasonal aerosol optical depth and black carbon in the Shiwalik Hills of the north western Himalayas: A case study of the Doon valley, India, *Int. J. Geol. Earth Environ. Sci.*, *2*, 173–192.

Kaufman, Y. J., et al. (1997), Passive remote sensing of tropospheric aerosol and atmospheric correction for the aerosol effect, *J. Geophys. Res. Atmos.*, *102*(D14), 16,815–16,830.

Kedia, S., and S. Ramachandran (2009), Variability in aerosol optical and physical characteristics over the Bay of Bengal and the Arabian Sea deduced from Ångström exponents, *J. Geophys. Res.*, *114*(D14), doi:10.1029/2009JD011950.

Kedia, S., S. Ramachandran, A. Kumar, and M. M. Sarin (2010), Spatiotemporal gradients in aerosol radiative forcing and heating rate over Bay of Bengal and Arabian Sea derived on the basis of optical, physical, and chemical properties, *J. Geophys. Res.*, *115*, doi:10.1029/2009JD013136.

Kedia, S., and S. Ramachandran (2011), Seasonal variations in aerosol characteristics over an urban location and a remote site in western India, *Atmos. Environ.*, *45*, 2120–2128.

Kedia, S., S. Ramachandran, T. A. Rajesh, and R. Srivastava (2012), Aerosol absorption over Bay of Bengal during winter: Variability and sources, *Atmos. Environ.*, *54*, 738–745.

Kirchstetter, T. W., T. Novakov, and P. V. Hobbs (2004), Evidence that the spectral dependence of light absorption by aerosols is affected by organic carbon, *J. Geophys. Res. Atmos.*, *109*(D21), 1–12.

Kompalli, S. K., S. S. Babu, K. K. Moorthy, V. S. Nair, M. M. Gogoi, and J. P. Chaubey (2013), Seasonal variation in the spatial distribution of aerosol black carbon over Bay of Bengal: A synthesis of multi-campaign measurements, *Atmos. Environ.*, *64*, 366–373.

Kovalev, V. A., W. E. Eichinger, and W. Eichinger (2004), *Elastic lidar: theory, practice, and analysis methods*, John Wiley & Sons.

Kumar, K. R., K. Narasimhulu, G. Balakrishnaiah, B. Reddy, K. R. Gopal, R. Reddy, S. Satheesh, K. K. Moorthy, and S. S. Babu (2011), Characterization of aerosol black carbon over a tropical semi-arid region of Anantapur, India, *Atmos. Res.*, *100*(1), 12–27.

Lau, K.-M., M.-K. Kim, and K.-M. Kim (2006), Asian summer monsoon anomalies induced by aerosol direct forcing: The role of the Tibetan Plateau, *Clim. Dyn.*, *26*, 855–864.

Levy, R. C., L. A. Remer, S. Mattoo, E. F. Vermote, and Y. J. Kaufman (2007), Secondgeneration operational algorithm: Retrieval of aerosol properties over land from inversion of moderate resolution imaging spectroradiometer spectral reflectance, *J. Geophys. Res. Atmos.*, *112*(D13), doi:10.1029/2006JD007811.

Lewis, K., W. P. Arnott, H. Moosmüller, and C. E. Wold (2008), Strong spectral variation of biomass smoke light absorption and single scattering albedo observed with a novel dual-wavelength photoacoustic instrument, *J. Geophys. Res. Atmos.*, *113*(D16), doi:10.1029/2007JD009699.

Li, C., et al. (2016), Sources of black carbon to the Himalayan-Tibetan Plateau glaciers, *Nat. Commun.*, *7*(12574), 1–7.

Li, Z., et al. (2009), Uncertainties in satellite remote sensing of aerosols and impact on monitoring its long-term trend: a review and perspective, *Ann. Geophys.*, *27*(7), 2755–2770.

Mauderly, J. L., and J. C. Chow (2008), Health effects of organic aerosols, *Inhalation Toxicol.*, *20*(3), 257–288.

McClatchey, R., R. Fenn, J. Salby, F. Volz, and J. Garing (1972), *Optical Properties of the Atmosphere*, Environ. Res. Pap., 411, 3rd ed., 2-8 pp., AFCRL, Air Force Systems Command, United States Air Force.

Mishchenko, M. I., L. D. Travis, and A. Macke (1997), *Light scattering by nonspherical particles in the atmosphere: An overview*, Deepak, Hampton, VA.

Moorthy, K. K., S. Babu, S. K. Satheesh, J. Srinivasan, and C. B. S. Dutt (2007), Dust absorption over the ''Great Indian Desert'' inferred using ground-based and satellite remote sensing, *J. Geophys. Res.*, *112*, doi:10.1029/2006JD007,690.

Nair, V. S., et al. (2007), Wintertime aerosol characteristics over the Indo-Gangetic Plain (IGP): Impacts of local boundary layer processes and long-range transport, *J. Geophys. Res. Atmos.*, *112*(D13), doi:10.1029/2006JD008099.

Niranjan, K., B. M. Rao, P. S. Brahmanandam, B. L. Madhavan, V. Sreekanth, and K. K. Moorthy (2005), Spatial characteristics of aerosol physical properties over the northeastern parts of peninsular India, *Ann. Geophys.*, *23*, 3219–3227.

Niranjan, K., B. Spandana, T. A. Devi, V. Sreekanth, and B. Madhavan (2011), Measurements of aerosol intensive properties over Visakhapatnam, India for 2007, in *Ann. Geophys.*, vol. 29, p. 973.

Pandithurai, G., R. T. Pinker, T. Takamura, and P. C. S. Devara (2004), Aerosol radiative forcing over a tropical urban site in India, *Geophys. Res. Lett.*, *31*, doi:10.1029/2004GL019702.

Panicker, A., G. Pandithurai, P. Safai, S. Dipu, and D.-I. Lee (2010), On the contribution of black carbon to the composite aerosol radiative forcing over an urban environment, *Atmos. Environ.*, *44*(25), 3066–3070.

Pant, P., P. Hegde, U. Dumka, R. Sagar, S. Satheesh, K. K. Moorthy, A. Saha, and M. Srivastava (2006), Aerosol characteristics at a high-altitude location in central Himalayas: Optical properties and radiative forcing, *J. Geophys. Res. Atmos.*, *111*(D17), doi:10.1029/2005JD006768.

Panwar, T., R. K. Hooda, H. Lihavainen, A. Hyvarinen, V. Sharma, and Y. Viisanen (2013), Atmospheric aerosols at a regional background Himalayan site Mukteshwar, India, *Environ. Monit. Assess.*, *185*(6), 4753–4764.

Park, S. S., A. D. Hansen, and S. Y. Cho (2010), Measurement of real time black carbon for investigating spot loading effects of aethalometer data, *Atmos. Environ.*, *44*(11), 1449–1455.

Pathak, B., G. Kalita, K. Bhuyan, P. Bhuyan, and K. K. Moorthy (2010), Aerosol temporal characteristics and its impact on shortwave radiative forcing at a location in the northeast of India, *J. Geophys. Res. Atmos.*, *115*(D19), doi:10.1029/2009JD013462.

Penner, J. E., C. C. Chuang, and K. Grant (1998), Climate forcing by carbonaceous and sulfate aerosols, *Clim. Dyn.*, *14*(12), 839–851.

Pilinis, C., N. Pandis, and J. Seinfeld (1995), Sensitivity of direct climate forcing by atmospheric aerosols to aerosol size and composition, *J. Geophys. Res.*, *100*, doi:10.1029/95JD02119.

Rajesh, T. A., and S. Ramachandran (2017), Characteristics and source apportionment of black carbon aerosols over an urban site, *Environ. Sci. and Pollut. Res.*, *24*(9), 8411–8424.

Rajesh, T. A., and S. Ramachandran (2018), Black carbon aerosol mass concentration, absorption and single scattering albedo from single and dual spot aethalometers: Radiative implications, *J. Aerosol Sci.*, *119*, 77–90.

Raju, M., P. Safai, P. Rao, P. Devara, and K. Budhavant (2011), Seasonal characteristics of black carbon aerosols over a high altitude station in southwest India, *Atmos. Res.*, *100*(1), 103–110.

Ramachandran, S., V. Ramaswamy, G. L. Stenchikov, and A. Robock (2000), Radiative impact of the Mount Pinatubo volcanic eruption: Lower stratospheric response, *J. Geophys. Res. Atmos.*, *105*(D19), 24,409–24,429.

Ramachandran, S. (2005), Premonsoon shortwave aerosol radiative forcings over the Arabian Sea and tropical Indian Ocean: Yearly and monthly mean variabilities, *J. Geophys. Res.*, *110*(D7), doi:10.1029/2004JD005563.

Ramachandran, S., R. Rengarajan, A. Jayaraman, M. M. Sarin, and Sanat. K. Das, (2006), Aerosol radiative forcing during clear, hazy, and foggy conditions over a continental polluted location in north India, *J. Geophys. Res.*, *111*(D20), doi:10.1029/2006JD007142.

Ramachandran, S., and T. A. Rajesh (2007), Black carbon aerosol mass concentrations over Ahmedabad, an urban location in western India: Comparison with urban sites in Asia, Europe, Canada, and the United States, *J. Geophys. Res.*, *112*(D6), doi:10.1029/2006JD007488.

Ramachandran, S., and R. Cherian (2008), Regional and seasonal variations in aerosol optical characteristics and their frequency distributions over India during 2001-2005, *J. Geophys. Res. Atmos.*, *113*(D8), doi:10.1029/2007JD008560.

Ramachandran, S., and T. A. Rajesh (2008), Asymmetry parameters in the lower troposphere derived from aircraft measurements of aerosol scattering coefficients over tropical India, *J. Geophys. Res.*, *113*(D16), doi:10.1029/2008JD009795.

Ramachandran, S., and S. Kedia (2010), Black carbon aerosols over an urban region: Radiative forcing and climate impact, *J. Geophys. Res.*, *115*(D10), doi:10.1029/2009JD013560.

Ramachandran, S., and S. Kedia (2011), Aerosol radiative effects over an urban location and a remote site in western India: Seasonal variability, *Atmos. Environ.*, *45*, 7415–7422.

Ramachandran, S., R. Srivastava, S. Kedia, and T. A. Rajesh (2012), Contribution of natural and anthropogenic aerosols to optical properties and radiative effects over an urban location, *Environ. Res. Lett.*, *7*(3), 034,028.

Ramachandran, S., and S. Kedia (2012), Radiative effects of aerosols over Indo-Gangetic plain: environmental (urban vs. rural) and seasonal variations, *Environ. Sci. and Pollut. Res.*, *19*(6), 2159–2171.

Ramachandran, S., S. Kedia, and V. Sheel (2015), Spatiotemporal characteristics of aerosols in India: Observations and model simulations, *Atmos. Environ.*, *116*, 225–244.

Ramanathan, V., P. J. Crutzen, J. T. Kiehl, and D. Rosenfeld (2001a), Atmosphere: Aerosols, climate, and the hydrological cycle, *Science*, *294*, 2119–2124.

Ramanathan, V., et al. (2001b), Indian Ocean Experiment: An integrated analysis of the climate forcing and effects of the great Indo-Asian haze, *J. Geophys. Res.*, *106*(D22), 28,371–28,398.

Ramanathan, V., et al. (2005), Atmospheric Brown Clouds: Impacts on South Asian Climate and Hydrological Cycle, *102*, 5326–33.

Ramanathan, V., and G. Carmichael (2008), Global and regional climate changes due to black carbon, *Nat. Geosci.*, *1*, 221–227.

Remer, L. A., et al. (2008), Global aerosol climatology from the MODIS satellite sensors, *J. Geophys. Res. Atmos.*, *113*(D14), doi:10.1029/2007JD009661.

Ricchiazzi, P., S. Yang, C. Gautier, and D. Sowle (1998), SBDART: A research and teaching software tool for plane-parallel radiative transfer in the Earth's atmosphere, *Bull. Am. Meteorol. Soc.*, *79*(10), 2101–2114.

Safai, P., M. Raju, K. Budhavant, P. Rao, and P. Devara (2013), Long term studies on characteristics of black carbon aerosols over a tropical urban station Pune, India, *Atmos. Res.*, *132-133*, 173–184.

Sandradewi, J., A. Prévôt, E. Weingartner, R. Schmidhauser, M. Gysel, and U. Baltensperger (2008), A study of wood burning and traffic aerosols in an Alpine valley using a multi-wavelength Aethalometer, *Atmos. Environ.*, *42*(1), 101–112.

Sarkar, C., A. Chatterjee, A. K. Singh, S. K. Ghosh, and S. Raha (2015), Characterization of black carbon aerosols over Darjeeling - a high altitude Himalayan station in eastern India, *Aeros. Air Qual. Res.*, *15*(2), 465–478.

Schmid, O., P. Artaxo, W. P. Arnott, D. Chand, L. V. Gatti, G. P. Frank, A. Hoffer, M. Schnaiter, and M. O. Andreae (2006), Spectral light absorption by ambient aerosols influenced by biomass burning in the Amazon basin. I: Comparison and field calibration of absorption measurement techniques, *Atmos. Chem. Phys.*, *6*(11), 3443–3462.

Seinfeld, J., and S. Pandis (1998), *Atmospheric Chemistry and Physics: From Air Pollution to Climate Change*, John Wiley, Hoboken, N. J.

Sharma, D., A. Srivastava, K. Ram, A. Singh, and D. Singh (2017), Temporal variability in aerosol characteristics and its radiative properties over Patiala, northwestern part of India: Impact of agricultural biomass burning emissions, *Environ. Pollut.*, *231*, 1030–1041.

Singh, B. P., et al. (2015), Seasonal inhomogeneity of soot particles over the central Indo-Gangetic Plains, India: Influence of meteorology, *J. Meteorol. Res.*, *29*(6), 935–949.

Singh, S., K. Soni, T. Bano, R. S. Tanwar, S. Nath, and B. C. Arya (2010), Clear-sky direct aerosol radiative forcing variations over mega-city Delhi, *Ann. Geophys.*, *28*(5), 1157–1166.

Soni, K., S. Singh, T. Bano, R. Tanwar, S. Nath, and B. Arya (2010), Variations in single scattering albedo and ångström absorption exponent during different seasons at Delhi, India, *Atmos. Environ.*, *44*(35), 4355–4363.

Spencer, M. T., J. C. Holecek, C. E. Corrigan, V. Ramanathan, and K. A. Prather (2008), Size-resolved chemical composition of aerosol particles during a monsoonal transition period over the Indian Ocean, *J. Geophys. Res.*, *113*(D16), doi:10.1029/2007JD008657.

Sreekanth, V., K. Niranjan, and B. L. Madhavan (2007), Radiative forcing of black carbon over eastern India, *Geophys. Res. Lett.*, *34*, doi:10.1029/2007GL030377.

Srivastava, A. K., S. Singh, P. Pant, and U. C. Dumka (2012), Characteristics of black carbon over Delhi and Manora Peak: comparative study, *Atmos. Sci. Lett.*, *13*(3), 223–230.

Srivastava, A., K. Ram, S. Singh, S. Kumar, and S. Tiwari (2015), Aerosol optical properties and radiative effects over Manora Peak in the Himalayan foothills: seasonal variability and role of transported aerosols, *Sci. Total Environ.*, *502*, 287–295.

Srivastava, A. K., D. Bisht, S. Singh, N. Kishore, V. Soni, S. Singh, and S. Tiwari (2018), Scattering and absorption characteristics of aerosols at an urban megacity over IGB: Implications to radiative forcing, *Atmos. Res.*, *205*, 107–117.

Stamnes, K., S. C. Tsay, W. Wiscombe, and K. Jayaweera (1988), Numerically stable algorithm for discrete-ordinate-method radiative transfer in multiple scattering and emitting layered media, *Appl. Opt.*, *27*, 2502–2509.

Stull, R. (1988), *An Introduction to Boundary Layer Meteorology*, Atmospheric and Oceanographic Sciences Library, Springer Netherlands.

Textor, C., et al. (2006), Analysis and quantification of the diversities of aerosol life cycles within AeroCom, *Atmos. Chem. Phys.*, *6*(7), 1777–1813.

Tiwari, S., A. Srivastava, D. Bisht, P. Parmita, M. K. Srivastava, and S. Attri (2013), Diurnal and seasonal variations of black carbon and PM2.5 over New Delhi, India: Influence of meteorology, *Atmos. Res.*, *125-126*, 50–62.

Toledano, C., V. E. Cachorro, A. M. de Frutos, B. Torres, A. Berjn, M. Sorribas, and R. S. Stone (2009), Airmass classification and analysis of aerosol types at El Arenosillo (Spain), *J. Appl. Meteorol. Clim.*, *48*(5), 962–981.

Twomey, S. (1977), *Atmospheric aerosols*, Elsevier Scientific Publishing Co., New York, USA.

Udayasoorian, C., R. M. Jayabalakrishnan, A. R. Suguna, M. M. Gogoi, and S. Suresh Babu (2014), Aerosol black carbon characteristics over a high-altitude western ghats location in southern India, *Ann. Geophys.*, *32*(10), 1361–1371.

Verma, S., D. Prakash, A. K. Srivastava, and S. Payra (2017), Radiative forcing estimation of aerosols at an urban site near the Thar desert using ground-based remote sensing measurements, *Aeros. Air Qual. Res.*, *17*(5), 1294–1304.

Virkkula, A., T. Mäkelä, R. Hillamo, T. Yli-Tuomi, A. Hirsikko, K. Hämeri, and I. K. Koponen (2007), A simple procedure for correcting loading effects of aethalometer data, *J. Air Waste Manage. Assoc.*, *57*(10), 1214–1222.

Wang, C., D. Kim, A. M. Ekman, M. C. Barth, and P. J. Rasch (2009), Impact of anthropogenic aerosols on Indian summer monsoon, *Geophys. Res. Lett.*, *36*(21), doi:10.1029/2009GL040114.

Wang, F., D. Chen, S. Cheng, J. Li, M. Li, and Z. Ren (2010), Identification of regional atmospheric PM10 transport pathways using HYSPLIT, MM5-CMAQ and synoptic pressure pattern analysis, *Environ. Modell. Softw.*, *25*(8), 927–934.

Wang, Y., P. K. Hopke, and M. J. Utell (2011), Urban-scale spatial-temporal variability of black carbon and winter residential wood combustion particles, *Aeros. Air Qual. Res.*, *11*(5), 473–481.

Warneck, P. (1988), *Chemistry of the Natural Atmosphere*, *Int. Geophy. Ser.*, vol. 71, Academic Press.

Weingartner, E., H. Saathoff, M. Schnaiter, N. Streit, B. Bitnar, and U. Baltensperger (2003), Absorption of light by soot particles: Determination of the absorption coefficient by means of aethalometers, *J. Aerosol Sci.*, *34*, 1445–1463.

Whitby, K. T. (1978), The physical characteristics of sulfur aerosols, *Atmos. Environ.*, *12*, 135–159.

Wielicki, B. A., T. Wong, N. Loeb, P. Minnis, K. Priestley, and R. Kandel (2005), Changes in Earth's Albedo Measured by Satellite, *Science*, *308*(5723), 825–825.

Wiscombe, W., and G. Grams (1976), The backscattered fraction in two-stream approximations, *J. Atmos. Sci.*, *33*(12), 2440–2451.

Xianda, G., C. Zhang, H. Chen, S. A. Nizkorodov, J. Chen, and X. Yang (2016), Size distribution and mixing state of black carbon particles during a heavy air pollution episode in Shanghai, *Atmos. Chem. Phys.*, *16*(8), 5399–5411.